A Top Quark Mass Measurement using a Matrix Element Method

Jacob Linacre
St. John's College College, Oxford

Thesis submitted in fulfilment of the requirements for the degree of
Doctor of Philosophy at the University of Oxford

Trinity Term, 2009

Abstract

A measurement of the mass of the top quark is presented, using top-antitop pair ($t\bar{t}$) candidate events for the lepton+jets decay channel. The measurement makes use of Tevatron $p\bar{p}$ collision data at centre-of-mass energy $\sqrt{s} = 1.96$ TeV, collected at the CDF detector. The top quark mass is measured by employing an unbinned maximum likelihood method where the event probability density functions are calculated using signal ($t\bar{t}$) and background (W+jets) matrix elements, as well as a set of parameterised jet-to-parton mapping functions. The likelihood function is maximised with respect to the top quark mass, the fraction of signal events, and a correction to the jet energy scale (JES) of the calorimeter jets. The simultaneous measurement of the JES correction (Δ_{JES}) provides an *in situ* jet energy calibration based on the known mass of the hadronically decaying W boson. Using 578 lepton+jets candidate events corresponding to 3.2 fb^{-1} of integrated luminosity, the top quark mass is measured to be $m_t = 172.4 \pm 1.4\,(\mathrm{stat} + \Delta_{\mathrm{JES}}) \pm 1.3\,(\mathrm{syst})$ GeV/c^2, one of the most precise single measurements to date.

For my parents.

Acknowledgements

I'd like to thank all of the people who have contributed to the completion of this analysis. My supervisor, Pete Renton, and my advisor, Sasha Golossanov, have always been there to answer my questions, and provided valuable insight into the problems I encountered. In particular, I'd like to thank Sasha for showing me the ropes, and Daryl Hare for helping acquaint me with C++ and for all of his hard work on the analysis. I'd also like to thank Florencia Canelli and Eva Halkiadakis for all of their important input at our weekly meetings, and for keeping us on track. Finally, I'd like to thank our analysis reviewers, the top and top mass group conveners, and all of the other people who took part in the blessing of the analysis, for the interesting questions they asked.

Contents

List of Figures

List of Tables

Introduction

Experimental particle physics is predominated by particle accelerators, which produce the high energy particle collisions necessary to probe the properties of the fundamental particles and their interactions.

The analysis presented in this thesis was completed at the Fermi National Accelerator Laboratory (Fermilab) in Batavia, IL, USA. At Fermilab, protons and antiprotons are accelerated in opposite directions in a 4-mile circumference ring known as the Tevatron, the highest energy particle accelerator in operation as of September 2009. The protons and antiprotons collide at two points around the ring, where the results are measured using large multi-purpose detectors. The detector used in this analysis is the Collider Detector at Fermilab (CDF).

The top quark is the heaviest known fundamental particle, and the measurement of its mass is the focus of this thesis. The top quark mass is an intrinsic parameter of the Standard Model (SM) of particle physics, and its precise measurement can provide a consistency test of the model. It can also impose constraints on other parameters of the model, most pertinently the mass of the SM Higgs boson.

In experimental particle physics, top quarks have so far been produced only at the Tevatron, the only collider operating at sufficiently high energy. The analysis presented in this thesis uses an advanced statistical method based on the SM description of top quark production and decay, known as a "matrix element method", to extract a precise top quark mass measurement from the CDF data.

Chapter 1 gives an overview of the particle physics theory necessary for the construction of this analysis, including a description of the SM and the properties of the top quark. The apparatus necessary to collect the data used in this analysis, the Fermilab accelerator complex and the CDF detector, are described in Chapter 2. The reconstruction of that data into physically meaningful quantities, and the selection of the data to be used in the analysis, are described in Chapter 3. The simulation of data is an important part of the construction and calibration of the measurement method, and is described in Chapter 4. Chapters 1-4 are primarily informative, and serve as a base on which to build the analysis; there are no novel additions from the author in these areas.

The construction of the method of measurement is described in Chapter 5. The method is based on a previous analysis [1], but there are many new contributions from the author. First, there were significant problems with the old method, which required extensive investigation and ultimately rectification. These consisted mostly of mistakes and oversights, many significantly biasing the measurement. Second, with much of the general top quark analysis procedure already well defined, it is the jet-to-parton mapping functions that offer the best opportunity to improve many important details of the physical description. These are described in Chapter 6, and there were significant contributions in this section from the author, including the introduction of new jet-to-parton mapping functions for the jet angles.

Once constructed, the measurement method must be tested and calibrated, and this is detailed in Chapter 7. The systematic uncertainties of the measurement are calculated, based on standard CDF procedures, in Chapter 8. The results of the measurement are presented in Chapter 9, and conclusions, including implications for the mass of the Higgs boson, are given in Chapter 10.

Chapter 1

Theoretical Overview

This chapter gives a brief outline of the particle physics theory used as a basis for this analysis. For a more detailed account see, for example, books [2, 3, 4].

1.1 The Standard Model

The Standard Model (SM) of particle physics is a theory describing the elementary particles and three of the fundamental interactions between them. The theory is incomplete in that it does not describe gravity, the fourth known fundamental interaction, but is remarkably accurate in its description of the remaining three: electromagnetism and the strong and weak interactions. The elementary particles of the SM and their masses are summarised in Table 1.1.

The SM is constructed as a gauge theory, with the elementary particles corresponding to the fields invariant under the transformations of the symmetry group ("gauge group") $SU(3)_C \times SU(2)_L \times U(1)_Y$. $SU(3)_C$ is the gauge group for Quantum Chromodynamics (QCD) [6, 7], the theory of the strong interaction via the colour force. Particles corresponding to $SU(3)_C$ triplets are known as quarks. They carry colour charge and can thus interact via

Quarks	Mass	Leptons	Mass
u, up	~ 2 MeV/c^2	ν_e, e-neutrino	< 2.2 eV/c^2
d, down	~ 5 MeV/c^2	e, electron	0.51100 MeV/c^2
c, charm	~ 1.3 GeV/c^2	ν_μ, μ-neutrino	< 170 keV/c^2
s, strange	~ 0.1 GeV/c^2	μ, muon	105.66 MeV/c^2
t, top	173.1 GeV/c^2	ν_τ, τ-neutrino	< 15.5 MeV/c^2
b, bottom	~ 4.2 GeV/c^2	τ, tauon	1776.8 MeV/c^2

Table 1.1: Fundamental Fermions. Apart from the top quark, the quark masses are inferred from their bound states using various models and are therefore approximate. Note that the stated value of the top quark mass is the world average as of March 2009 [5], which does not include the result of this analysis.

	Generation						
Quark Type	I	II	III	T	T_3	Y	$Q = T_3 + Y/2$
L doublets	$\begin{pmatrix} u_L \\ d_L \end{pmatrix}$	$\begin{pmatrix} c_L \\ s_L \end{pmatrix}$	$\begin{pmatrix} t_L \\ b_L \end{pmatrix}$	$1/2$	$\begin{pmatrix} 1/2 \\ -1/2 \end{pmatrix}$	$1/3$	$\begin{pmatrix} 2/3 \\ -1/3 \end{pmatrix}$
R singlet (q)	u_R	c_R	t_R	0	0	$4/3$	$2/3$
R singlet (q')	d_R	s_R	b_R	0	0	$-2/3$	$-1/3$

Table 1.2: Quarks and their electroweak quantum numbers. Left-handed quarks form $SU(2)_L$ doublets while right-handed quarks form $SU(2)_L$ singlets.

	Generation						
Lepton Type	I	II	III	T	T_3	Y	$Q = T_3 + Y/2$
L doublets	$\begin{pmatrix} \nu_{e\,L} \\ e_L \end{pmatrix}$	$\begin{pmatrix} \nu_{\mu\,L} \\ \mu_L \end{pmatrix}$	$\begin{pmatrix} \nu_{\tau\,L} \\ \tau_L \end{pmatrix}$	$1/2$	$\begin{pmatrix} 1/2 \\ -1/2 \end{pmatrix}$	-1	$\begin{pmatrix} 0 \\ -1 \end{pmatrix}$
R singlet	e_R	μ_R	τ_R	0	0	-2	-1

Table 1.3: Leptons and their electroweak quantum numbers. Left-handed leptons form $SU(2)_L$ doublets while right-handed leptons form $SU(2)_L$ singlets.

the colour force. Particles that do not carry colour charge ($SU(3)_C$ singlets) do not interact strongly and are known as leptons. Free quarks are not observed in nature, and exist only in colourless bound states. Leptons, which are naturally colourless, exist as free particles.

Quarks and leptons are all spin-1/2 fermions and the two types behave in similar ways via the unified electroweak (EW) interaction, which is described by the Glashow-Weinberg-Salam (GSW) [8, 9, 10] model. The GSW model is a chiral gauge theory, meaning that the weak interactions of particles are dependent on their chirality, and has gauge group $SU(2)_L \times U(1)_Y$, with further subdivision of particle types dictated by the symmetry properties of this group (see Tables 1.2 and 1.3). The chirality of a particle describes its handedness, a property related to the $SU(2)_L$ weak interaction charge known as weak isospin, T. Fermions with negative chirality are "left-handed" (L) and have weak isospin $T = 1/2$, thus forming $SU(2)_L$ doublets: "up type" quarks (q) have third component of weak isospin $T_3 = 1/2$, and the opposite "down type" quarks (q') have $T_3 = -1/2$; the same distinction is seen in leptons with neutrinos (ν) having $T_3 = 1/2$ and charged leptons (ℓ) having $T_3 = -1/2$. Fermions with positive chirality are "right-handed" (R) and have $T = 0$, thus forming $SU(2)_L$ singlets. Both up-type and down-type quarks can exist in right-handed states, but the same is not true for leptons, with only charged leptons, and not neutrinos, existing in right-handed states in the SM[1]. The weak hypercharge, Y, is the quantum number associated with the $U(1)_Y$ group. It is related to electric charge, Q, by $Q = T_3 + Y/2$.

All types of quarks and leptons are further divided into three "generations" with similar properties (see Tables 1.2 and 1.3). All quarks and leptons also have associated antiparticles (denoted by a bar, e.g. $\bar{q}$), which have opposite quantum numbers and chirality. The

[1]The nonexistence of right-handed neutrinos in the SM is related to the fact that neutrinos are assumed to be massless, which is discussed later in this section.

Interaction	Gauge Boson	Mass (GeV/c^2)	T_3	Y	Q
strong	8 g	0	0	0	0
weak	W^+	80.4	1	0	1
weak	W^-	80.4	-1	0	-1
weak	Z^0	91.2	0	0	0
EM	γ	0	0	0	0

Table 1.4: Gauge bosons of the Standard Model, and their masses and electroweak quantum numbers.

behaviour of antiparticles is not quite identical to that of their corresponding particles due to CP violation, although such effects are expected to be small enough to be neglected in this analysis. CP is the combination of the charge conjugation operator C and the parity operator P that together act to take a particle to its antiparticle, and CP violation is the contravention of CP, or particle-antiparticle, symmetry.

Each of the gauge symmetry groups of the SM has an associated set of generators corresponding to the possible gauge transformations of the group. The demand for local gauge invariance means that each generator gives rise to an associated gauge field. The gauge field quanta, "gauge bosons", act as mediators of the fundamental interactions of their symmetry group. The gauge bosons in the SM all have spin 1, and those for $SU(3)_C$ (QCD) are known as gluons while those for $SU(2)_L \times U(1)_Y$ (the unified EW interaction) are the W^+, W^-, Z^0, and the photon, γ. Gluons, of which there are eight types, only couple to particles with colour charge (i.e. quarks, or other gluons). W^+ and W^- couple to all left-handed particles (and their right-handed antiparticles), Z^0 couples to both left- and right-handed particles (although with different coupling strengths), and γ couples to all electrically charged particles, with the same coupling strength for left- and right-handed particles. The gauge bosons of the SM and their couplings are summarised in Table 1.4 and Figure 1.1.

Couplings are often represented diagrammatically as vertices of particle lines in Feynman diagrams (see Figure 1.2). Each Feynman diagram represents the amplitude for the process it depicts, which is completely described by the invariant amplitude, or "matrix element", $\mathcal{M}$, for that process. Each vertex in the diagram introduces a factor of the interaction coupling constant, g, into the matrix element. For any given set of initial- and final-state particles, the Feynman diagram(s) with the least number of vertices represent the Leading Order (LO) contribution(s) to that process. However, diagrams can also be constructed with an arbitrarily large number of vertices, and the sum of all such invariant amplitudes gives the total matrix element for the process. Physical quantities, such as cross-sections and lifetimes, depend on $\mathcal{M}^2$, and the highest power of g^2 above LO to which the expression for $\mathcal{M}^2$ is expanded defines the order of the calculation. Calculations to higher than Leading Order are referred to as Next-to-Leading-Order (NLO), and then Next-to-Next-to-Leading-Order (NNLO), and so on. Such calculations are referred to as perturbative calculations, and when $g \ll 1$ the higher order contributions rapidly become negligibly small.

In QCD, g_s decreases with increasing squared four-momentum transfer Q^2. For high-Q^2 interactions, such as the pair-production of top quarks, $g_s \ll 1$ and the matrix element

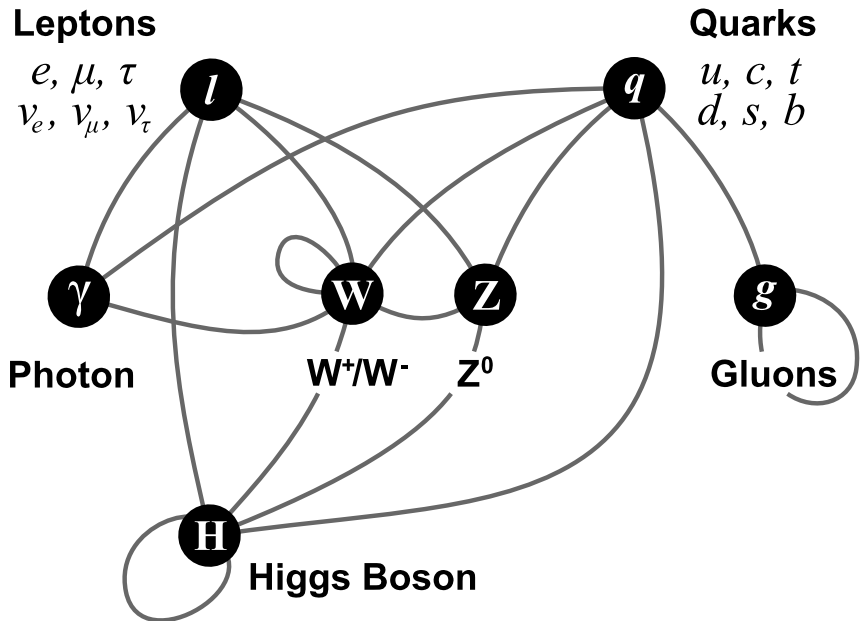

Figure 1.1: Couplings of the Standard Model gauge bosons.

for the process may be reasonably approximated using only the LO diagrams. However, g_s becomes large for low-Q^2 processes such as hadronisation, meaning such amplitudes cannot be calculated perturbatively.

The $SU(3)_C \times SU(2)_L \times U(1)_Y$ symmetry described so far is exact, and consequently predicts all of the SM fermions and bosons to be massless. The large observed masses of the weak interaction W and Z bosons (Table 1.4) can be explained by a spontaneous breaking of the weak isospin $SU(2)_L$ symmetry, caused by a predicted Higgs scalar field. The Higgs field would also couple to fermions ("Yukawa couplings"), accounting for their observed non-zero masses. The SM Higgs field, ϕ, is described by an $SU(2)_L$ doublet of complex scalar fields (Table 1.5). After spontaneous symmetry breaking, three of the four Higgs fields can be reduced to zero by gauge transformations, giving rise to the longitudinal polarisation states of the W^+, W^- and Z^0 bosons necessary for them to be massive. A single neutral massive scalar field remains, the Higgs boson, H [11]. Unlike the other SM particles, the Higgs boson has yet to be discovered.

Although the SM Higgs boson can account for the observed fermion masses, the theory does not make any prediction of the individual masses, nor why they have such a large range. In fact, in the SM each fermion mass is set by its empirically-determined Yukawa coupling, which requires the introduction of an additional parameter in the theory for each fermion mass.

In the SM, neutrinos are assumed to be massless. For a massless particle, chirality can be exactly identified with the sign of the projection of the particle's spin on its direction of motion, known as the helicity. Furthermore, helicity is Lorentz-invariant for massless particles, so the handedness of SM neutrinos must also be conserved. Since neutrinos carry no colour or electric charge, only left-handed neutrinos can be involved in any SM interaction,

Higgs field	T	T_3	Y	Q
$\phi = \begin{pmatrix} \phi^+ \\ \phi^0 \end{pmatrix}$	$1/2$	$\begin{pmatrix} 1/2 \\ -1/2 \end{pmatrix}$	1	$\begin{pmatrix} 1 \\ 0 \end{pmatrix}$

Table 1.5: The Standard Model Higgs field, ϕ, and its electroweak quantum numbers. The components ϕ^+ and ϕ^0 are both complex, so there are four fields in total.

and thus the SM predicts only left-handed neutrinos (see Table 1.3). However, the recent observations of neutrino oscillations are incompatible with massless neutrinos.

Particles of different generations are generally distinct due to their different masses, and particles thus described are said to be in "mass eigenstates"[2]. However, the W boson does not directly couple to mass eigenstates, and instead couples to mixed-generation T_3 eigenstates that are known as "weak interaction eigenstates". In the GSW model, this "weak mixing" between generations of quarks is parameterised by the Cabibbo-Kobayashi-Maskawa (CKM) matrix, with the weak interaction eigenstates denoted by a prime:

$$\begin{bmatrix} |d'\rangle \\ |s'\rangle \\ |b'\rangle \end{bmatrix} = \begin{bmatrix} V_{ud} & V_{us} & V_{ub} \\ V_{cd} & V_{cs} & V_{cb} \\ V_{td} & V_{ts} & V_{tb} \end{bmatrix} \begin{bmatrix} |d\rangle \\ |s\rangle \\ |b\rangle \end{bmatrix}. \tag{1.1.1}$$

The quantity $|V_{ij}|^2$ therefore describes the probability of a coupling between mass eigenstates i and j, and can be measured experimentally. The parameters V_{ij} are not predicted by theory, and the quantities $|V_{ij}|$ are taken from experimental results [12]:

$$\begin{bmatrix} |V_{ud}| & |V_{us}| & |V_{ub}| \\ |V_{cd}| & |V_{cs}| & |V_{cb}| \\ |V_{td}| & |V_{ts}| & |V_{tb}| \end{bmatrix} = \begin{bmatrix} 0.97419 \pm 0.00022 & 0.2257 \pm 0.0010 & 0.00359 \pm 0.00016 \\ 0.2256 \pm 0.0010 & 0.97334 \pm 0.00023 & 0.0415^{+0.0010}_{-0.0011} \\ 0.00874^{+0.00026}_{-0.00037} & 0.0407 \pm 0.0010 & 0.999133^{+0.000044}_{-0.000043} \end{bmatrix}. \tag{1.1.2}$$

The tight constraints on $|V_{tb}|$ are provided not by direct measurement, but by the requirement of the matrix to be unitary along with the assumption of three generations.

A similar weak mixing matrix (Maki-Nakagawa-Sakata, MNS) exists for leptons, but is not relevant to this analysis.

1.2 The Top Quark

The top quark is the up-type third-generation quark. The existence of the third generation of particles was indicated by the 1964 discovery of CP violation in neutral kaons [13]. The down-type third-generation quark, the bottom quark, was discovered in 1977 [14], and the top quark was discovered at Fermilab in 1995 [15, 16].

[2]For massless or otherwise degenerate particles, e.g. neutrinos, the mass eigenstates could be defined as an arbitrary mixture of the generations.

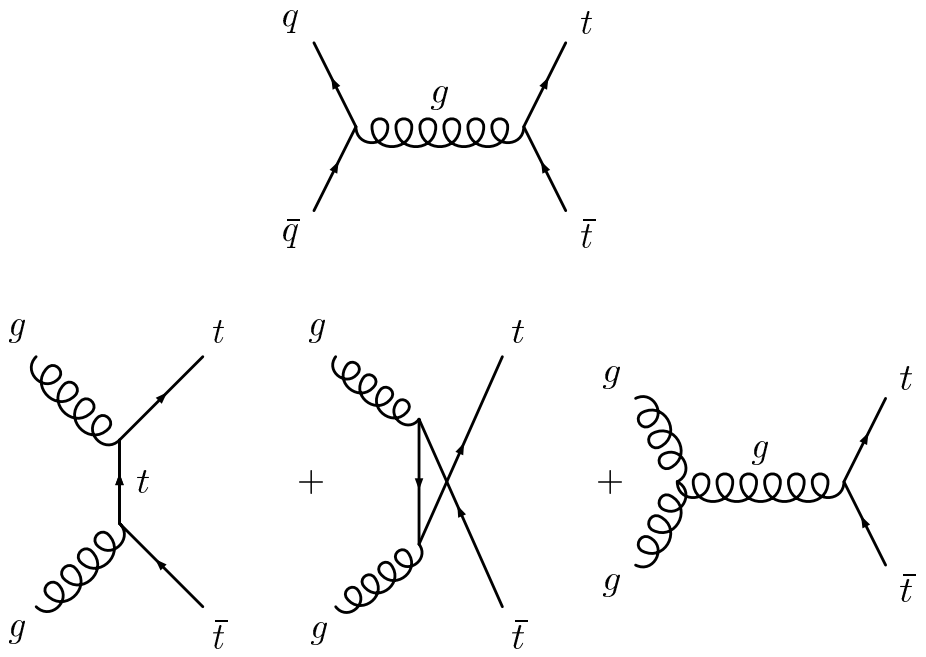

Figure 1.2: Feynman diagrams illustrating leading order top quark pair production.

1.2.1 Production

The dominant top quark production process is pair-production via the strong interaction, illustrated in Figure 1.2. At CDF, these processes are initiated using $p\bar{p}$ collisions at centre-of-mass energy $\sqrt{s} = 1.96$ TeV (see Section 2.1.3). Each such collision may be approximated to involve two "partons", constituents of the proton and antiproton, that may be identified as quarks, antiquarks, or gluons.

Each parton carries a longitudinal fraction x_{Bj} of the 0.98 TeV/c proton or antiproton momentum, and each collision involves a four-momentum transfer Q between the partons. The probability density for finding a parton with longitudinal momentum fraction x_{Bj}, at a given Q, is described by the proton (or antiproton) Parton Distribution Function (PDF) for that parton. For collisions at 1.96 TeV, the PDFs for the valence quarks[3] dominate in the high-Q^2 collisions required for top quark production. Overall, $q\bar{q}$ collisions produce about 85% of observed top quarks at CDF, while the remaining 15% come from gluon collisions.

The SM theoretical cross-section for $p\bar{p} \to t\bar{t}$ has been calculated to Next-to-Next-to-Leading Order (NNLO) [17], for $m_t = 175$ GeV/c^2 and $\sqrt{s} = 1.96$ TeV, to be $\sigma_{p\bar{p}\to t\bar{t}}^{\mathrm{NNLO_{approx}}} = 7.09^{+0.34}_{-0.41}$ pb.

Top quarks can also be produced singly via the weak interaction, a process known as single top quark production and illustrated in Figure 1.3. Top quarks produced in this way are more difficult to identify and only recently experimentally confirmed.[4] The SM theoretical cross-section for $p\bar{p} \to t + X$ has been calculated at NLO with NNLO and

[3]The valence quarks of the proton are its "real" constituent quarks, *uud*, as opposed to the "virtual" quarks and gluons that fluctuate in and out of existence.

[4]Single top quark production was discovered at CDF and DØ in March 2009 [18, 19].

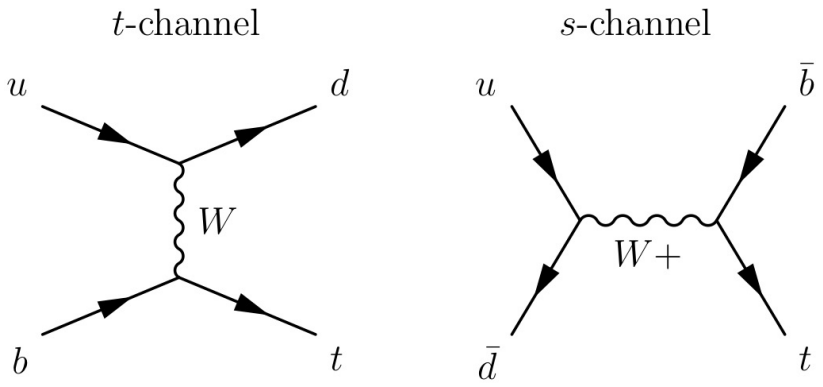

Figure 1.3: Feynman diagrams illustrating leading order "t"-channel and "s"-channel single top quark production.

NNNLO threshold soft-gluon corrections [20], for $m_t = 175$ GeV/c^2 and $\sqrt{s} = 1.96$ TeV, to be $\sigma_{t+s}^{\text{NLO+corr}} = 1.57 \pm 0.06$ pb. This includes "t"-channel and "s"-channel single top production but not associated tW production ($bg \rightarrow tW^-$), for which the cross-section is very small at the Tevatron (~ 0.07 pb).

This analysis is intended only to measure the top quark mass using pair-produced top quarks, and treats the topologically incompatible single top quark production as a background process (Section 1.3).

1.2.2 Decay

As the most massive of quarks, the top quark is very unstable. It decays rapidly with lifetime $\tau_t \sim 10^{-25}$ s, fast enough that it has essentially no time to interact and may be considered as a free quark. This allows a direct measurement of its mass from the daughter particles from its decay, and as a result the top quark mass is the best measured of the quarks (Figure 1.4).

Top quarks decay via the weak interaction, almost invariably ($|V_{tb}|^2 \sim 99.8\%$) to a W boson and a b-quark (Figure 1.6). Decays to $W + s$ or $W + d$ are strongly supressed via the small off-diagonal CKM matrix quantities $|V_{ts}|$ and $|V_{td}|$ (see Equation 1.1.2).

The W boson decays into lower-mass fermion-antifermion pairs with combined $|T_3| = 1$: a charged lepton and a neutrino, "leptonic decay"; or an up-type quark and a down-type quark, "hadronic decay". The branching ratios for leptonic W boson decay are approximately $\frac{1}{9}$ for each of the 3 generations, while the sum of the hadronic branching ratios makes up the remaining $\sim \frac{2}{3}$. With one W boson produced from each of the two top quark decays, this results in three distinct decay channels for pair-produced top quarks.

- *Dilepton channel*, where both W bosons decay leptonically.
- *Lepton+jets channel*, where one W boson decays leptonically, the other hadronically.
- *All-hadronic channel*, where both W bosons decay hadronically.

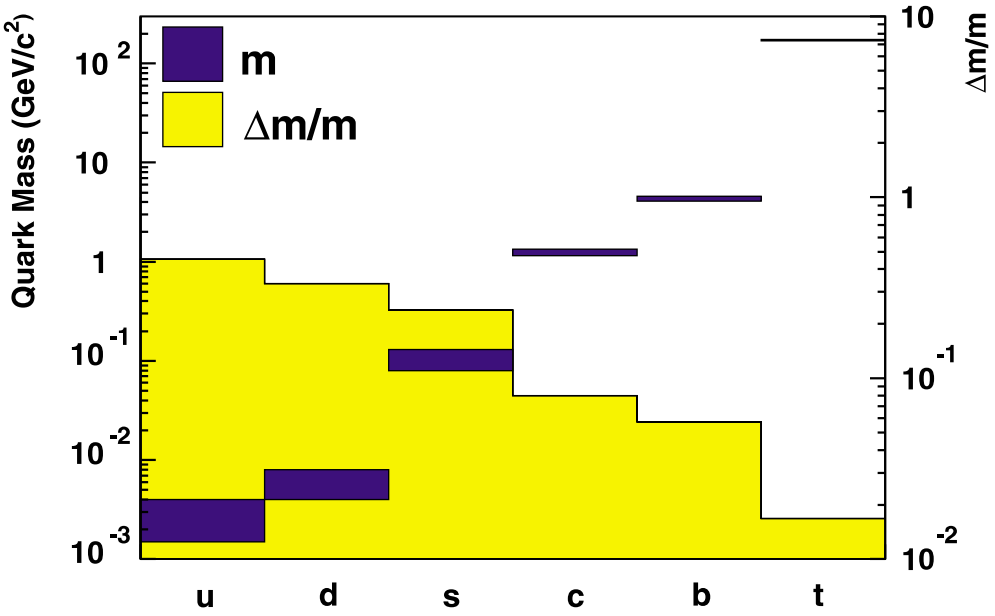

Figure 1.4: Quark masses (blue bars) and their relative uncertainties (yellow histogram). The top quark mass has the lowest relative uncertainty largely due to its short lifetime, which effectively allows the measurement of the mass of the bare quark.

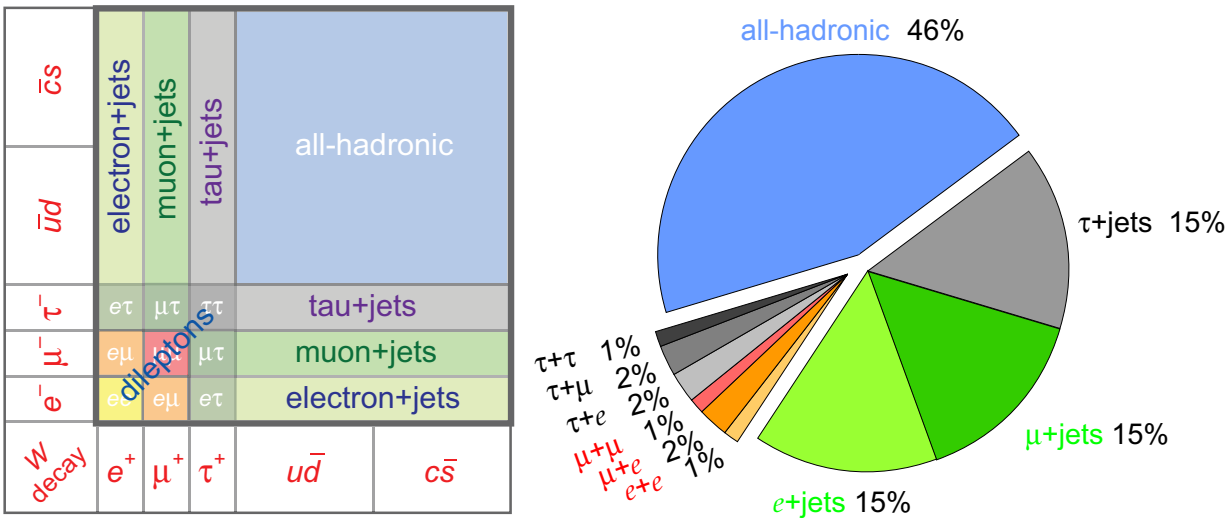

Figure 1.5: Left: How the $t\bar{t}$ decay channels are classified based on the two independent W-boson decays; the areas of the boxes represent the approximate branching ratios. Right: Approximate branching ratios represented in a pie chart.

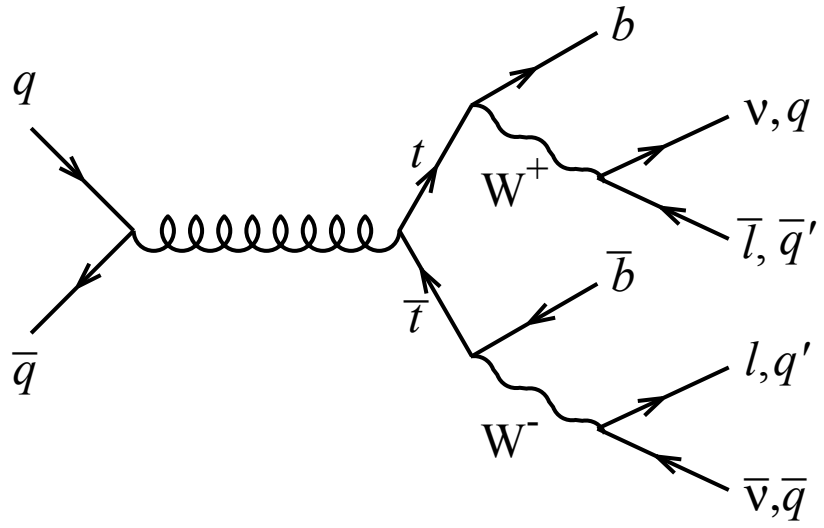

Figure 1.6: Feynman diagram illustrating the decay of pair-produced top quarks. The two modes of W boson decay result in three distinct decay channels for pair-produced top quarks.

The $t\bar{t}$ decay topologies and their approximate branching ratios are summarised in Figure 1.5. Since tauons are difficult to measure in the CDF detector, decay channels containing tauons are not considered for use in this analysis and are categorised separately. The remaining approximate branching ratios are therefore 5%, 30%, and 46% for the dilepton, lepton+jets, and all-hadronic channels respectively.

Of the three channels, the lepton+jets channel provides the best statistical sensitivity to the top quark mass and is the channel used in this analysis. It has a relatively large branching ratio combined with much less background contamination than the all-hadronic channel, and only one final-state neutrino meaning that the kinematics are not severely underconstrained as in the dilepton channel.

The relatively long lifetime of the b-quark means that it forms bound states with other quarks, a process known as "hadronisation". The lifetime of the b-quark hadrons is known to be $\tau_b \sim 10^{-12}$ s, meaning that the b-quarks can be identified ("tagged") by detecting the displaced secondary vertices signifying the decay of a b-quark hadron (Section 3.3.3).

Note that in this analysis, top and antitop quark decays are treated as identical processes apart from the replacement of particles with their antiparticles. They are therefore interchangeable in any illustrative diagrams and topologies.

1.2.3 Significance of the top quark mass

The top quark mass, m_t, is a fundamental parameter of the SM, and is of particular importance due to its strikingly large value. As a result, it has a large effect on radiative corrections to electroweak processes and has a Yukawa coupling to the Higgs field of $\mathcal{O}(1)$, providing a possible insight into the mechanism of electroweak symmetry breaking.

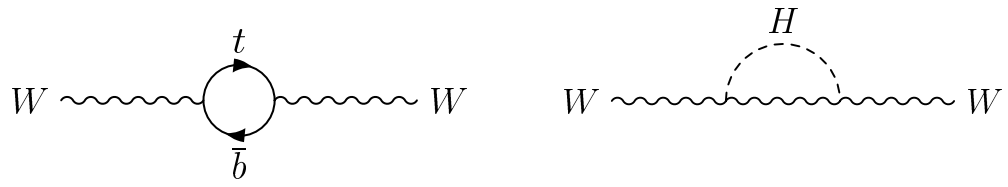

Figure 1.7: NLO radiative corrections to m_W, left diagram $\propto m_t^2$ and right diagram $\propto \ln m_H$.

The Higgs boson mass, m_H, is not predicted by the SM, but constraints on its value can be derived from the calculation of radiative corrections to the W boson mass, m_W, and other precision electroweak variables. These corrections depend primarily on m_H and m_t (Figure 1.7). Precision measurements of m_W and m_t therefore provide direct constraints on m_H (Figure 1.8). Similar constraints can also be imposed in new physics models such as the Minimal Supersymmetric Standard Model (MSSM) [21], also illustrated in Figure 1.8, where the mass of the lightest neutral Higgs boson is constrained.

1.3 Background processes

Since the total $p\bar{p}$ inelastic cross-section $\sigma_{p\bar{p}} \sim 80$ mb, the number of collisions, or "events", that result in top quark pair production is just a tiny fraction ($\sigma_{p\bar{p}\to t\bar{t}}/\sigma_{p\bar{p}} \sim 10^{-10}$) of the total number of events. Many of these undesirable events can be eliminated by the event selection criteria detailed in Chapter 3. Other processes, known as "background" processes, can mimic the lepton+jets decay signature, being indistinguishable from true $t\bar{t}$ events in the detector and providing spurious information about the top quark mass. The backgrounds expected to contribute to the final data sample are described in Section 4.4.

This analysis is optimised to reduce the effect of the background events, both in the construction of the event probability density function (Chapter 5) and in the calibration of the measurement (Chapter 7).

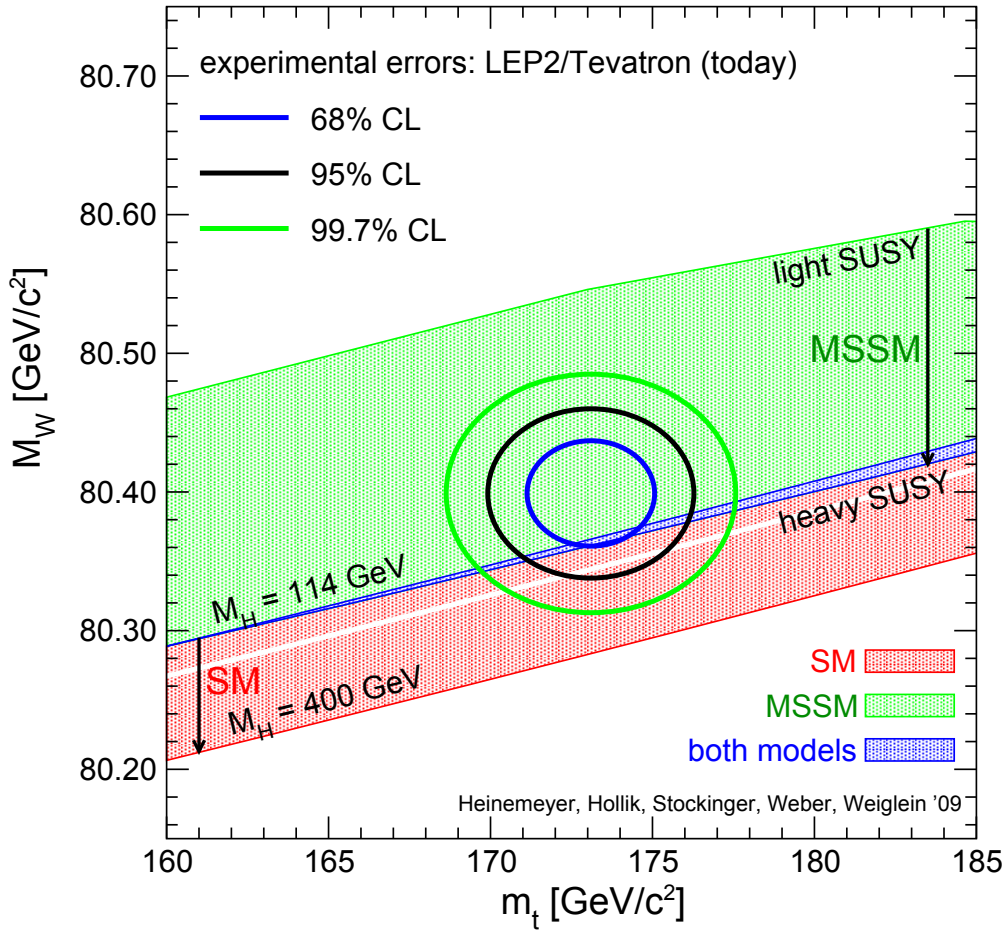

Figure 1.8: m_W vs m_t as a function of m_H, updated from [21]. The world average measurements of m_W and m_t provide the constraints illustrated by the ellipses. The regions allowed by theory, and so far not experimentally excluded, are coloured red for the SM and green for the MSSM.

Chapter 2

Experimental Apparatus

As discussed in Chapter 1, the pair-production of top quarks requires particle collisions at high energy. At Fermilab those particles are chosen to be protons and antiprotons, counter-rotating in a 6.3 km circumference synchrotron (the Tevatron) at energies of 0.98 TeV.

This chapter provides a brief description of the experimental apparatus relevant to this analysis. A full description of the Fermilab accelerator complex is given in [22], while a full description of the CDF detector is provided in [23].

2.1 Accelerator complex

The production and the various stages of the acceleration of the proton and antiproton beams is described in this section. A schematic of the accelerator complex is shown in Figure 2.1.

2.1.1 Proton source

The initial source of protons is hydrogen gas. The hydrogen atoms are ionized to H^-, allowing a successive acceleration to 750 keV using a Cockroft-Walton generator. The H^- ions are then transferred to the Linac, a 150 m long linear accelerator, where they are accelerated to 400 MeV using Radio Frequency (RF) cavities. At this stage the ions are passed through a carbon foil, removing the electrons and leaving a beam of protons which is injected into the Booster. The Booster is a synchrotron of 150 m diameter filled with bending magnets, where the protons are accelerated in RF cavities. The RF and magnetic field strength are both gradually increased, bringing the proton energy to 8 GeV. The protons then enter the Main Injector, a larger synchrotron of 1 km diameter, where they are accelerated to an energy of 150 GeV ready for injection into the Tevatron. The Main Injector is also used in antiproton production and acceleration, as described in Section 2.1.2.

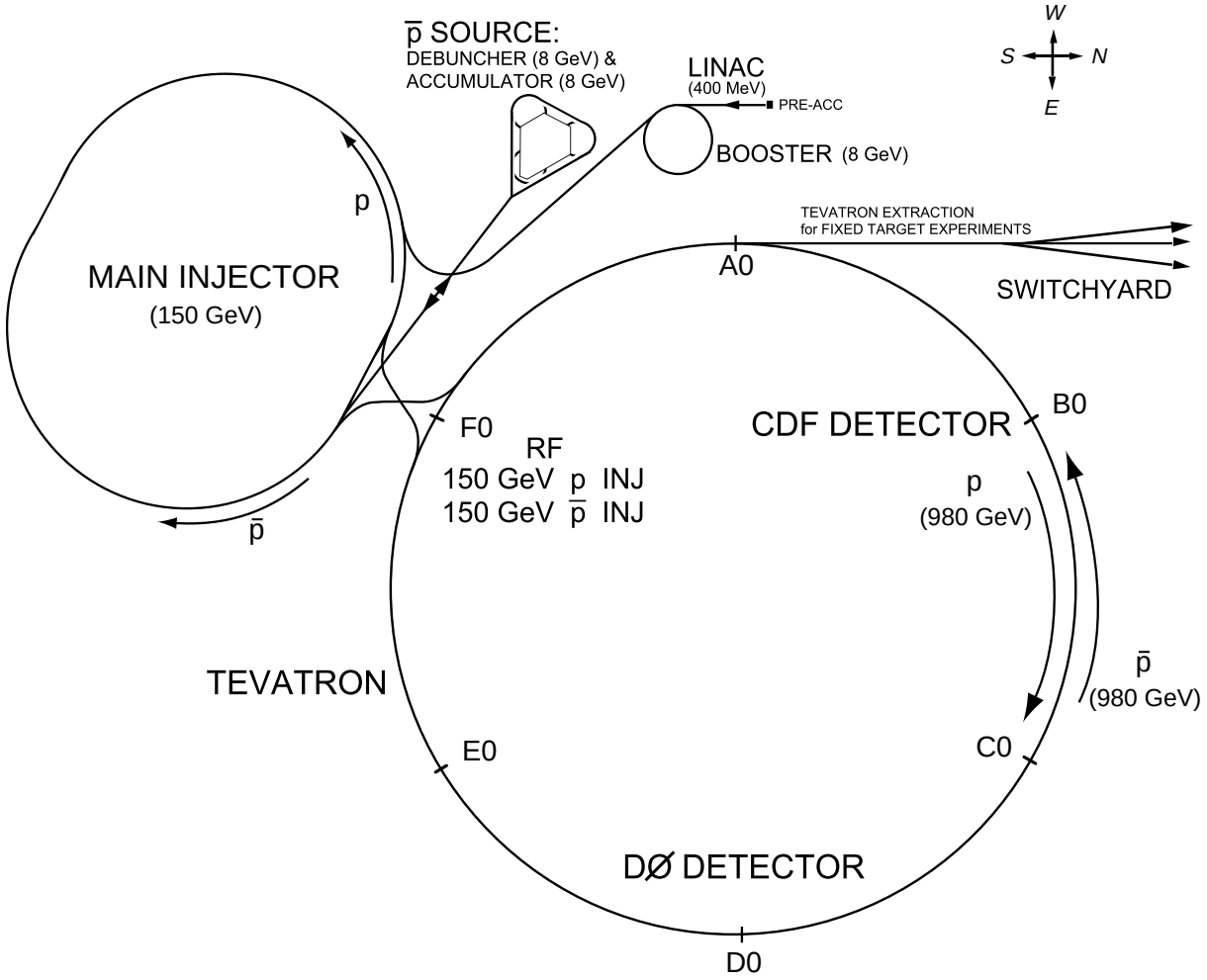

Figure 2.1: Schematic of the Fermilab accelerator complex, illustrating the components used in the production and acceleration of the proton and antiproton beams as well as the location of the CDF detector.

2.1.2 Anti-Proton source

Since there is no ready source of antiprotons, they must first be manufactured. Protons in the Main Injector are accelerated to an energy of 120 GeV before being collided with a stationary nickel alloy target, and the various by-products of the collisions include antiprotons. This is an inefficient process yielding just 20 antiprotons for every million incident protons, and makes antiproton production the major factor in limiting overall collider luminosity. The antiprotons are identified and separated with the use of a magnetic field, with particles of different masses and charges following different helical trajectories. The antiprotons in the resulting beam have an average energy of about 8 GeV, although with a large energy spread. The beam is transferred to the Debuncher, a triangular synchrotron of 90 m radius, where the energy spread is reduced to form a continuous beam at 8 GeV. The transverse momentum spectrum is also reduced using stochastic cooling, a negative feedback technique [24].

Every few seconds, the antiprotons are transferred in a pulse to the Accumulator, a

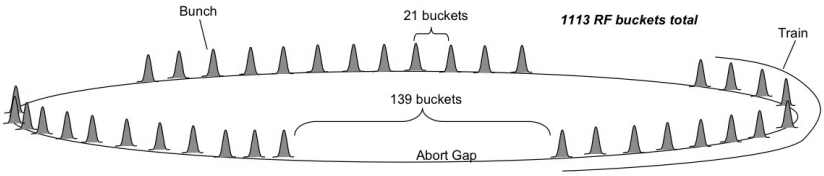

Figure 2.2: Tevatron bunch structure. The proton and antiproton beams are both divided into 36 bunches of particles, composing 3 trains of 12 bunches that are separated by abort gaps. Separations are given in terms of the number of RF buckets.

second 8 GeV triangular synchrotron housed in the same tunnel as the Debuncher, where antiprotons are stored at a rate of up to 3×10^{11} $\bar{p}$/hour. The Accumulator can hold up to about 10^{12} antiprotons, after which the accumulated beam is transferred to the Recycler, an 8 GeV permanent-magnet synchrotron sharing the same tunnel as the Main Injector. The Recycler employs electron cooling to reduce the longitudinal momentum spread of the beam, as well as further stochastic cooling. The Recycler can hold up to 5×10^{12} antiprotons, which typically take around 20 hours to store. Finally, the antiprotons are injected into the Main Injector, in the opposite direction to the protons, where they too are accelerated to an energy of 150 GeV ready for injection into the Tevatron.

2.1.3 The Tevatron

The Tevatron is a superconducting synchrotron of 2 km diameter, into which counter-rotating proton and antiproton beams are injected from the Main Injector at an energy of 150 GeV. After beam injection the magnetic field of the superconducting magnets is ramped up to 4.2 T, allowing the acceleration in RF cavities of the proton and antiproton beams both to 980 GeV. Quadrupole focussing magnets are used to bring the two beams into contact at two collision points: the CDF detector and the DØ detector (see Figure 2.1). The beams are kept apart for the remainder of the rotation using electrostatic separators.

The proton and antiproton beams are both divided into 36 "bunches" of particles, composing 3 "trains" of 12 bunches that are separated by "abort gaps" (Figure 2.2). Within the trains the bunches pass the collision point every 396 ns (when at an energy of 980 GeV), and the proton-antiproton bunch crossings are synchronised at the collision point to give a corresponding collision rate of $f_0 = 2.53$ MHz at centre-of-mass energy $\sqrt{s} = 1.96$ TeV. The instantaneous luminosity of the collisions is given by

$$\mathcal{L} \simeq \frac{N_p N_{\bar{p}} f_0}{A}, \tag{2.1.1}$$

where N_p and $N_{\bar{p}}$ are the number of protons or antiprotons in each bunch, and A is the effective area of collision. At the beginning of a store, $\mathcal{L}$ typically reaches 3×10^{32} cm^{-2}s^{-1}, whereafter it diminishes exponentially as N_p and $N_{\bar{p}}$ decrease following collisions and beam losses. The abort gaps are necessary to allow the termination of the beam, typically once $\mathcal{L}$ drops below a level suitable for data-taking.

The interaction rate for a given process is given by multiplying the instantaneous luminosity by the process cross-section:

$$\frac{dN}{dt} = \mathcal{L}\sigma. \tag{2.1.2}$$

Taking the NNLO theoretical $t\bar{t}$ cross-section $\sigma_{p\bar{p}\to t\bar{t}}^{\mathrm{NNLO_{approx}}} = 7.09^{+0.34}_{-0.41}$ pb, the peak $t\bar{t}$ production rate is about $3 \times 10^{32} \times 7.09 \times 10^{-36} \simeq 0.002$ Hz, or roughly once every 8 minutes.

The integrated luminosity, $\mathcal{L}_{\mathrm{int}}$, is used as a measure of the amount of data delivered to the detector, and is calculated by integrating the instantaneous luminosity over time:

$$\mathcal{L}_{\mathrm{int}} = \int \mathcal{L}\, dt. \tag{2.1.3}$$

2.2 The CDF Detector

The Collider Detector at Fermilab (CDF) is a large multi-purpose particle detector. It is azimuthally and forward-backward symmetric, and is illustrated schematically in Figure 2.3.

The CDF detector is described using a right-handed co-ordinate system. The z axis points along the beam-line, in the direction of proton travel. The x axis points radially outwards through the centre of the detector from the centre of the Tevatron ring, and the y axis points vertically upwards. The azimuthal symmetry of the detector suggests the use of a cylindrical polar co-ordinate system, where x and y are replaced with distance $r = \sqrt{x^2 + y^2}$ and azimuthal angle ϕ, where ϕ is defined as the angle in the transverse (x, y) plane from the positive x-axis. It is sometimes more convenient to express the co-ordinates in a spherical system, where the polar angle θ is defined as the angle from the positive z-axis and the distance r is redefined as the total distance from the centre of the detector $r = \sqrt{x^2 + y^2 + z^2}$.

Since most of the calculations based on measured variables involve special relativity, it is also useful to have measurable quantities that are invariant with respect to a Lorentz boost along the beam-line (the z axis). The azimuthal angle ϕ satisfies this criterion, but the polar angle θ does not. However the rapidity, defined as

$$y \equiv \frac{1}{2} \ln \frac{E + p_z}{E - p_z}, \tag{2.2.1}$$

has Lorentz-invariant properties. The difference in rapidity between two particles, $y_2 - y_1$, is independent of any boost along the z axis, and in the low-mass limit y becomes equivalent to the pseudo-rapidity, η, which can be expressed in terms of θ:

$$y \overset{p \gg m}{\to} \eta \equiv -\ln \left[\tan \left(\frac{\theta}{2} \right) \right]. \tag{2.2.2}$$

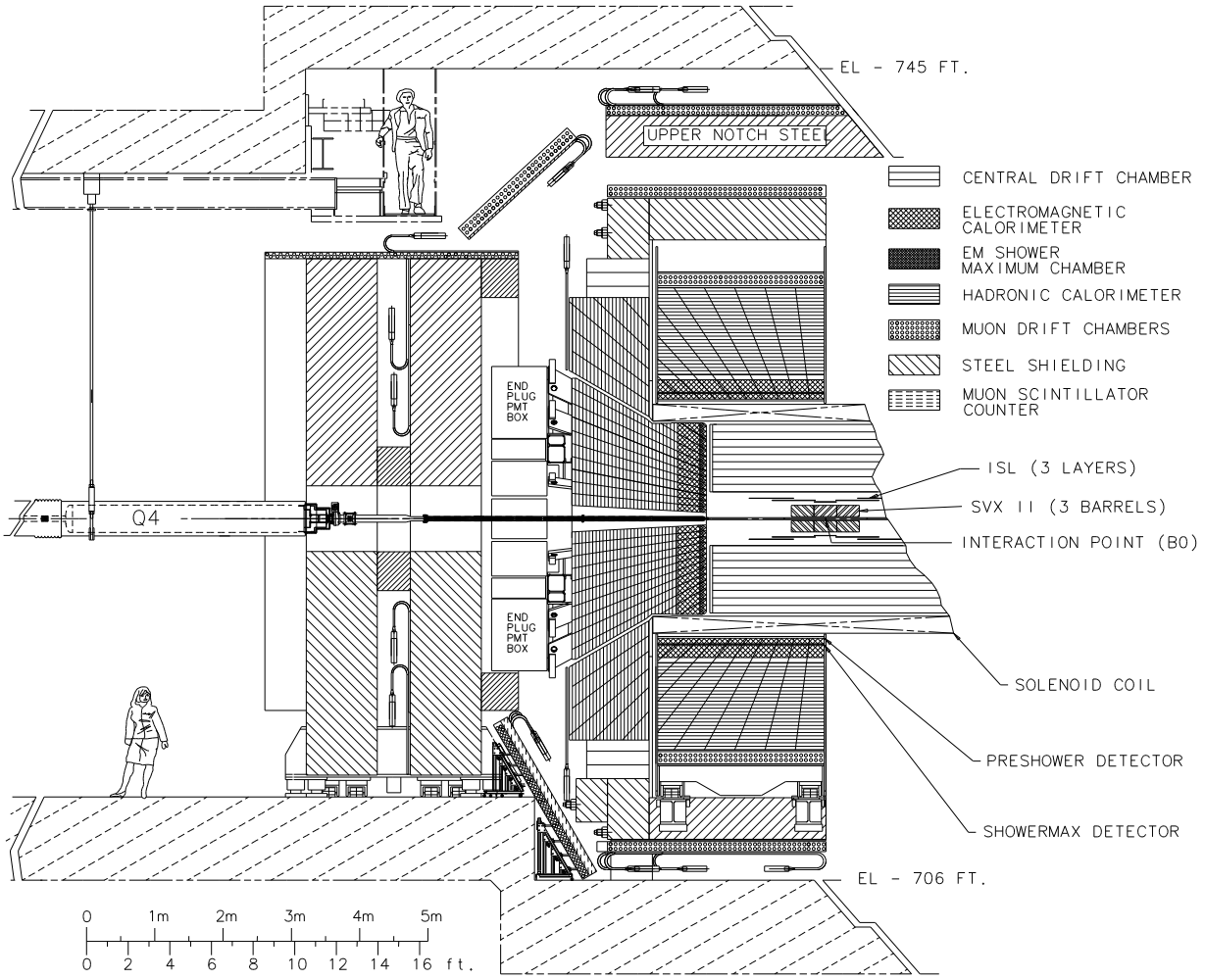

Figure 2.3: An elevation view of the CDF detector. Only one half of the symmetric detector is shown.

The remainder of this section details the detector components used in this analysis, from the beam-line outwards.

2.2.1 The Tracking System

The CDF tracking system, illustrated in Figure 2.4, is immersed in a 1.4 T magnetic field aligned parallel to the beam. The field is generated by a superconducting solenoid magnet of radius 1.5 m and 5 m length. Charged particles in the magnetic field follow helical trajectories depending on their charge and transverse momentum, allowing measurement of those quantities. The tracking system consists of a silicon microstrip tracking detector (the Silicon Tracker) surrounded by an open-cell wire drift chamber (the COT).

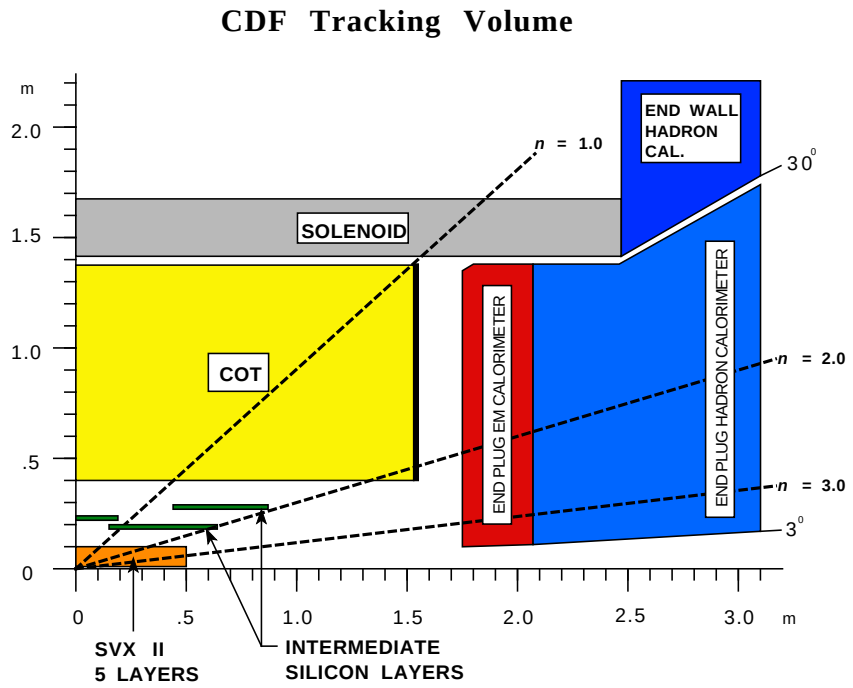

Figure 2.4: Schematic of the CDF Tracking Volume.

The Silicon Tracker

The silicon tracking detector provides accurate measurement of particle tracks near the beamline, which is of particular importance in identifying the secondary vertices characteristic of b-jets (b-tagging, Section 3.3.3). It comprises three sub-detectors: Layer 00 (L00), Silicon VerteX detector II (SVXII), and the Intermediate Silicon Layers (ISL).

The innermost component is L00, a single sided layer of silicon wafers mounted directly on the beam pipe at $r = 1.6$ cm and covering the region $|z| < 45$ cm. Its closeness to the beam allows for high precision in track impact parameter measurements, with corresponding improvements in b-tagging efficiency. Being single-sided, it provides only axial (r, ϕ) measurements.

The main sub-detector is the SVXII, positioned outside L00 and composed of 3 consecutive barrels (Figure 2.5), each spanning a region 29 cm in z for a combined coverage of $|z| < 45$ cm. Each barrel consists of 5 silicon layers extending from $r = 2.4$ cm to $r = 10.7$ cm. The silicon layers are double-sided, allowing simultaneous axial (r, ϕ) and stereo (r, z) measurements for full three-dimensional track reconstruction.

The outermost silicon tracker component is the ISL, providing a further 3 double-sided layers of coverage from $r = 20$ cm to $r = 29$ cm. The two layers at the extremities provide tracking in a region where the COT coverage is incomplete ($1 < |\eta| < 2$). The central layer provides intermediate tracking between the SVXII and the COT.

The combined impact parameter sensitivity of the silicon tracking detector is about 40 μm.

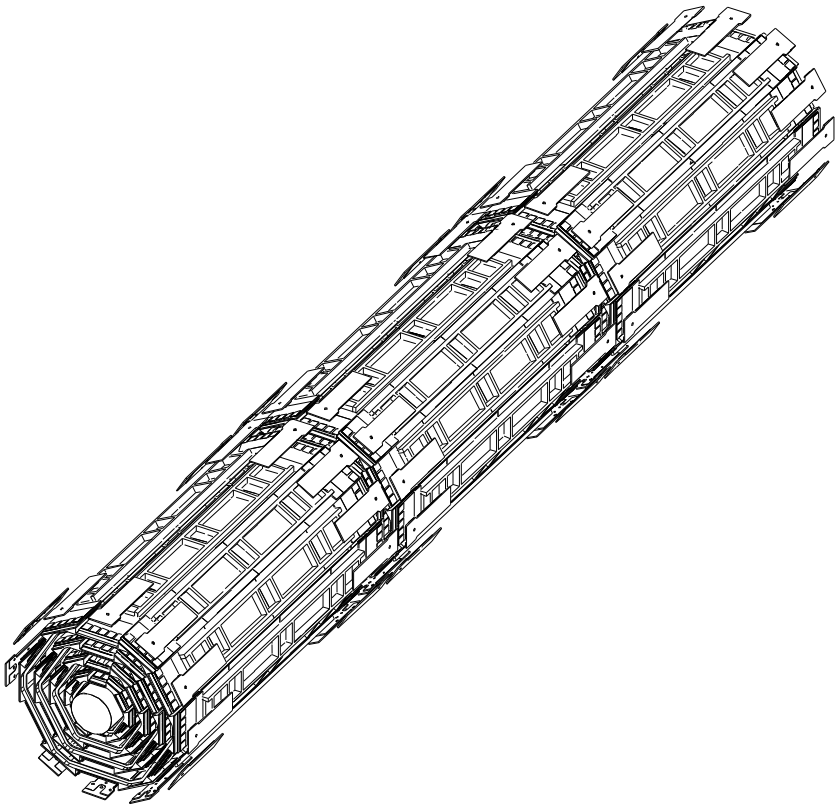

Figure 2.5: An illustration of the three SVXII barrels.

The Central Outer Tracker

The Central Outer Tracker (COT) [25] is a cylindrical open-cell drift chamber divided into 8 superlayers spanning radii $43 < r < 132$ cm, completely covering pseudo-rapidity region $|\eta| < 1$. The superlayers provide alternatively stereo and axial measurements and are subdivided into cells, each containing 12 sub-layers of wires (Figure 2.6). A track passing through the entire depth of the COT will therefore have 48 stereo and 48 axial measurements, providing a typical p_T resolution of $\sigma(p_T)/p_T \simeq 0.0015\ p_T$. Tracks with $|\eta| > 1$ no longer pass through all superlayers, reducing the resolution of the measurement up until $|\eta| = 2$ after which there is no coverage. The efficiency for finding charged particle tracks is almost 100% for $|\eta| < 1$, but falls to $\sim 40\%$ for $|\eta| = 2$.

The COT chamber is filled with a "fast" gas mixture (50% argon, 50% ethane), resulting in a maximum electron drift time of 100 ns which is shorter than the bunch crossing rate and prevents a build-up of events.

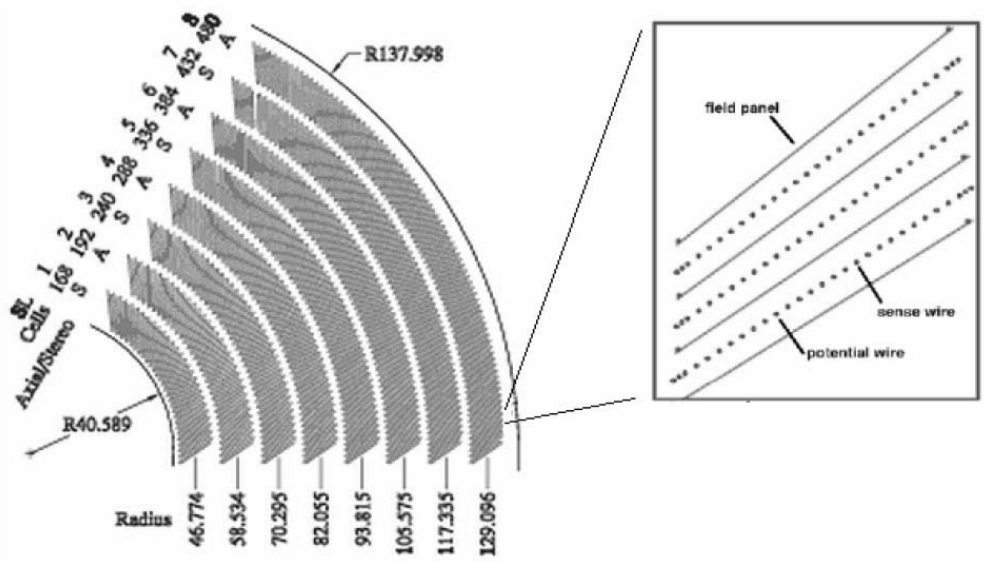

Figure 2.6: Schematic of a section of the COT. The superlayers provide alternatively stereo (S) and axial (A) measurements, and each contains 12 sub-layers of wires. The diagram also gives the distance r (in cm) of each superlayer from the centre of the detector, and the number of cells composing each superlayer.

2.2.2 The Calorimeters

The calorimeters are situated outside the tracking system and are used to measure the energy of entering particles (see Figures 2.3 and 2.7). Before reaching the calorimeters, particles have not encountered much absorbing material and retain most of their energy. Calorimeters are filled with layers of dense absorbing material which causes particles to deposit their energy through radiation and collisions, detected in the alternate layers of scintillator.

Electrons and photons are detected in the electromagnetic (EM) calorimeters, where lead is used as the absorbing material. In matter, high energy electrons lose energy mainly through bremsstrahlung (radiation of photons), while high energy photons lose energy primarily through electron-positron pair-production. The resulting chain of duplicating particles is called an "electromagnetic shower". The electromagnetic showers produced in the EM calorimeters are detected in the scintillator layers. The depths of the EM calorimeters are characterised in terms of X_0, the radiation length of the medium. X_0 describes the mean length of the material that an electron must traverse to lose all but $1/e$ of its original energy, and also corresponds to $\sim 7/9$ of the mean free path for pair-production by a high-energy photon.

Hadrons are detected in the hadron calorimeters, where iron is used as the absorbing material. Hadrons can strongly interact with the iron nuclei, producing "hadronic showers", which are again detected in the scintillator layers. Hadron calorimeters also sample EM showers from the EM decay of hadrons. The depths of the hadron calorimeters are characterised in terms of Λ_0, the interaction length of the medium. Λ_0 describes the mean free path of a particle before undergoing an inelastic nuclear interaction.

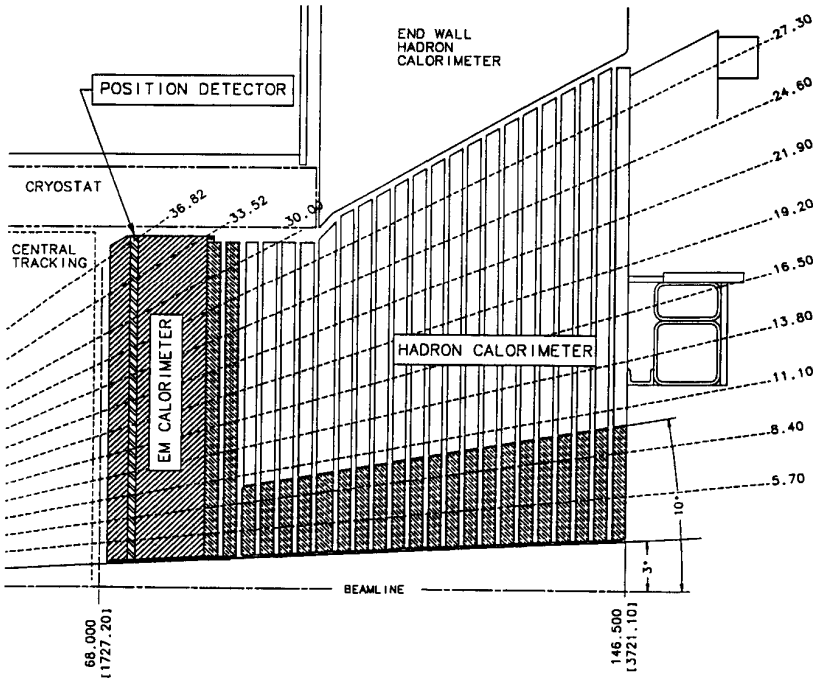

Figure 2.7: A cross-section of the Plug (PEM, PHA) and end-wall (WHA) calorimeters. Note that the labelled angles are measured in θ rather than η.

	CEM	PEM	CHA	WHA	PHA
Resolution	$\frac{13.5\%}{\sqrt{E_T}} \oplus 1.5\%$	$\frac{16\%}{\sqrt{E}} \oplus 1\%$	$\frac{50\%}{\sqrt{E_T}} \oplus 3\%$	$\frac{75\%}{\sqrt{E_T}} \oplus 4\%$	$\frac{80\%}{\sqrt{E}} \oplus 5\%$
Depth	18 X_0, 1 Λ_0	23 X_0, 1 Λ_0	4.7 Λ_0	4.7 Λ_0	6.8 Λ_0
η coverage	$\lvert\eta\rvert < 1.1$	$1.1 < \lvert\eta\rvert < 3.6$	$\lvert\eta\rvert < 0.9$	$0.7 < \lvert\eta\rvert < 1.3$	$1.2 < \lvert\eta\rvert < 3.6$

Table 2.1: Calorimeter energy resolution, depth, and $|\eta|$ coverage.

Since $X_0 \ll \Lambda_0$, the EM calorimeters are placed inside the hadron calorimeters. Electrons and photons will deposit most of their energy in the EM calorimeters, with hadrons largely passing though and depositing their energy in the hadron calorimeters. The EM calorimeters are the Central and Plug EM calorimeters, the CEM and PEM, covering $|\eta| < 1.1$ and $1.1 < |\eta| < 3.6$ respectively. The hadron calorimeters again consist of Central and Plug components: the CHA covering $|\eta| < 0.9$, and the PHA covering $1.2 < |\eta| < 3.6$. There is also an end Wall Hadron calorimeter (WHA) covering $0.7 < |\eta| < 1.3$ due to the gap in the η coverage of the CHA and PHA. The resolution, η coverage, and depth (measured in terms of Λ_0 and/or X_0 as appropriate) of the five calorimeter sections are summarised in Table 2.1.

The calorimeters are all sub-divided into "towers" (Figure 2.8), each independently measuring the energy deposited in that region. Each tower combines an EM component and a hadronic component, and the calorimetry system has a total of 1536 towers. In the central calorimeters, each tower covers $(\Delta\eta, \Delta\phi) = (0.11, 15°)$, while in the WHA each tower covers $(0.11, 7.5°)$. In the plug calorimeters (Figure 2.7), $(\Delta\eta, \Delta\phi) = (0.16, 7.5°)$ in the region $\eta < 2.11$, while in the region $\eta > 2.11$, $\Delta\phi$ is 15° and $\Delta\eta$ ranges from 0.2 to 0.6.

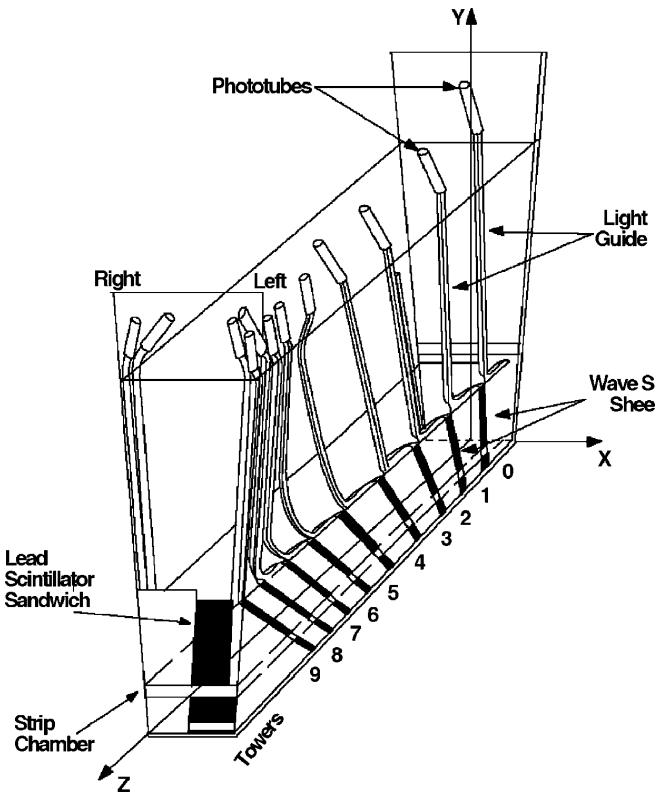

Figure 2.8: A ϕ wedge of CEM calorimeter towers. The ten $(\Delta\eta, \Delta\phi) = (0.11, 15^\circ)$ towers are labelled.

The CEM and PEM also house proportional chambers, the CES and the PES, at approximately the shower maximum depth, and allow for a position measurement of the shower and thus potentially the matching of the shower with a particle track.

Unlike electrons, muons pass though the calorimetry system due to their high mass ($m_\mu \simeq 200\ m_e$, greatly reducing bremsstrahlung which goes as m^{-4}) and the fact that they do not interact strongly with nuclei. Neutrinos, which do not radiate due to their lack of electric charge and only interact weakly, also pass though the calorimetry system.

2.2.3 The Muon Detectors

The muon detectors are the outermost component of the CDF detector, and are placed outside a heavy metal shielding to prevent other particles that might be mistaken for muons from reaching the detectors. There are four muon systems, illustrated in Figures 2.3 and 2.9. The Central MUon detector (CMU) covers pseudorapidity region $|\eta| < 0.6$, while the Central Muon eXtension (CMX) covers pseudorapidity region $0.6 < |\eta| < 1.0$. The Central Muon uPgrade (CMP) also covers $|\eta| < 0.6$, and is separated from the CMU by a further 60 cm of steel, blocking charged pions that may have made their way to the CMU. The Intermediate MUon detector (IMU) covers $1.0 < |\eta| < 1.5$ and is not used in this analysis.

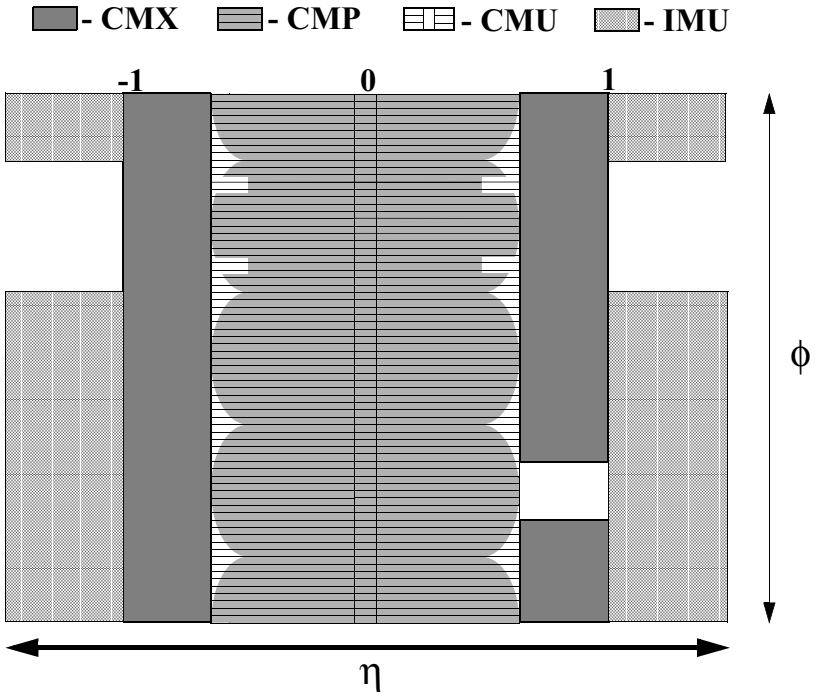

Figure 2.9: The η and ϕ coverage of the CDF muon detectors. Note that the IMU is not used in this analysis.

Each detector consists of chambers composed of four concentric layers of rectangular cells. The cells are planar drift chambers filled with a 50% argon, 50% ethane gas mixture and a single high-voltage steel sense-wire running parallel to the beam position. On average, a muon will traverse 6 cells, and the resulting information is used to form track segments, called "stubs". The stubs are then matched to tracks from the tracking system.

2.2.4 The Luminosity Counters

The beam instantaneous luminosity is determined using gas Cherenkov counters, located close to the beam-line in the forward and backward $3.7 < |\eta| < 4.7$ regions, which measure $\mu_{p\bar{p}}$, the number of inelastic $p\bar{p}$ collisions per bunch crossing. The instantaneous luminosity can then be calculated using

$$\mathcal{L} = \frac{\mu_{p\bar{p}} f_0}{\sigma_{p\bar{p}}}, \tag{2.2.3}$$

where $\sigma_{p\bar{p}}$ is the total inelastic cross-section for $p\bar{p}$ collisions, which has been measured to within a 4% uncertainty [26, 27]. The measured $\mu_{p\bar{p}}$ also has an uncertainty of about 4%, leading to an uncertainty on the luminosity $\delta\mathcal{L}/\mathcal{L} \simeq 6\%$.

Chapter 3

Event Reconstruction and Selection

Approximately one hard $p\bar{p}$ scattering, or "event", occurs at the CDF detector at every bunch crossing. The resulting spray of particles is detected in the various detector components, which then read-out the event information.

3.1 Trigger System

Bunch crossings occur every 396 ns at the CDF detector (Section 2.1.3), meaning events are observed at the CDF detector at a rate of about 2.5 MHz. Since each event produces about 250 kb of data, the recording of all CDF events would require the recording of data at a sustained rate of almost 1 Tb/s, which is not feasible with current technology. However, the vast majority of events do not contain valuable information and can be discarded, which is achieved using the trigger system. At CDF, the trigger system comprises 3 levels which are successively more selective. The three trigger levels are illustrated in Figure 3.1 and are described in the remainder of this section.

3.1.1 Level 1 Trigger

Events arrive at the Level 1 (L1) trigger at a rate of 2.53 MHz. Due to the high rate, the L1 "pipeline" can hold the data for just 5.5 μs before it must move on to the next event. L1 must therefore base its selection decision on simple and quickly measured quantities. This occurs in three parallel hardware streams. The XFT (eXtremely Fast Tracker) reconstructs approximate tracks in the COT. The calorimeter trigger looks for large energy releases in the calorimeters which may indicate electrons, photons or jets, and also the missing transverse energy indicative of a neutrino. The muon trigger looks for "stubs" (track segments) in the muon chambers, which can be matched to XFT tracks. The results of the three streams are combined to decide whether to accept the event (Figure 3.2). The maximum L1 accept rate is 50 kHz.

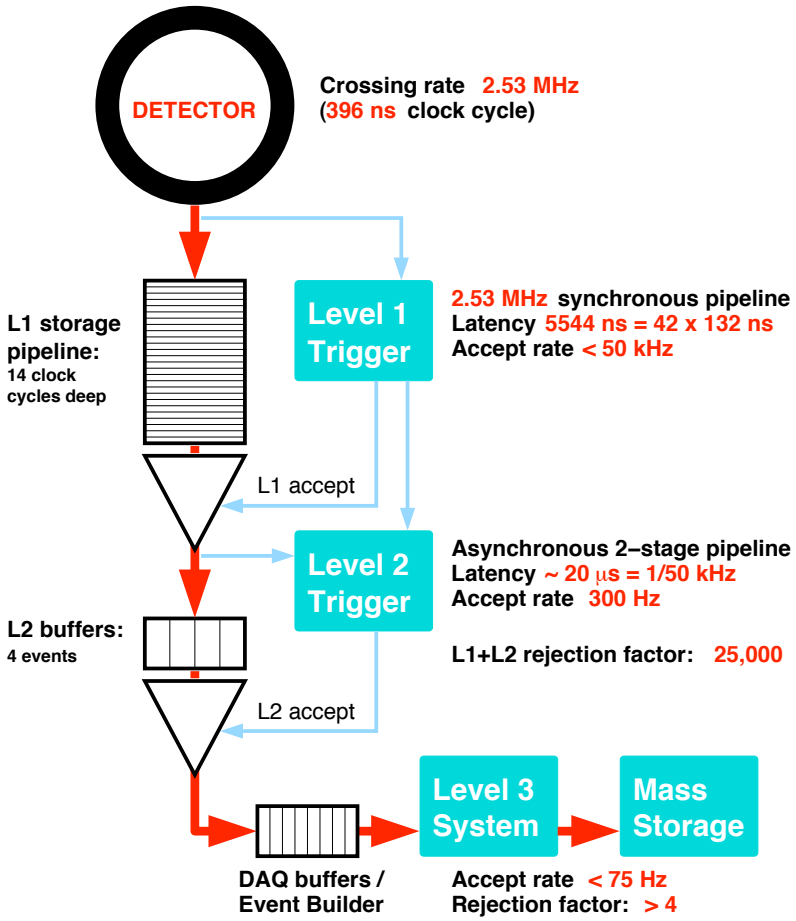

Figure 3.1: A schematic of the CDF trigger system.

3.1.2 Level 2 Trigger

Events accepted at L1 are stored in one of the four asynchronous Level 2 (L2) buffers, where they remain during the ~ 20 μs it takes for the L2 decision to be made. As a result some events passing L1 are lost when the buffers are full, a process known as "dead time", which is typically kept below 5%. Since the L2 trigger has about 5 times as long as L1 to make its decision, it is able to use more accurately reconstructed quantities and therefore be more selective. The energy deposits in the calorimeters are clustered, allowing approximate electron or jet energy measurement. The XFT tracks are matched with CES shower-max information or muon stubs, improving the electron and muon signatures. The Silicon Vertex Tracker (SVT) reconstructs tracks in the silicon tracking system, and is able to identify displaced vertices. This is all achieved using custom hardware and modified commercial microprocessors, and again the results are combined to make a decision (Figure 3.2). The L2 trigger has a maximum accept rate of 300 Hz.

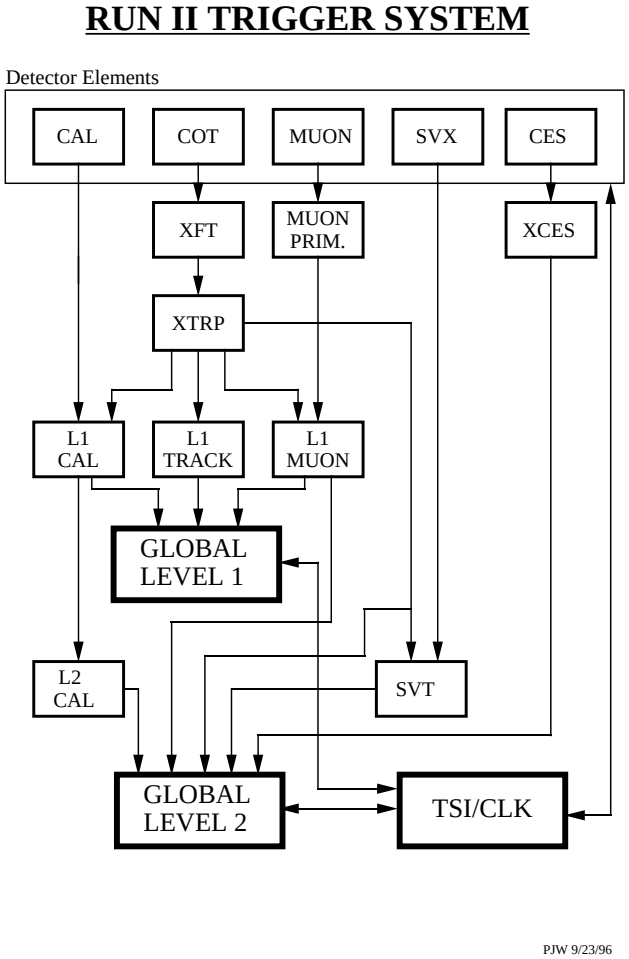

Figure 3.2: The Level 1 and Level 2 trigger decision components.

3.1.3 Level 3 Trigger

The Level 3 (L3) trigger performs a full event reconstruction using a specialised version of the CDF offline reconstruction software (described in Section 3.2), with less stringent cuts. It runs on a farm of PCs and returns a decision with a maximum accept rate of 75 Hz. This rate is sufficiently low that all L3 accepted events can be stored on tape for offline analysis.

3.2 Event reconstruction

Events from the lepton+jets decay channel (Section 1.2.2) have topology $t\bar{t} \to W^+b\,W^-\bar{b} \to \ell^+\nu_\ell b\;\bar{q}q'\bar{b}$. The final state particles, with the exception of the neutrino, are observed as a series of tracks and jets in the detector.

3.2.1 Tracks

The tracking system is immersed in a 1.4 T magnetic field, bending the trajectories of charged particles into helices (Section 2.2.1). As charged particles pass through the tracking system they produce a series of "hits" (position measurements) in the Silicon Tracker and in the COT, which when combined constitute the particle track. All of the tracking information from each event must be combined into a set of reconstructed tracks. This is achieved using a staged offline algorithm [28], working from the COT tracks radially inwards through the Silicon Tracker so as to reconstruct the fully fiducial tracks first. Helical shapes are then fitted to the reconstructed tracks, allowing measurement of the particles' momentum, trajectory, origin and charge. At CDF, this information is described by the following five parameters.

- ϕ, the azimuthal angle of particle; defined as the azimuthal angle of the reconstructed helix, at its closest approach to the primary interaction point.
- $\cot(\theta)$, the cotangent of the polar angle of the particle, and related to the particle's z-momentum p_z and transverse momentum p_T via $\cot(\theta) = p_z/p_T$.
- d_0, the transverse impact parameter of the reconstructed helix, with respect to the primary interaction vertex.
- z_0, the longitudinal impact parameter of the reconstructed helix, with respect to the primary interaction vertex.
- c, the curvature of the reconstructed helix in the transverse plane. Related to the radius of curvature R_C by $c = q/(2R_C)$, where q is the electric charge of the particle.

The particle's transverse momentum is directly proportional to its radius of curvature R_C via

$$p_T = |B\, q\, R_C|, \tag{3.2.1}$$

where B is the magnetic field. With muons and electrons the only particles for which the tracking information is used to make momentum measurements, it is known that $q = \pm e$, meaning that p_T can be determined from R_C. The sign of the charge is given by the direction of curvature of the helix. Overall, tracks reconstructed using the combined COT and Silicon Tracker information have a typical p_T resolution of $\sigma(p_T)/p_T \simeq 0.0007\ p_T$, compared with $\sigma(p_T)/p_T \simeq 0.0015\ p_T$ when using just the COT (Section 2.2.1). The measurement of R_C becomes less precise as R_C increases, explaining the p_T dependence of the p_T resolutions.

The track measurements provide all of the reconstructed muon quantities, as well as the initial momentum direction of reconstructed electrons[1]. The Silicon Tracker also provides most of the sensitivity for the impact parameter measurement, which is useful for secondary vertex b-tagging (Section 3.3.3).

[1]Electron energy measurement is made using the calorimetry system (Section 3.2.3), as the track momentum is likely to be an underestimate of the initial electron momentum due to bremsstrahlung.

Muon stubs

Muon track segments, or stubs, are a set of hits in one of the muon detectors consistent with the passage of a muon. To be identified as a stub, hits are required in at least three of the detector's four layers. A straight line is then fitted to the hits, determining the approximate trajectory of the muon and allowing matching with an extrapolated track.

Beam Profile and Primary interaction vertex

Information about the beam profile and the primary interaction vertex is derived from the tracking information. The transverse profile of the beam can be described by a Gaussian in the cylindrical co-ordinate r, with an RMS of about 26 μm [29]. The beam profile is also roughly Gaussian in z, with an RMS of about 25 cm.

The primary interaction vertex describes the location of the hard $p\bar{p}$ scattering. Its location for a given event is found by extrapolating well-measured tracks back to a point of common origin. The known beam-line (from the primary interaction vertices of previous events) is used as a constraint and an iterative algorithm removes the tracks that disagree with the weighted average position.

More than one collision can occur at each bunch crossing, particularly at high luminosity, leading to more than one primary interaction vertex. In this analysis, the event vertex is taken to be the one closest in z to the charged lepton track at the beam-line.

3.2.2 Jets

Unlike leptons, quark tracks and energies cannot be directly measured by the detector. The process of hadronisation - where quarks fragment and form colourless bound states with other quarks - results in a collimated shower of particles (a "particle jet") which deposit energy in the calorimeters, known as a "jet". That information must somehow be reconstructed to find the energy and direction of the particle jet, and ultimately the energy and direction of the original quark (henceforth referred to generically as a "parton"). The relationship between the measured and particle jets is illustrated in Figure 3.3.

Jets are reconstructed from the energy deposits in the calorimeter towers. Each tower consists of an EM component and a hadronic (had) component (Section 2.2.2). The towers whose information is thought to represent a single parton are identified and "clustered" using the CDF `JETCLU` algorithm [30, 31]. This is achieved first by identifying the "seed towers", the towers i with deposited transverse energy $E_T^i > 1$ GeV. E_T^i is defined as

$$E_T^i = E_{\rm EM}^i \sin(\theta_{\rm EM}^i) + E_{\rm had}^i \sin(\theta_{\rm had}^i), \tag{3.2.2}$$

where $\theta_{\rm EM}^i$ and $\theta_{\rm had}^i$ are the polar angles[2] of the EM and hadronic towers i from the interaction point z, and $E_{\rm EM}^i$ and $E_{\rm had}^i$ are the energy deposits in the EM part and the hadronic part

[2]The angles $\theta_{\rm EM}^i$ and $\theta_{\rm had}^i$ differ slightly when $z \neq 0$.

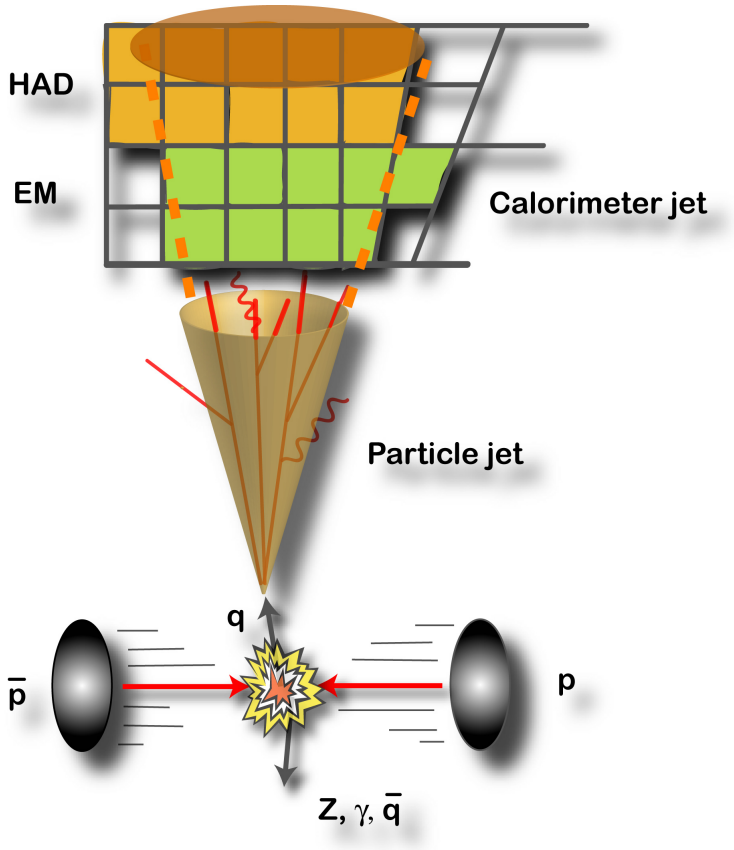

Figure 3.3: The development of a calorimeter jet from a quark. The energy of the particle jet must be reconstructed from the jet measured in the calorimeters.

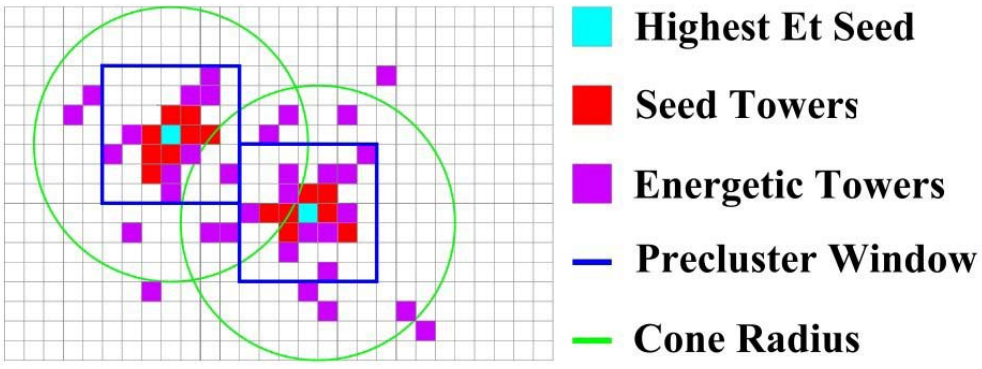

Figure 3.4: An illustration of tower clustering. Preclusters are created in a window around the highest E_T seed towers by combining the adjacent seed towers. A cluster is then created in the cone of radius $R = 0.4$ about the precluster centroid.

of the tower. Each jet is likely to have many such seed towers, so "preclusters" are created, starting with the seed with highest E_T^i, by combining adjacent seed towers within a given window in (η, ϕ) space (see Figure 3.4). Additional preclusters are then created in the same way using the remaining seed towers. Next, the (η, ϕ) centroid of each precluster is calculated, weighting the towers by E_T^i:

$$\eta^{\text{jet}} = \sum_{\text{towers}} \frac{\eta^i E_T^i}{\sum_{\text{towers}} E_T^i} \tag{3.2.3}$$

$$\phi^{\text{jet}} = \sum_{\text{towers}} \frac{\phi^i E_T^i}{\sum_{\text{towers}} E_T^i}. \tag{3.2.4}$$

For each precluster, a cluster is created in the cone of radius $R = 0.4$ about the precluster centroid, where $R \equiv \sqrt{(\Delta\eta)^2 + (\Delta\phi)^2}$, and all towers within the cone with $E_T^i > 100$ MeV [3] are added to the cluster. The centroid is recalculated with the new towers and a new cluster within $R = 0.4$ is created. If new towers are added to the cluster the centroid must be recalculated, and the process continues iteratively until a stable cluster of towers is found. Note that $\Delta\eta$ and $\Delta\phi$, and hence R, are Lorentz-invariant, making the jet reconstruction independent of frame of reference.

In the case of the partial overlap of two[4] clusters, the E_T^i of the shared towers are summed and compared with the E_T of the lower-energy cluster. If the shared E_T is greater than 50% of that of the lower-energy cluster, the two clusters are combined to form a single jet. If not, the two clusters are identified with two jets and shared towers are allocated to the closest cluster.

The jet 4-momentum can then be calculated, assuming a massless parton:

$$\begin{aligned}
E^{\text{jet}} &= \sum_{\text{towers}} \left(E^i_{\text{EM}} + E^i_{\text{had}}\right) \\
p_x^{\text{jet}} &= \sum_{\text{towers}} \left(E_T^i \cos(\phi^i)\right) \\
p_y^{\text{jet}} &= \sum_{\text{towers}} \left(E_T^i \sin(\phi^i)\right) \\
p_z^{\text{jet}} &= \sum_{\text{towers}} \left(E^i_{\text{EM}} \cos(\theta^i_{\text{EM}}) + E^i_{\text{had}} \cos(\theta^i_{\text{had}})\right),
\end{aligned} \tag{3.2.5}$$

where E_T^i is as defined in Equation 3.2.2 and $\phi^i = \phi^i_{\text{EM}} = \phi^i_{\text{had}}$ is the azimuthal angle of tower i.

[3] This E_T^i cut retains those towers with energies well above the level of electronic noise.

[4] If more than two clusters overlap, the two clusters with highest E_T are considered first.

3.2.3 Electron energies

Electron energies are measured in the calorimetry system in much the same way as jet energies. Towers corresponding to the electron track direction are ordered in E_T, with the highest E_T tower taken as the initial seed tower. Towers adjacent in η are added to the cluster if their energy exceeds 100 MeV, meaning a cluster will consist of just 1, 2 or 3 towers (all cluster towers must be in the same ϕ wedge). In the CES detector, channels exceeding a threshold are also clustered. Fitting the cluster profile (in z) with the expected shower profile, taken from test beam electrons, provides an accurate measurement of the shower position.

3.2.4 Jet energy corrections

When jets enter the detector, the effects of particle showering, detector response and noise, as well as energy from additional hard scatterings from the same beam crossing, adversely affect the initial jet reconstruction. The `JETCLU` reconstruction algorithm itself can also misrepresent the particle jets, for example when energy is deposited outside the defined cone.

The jet 4-momenta from Equations 3.2.5 represent the calorimeter jets of Figure 3.3. The aim of the jet energy corrections is to correct the energies of the calorimeter jets so that they represent the particle jets of Figure 3.3, that is, the corrected jet momenta should give the sum of the momenta of the hadrons, leptons, and photons within the jet cone.

The CDF jet energy corrections [31] are divided in levels and are applied sequentially. Each level has a significant systematic uncertainty, which when combined make up the overall Jet Energy Scale (JES) uncertainty σ_j. The uncertainties of individual jet measurements are therefore correlated, and for jets with $E_T > 50$ GeV the fractional uncertainty $\sigma_j/E_j \sim 3\%$ (see Figure 3.11). If this was included as a systematic uncertainty on the measured m_t it would reduce the measurement precision drastically; in fact, each 1% of fractional JES uncertainty adds about 1 GeV/c^2 uncertainty to the measured m_t [32]. In this analysis, the effect of the JES uncertainty is reduced by the use of an *in situ* calibration of the JES, described in Section 4.3.

The jet energy corrections used in this analysis, relating the particle-level jets to the measured jets, are described by Equation 3.2.6:

$$p_T^{\text{particle}} = \left(p_T^{\text{jet}} \times C_{\text{Level 1}} - C_{\text{Level 4}}\right) \times C_{\text{Level 5}}, \tag{3.2.6}$$

with the corrections $C_{\text{Level i}}$ of the various Levels described in the remainder of this section.

Calibration (Level 0)

The initial energy calibration of the calorimeters is referred to as "Level 0" of the jet energy corrections [31]. The EM calorimeters are calibrated with the use of $Z \to e^+e^-$ data (Section

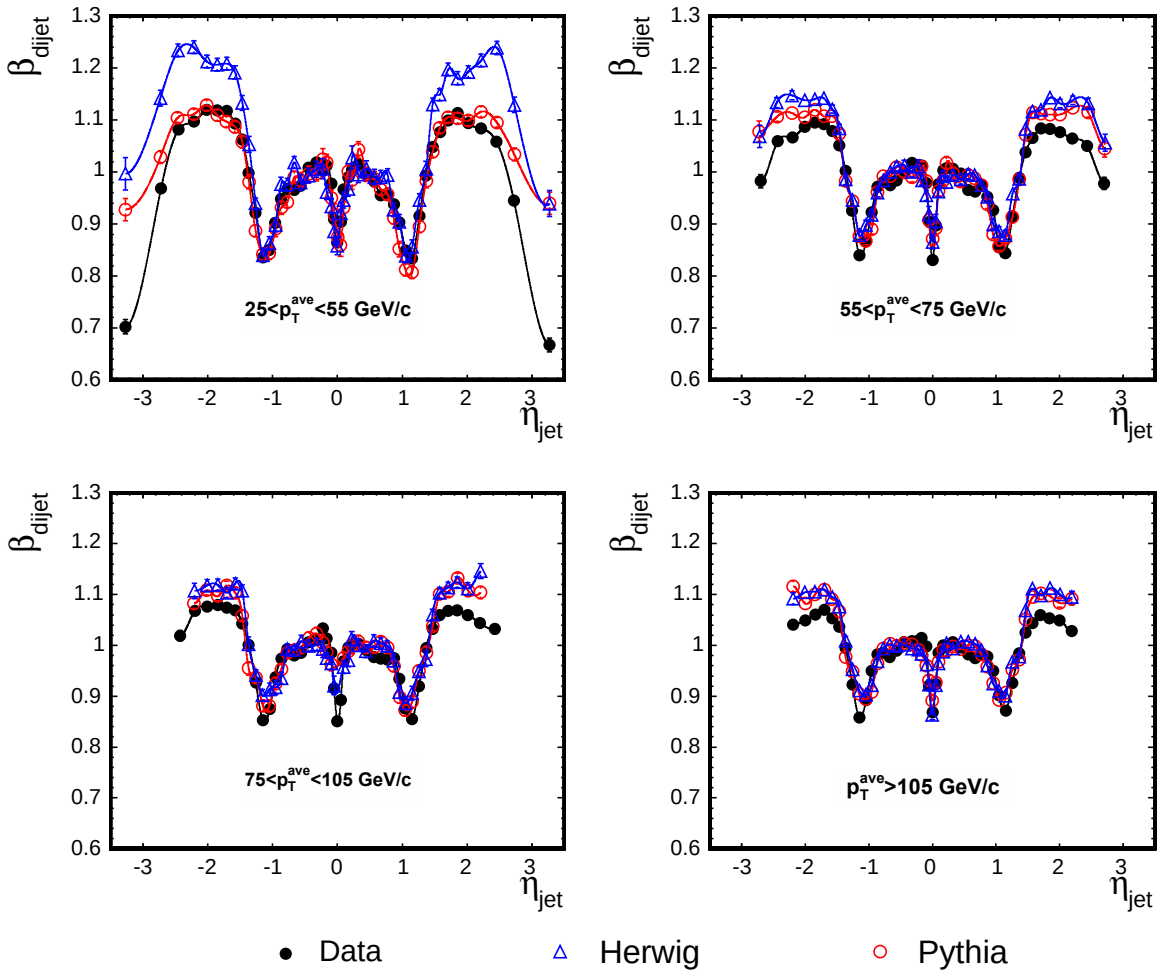

Figure 3.5: The non-uniform jet energy response in η, before Level 1 correction. The correction $C_{\text{Level 1}}$ is taken from $1/\beta_{\text{dijet}}$. Note that `PYTHIA` and `HERWIG` refer to two different types of Monte Carlo simulated events, which will be discussed in Section 4.2. The simulations agree well with the data up to $|\eta| < 1.4$, while for $|\eta| > 1.4$ and $p_T < 55$ GeV/c the `HERWIG` simulation differs significantly from both the data and the `PYTHIA` simulation. Due to this large discrepancy, `HERWIG` dijet events are not used in the determination of the Level 1 correction or its systematic uncertainty [31].

3.2.5), while the hadronic calorimeters are initially calibrated using a test beam of 50 GeV charged pions. Further calibrations are made using laser systems, and ^{137}Cs and ^{60}Co sources.

Level 1

Level 1, "relative scale", makes η-dependent corrections to the measured jet energies to make the initial non-uniform jet energy response (Figure 3.5) uniform in η. The "dijet balance" technique is used [31], which uses the fact that the transverse momenta p_T of the two jets in a $2 \rightarrow 2$ process should be equivalent to relatively calibrate two different regions of the calorimeters. The central calorimeters are better calibrated and understood, and the region $0.2 < |\eta| < 0.6$ is free of cracks and non-instrumented areas and is chosen as the baseline. The resulting correction is based on events with exactly two jets ("dijet" events), one inside the region $0.2 < |\eta| < 0.6$ ("trigger jet") and one outside that region ("probe jet").

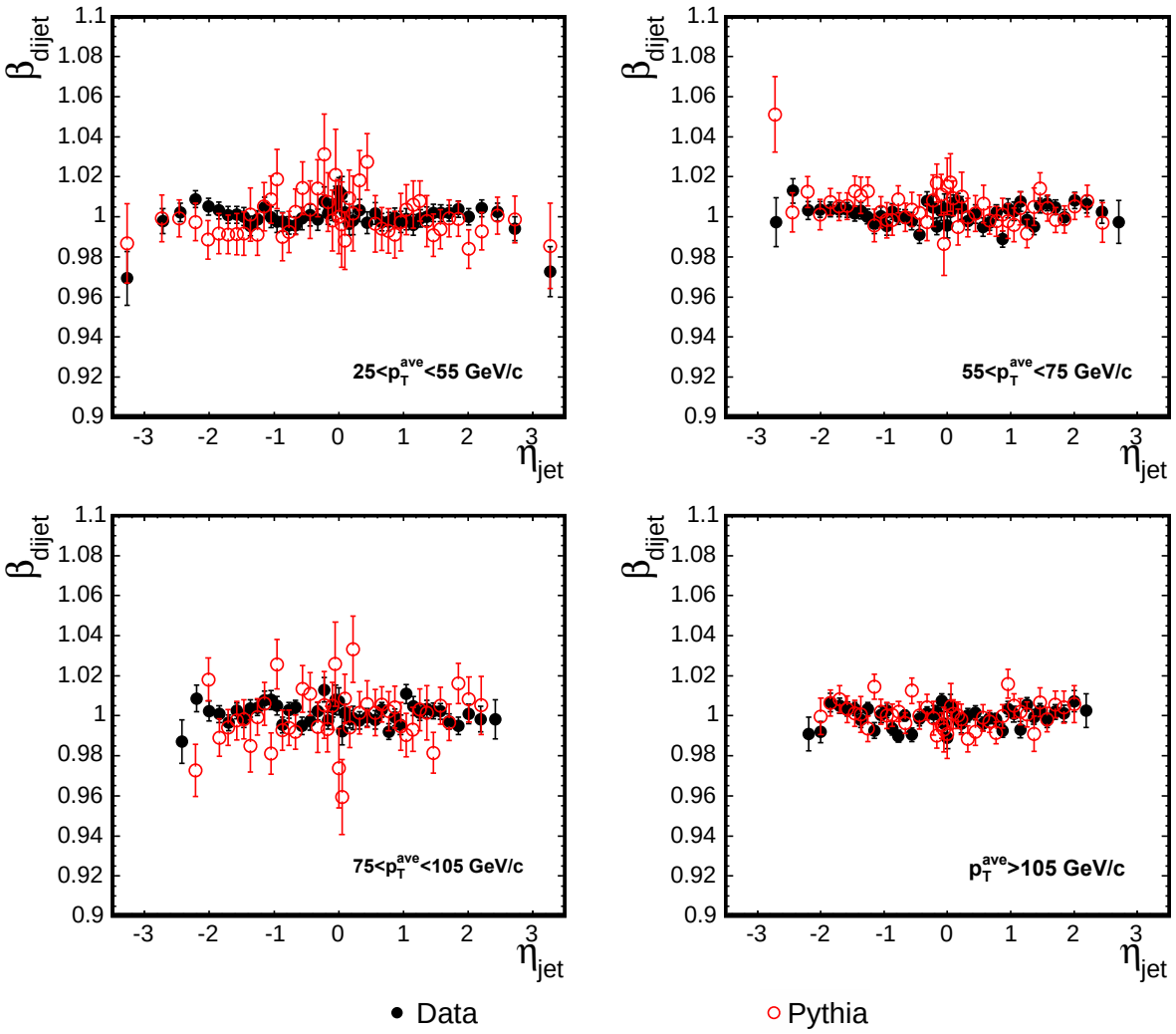

Figure 3.6: The uniform jet energy response in η after Level 1 correction. The remaining discrepancies are due to the limitations of the parameterisation of the η- and p_T-dependence of the correction.

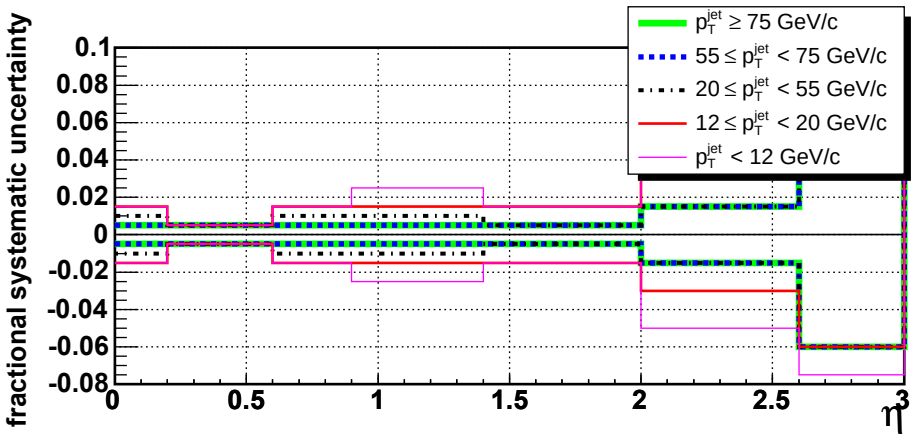

Figure 3.7: Level 1 correction fractional systematic uncertainty. The uncertainty is $|\eta|$- and p_T-dependent.

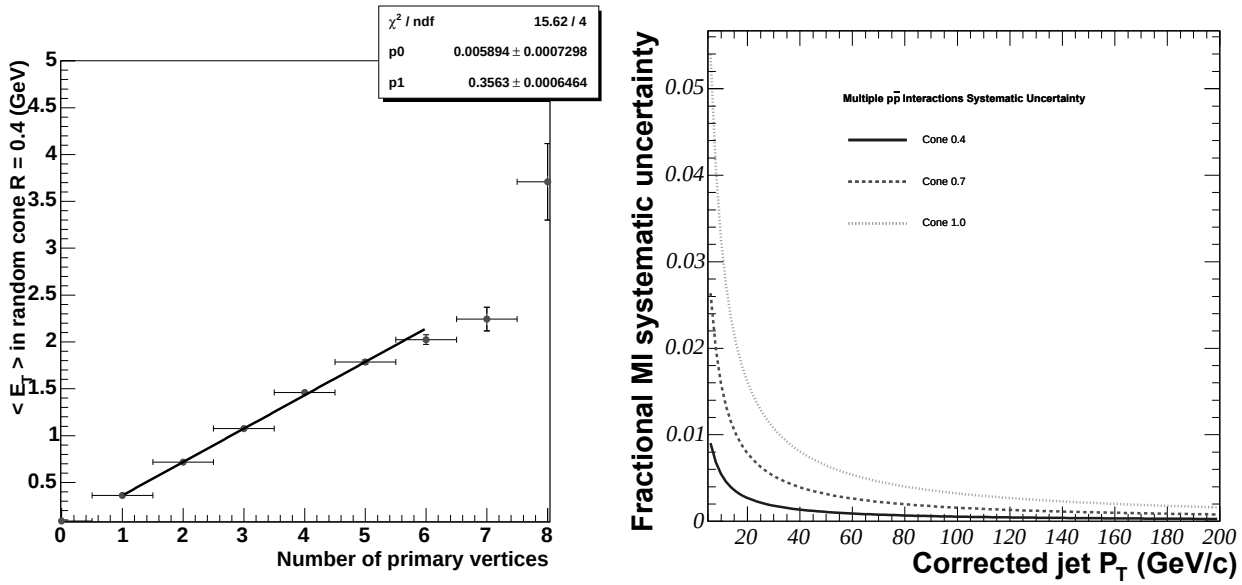

Figure 3.8: The Level 4 correction. Left: the average E_T deposited in a random cone of $R = 0.4$ increases linearly with the number of primary vertices observed in the minimum bias event. Right: the fractional systematic uncertainty as a function of p_T.

The correction is a function of η and p_T (Figure 3.5), and is defined as $C_{\text{Level 1}} = 1/\beta_{\text{dijet}}$, where $\beta_{\text{dijet}} = p_T^{\text{probe}}/p_T^{\text{trigger}}$. It ranges between approximately +15% and -15%, and after Level 1 correction the response of the calorimetry system is almost flat with respect to η, with $\beta_{\text{dijet}}^{\text{corrected}} = 1$ (Figure 3.6). The systematic uncertainty associated with the correction is estimated by varying the selection criteria for the 2-jet events and the fitting procedure, and is plotted as the fractional systematic uncertainty in Figure 3.7.

Levels 2 and 3

Levels 2 and 3 are obsolete.

Level 4

Level 4, "multiple interactions", corrects for the effects of multiple $p\bar{p}$ interactions in a single bunch crossing. The energy from a secondary collision could contaminate the cone of a measured jet, and the Level 4 correction acts to, on average, subtract that contribution. The correction, $C_{\text{Level 4}}$, is typically about 1% of the jet p_T, and is derived from minimum bias data[5] by measuring the average E_T deposited in a jet cone (with $R = 0.4$) as a function of the number of primary vertices observed in the event (Figure 3.8). The systematic uncertainty associated with this correction is approximately 15% of the correction itself, or $\sim 0.2\%$ of the jet p_T (Figure 3.8).

[5]Minimum bias events come from the soft scatterings always present as a background to the hard scatterings interesting to this analysis.

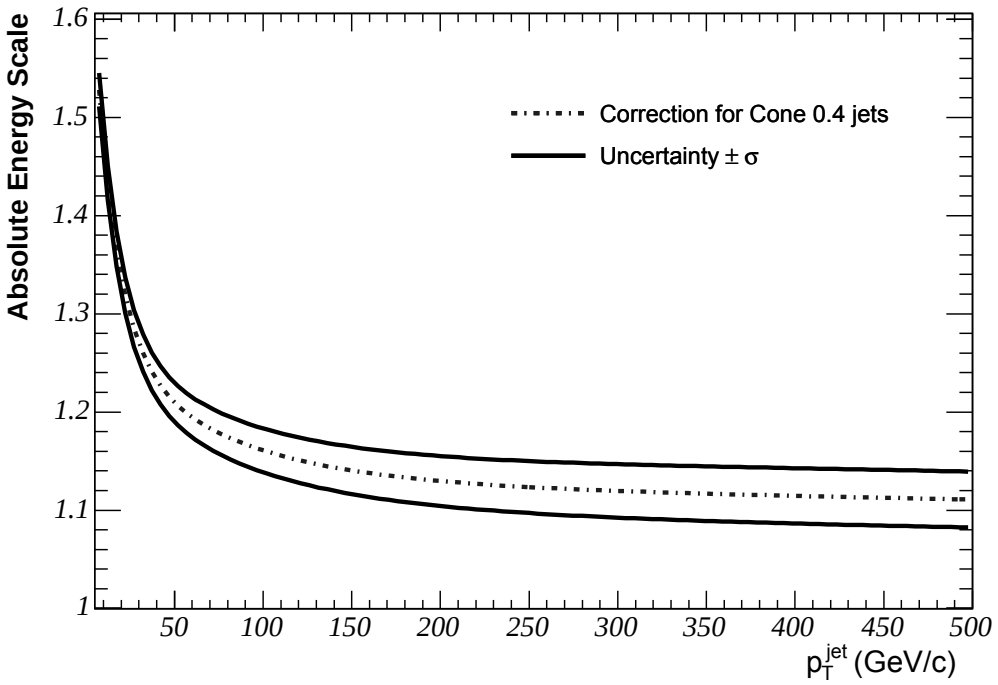

Figure 3.9: The Level 5 jet energy correction $C_{\text{Level 5}}$ ("absolute energy scale") as a function of p_T.

Level 5

The level 5 corrections are known as "absolute scale", and correct the measured jet energies for calorimeter non-linear response and energy loss in the non-instrumented areas of the calorimeters. The correction is derived using simulated events, from which a mapping from the calorimeter-level to the particle-level can be parameterised as a function of p_T. The measured jet energy is corrected so that the total p_T in the jet cone of $R = 0.4$ matches that of the particles within a radius $R = 0.4$ about the parton direction, and the correction factor, $C_{\text{Level 5}}$, is typically between 1.1 and 1.3 (Figure 3.9). The fractional systematic uncertainty associated with this correction, mainly a result of modelling uncertainties, is plotted in Figure 3.10.

Levels 6-8

Correction Levels 6 to 8 attempt to correct the particle-level jet to the parton-level, and are not used in this analysis. Instead, specialised "Transfer Functions" (Chapter 6) are formulated for that purpose. Levels 6-8 are briefly described here because the processes they describe introduce additional uncertainties into the measured jet energies, so their systematic uncertainties contribute to the overall jet energy uncertainty σ_j.

Level 6, "underlying event", subtracts the energy deposits associated with the spectator partons in the $p\bar{p}$ collision. It is estimated using minimum bias events with only one primary vertex.

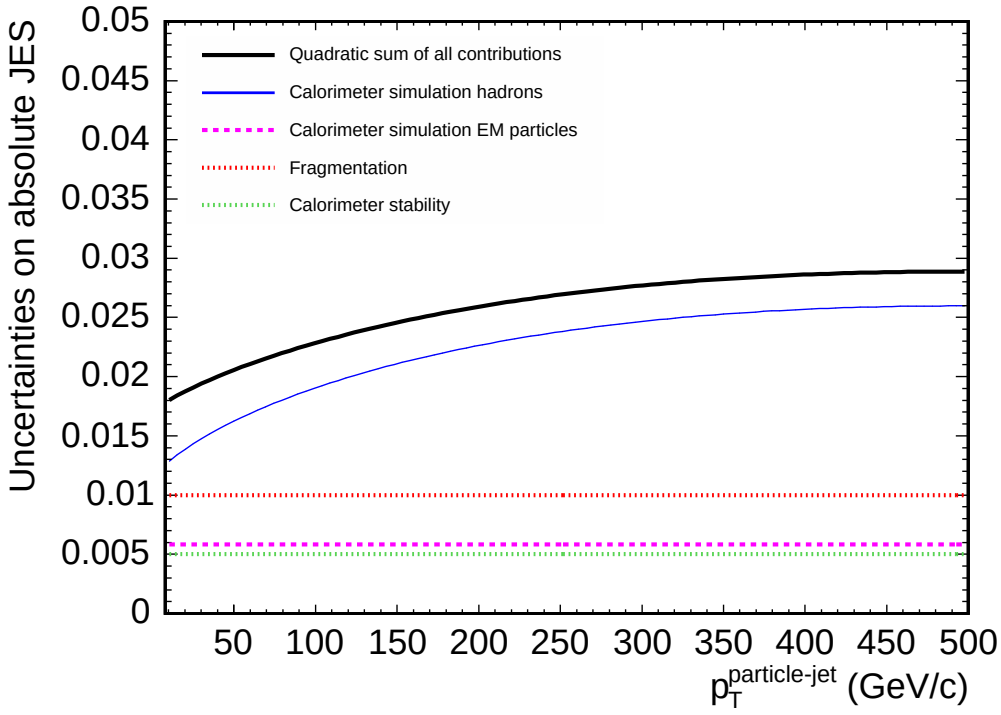

Figure 3.10: The Level 5 correction fractional systematic uncertainty as a function of p_T. The solid black line shows the total while the other lines show the individual contributions.

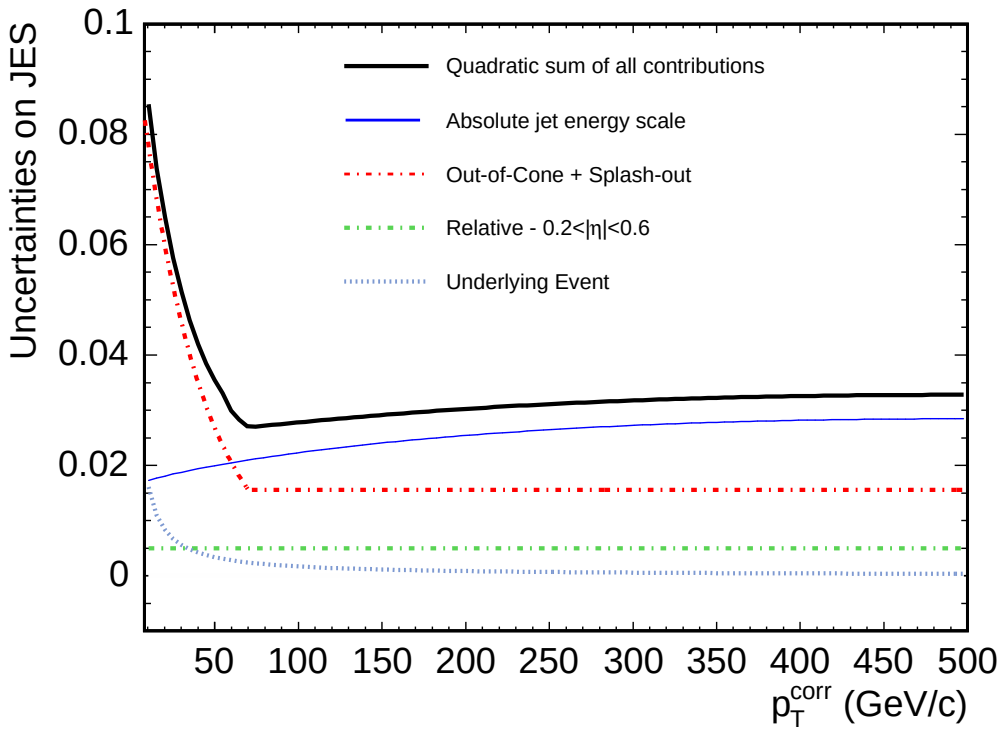

Figure 3.11: The combined fractional JES systematic uncertainty, σ_j/E_j, as a function of p_T. The solid black line shows the total while the other lines show the contributions of each Level.

Level 7, "out-of-cone", corrects the particle-level energy to the parton-level energy by correcting for the leakage of energy outside the jet cone. Only leakage up to a radius $R = 1.3$ is considered.

Level 8, "splash-out", is an estimated uncertainty only, accounting for the energy leakage for $R > 1.3$.

The fractional systematic uncertainties of Levels 6-8, are shown in Figure 3.11. The combined fractional systematic uncertainty of all of the Levels, σ_j/E_j, is calculated as the sum in quadrature of the Levels, and is also plotted in Figure 3.11.

3.2.5 Lepton energy calibration

Electron energies are calibrated by setting an absolute energy scale based on $Z \rightarrow e^+e^-$ data, where the invariant mass of the electron and positron can be tuned to the known Z boson mass of 91.18 GeV/c^2. This energy scale is known to within 0.034%. Corrections are also made for instrumental effects such as detector edge effects and losses.

The muon momentum scale is calibrated in a similar way using $Z \rightarrow \mu^+\mu^-$ and $J/\psi \rightarrow \mu^+\mu^-$ data, and is known to within 0.021%.

3.3 Event selection

The basic event selection criteria reflect the lepton+jets final-state particles, $\ell^+\nu_\ell b\ \bar{q}q'\bar{b}$, requiring that each event must have exactly one electron or muon and exactly four jets. Further requirements are then imposed to reduce the number of background events passing selection.

3.3.1 Lepton selection requirements

The most obvious signature of the lepton+jets final state is a high-p_T charged lepton. Central ($|\eta| < 1.1$) leptons are preferred due to the lower proportion of background events in that region. As such, the presence of a high-p_T central electron or muon becomes the primary criterion for event selection.

The specific trigger and selection requirements for electrons and muons are summarised in the following two sections. For both electrons and muons the first requirement is imposed in track reconstruction, with the helical track of any primary electron or muon constrained to originate from the beam line. COT tracks are required to have segments in at least 3 axial and 2 stereo superlayers, with each segment made up of at least 5 hits from the 12 wires in each sub-layer (see Section 2.2.1). Additionally, the z co-ordinate of the lepton track must be less than 5 cm from the event vertex, at the beam-line, and the vertex z position is required to be within 60 cm of the centre of the detector in order to ensure good event reconstruction.

Electrons

For consideration for use in this analysis, events with a final state electron candidate must be accepted by the CEM trigger. The name of this trigger refers to the calorimeter component used by the trigger (Section 2.2.2), and electron candidates therefore must have $|\eta| < 1.1$. Level 1 (L1) of the CEM trigger requires an energy release of at least 8 GeV in a central calorimeter tower, with the ratio of energy deposits in the hadronic part (the CHA) to those in the EM part (the CEM), $E_{\rm had}/E_{\rm EM} < 0.125$ [33]. It also requires an XFT track with $p_T > 8$ GeV/c, and pointing in a direction corresponding to the position of the tower. L2 of the trigger refines this by clustering the calorimeter towers, adding the energy in neighbouring towers with $E_T > 7.5$ GeV to that of the L1 tower, with the cluster required to have $E_T > 16$ GeV and $E_{\rm had}/E_{\rm EM} < 0.125$. At L3 a fully-reconstructed track with $p_T > 9$ GeV/c must, when extrapolated into the calorimetry system, intersect within 8 cm in z with an EM cluster with $E_T > 18$ GeV/c, again with $E_{\rm had}/E_{\rm EM} < 0.125$, and with a shower profile consistent with that expected from test beam electrons.

Having passed the CEM trigger, the electron candidate is subject to further requirements (or "cuts") in the offline reconstruction software. Electron candidates passing these requirements are called "tight electrons". The cluster must have $E_T > 20$ GeV, with the $E_{\rm had}/E_{\rm EM}$ requirement also stricter with $E_{\rm had}/E_{\rm EM} < 0.055 + 0.00045 \times (E_{\rm had} + E_{\rm EM})$ [33]; the energy dependence of the cut allows for the fact that higher energy EM showers are more likely to extend beyond the EM calorimeters and deposit some of their energy in the hadronic calorimeters. The candidate track must have $p_T > 10$ GeV/c, and the ratio of p_T to the E_T of the corresponding cluster must be greater than $\frac{1}{2}$ [6]; this requirement is dropped for $p_T > 50$ GeV/c due to the difficulties with accurately measuring the radius of curvature of high-p_T tracks. The cluster must also be "isolated", with the isolation $I < 0.1$ where I is defined as the ratio of the additional transverse energy in a cone of radius $R = 0.4$ around the cluster to the transverse energy of the cluster itself.

The position of the electromagnetic shower as measured by the CES is matched to the position of the extrapolated track. The distances in (r, ϕ) and z, Δx and Δz, must have $|\Delta z| \leq 3.0$ cm and $-3.0 \leq q|\Delta x| \leq 1.5$ cm [33]. The limits on $|\Delta x|$ are asymmetric and signed by the electric charge q (in units of e) to allow for the change in electron or positron momentum due to bremsstrahlung. Electrons coming from $\gamma \rightarrow e^+e^-$ conversions are accounted for by rejecting candidate electrons for which an oppositely charged track is found with appropriate kinematics.

Candidate electrons passing all the above requirements except for the isolation cut are called "loose electrons".

[6] The p_T of the electron track can be lower than would be suggested by the energy deposits in the calorimeter due to electron bremsstrahlung.

Muons

For consideration for use in this analysis, events with a final state muon candidate must be accepted by the CMUP or CMX triggers[7], meaning that only muons with $|\eta| < 1.0$ are considered. The CMUP trigger requires the muon to be seen in both the CMU and the CMP, effectively vetoing charged pions that would be unlikely to pass through to the CMP.

At L1, the CMUP trigger requires an XFT track with $p_T > 4$ GeV/c, matched to muon stubs in both the CMU and CMP chambers. The CMX trigger requires an XFT track with $p_T > 8$ GeV/c, matched to a muon stub in the CMX chambers. At L2 there is tighter matching between the tracks and stubs, and the XFT track p_T cut is increased to 15 GeV/c for both CMUP and CMX triggers. At L3, with fully reconstructed tracks and muon stubs, a track with $p_T > 18$ GeV/c must match a stub in the muon chambers within 10 cm in the transverse plane and, for CMU and CMX stubs, must also match the stub within 20 cm in z [33].

Having passed the CMUP or CMX trigger, the muon candidate is subject to further cuts in the offline reconstruction software. Muon candidates passing these requirements are called "tight muons". The track transverse momentum requirement is increased to $p_T \geq 20$ GeV/c. The track must be isolated, with the isolation $I < 0.1$ where I is defined as the ratio of the additional transverse energy deposited in a cone of radius $R = 0.4$ around the track direction to the transverse energy of the muon track. The energy deposits in the calorimeter towers matching the extrapolated track must also be small enough to be consistent with a minimum ionising particle: $E_{\text{had}} < 6 + 0.0280\,(p - 100)$ GeV (or $E_{\text{had}} < 6$ GeV for $p < 100$ GeV/c), and $E_{\text{EM}} < 2 + 0.0115\,(p - 100)$ GeV (or $E_{\text{EM}} < 2$ GeV for $p < 100$ GeV/c) [33].

The distance, Δx, between the extrapolated track and the muon stub(s) in the transverse plane must be $|\Delta x| < 3.0$ cm for CMU stubs, $|\Delta x| < 5.0$ cm for CMP stubs, and $|\Delta x| < 6.0$ cm for CMX stubs [33]. Unlike the electron requirements, the $|\Delta x|$ limits are symmetric and account for the effects of multiple scattering of the muon as it traverses the shielding. To reject secondary muons (from semi-leptonic b-decays or cosmic rays), the transverse impact parameter must be $|d_0| < 0.02$ cm (or $|d_0| < 0.2$ cm if the track has no silicon hits). Muons from cosmic rays are also rejected due to the discrepancies of their track time relative to the beam-crossing time.

As for the electrons, candidate muons passing all of the tight muon requirements except for the isolation cut are called "loose muons". The same name is also given to candidates which have a stub in only the CMU or CMP, but pass all other requirements.

3.3.2 Missing E_T

Large missing E_T ($\not\!\!E_T$) is also a characteristic feature of lepton+jets channel decays. The transverse energies of the incoming partons are very small relative to the longitudinal beam energy of 980 GeV, and due to momentum conservation this is also true of the combined set

[7] Here, the names of the triggers refer to the muon system component(s) used by the triggers.

of final state particles. However, the neutrino remains undetected, resulting in a non-zero vector sum of the transverse momenta of the detected particles.

Since the measurement of particle transverse momentum is, except for muons, carried out in the calorimeters, the magnitude of the vector sum is expressed as the missing transverse energy, $\not\!\!E_T$:

$$\not\!\!E_T = \left| \sum_{\text{towers}} E_T^i \hat{n}_T^i \right|, \tag{3.3.1}$$

where $\hat{n}_T^i$ is the unit vector pointing to tower i in the transverse plane. Only calorimeter towers with $|\eta| < 3.6$ are included in the sum, and the measurements of calorimeter towers corresponding to jets with $E_T > 8$ GeV and $|\eta| < 2.5$ are corrected to Level 5 (see Section 3.2.4). In muon events, the transverse energy in the calorimeter towers traversed by the muon is not included in the sum, and the transverse energy associated with their tracks is added to the sum [33]. All events are required to have $\not\!\!E_T > 20$ GeV.

3.3.3 Secondary Vertex b-tagging

The identification of a jet as originating from a b-quark is known as b-tagging. This information helps with jet-parton identification, and is also important in reducing the proportion of background events due to the relative rarity of b-quarks in background processes.

The b-quark hadrons resulting from top quark decays are usually highly boosted, resulting in a significant time dilation factor multiplying their $\tau_b \sim 10^{-12}$ s lifetimes. The b-quark hadrons therefore typically travel a few millimetres before decaying, creating a secondary vertex (Figure 3.12) that can be detected by the high-precision silicon tracker. A similar signature can be seen in jets originating from a c-quark, but the b-tagging algorithm is designed to minimise the c-quark contribution.

The b-tagging algorithm first looks at the tracks corresponding to the relevant jet. To allow accurate vertex reconstruction, there must be at least two tracks with $p_T \geq 1$ GeV/c, or one such track along with at least two additional tracks with $p_T \geq 0.5$ GeV/c. The transverse distance, $L_{2\text{D}}$, to the primary interaction vertex is then calculated (Figure 3.12). The jet is b-tagged if $L_{2\text{D}} > 7.5 \times \sigma_{L_{2\text{D}}}$, where $\sigma_{L_{2\text{D}}}$ is the estimated uncertainty on the measurement of $L_{2\text{D}}$. The value of 7.5 is chosen for optimum efficiency and purity in simulated b-jets from top quark decay [34].

The average efficiency for tagging the b-jets in $t\bar{t}$ events is about 40%, while c-jets are tagged about 8% of the time [35]. A secondary vertex can also be reconstructed when poorly reconstructed tracks apparently cross each other near the primary interaction vertex. Such mistaken identification of a secondary vertex is called a mistag. Mistags can also result from the displaced decays of long-lived light particles such as K_s and Λ. In total, about 1% of light flavour jets are mistagged [35].

At least one of the four jets from each event is required to be b-tagged.

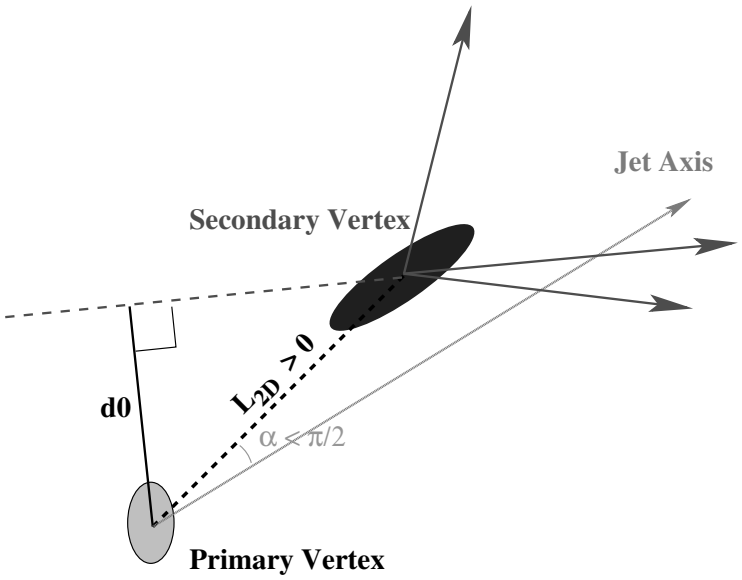

Figure 3.12: Secondary vertex b-tagging: b-quark hadrons typically travel a distance L_{2D} before decaying, creating a secondary vertex that can be detected by the high-precision silicon tracker.

3.3.4 Summary of event selection requirements

Using the information described in the previous sections, the event selection requirements can be summarised as follows.

- Exactly 4 jets with $|\eta| < 2.0$ and $E_T > 20$ GeV (after Level 5 corrections).
- 1 or more jets must be b-tagged.
- 1 and only 1 tight triggered lepton:
  - CEM electron with $E_T > 20$ GeV and $|\eta| < 1.1$.
  - CMUP or CMX muon with $p_T > 20$ GeV/c and $|\eta| < 1.0$.
- 0 loose leptons.
- $\not\!\!E_T > 20$ GeV (after Level 5 jet energy corrections).

Chapter 4

The Simulated and Experimental Data

4.1 The Experimental Data

Data taking at CDF is organised into time "periods", generally cycles of data taking between detector maintenance during which constant detector calibrations apply. This analysis makes use of CDF data up to period 19, including all data collected between February 4^{th}, 2002 and August 24^{th}, 2008, representing approximately 3.2 fb^{-1} of integrated luminosity. All of the detector subsystems important to this analysis were carefully monitored during those periods, and any segment of data for which there was a problem is excluded from consideration. A total of 578 candidate events pass this and the event selection requirements of Section 3.3.4 (Table 4.1). Of these events, 459 have 1 b-tag, 117 have 2 b-tags, and 2 have 3 b-tags.

4.2 Simulated Data

The use of simulated data is necessary in a number of areas of this analysis. Simulated signal ($t\bar{t}$) events are used to derive the jet-to-parton mapping functions ("Transfer Functions", Chapter 6). They are also required to derive the $t\bar{t}$ "Mean Acceptance Function" (Section 5.2.5), an important part of the normalisation of the event probability density function. Simulated $t\bar{t}$ events and simulated background events are also necessary to test and calibrate the measurement method (Chapter 7), prior to analysing the experimental data. Finally, the systematic uncertainties of the measurement are evaluated using simulated events (Chapter 8).

Events are simulated using various Monte Carlo (MC) event generators, which simulate the underlying physics processes and full event reconstruction in the detector. The parton-level information for each event is also stored, including the parton identity, decay chain, and kinematics. Comparisons between kinematic distributions in simulated data and experimental data ("validation", Section 4.5) show that the simulated data is in good agreement with the experimental data.

period	number of events
0d	70
0h	77
0i	53
8	24
9	33
10	51
11	43
12	23
13	42
14	9
15	30
16	12
17	24
18	54
19	32
total	578

Table 4.1: Number of selected data events for each period, corresponding to the total integrated luminosity of 3.2 fb^{-1} .

The MC event generators used in this analysis are `PYTHIA` [36], `ALPGEN 2.10` [37] and `MadEvent` [38]. `PYTHIA` uses leading-order matrix elements to generate the QCD hard scattering interaction. It then simulates hadronisation and parton showers with QCD radiation and fragmentation. `ALPGEN` is another leading-order matrix element generator that specialises in final states with a large number of jets, and is thus useful for background simulation. `ALPGEN` is used only to generate the hard scattering interaction, after which `PYTHIA` is used to simulate hadronisation and detection. `MadEvent` is a multi-purpose leading-order matrix element generator that can simulate events for any tree-level process. Like `ALPGEN`, it is used in conjunction with `PYTHIA`. The leading-order `CTEQ5L` [39] Parton Distribution Functions (Section 5.2.2) are used in the generation of all simulated events.

4.2.1 Signal events

Simulated signal events are all `PYTHIA 6.216` generated $t\bar{t}$ events, with various simulated top quark masses. The nominal sample has $m_t = 175$ GeV/c^2 and contains 4.8 million events, and is referred to as `ttop75`. Another 20 samples are used with masses ranging from 161 to 185 GeV/c^2. Each of these samples has approximately 1.2 million events.

"Good" and "bad" signal events

Not all `PYTHIA` $t\bar{t}$ events are well described by the lepton+jets signal hypothesis. Those that are well described are called "good" signal events, while those that are not are called "bad" signal events (see Section 5.5).

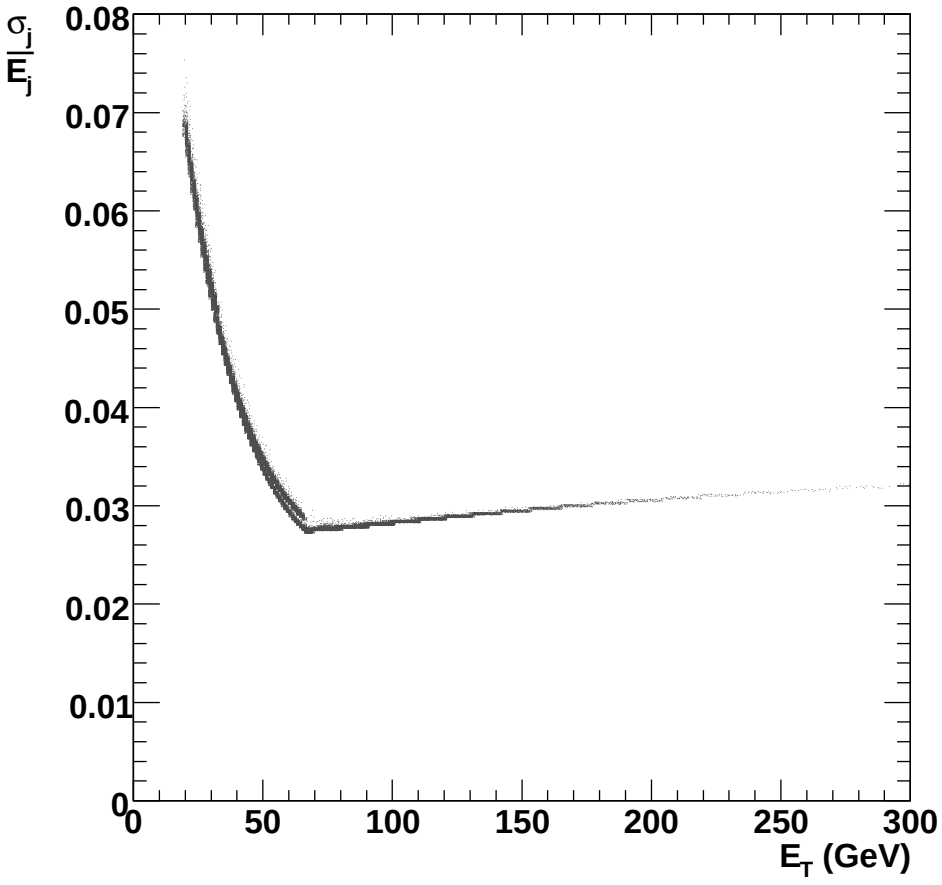

Figure 4.1: The fractional jet energy uncertainty, σ_j/E_j, plotted against jet transverse energy E_T. Note that the plot shows not just a line but a narrow distribution, as a result of the $|\eta|$-dependence of the Level 1 fractional systematic uncertainty (Figure 3.7).

4.3 The jet energy scale correction Δ_{JES}

The simulated events described in Section 4.2 accurately model those observed in data. However, there are significant systematic uncertainties associated with the calorimeter Jet Energy Scale (JES, Section 3.2.4), meaning that the jet energies measured in data may not be in accordance with those in the simulated events. This JES uncertainty may be treated as an overall systematic uncertainty of the measurement. However, such a treatment overestimates the uncertainty because the JES can be constrained[1] via the invariant mass of the two daughter jets of the hadronic-side W boson. This constraint allows the *in situ* measurement of a JES correction, Δ_{JES}, effectively calibrating the measured jet energies based on the known W boson mass. This replaces a large component of the systematic JES uncertainty with a typically much smaller statistical uncertainty associated with the measured Δ_{JES}.

[1]Clearly any such constraint can strictly only be imposed on the JES pertaining to jets from W boson decay. In practice, the constraint is imposed on all measured jets and the additional b-jet JES uncertainty is accounted for as a separate systematic uncertainty on the m_t measurement (Section 8.4).

The simplest description of the JES correction involves the use of a "scale factor" JES correction and requires the assumption that the energies E_j of reconstructed jets in experimental data look like those simulated in Monte Carlo once they have been corrected (to E'_j) by a constant factor $(1 + \Delta_{\text{JES}})$, i.e. $E'_j = (1 + \Delta_{\text{JES}})\, E_j$. Any given Δ_{JES} therefore imposes a constant percentage shift in jet energy.

However, it is known that the fractional uncertainty on the measurement of jet energies in the detector is not constant, and the energy measurement for each jet has an associated JES uncertainty, σ_j, as described in Section 3.2.4. The fractional uncertainty, σ_j/E_j, is plotted against jet transverse energy E_T in Figure 4.1. Note that this is effectively a sum in quadrature of the fractional uncertainties of the various Levels of jet energy correction plotted in Figure 3.11. Low E_T jets have much higher fractional uncertainties, which suggests that a constant scale factor JES description (as has been used in previous versions of this analysis [1]) may not be optimal. In fact, it seems to make most sense to allow those jets most affected by the JES uncertainty to shift more with respect to Δ_{JES}, which suggests the definition

$$E'_j = E_j - \Delta_{\text{JES}} \cdot \sigma_j, \tag{4.3.1}$$

that is, Δ_{JES} denotes the number of σ_j by which the jet energies in experimental data are shifted relative to the simulated data. Note that E_j is the Level-5-corrected measured jet energy, i.e. the estimated energy of the particle-level jet, while E'_j also allows for a Δ_{JES} shift in calorimeter response.

4.4 Background events

To create realistic samples of simulated data ("pseudoexperiments"), events for the background processes expected to contribute to the final data sample are also required. They are summarised here.

4.4.1 W+jets

A number of processes can result in the production of a W boson plus exactly 4 jets in the detector. If the W boson decays leptonically, such events mimic the lepton+jets decay channel. Events are simulated using the `ALPGEN 2.10` and `PYTHIA 6.325` generators, and subdivided into categories based on jet flavour. While it would be expected that a final state with four partons would result in four detected jets, events generated with fewer final state partons can still produce four jets in the detector. This can occur as a result of initial and final state radiation, fragmentation, and detector effects. As a result, the number of partons can be fewer than four, and in general W+jets background comprises $W + 4p$, $W + 3p$, $W + 2p$, $W + 1p$ and $W + 0p$ generated events.

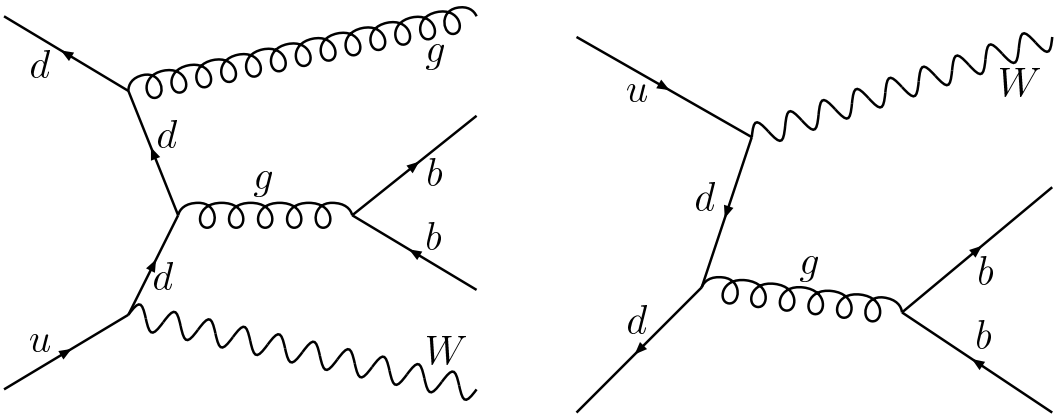

Figure 4.2: Example Feynman diagrams for $Wb\bar{b}$ background processes.

$Wb\bar{b}$

$Wb\bar{b}$ refers to the case where 2 of the 4 jets originate from b-quarks, and two examples of possible production processes are given in Figure 4.2. $Wb\bar{b}$ background produces an exact topological match to the decay signature of the lepton+jets channel, and can only be distinguished kinematically.

$Wc\bar{c}$

$Wc\bar{c}$ refers to the case where 2 of the 4 jets originate from c-quarks. Such events can be produced in a similar manner as $Wb\bar{b}$ (Figure 4.2). To mimic lepton+jets decays, at least one of the $Wc\bar{c}$ jets must be b-tagged. Since c-jets exhibit a similar secondary vertex to b-jets (Section 3.3.3) this is not uncommon, occurring in $\sim 12\%$ of $Wc\bar{c}$ events.

Wc

Wc refers to the case where 1 of the 4 jets originates from a c-quark, and an example of a possible production process is given in Figure 4.3a. To mimic lepton+jets decays, at least one of the Wc jets must be b-tagged.

W+light flavours

The remaining W+jets processes, where all jets originate from light flavoured quarks, are combined into the W+light flavours category. An example of a possible production process is given in Figure 4.3b. To mimic lepton+jets decays, at least one of the light jets must be mistagged (Section 3.3.3). This is relatively rare, occurring in about 3% of W+light flavours events.

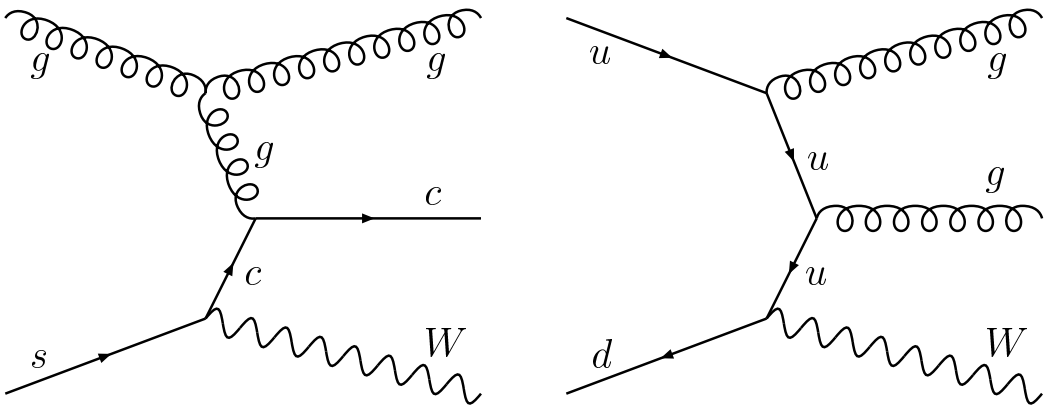

(a) **(b)**

Figure 4.3: Example (a) Wc and (b) W+light flavours Feynman diagrams.

4.4.2 Z+jets

Z+jets events can reproduce the lepton+jets decay signature if the Z-boson decays leptonically and one of the leptons is not detected. Z+jets events are also generated with `ALPGEN 2.10` and `PYTHIA 6.325`.

4.4.3 Diboson

Diboson backgrounds have two W or Z bosons produced alongside jets. The background processes are labelled "WW", "WZ" and "ZZ", depending on which two bosons were produced. In WW and WZ events, if one W decays leptonically and the remaining W or Z decays hadronically, the lepton+jets decay signature can be matched. ZZ events are unlikely to simulate lepton+jets decays and are not expected to significantly contribute to the background (see Table 4.2). Diboson events are generated with `PYTHIA 6.216`.

4.4.4 Single top

The single top contributions to the background events are produced in the two channels illustrated in Figure 1.3, t-channel and s-channel, and are generated using `MadEvent` and `PYTHIA 6.325`.

s-channel

s-channel single-top production results in a top quark and a b-jet. If the decay of the W boson from the top quark decay is leptonic, and two additional jets are present in the event, the lepton+jets signature is met.

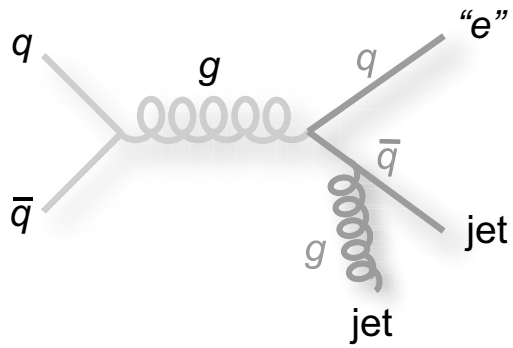

Figure 4.4: Example of a Non-W background process. One of the jets must be mistakenly reconstructed as an electron, "e".

t-channel

t-channel single top production requires an initial gq hard interaction, with the gluon splitting to $b\bar{b}$. One of these b-quarks exchanges a W boson with the initial state quark q, giving a top quark and a final state quark (see Figure 1.3). Combined with the remaining b-quark and one additional jet, this mimics the lepton+jets decay signature.

4.4.5 Non-W (QCD)

Non-W backgrounds refer to QCD interactions where the lepton does not come from a W or Z boson. Instead, one of the jets simulates ("fakes") an electron (Figure 4.4), while some event E_T is lost (either undetected or badly reconstructed), simulating $\not\!\!E_T$. Four additional jets are also needed to match the lepton+jets channel signature.

QCD events are not simulated, and are taken from the all-hadronic dataset. All selection requirements are identical to those for the data, except that the lepton is required to be non-isolated such that the sum of the E_T within a cone of radius $R = 0.4$ around the lepton is greater than 20% of the E_T of the lepton. A non-isolated lepton indicates hadronic activity and therefore a QCD process.

4.4.6 Sample composition

For each background process, it is necessary to know its expected fractional contribution to the data sample to allow for accurate simulation of the data. Table 4.2 gives the expected number of signal and background events, as determined by the CDF "Method II For You" [35, 40] code developed for lepton+jets channel analyses. Overall, $t\bar{t}$ signal events are expected to make up 76% of the data sample. Of the 24% of events expected to be background, 69% are W+jets events ($Wb\bar{b}$, $Wc\bar{c}$, Wc and W+light flavours), 19% are non-W while the other categories contribute just a combined 12%.

sample	number of events	% of total	% of background
$t\bar{t}$ signal	425.0 ± 58.9	76.0%	-
$Wb\bar{b}$	39.0 ± 12.7	7.0%	29.1%
non-W	25.0 ± 20.5	4.5%	18.7%
W+light flavours	22.5 ± 5.7	4.0%	16.8%
$Wc\bar{c}$	20.3 ± 6.7	3.6%	15.2%
Wc	10.7 ± 3.6	1.9%	8.0%
WW	4.2 ± 0.5	0.8%	3.1%
Z+light flavours	3.9 ± 0.5	0.7%	2.9%
single top (t-channel)	3.3 ± 0.3	0.6%	2.5%
single top (s-channel)	3.3 ± 0.3	0.6%	2.5%
WZ	1.5 ± 0.2	0.3%	1.1%
ZZ	0.4 ± 0.1	0.1%	0.3%
total	559.2 ± 67.0	100%	-
Observed (data)	578		

Table 4.2: Number of expected signal and background events as determined by "Method II For You", corresponding to the total integrated luminosity of 3.2 fb^{-1} . The percentages are used in the creation of pseudoexperiments and in the validation.

4.5 Validation

The event simulation is validated by comparing the distributions of kinematic properties in simulated data with those in experimental data. A large simulated data sample is created with the proportion of events from each category given by the numbers in Table 4.2, but with the total number of events scaled up to make the statistical uncertainties on the simulated distributions negligible compared to those on the distributions seen in data. The results are shown in Figures 4.5 and 4.6. For each pair of distributions, the Kolmogorov-Smirnov (K-S) probability and the χ^2 both indicate good agreement between the simulated data and the measured data.

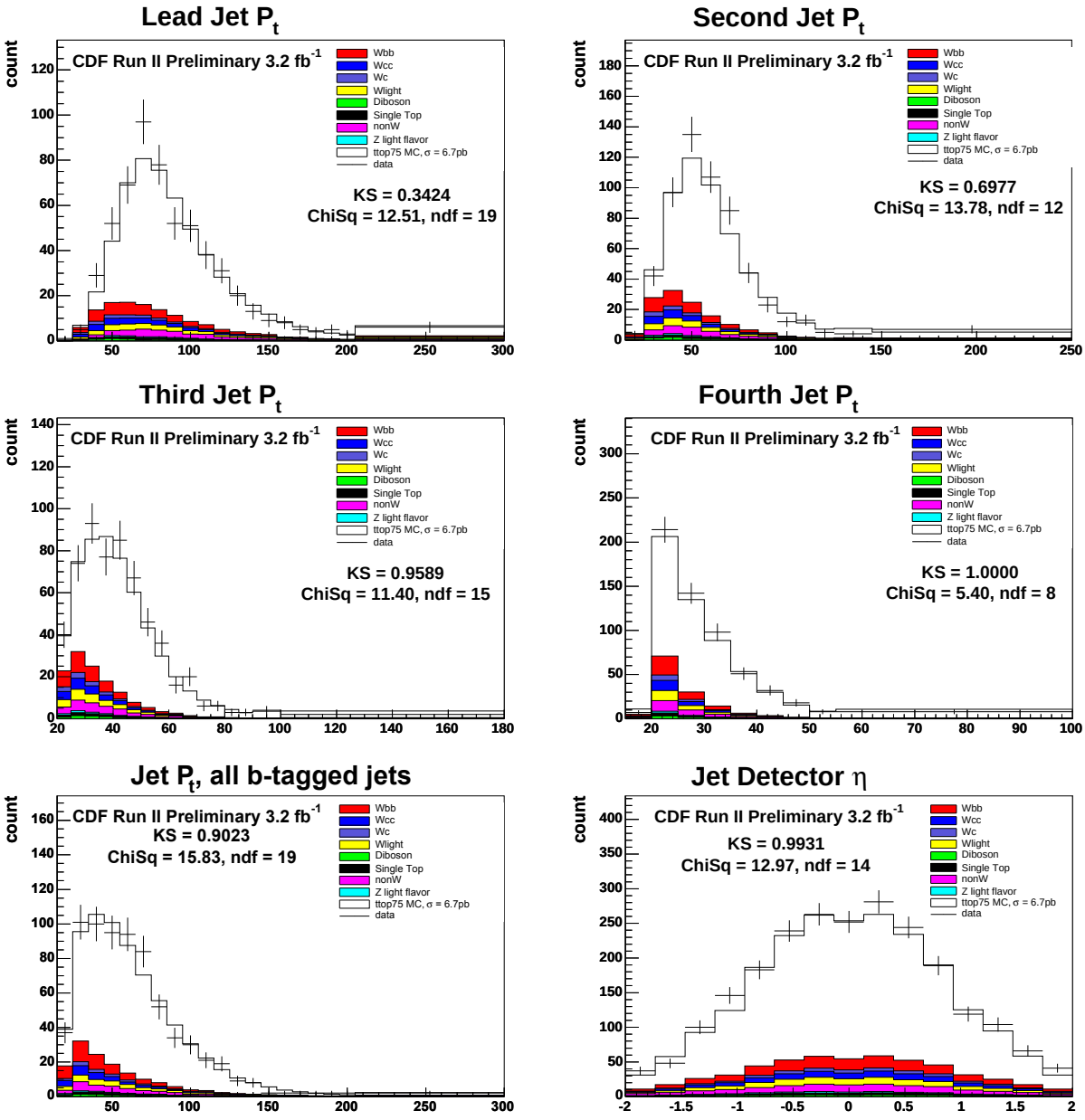

Figure 4.5: Various validation plots. In each case, the Kolmogorov-Smirnov (K-S) probability and the χ^2 both indicate good agreement between the simulated data and the measured data.

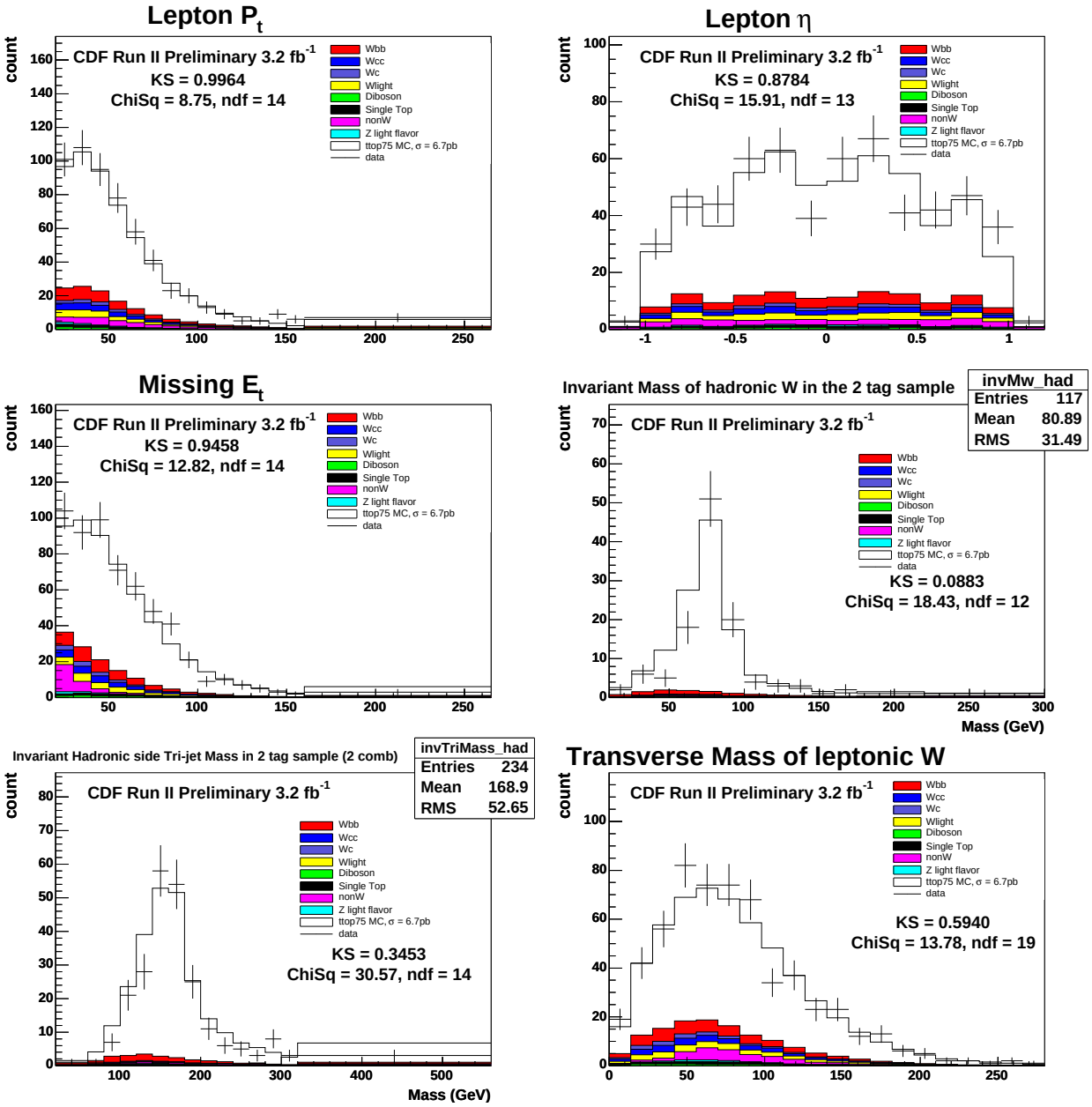

Figure 4.6: Various validation plots. In each case, the Kolmogorov-Smirnov (K-S) probability and the χ^2 both indicate good agreement between the simulated data and the measured data.

Chapter 5

Method of Measurement

The measurement of the top quark mass may appear to be a simple task. To make a direct measurement of the mass of a particle, it is sufficient only to know its energy E and three-momentum $\vec{p}^2$: $m^2 = E^2 - \vec{p}^2$. Since the top quark decays before it can hadronise (Section 1.2.2), it is possible in principle to ascertain those quantities directly from the daughter particles. In the lepton+jets decay channel (Section 1.2.2), one of the produced top and antitop quarks decays hadronically and the other leptonically with topology $p\bar{p} \to t\bar{t} \to W^+b\, W^-\bar{b} \to \ell^+\nu_\ell b\, \bar{q}q'\bar{b}$. The top quark mass on the "hadronic side" is therefore given by the invariant mass of the $\bar{b}$ and the two jets from the hadronic W decay ($\bar{q}q'$), and on the "leptonic side" by the invariant mass of the b, the lepton (ℓ), and the neutrino (ν_ℓ).

However, in practice there are a number of difficulties with this approach. First, the neutrino escapes the detector unmeasured. While its transverse momentum may be inferred by momentum conservation (assuming zero total momentum in the transverse plane), its longitudinal momentum is unconstrained because the initial momentum along the beamline is unknown (although the proton and antiproton each have energy 980 GeV, the momentum fraction of the colliding partons is unknown). A direct mass measurement is therefore not possible on the leptonic side. Second, while the lepton is readily identified (Section 3.3), it is not known which measured jet corresponds to which quark. With four quarks in total, this leaves $4! = 24$ permutations of jet-parton assignment so even on the hadronic side it is not possible to make an unambiguous measurement. Third, there is a good deal of uncertainty surrounding the calorimeter energy measurements of the jets, which require special treatment (Section 3.2.2). Finally, there are a number of other processes that can mimic the lepton+jets final state. These "background" processes are indistinguishable from true "signal" events in the detector, and provide spurious information about the top quark mass.

These difficulties mean that it is not practical to calculate the top quark mass, m_t, for each individual event, and instead information is extracted based on the information provided by the entire data sample. Generally, a maximum likelihood technique is used to estimate the most likely value of m_t given the analysed data. A technique known as the "template method" was used in the first measurements of m_t in 1995 [15, 16]. Such early implementations of the template method made use of simulated kinematic distributions at different supposed values of m_t, with the measured m_t determined by a binned maximum

likelihood fit to the distribution seen in data.

This analysis employs an unbinned maximum likelihood method, where an m_t-dependent probability density function (p.d.f.) is calculated for each event using theoretical knowledge of the production and decay of the top quark. The likelihood function has the simple form

$$\mathcal{L}(\vec{\boldsymbol{x}}; m_t, \Delta_{\text{JES}}, \nu_{\text{sig}}) = \prod_{i=1}^{n} P(\vec{x_i}; \vec{\alpha}), \tag{5.0.1}$$

where $\vec{x_i}$ represents the measured kinematic quantities (i.e. particle momenta) for event i, and $\vec{\boldsymbol{x}}$ represents the set of kinematic quantities in the whole sample of n events. The likelihood parameters are denoted $\vec{\alpha}$ and are the parameters to be measured; their measured values will be those that maximise the likelihood function. In this analysis, the likelihood parameters $\vec{\alpha}$ are the top quark mass, m_t; the jet energy scale correction, Δ_{JES}; and the signal fraction parameter, ν_{sig}.

Signal events are defined as events consistent with leading-order (LO) $t\bar{t}$ pair production and decay into the lepton+jets channel. In the SM, LO top quark pair-production and decay is a well understood process and is described by a LO matrix element (from which this analysis takes its name). The matrix element describes the invariant amplitude for a given initial and final state configuration (in this case $q\bar{q} \to t\bar{t} \to \ell^+\nu_\ell b\ \bar{q}q'\bar{b}$). A similar matrix element exists for the largest background in the analysis, W+jets production (Section 4.4). Making the approximation that these two processes completely describe each event in the data sample[1], together they can can be used to construct the p.d.f. for each event:

$$P(\vec{x}; \vec{\alpha}) = \nu_{\text{sig}} P_s(\vec{x}; m_t, \Delta_{\text{JES}}) + (1 - \nu_{\text{sig}}) P_b(\vec{x}; \Delta_{\text{JES}}), \tag{5.0.2}$$

where P_s and P_b are respectively the normalised p.d.f.s for signal and background events, and ν_{sig} is the measured signal fraction parameter (constrained $0 \leq \nu_{\text{sig}} \leq 1$).

5.1 Constructing the event p.d.f.s

The signal and background p.d.f.s P_s and P_b are constructed in analogous fashions, and this section therefore describes the p.d.f. for a general physical scattering process with the appropriate initial and final states. If the kinematic quantities are perfectly measured, the p.d.f. for producing a given parton-level final state is simply the normalised differential cross-section:

$$P(\vec{y}) = \frac{1}{\sigma} \frac{d^n\sigma}{d^n y}, \tag{5.1.1}$$

[1] Although there are other background processes (see Section 4.4), the use of just the W+jets matrix element is justified in Section 5.3.

where $\vec{y}$ denotes the n kinematic quantities describing the final state and σ is the total cross-section for the scattering process and normalises the p.d.f.

In reality, no quantities are perfectly measured and some are not measured at all. Measured quantities ($\vec{x}$) are translated into their corresponding parton level quantities ($\vec{y}$) by convolution with a jet-to-parton mapping function called a "Transfer Function" (described in detail in Chapter 6), and unmeasured quantities must be integrated over. The p.d.f. becomes

$$P(\vec{x}) = \frac{1}{\sigma} \int d\sigma \; W(\vec{x}, \vec{y}), \tag{5.1.2}$$

where $d\sigma$ is the differential cross-section and $W(\vec{x}, \vec{y})$ is the Transfer Function. Note that the Transfer Function only describes the subset $\vec{y}$ of the integration variables of $d\sigma$ that correspond to the measured quantities $\vec{x}$; for example, the neutrino momentum is included in $d\sigma$ but not in $\vec{x}$ or $\vec{y}$.

Since the colliding particles are p and $\bar{p}$, the differential cross-section must also be convolved with Parton Distribution Functions (PDFs):

$$P(\vec{x}) = \frac{1}{\sigma} \int d\sigma \; f(x^1_{\mathrm{Bj}}) f(x^2_{\mathrm{Bj}}) \; W(\vec{x}, \vec{y}) \; dx^1_{\mathrm{Bj}} dx^2_{\mathrm{Bj}}. \tag{5.1.3}$$

The PDFs $f(x_{\mathrm{Bj}})$ define the probability density for a colliding parton to carry a longitudinal momentum fraction x_{Bj}.

The generic differential cross-section for the production and decay of a parton into an n-body final state is given [12] in terms of the Lorentz-invariant matrix element $\mathcal{M}$ by

$$d\sigma = \frac{(2\pi)^4 |\mathcal{M}|^2}{4\sqrt{(q_1 \cdot q_2)^2 - m^2_{q_1} m^2_{q_2}}} d\Phi_n(q_1 + q_2; p_1, ..., p_n), \tag{5.1.4}$$

where q_1 and q_2 are the four momenta of the incident partons and m_{q_1} and m_{q_2} are their masses. The p_i are the four-momenta of the final-state partons, and $d\Phi_n$ is an element of the n-body Lorentz-invariant phase space given by

$$d\Phi_n(q_1 + q_2; p_1, ..., p_n) = \delta^4((q_1 + q_2) - \sum_{i=1}^{n} p_i) \prod_{i=1}^{n} \frac{d^3 p_i}{(2\pi)^3 2E_i}. \tag{5.1.5}$$

Since the 980 GeV collisions at the Tevatron mainly involve light quarks or gluons, $|\vec{q_i}| \gg m_{q_i}$ and the masses of the initial state partons may be neglected. Neglecting also any transverse momentum[2], the square-root in Equation 5.1.4 may be simplified to

$$\sqrt{(q_1 \cdot q_2)^2 - m^2_{q_1} m^2_{q_2}} \simeq 4 |\vec{q_1}| |\vec{q_2}|. \tag{5.1.6}$$

[2]Any effects of these approximations are corrected for in the measurement calibration (see Chapter 7).

Lepton+jets decays give rise to six final state particles: 4 quarks, a lepton, and a neutrino. Equation 5.1.3 can thus be expressed as

$$P(\vec{x}) = \frac{1}{\sigma}\frac{(2\pi)^4}{16}\int |\mathcal{M}|^2 \frac{f(x^1_{\rm Bj})}{|\vec{q_1}|}\frac{f(x^2_{\rm Bj})}{|\vec{q_2}|}W(\vec{x},\vec{y})d\Phi_6 dx^1_{\rm Bj}dx^2_{\rm Bj}, \tag{5.1.7}$$

where the 6-body phase space, $d\Phi_6$, is given by

$$d\Phi_6 = \delta^4((q_1+q_2) - \sum_{i=1}^{4q,l,\nu} p_i) \prod_{i=1}^{4q,l,\nu} \frac{d^3p_i}{(2\pi)^3 2E_i}, \tag{5.1.8}$$

where the i denote the 4 quarks ($4q$), a lepton (l), and a neutrino (ν).

The overall phase space is reduced by using the four-momentum conservation delta function to perform the integration over p^ν_x, p^ν_y, $x^1_{\rm Bj}$, and $x^2_{\rm Bj}$. Since the delta function constrains the total four-momentum and not directly the $x^i_{\rm Bj}$, this requires a change of variables of the integration over $x^1_{\rm Bj}$ and $x^2_{\rm Bj}$ to the total energy E and the total z-momentum p_z. Assuming that the colliding partons have no transverse momentum,

$$dx^1_{\rm Bj}dx^2_{\rm Bj} \simeq d\left(\frac{|\vec{q_1}|}{E_p}\right)\, d\left(\frac{|\vec{q_2}|}{E_{\bar{p}}}\right) = \frac{1}{2E_pE_{\bar{p}}} d\left(|\vec{q_1}| + |\vec{q_2}|\right) d\left(|\vec{q_1}| - |\vec{q_2}|\right), \tag{5.1.9}$$

where E_p and $E_{\bar{p}}$ are the proton and antiproton energies of 980 GeV, and assuming also massless colliding partons gives

$$\begin{aligned} (|\vec{q_1}| + |\vec{q_2}|) &\simeq E \\ (|\vec{q_1}| - |\vec{q_2}|) &\simeq p_z. \end{aligned} \tag{5.1.10}$$

That leaves an overall phase space given by

$$d\tilde{\Phi} = \frac{1}{2E_pE_{\bar{p}}}\frac{dp^z_\nu}{(2\pi)^3 2E_\nu}\prod_{i=1}^{4q,l}\frac{d^3p_i}{(2\pi)^3 2E_i}. \tag{5.1.11}$$

The jet momenta are then converted to spherical coordinates[3]. That gives

$$d\tilde{\Phi} = \frac{1}{(2\pi)^{18}2^6}\frac{1}{2E_pE_{\bar{p}}}\frac{dp^z_\nu d^3p_l}{E_lE_\nu}\prod_{i=1}^{4q}\frac{\rho_i^2 d\rho_i d\Omega_i}{E_i}, \tag{5.1.12}$$

where the ρ_i and Ω_i are the momentum magnitude and solid angle of quark i.

In general, it is not possible to distinguish between the four jets in the final state, so an average must be taken over all $4! = 24$ possible permutations of jet-parton identification. The general p.d.f. for lepton+jets final states is therefore given by

[3]Spherical co-ordinates allow a more natural description since the detector measures the angles of particles rather than the Cartesian components of their 3-momenta.

$$P^{\text{ideal}}(\vec{x}) = \frac{1}{\sigma}\frac{(2\pi)^4}{16\cdot 24}\sum_{\text{perm}}^{24}\int |\mathcal{M}|^2 \frac{f(x^1_{\text{Bj}})}{|\vec{q_1}|}\frac{f(x^2_{\text{Bj}})}{|\vec{q_2}|}W(\vec{x},\vec{y})d\tilde{\Phi}, \tag{5.1.13}$$

where the reason for the introduction of the superscript "ideal" is explained in the next section (Section 5.1.1).

5.1.1 Acceptance

The p.d.f. in Equation 5.1.13 is idealised in that it is constructed assuming that the events it describes cover the kinematic phase-space of all possible measurements $\vec{x}$. Since in practice this phase-space is always limited by the physical properties of the detector apparatus and the event selection, an overall event "acceptance" function, $Acc(\vec{x})$, is introduced, describing these effects. Acceptance is defined as the fraction of fully reconstructed events passing selection out of the total possible number, for each set of measurable parameters $\vec{x}$. The idealised p.d.f. in Equation 5.1.13 is therefore multiplied by the acceptance function:

$$P(\vec{x}) = Acc(\vec{x})P^{\text{ideal}}(\vec{x}). \tag{5.1.14}$$

The acceptance function $Acc(\vec{x})$ is solely a property of the detector and event selection procedure, and is also independent of the likelihood parameters. It can therefore be neglected in the likelihood function (Equation 5.0.1), because any overall constant factor in the product has no effect on the outcome of the likelihood maximisation. However, the acceptance term does affect the normalisation of the p.d.f., introducing a term known as the "mean acceptance function" which can depend on the likelihood parameters:

$$\overline{Acc}(\vec{\alpha}) \equiv \int Acc(\vec{x})\ P^{\text{ideal}}(\vec{x};\vec{\alpha})\ d\vec{x}, \tag{5.1.15}$$

where the potential dependence of P^{ideal}, and thus the mean acceptance function $\overline{Acc}$, on the likelihood parameters $\vec{\alpha}$ has been made explicit. Thus, removing the factor $Acc(\vec{x})$ from the p.d.f. (except in the calculation of its normalisation), the final p.d.f. is defined as

$$P(\vec{x};\vec{\alpha}) \equiv \frac{1}{\overline{Acc}(\vec{\alpha})}P^{\text{ideal}}(\vec{x};\vec{\alpha}), \tag{5.1.16}$$

where P^{ideal} is taken from Equation 5.1.13.

Since the mean acceptance function only enters the expression for $P(\vec{x})$ (Equation 5.1.16) as an additional factor in the normalisation, the idealised part $P^{\text{ideal}}(\vec{x})$ can be evaluated independently. The mean acceptance function $\overline{Acc}(\vec{\alpha})$ for the p.d.f. can then be calculated using Monte Carlo integration (see Section 5.2.5). Note that it is therefore not necessary to directly parameterise $Acc(\vec{x})$.

In Sections 5.2 and 5.3, the specific $t\bar{t}$ and W+jets p.d.f.s P_s and P_b are derived from Equations 5.1.13 and 5.1.16 using their respective matrix elements and specific integration techniques.

5.2 The signal p.d.f. P_s

The signal p.d.f. P_s describes the leading-order $t\bar{t}$ pair production and decay into the lepton+jets channel, and contains all of the information about the top quark mass. It is calculated numerically (Section 5.2.4), and the approximations and changes of variables described in this section are designed to optimise the CPU time needed for the calculation.

5.2.1 $t\bar{t}$ matrix element

The leading-order $t\bar{t}$ matrix element used in this analysis represents only the quark-antiquark collision production process of Figure 1.2. This approximation is reasonable since it accounts for about 85% of $t\bar{t}$ pairs produced at CDF (as calculated to NLO). Its effect is considered as a systematic uncertainty of the measurement[4], and is found to be very small (Section 8.8).

The matrix element used in this analysis was evaluated by Mahlon and Parke, averaging over initial spins and colours and summing over final spins and colours [41]. Making the approximation of ignoring the spin correlations between the t and $\bar{t}$ [5], the matrix element may be expressed as

$$\sum |\mathcal{M}|^2 = \frac{g_s^4}{9} F \bar{F} (2 - \beta^2 \sin^2 \theta_{qt}), \tag{5.2.1}$$

where g_s is the strong coupling constant and θ_{qt} describes the angle in the $t\bar{t}$ centre-of-mass frame between the direction of the incoming partons and the outgoing top quarks. The terms F and $\bar{F}$ are identical in form and respectively describe the leptonic and hadronic decay of the top quark:

$$F = \frac{g_W^4}{4} \frac{(m_t^2 - m_{\bar{e}\nu}^2)}{(m_{b\bar{e}\nu}^2 - m_t^2)^2 + m_t^2 \Gamma_t^2} \frac{m_t^2(1 - c_{\bar{e}b}^2) + m_{\bar{e}\nu}^2 (1 + c_{\bar{e}b})^2}{(m_{\bar{e}\nu}^2 - m_W^2)^2 + m_W^2 \Gamma_W^2} \tag{5.2.2}$$

$$\bar{F} = \frac{g_W^4}{4} \frac{(m_t^2 - m_{d\bar{u}}^2)}{(m_{\bar{b}d\bar{u}}^2 - m_t^2)^2 + m_t^2 \Gamma_t^2} \frac{m_t^2(1 - c_{d\bar{b}}^2) + m_{d\bar{u}}^2 (1 + c_{d\bar{b}})^2}{(m_{d\bar{u}}^2 - m_W^2)^2 + m_W^2 \Gamma_W^2}, \tag{5.2.3}$$

where g_W is the weak coupling constant and c_{ij} represents the cosine of the angle ϕ_{ij} between particle i and particle j in the rest frame of the relevant W boson (Figure 5.1). Note that the subscript "e" denotes either an electron or a muon, "u" and "d" represent up-type and

[4] Note that about 95% of the `PYTHIA` $t\bar{t}$ events come from $q\bar{q}$ collisions (5% from gg) since they are only simulated to leading-order; the effect of this approximation is covered by the same systematic.

[5] This approximation is expected to have negligible effect and is accounted for as part of the MC generator systematic uncertainty (Section 8.1).

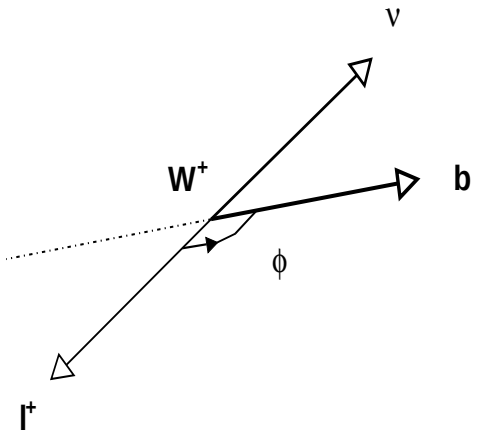

Figure 5.1: Definition of ϕ_{ij} (in this case $\phi_{\bar{e}b}$), the angle between particle i and particle j in the rest frame of the parent W boson of particle i.

down-type quarks, while "b" specifically denotes bottom quarks. Γ_t and Γ_W are the widths of the top quark and W boson, and since $\Gamma_t \ll m_t$ the narrow-width approximation can be made in the Breit-Wigners for the top quark decay:

$$\frac{1}{(m^2 - m_t^2)^2 + m_t^2\Gamma_t^2} \approx \frac{\pi}{m_t\Gamma_t}\delta(m^2 - m_t^2). \tag{5.2.4}$$

This approximation is desirable because the delta functions will eventually allow for the removal of two dimensions of the P_s integration (Section 5.2.3), with corresponding savings in CPU time.

Since it is impossible to distinguish between the d- and u-jets in the detector, and using the fact that $c_{d\bar{b}} = -c_{\bar{u}\bar{b}}$, $\bar{F}$ is symmetrised by taking the average of the two possible assignments. That leaves

$$F = \frac{g_W^4}{4}\frac{\pi(m_t^2 - m_{\bar{e}\nu}^2)}{m_t\Gamma_t}\frac{m_t^2(1 - c_{\bar{e}b}^2) + m_{\bar{e}\nu}^2(1 + c_{\bar{e}b})^2}{(m_{\bar{e}\nu}^2 - m_W^2)^2 + m_W^2\Gamma_W^2}\delta(m_{b\bar{e}\nu}^2 - m_t^2) \tag{5.2.5}$$

$$\bar{F} = \frac{g_W^4}{4}\frac{\pi(m_t^2 - m_{d\bar{u}}^2)}{m_t\Gamma_t}\frac{m_t^2(1 - c_{d\bar{b}}^2) + m_{d\bar{u}}^2(1 + c_{d\bar{b}}^2)}{(m_{d\bar{u}}^2 - m_W^2)^2 + m_W^2\Gamma_W^2}\delta(m_{\bar{b}d\bar{u}}^2 - m_t^2), \tag{5.2.6}$$

where d now denotes either one of the two jets from the hadronically decaying W boson. As a result of the two jets being treated indistinguishably, the number of remaining jet-parton assignments in the sum of Equation 5.1.13 is halved from 24 to 12. Later, the number is further reduced by using b-tagging information (see Section 3.3.3), resulting in an average over 6 assignments for single-tagged events and 2 for double-tagged events. In the rare case of more than 2 b-tags, the average is taken over all 12 possible assignments[6].

[6]Events with more than 2 b-tags are likely to have at least one misidentified b-jet (a "mistag"), and so b-tagging information is disregarded. Only two such events, both with 3 b-tags, are seen in the 578-event data sample

The expression for Γ_t is derived from the standard expression for three-body top decay [12]:

$$d\Gamma_t = \frac{1}{2^7(2\pi)^5}\frac{|\mathcal{M}|^2}{m_t}\left(1-\frac{m_W^2}{m_t^2}\right)dm_W^2 d\Omega_W d\Omega_e. \tag{5.2.7}$$

Taking the top decay matrix element from Equation 5.2.5 (i.e. still using the narrow width approximation for the top quark) gives [1]

$$\Gamma_t = \frac{g_W^4 m_t^3 \Theta}{3\ 2^6(2\pi)^3}\frac{1-3(m_W/m_t)^4+2(m_W/m_t)^6}{m_W\Gamma_W}, \tag{5.2.8}$$

where

$$\Theta \equiv \arctan\left[\frac{(m_t-m_b)^2-m_W^2}{m_W\Gamma_W}\right] - \arctan[\frac{-m_W^2}{m_W\Gamma_W}]. \tag{5.2.9}$$

Note, however, that due to the narrow width approximation this analysis is insensitive to the form of Γ_t, the factor Γ_t^2 in the P_s matrix element $|\mathcal{M}|^2$ being cancelled by the same factor Γ_t^2 in the normalisation $\sigma(m_t)$ (Section 5.2.5). This analysis therefore neglects the effects of the m_t-dependence of the top quark width Γ_t, and any consequences of this approximation are accounted for in the measurement calibration (Chapter 7).

5.2.2 PDFs

The probability density for finding a parton with longitudinal momentum fraction x_{Bj} at a given squared four-momentum transfer Q^2 is described by the proton Parton Distribution Function (PDF) for that parton. The antiproton PDFs are the same as for the proton, with the proton PDF for a given parton also describing the parton's antiparticle in the antiproton. In this analysis, Version 5.0 of the `CTEQ` leading-order PDFs (`CTEQ5L`) are used [39]. The partons involved in the scattering are assumed to be only the valence *uud* quarks of the proton, and taking the average over their PDFs gives

$$f(x_{\mathrm{Bj}}^i, Q^2) = \frac{\texttt{CTEQ5L}_u(x_{\mathrm{Bj}}^i, Q^2) + \texttt{CTEQ5L}_d(x_{\mathrm{Bj}}^i, Q^2)}{3}, \tag{5.2.10}$$

where

$$Q^2 = \frac{(M_T^{\mathrm{had}\,t})^2 + (M_T^{\mathrm{lep}\,t})^2}{2}. \tag{5.2.11}$$

The M_T are the transverse top quark masses on the hadronic and leptonic sides, where M_T^2 is defined as $M_T^2 = m_t^2 + p_x^2 + p_y^2$, and the form of Q^2 was chosen for consistency with `PYTHIA` [36].

5.2.3 P_s integration variables

For use in the calculation of P_s, the quark integration variables in Equation 5.1.12 are labelled to represent the four corresponding jets. The subscripts bh, bl, $j1$, and $j2$ represent, respectively, the hadronic- and leptonic-side b-jets and the two indistinguishable jets from the hadronically decaying W boson. The charged lepton and neutrino variables continue to be represented by the subscripts l and ν.

The integration variables include the large regions of $d\rho_{bh}$, $d\rho_{bl}$, $d\rho_{j1}$, $d\rho_{j2}$, and dp_ν^z. This large multi-dimensional phase-space is not optimal for numerical integration, and the narrow Breit-Wigners in Equations 5.2.5 and 5.2.6 suggest a natural replacement. The four momentum variables $d\rho_{bh}$, $d\rho_{bl}$, $d\rho_{j2}$, and dp_ν^z are therefore changed to the hadronic-side and leptonic-side top quark and W boson squared-masses, denoted as m_{th}^2, m_{tl}^2, m_{Wh}^2, and m_{Wl}^2. The Jacobian determinant J for this transformation is

$$J = \left| \frac{\partial m_{th}^2 \partial m_{Wh}^2 \partial m_{tl}^2 \partial m_{Wl}^2}{\partial \rho_{bh} \partial \rho_{j2} \partial \rho_{bl} \partial p_\nu^z} \right| = \partial_{11}\partial_{22}(\partial_{33}\partial_{44} - \partial_{34}\partial_{43}), \tag{5.2.12}$$

where

$$\partial_{11} \equiv \frac{\partial m_{th}^2}{\partial \rho_{bh}} = 2\left(\frac{\rho_{bh}}{E_{bh}}E_{j1} - \rho_{j1}\cos\alpha_{b1}\right) + 2\left(\frac{\rho_{bh}}{E_{bh}}E_{j2} - \rho_{j2}\cos\alpha_{b2}\right) \tag{5.2.13}$$

$$\partial_{22} \equiv \frac{\partial m_{Wh}^2}{\partial \rho_{j2}} = 2\left(\frac{\rho_{j2}}{E_{j2}}E_{j1} - \rho_{j1}\cos\alpha_{12}\right) \tag{5.2.14}$$

$$\partial_{43} \equiv \frac{\partial m_{Wl}^2}{\partial \rho_{bl}} = 2\left[\frac{\partial p_\nu^x}{\partial \rho_{bl}}\left(\frac{\rho_e}{\rho_\nu}p_\nu^x - p_e^x\right) + \frac{\partial p_\nu^y}{\partial \rho_{bl}}\left(\frac{\rho_e}{\rho_\nu}p_\nu^y - p_e^y\right)\right] \tag{5.2.15}$$

$$\partial_{44} \equiv \frac{\partial m_{Wl}^2}{\partial p_\nu^z} = 2\left(\frac{\rho_e}{\rho_\nu}p_\nu^z - p_e^z\right) \tag{5.2.16}$$

$$\partial_{34} \equiv \frac{\partial m_{tl}^2}{\partial p_\nu^z} = \partial_{44} + 2\left(\frac{E_{bl}}{\rho_\nu}p_\nu^z - \rho_{bl}\cos\theta_{bl}\right) \tag{5.2.17}$$

$$\begin{aligned}\partial_{33} \equiv \frac{\partial m_{tl}^2}{\partial \rho_{bl}} &= \partial_{43} + 2\left(\frac{\rho_{bl}}{E_{bl}}\rho_e - \rho_e\cos\alpha_{eb}\right) + 2\left[\frac{\rho_{bl}}{E_{bl}}\rho_\nu + \frac{E_{bl}}{\rho_\nu}\left(\frac{\partial p_\nu^x}{\partial \rho_{bl}}p_\nu^x + \frac{\partial p_\nu^y}{\partial \rho_{bl}}p_\nu^y\right)\right] \\ &- 2\left[\sin\theta_{bl}\cos\phi_{bl}\left(p_\nu^x + \rho_{bl}\frac{\partial p_\nu^x}{\partial \rho_{bl}}\right) + \sin\theta_{bl}\sin\phi_{bl}\left(p_\nu^y + \rho_{bl}\frac{\partial p_\nu^y}{\partial \rho_{bl}}\right) + \cos\theta_{bl}p_\nu^z\right]\end{aligned} \tag{5.2.18}$$

where the angles α_{ij} are the angles between particles i and j in the lab frame and

$$\frac{\partial p_\nu^x}{\partial \rho_{bl}} = -\sin\theta_{bl}\cos\phi_{bl} \tag{5.2.19}$$

$$\frac{\partial p_\nu^y}{\partial \rho_{bl}} = -\sin\theta_{bl}\sin\phi_{bl}. \tag{5.2.20}$$

Note that despite the change of integration variables, the integrand and the Jacobian are still chosen to be expressed in terms of the momentum variables. These momentum variables must therefore be calculated from the mass-squared variables, and the solution takes the form of an eighth-order polynomial. By temporarily neglecting the mass of the leptonic-side b-quark this is reduced to a fourth-order polynomial, the solutions of which are obtained analytically

with a quartic equation solver. The up-to two real solutions are summed; details of the calculation of these solutions are given in Appendix A. The colliding parton longitudinal momenta are also calculated, for use in the PDFs (Appendix A.3).

After the change of variables, the narrow width approximation delta functions in Equations 5.2.5 and 5.2.6 remove the two integrations over the hadronic- and leptonic-side top quark masses. Thus, the event top quark masses for the t and $\bar{t}$ are both set to the same value of m_t in the likelihood function.

After the variable transformation and narrow-width approximation, the phase space in Equation 5.1.12 becomes

$$d\tilde{\Phi} = \frac{1}{(2\pi)^{18}2^6}\frac{1}{2E_pE_{\bar{p}}}\frac{1}{J}\frac{\rho_{bh}^2\rho_{j1}^2\rho_{j2}^2\rho_{bl}^2}{E_{bh}E_{j1}E_{j2}E_{bl}E_lE_\nu}d^3p_l dm_{Wl}^2 dm_{Wh}^2 d\rho_{j1}d\Omega_{bh}d\Omega_{bl}d\Omega_{j1}d\Omega_{j2}, \quad (5.2.21)$$

where the four quarks are now explicitly identified with their resulting jets: $j1$ and $j2$ are the two hadronic-side W jets, assumed massless, and bh and bl are respectively the hadronic-side and leptonic-side b jets, assumed to have mass $m_b = 4.8$ GeV/c^2. The expression for P_s^{ideal} is then taken directly from Equation 5.1.13,

$$P_s^{\text{ideal}}(\vec{x}; m_t, \Delta_{\text{JES}}) = \frac{1}{\sigma(m_t)}\frac{(2\pi)^4}{16\, n_{\text{assign}}}\sum_{\text{assign}}^{2,6,12}\int |\mathcal{M}(m_t)|^2\frac{f(x_{\text{Bj}}^1)}{|\vec{q_1}|}\frac{f(x_{\text{Bj}}^2)}{|\vec{q_2}|}W(\vec{x},\vec{y},\Delta_{\text{JES}})d\tilde{\Phi}, \quad (5.2.22)$$

where dependencies on the likelihood parameters m_t and Δ_{JES} have been made explicit and the number of jet-parton assignments in the sum is understood to be 2, 6 or 12 as determined by the b-tagging information.

5.2.4 P_s integration technique

The ideal signal p.d.f. P_s^{ideal} (Equation 5.2.22) is calculated using the `VEGAS` [42] adaptive Monte Carlo integration algorithm. The `VEGAS` algorithm is based on importance sampling, meaning that the sampling points used in the integration are concentrated in the regions of the p.d.f. that make the largest contribution to the final integral.

The cross-section normalisation $\sigma(m_t)$ is removed from Equation 5.2.22 in the calculation; the overall normalisation, including mean acceptance function, is calculated separately (Section 5.2.5).

To reduce CPU time, it is necessary to further reduce the number of dimensions in the integral from the 14 in the phase space of Equation 5.2.21. This is achieved by making approximations in the Transfer Function (see Chapter 6), briefly summarised here: the three dimensions of lepton momentum integration d^3p_l are removed by assuming that the Transfer Function is a delta function in those quantities (i.e. $\delta^3(\vec{p_l^y} - \vec{p_l^x})$), and the eight dimensions

of jet angle integration ($d\Omega_{bh}d\Omega_{bl}d\Omega_{j1}d\Omega_{j2}$) are replaced by just two angular dimensions ($d\cos(\alpha_{12})\, d\cos(\alpha_{Wb})$), via a change of variables again with assumed delta functions. The resulting integral has just the following five dimensions: $dm^2_{Wl}dm^2_{Wh}d\rho_{j1}d\cos(\alpha_{12})d\cos(\alpha_{Wb})$ (see Equation 6.3.2).

The number of sampling points, and thus the CPU time, required by the `VEGAS` algorithm is also strongly dependent on the shape of the integrand. Integrands with high, narrow peaks require more sampling points. To smooth out the final integrand, an additional two changes of variable are made, removing the W boson Breit-Wigners in Equations 5.2.5 and 5.2.6:

$$\int \frac{dm^2}{(m^2 - m_W^2)^2 + m_W^2\Gamma_W^2} \rightarrow \int \frac{d\mu}{m_W\Gamma_W}, \tag{5.2.23}$$

where m is the event W boson mass (m_{Wh} or m_{Wl}) and m_W is the pole mass of the W boson, $m_W = 80.4$ GeV/c^2. This implies μ is defined such that

$$m^2 = m_W\Gamma_W \tan\mu + m_W^2. \tag{5.2.24}$$

Thus, the final form of P_s^{ideal} does not contain any Breit-Wigners, and the five integration variables are $d\mu_{Wl}$, $d\mu_{Wh}$, $d\rho_{j1}$, $d\cos(\alpha_{12})$, and $d\cos(\alpha_{Wb})$.

A total of 10000 integration sampling points is found to be sufficient to obtain a reliable result[7], with the result for each jet-parton assignment taking approximately 4 seconds to evaluate using a typical (2.0 GHz) CPU. For each event, the m_t and Δ_{JES} dependence of $P_s^{\text{ideal}}(\vec{x}; m_t, \Delta_{\text{JES}})$ is scanned over a two-dimensional grid of 31 m_t points by 17 Δ_{JES} points (see Section 5.4). Since the result is initially evaluated for all 12 jet-parton assignments, this gives a total of $12 \times 31 \times 17 = 6324$ integrations for each event, taking approximately 7 hours of CPU time per event. Since approximately 100000 simulated events are used in the calibration of the analysis and in the evaluation of its systematic uncertainties, this results in a total analysis computation time of about 80 CPU years. This is only achievable by running the integrations for many events in parallel with the use of large distributed computing networks.

5.2.5 P_s normalisation

The normalisation for P_s^{ideal} (Equation 5.2.22) is just the $p\bar{p} \rightarrow t\bar{t}$ cross-section $\sigma(m_t)$. Rather than using the theoretical leading-order cross-section as in previous versions of this analysis, $\sigma(m_t)$ is calculated using the same `VEGAS` integration algorithm and similar C++ code as for P_s (Section 5.2.4). This has two benefits: first, it ensures the normalisation is consistent with the p.d.f., and second it provides a good cross-check for the analysis C++ code.

[7]This was tested by increasing the sampling points by a factor of 10, which had negligible effect on the overall likelihood function.

An equation for the cross-section normalisation $\sigma(m_t)$ comes from Equation 5.2.22, with the requirement $\int P_s^{\text{ideal}}(\vec{x})d\vec{x} = 1$:

$$\sigma(m_t) = \int \frac{(2\pi)^4}{16} \int |\mathcal{M}(m_t)|^2 \frac{f(x^1_{\text{Bj}})}{|\vec{q_1}|} \frac{f(x^2_{\text{Bj}})}{|\vec{q_2}|} W(\vec{x}, \vec{y}, \Delta_{\text{JES}}) d\tilde{\Phi} d\vec{x}, \tag{5.2.25}$$

where the average over jet-parton assignments is no longer necessary because the value of the integral is the same in each case. The integral of the Transfer Function over the measured quantities, $\int W(\vec{x}, \vec{y}, \Delta_{\text{JES}})\, d\vec{x} = 1$ by construction (Chapter 6), and only the integral of the parton-level differential cross-section and PDFs remains:

$$\sigma(m_t) = \frac{(2\pi)^4}{16} \int |\mathcal{M}(m_t)|^2 \frac{f(x^1_{\text{Bj}})}{|\vec{q_1}|} \frac{f(x^2_{\text{Bj}})}{|\vec{q_2}|} d\tilde{\Phi}. \tag{5.2.26}$$

Here, the integration must be performed over the total 14 dimensions of phase space $d\tilde{\Phi}$ (Equation 5.2.21). The variable changes of Equation 5.2.23 are again used, and the number of integration sampling points is increased to 2×10^8 with a corresponding increase in evaluation time to ~ 20 CPU hours. The integral is evaluated at 39 points between $m_t = 134$ GeV/c^2 and $m_t = 210$ GeV/c^2, with a spacing of 2 GeV/c^2 between points. The results are plotted in Figure 5.2 along with the theoretical leading-order cross-section for comparison[8]. It can be seen that the agreement is good, and $\sigma(m_t)$ is taken from a fit to the points with a 5^{th} order polynomial. Note that since it is only necessary to evaluate $\sigma(m_t)$ once, the very high (~ 20 hours) CPU-time per integration is not a problem.

With P_s^{ideal} normalised, it remains only to calculate the mean acceptance function. From Equation 5.1.15, the mean acceptance function for P_s is defined as:

$$\overline{Acc}(m_t, \Delta_{\text{JES}}) \equiv \int Acc(\vec{x})\ P_s^{\text{ideal}}(\vec{x}; m_t, \Delta_{\text{JES}})\ d\vec{x}. \tag{5.2.27}$$

This integral can be approximated for any pair of values of m_t and Δ_{JES} as a sum over n_{events} simulated events generated with p.d.f. $P_s^{\text{ideal}}(\vec{x}; m_t, \Delta_{\text{JES}})$, a technique known as Monte Carlo integration:

$$\overline{Acc}(m_t, \Delta_{\text{JES}}) \approx \sum_{\text{events}} Acc(\vec{x_i}) \frac{1}{n_{\text{events}}(m_t, \Delta_{\text{JES}})}. \tag{5.2.28}$$

[8]Constant factors in $\sigma(m_t)$ are irrelevant and thus often neglected in the C++ code. The calculated $\sigma(m_t)$ is therefore scaled to match the theoretical $\sigma(m_t)$ at $m_t = 150$ GeV/c^2 in the comparison.

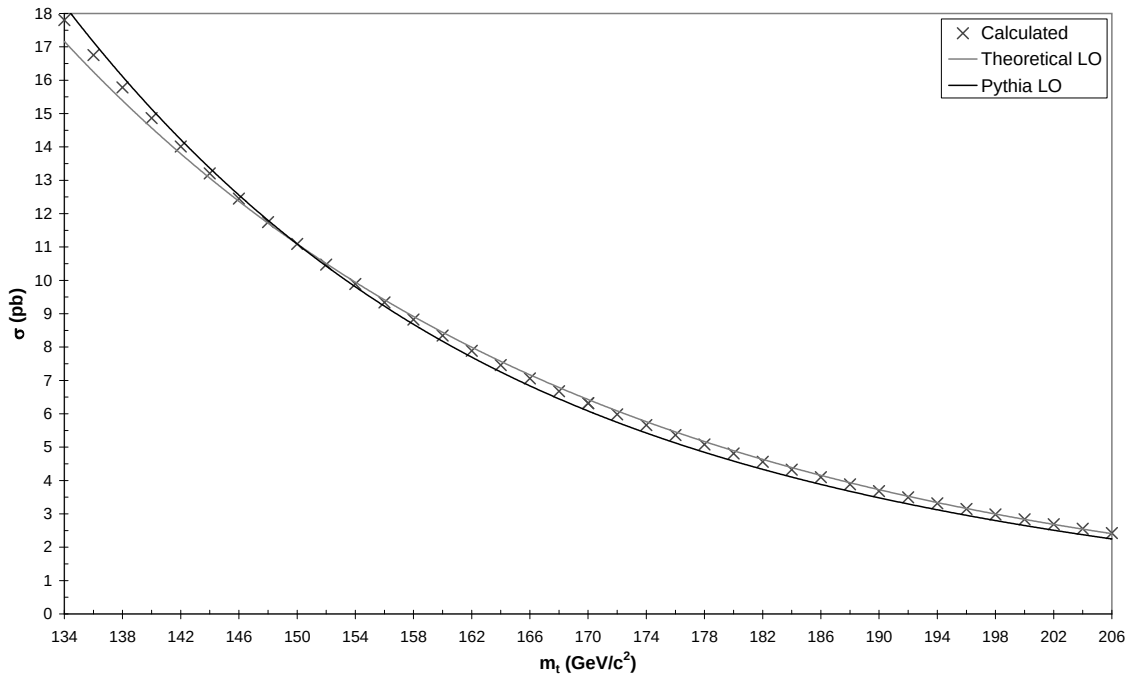

Figure 5.2: Calculated cross-section $\sigma(m_t)$ (crosses), with the PYTHIA LO cross-section (black line) and an exponential fit to the theoretical LO cross-section (grey line) for comparison. Due to the neglect of constant factors in the calculation, the three are scaled to match at $m_t = 150$ GeV/c^2.

Since the acceptance for any one event with measured quantities $\vec{x_i}$ is either 0 or 1, Equation 5.2.28 simplifies to

$$\overline{Acc}(m_t, \Delta_{\text{JES}}) \approx \frac{n_{\text{accepted}}(m_t, \Delta_{\text{JES}})}{n_{\text{events}}(m_t, \Delta_{\text{JES}})}, \tag{5.2.29}$$

the mean acceptance of generated events.

PYTHIA events are assumed to be produced with the p.d.f. P^{ideal} (this is somewhat justified by the fact that the Transfer Functions are derived from PYTHIA events), so $\overline{Acc}(m_t, \Delta_{\text{JES}})$ is just the mean acceptance of PYTHIA events. The simulated mean acceptance distribution is fitted to a 2D 4$^{\text{th}}$ order polynomial (Figure 5.3), defining the mean acceptance function $\overline{Acc}(m_t, \Delta_{\text{JES}})$ to be used in the measurement.

The fully normalised $t\bar{t}$ p.d.f. P_s is therefore given by

$$P_s(\vec{x}) = \frac{1}{\overline{Acc}(m_t, \Delta_{\text{JES}})\, \sigma(m_t)} \frac{(2\pi)^4}{16\, n_{\text{assign}}} \sum_{\text{assign}}^{2,6,12} \int |\mathcal{M}(m_t)|^2 \frac{f(x^1_{\text{Bj}})}{|\vec{q_1}|} \frac{f(x^2_{\text{Bj}})}{|\vec{q_2}|} W(\vec{x}, \vec{y}, \Delta_{\text{JES}}) d\tilde{\Phi}. \tag{5.2.30}$$

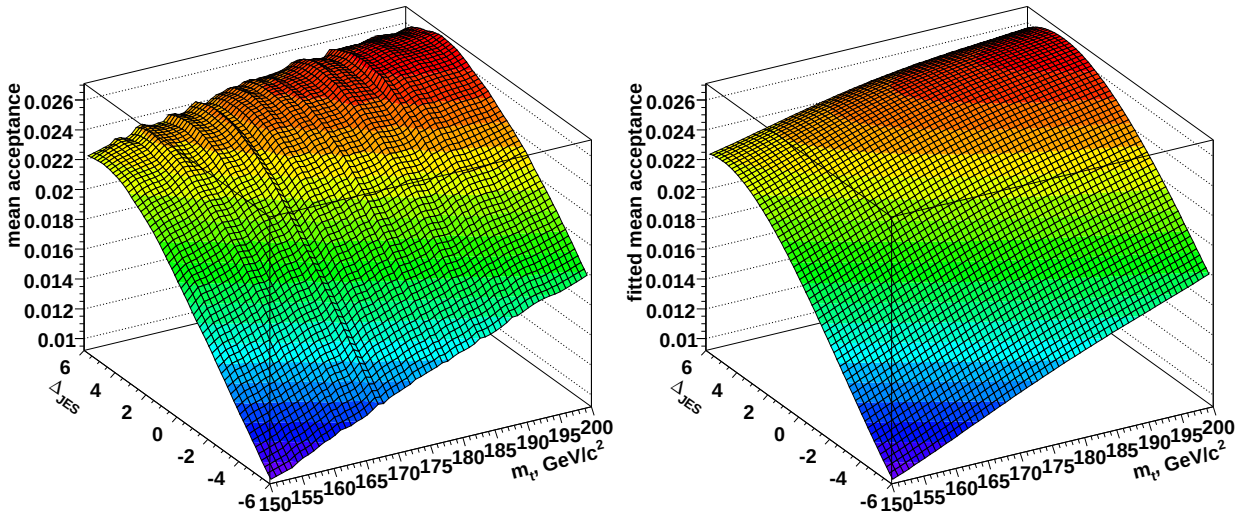

Figure 5.3: The mean acceptance function $\overline{Acc}(m_t, \Delta_{\mathrm{JES}})$). Left: histogram of the results of the Monte Carlo integration (Equation 5.2.29). Right: 2D 4$^{\mathrm{th}}$ order polynomial fit (χ^2/n.d.f. = 0.92).

5.3 The background p.d.f. P_b

Equation 5.1.13 represents a general p.d.f. for lepton+jets signature decays. For the background p.d.f. P_b, a W+jets matrix element is used. Although the main background in this analysis comes from W+jets production (69%, see Table 4.2), the remaining 31% is not from W+jets production and therefore not theoretically represented in this analysis. The response of P_b to the various background types is looked at in Section 5.6, and any bias caused by the background types that are not well described is corrected for in the measurement calibration (Section 7.3).

5.3.1 W+jets Matrix Element

The W+jets p.d.f. uses a matrix element calculated with Version 3.0 of the `VECBOS` Monte Carlo event generator [43]. The invariant amplitude comes from several leading-order diagrams for W+4 partons production and includes an average over initial spins and sum over final spins as well as a sum over quark flavours (u, d, s and c).

5.3.2 P_b integration technique

The W+jets p.d.f. includes a 16-dimensional integral, requiring numerous evaluations of the `VECBOS` matrix element. Since the `VECBOS` matrix element is not analytic and is much more complex than the $t\bar{t}$ matrix element, it requires much more CPU time to be evaluated. A `VEGAS` integration in the manner of the signal p.d.f. is therefore prohibitive.

A customised Monte Carlo method of integration was therefore developed, with many approximations, giving reasonable convergence within a practicable amount of CPU time. The initial expression for P_b^{ideal} is taken from Equation 5.1.13:

$$P_b^{\text{ideal}}(\vec{x}) = \frac{1}{\sigma}\frac{(2\pi)^4}{16\cdot 24}\sum_{\text{perm}}^{24}\int |\mathcal{M}|^2 \frac{f(x^1_{\text{Bj}})}{|\vec{q_1}|}\frac{f(x^2_{\text{Bj}})}{|\vec{q_2}|}W(\vec{x},\vec{y})d\Phi. \tag{5.3.1}$$

Note that all 24 permutations of jet-parton assignment must be averaged since b-tagging information does not favour any particular assignment in W+jets events.

From Equation 5.1.12, the phase space is modified by a change of variables from the longitudinal component of the neutrino momentum, p_ν^z, to the squared-mass of the leptonically decaying W boson[9], m^2_{Wl}, using Equation 5.2.16. Quark and lepton masses are neglected, and the phase space becomes

$$d\Phi = \frac{1}{(2\pi)^{18}2^6}\frac{1}{2E_pE_{\bar{p}}}\frac{1}{2\rho_e(\rho_e p_\nu^z - p_e^z\rho_\nu)}dm^2_{Wl}d^3p_l\prod_{i=1}^{4q}\rho_i d\rho_i d\Omega_i. \tag{5.3.2}$$

To reduce CPU time, the integral over dm^2_{Wl} is removed, constraining the W boson mass to 80.4 GeV/c^2 [10]. After this approximation, the sum over the two possible p_ν^z solutions of the change of variables must be explicitly included in the p.d.f.

As for P_s the dimensions of the phase space are further reduced by making assumptions about the Transfer Function $W(\vec{x},\vec{y})$. In this case, as well as the lepton momentum d^3p_l all jet angles $d\Omega_i$ are assumed to be well measured, meaning that the Transfer Function is a delta function in those quantities. The dimensions of the phase-space are thus reduced to just the four parton energies $d\rho_i$:

$$d\Phi = \frac{1}{(2\pi)^{18}2^6}\frac{1}{2E_pE_{\bar{p}}}\frac{1}{2\rho_e(\rho_e p_\nu^z - p_e^z\rho_\nu)}\prod_{i=1}^{4q}\rho_i d\rho_i. \tag{5.3.3}$$

To reduce CPU time further, P_b is assumed to have no Δ_{JES} dependence, and the integration is only evaluated at $\Delta_{\text{JES}} = 0$. As a result, P_b is just a constant for each event and does not introduce any shape into the likelihood function, acting just as a discriminant against the P_s contribution from events with $P_b \gtrsim P_s$.

Removing all constant factors (since due to the approximate integration procedure the P_b cross-section normalisation σ cannot be accurately calculated) and now explicitly including only the jet energy Transfer Functions $W_E^i(\rho_i^x,\rho_i^y)$, P_b can be expressed as

$$P_b(\vec{x}) = \int \sum_{\text{perm}}^{24}\sum_{p_\nu^z}^{2}|\mathcal{M}|^2\frac{f(x^1_{\text{Bj}})}{|\vec{q_1}|}\frac{f(x^2_{\text{Bj}})}{|\vec{q_2}|}\frac{1}{\rho_e(\rho_e p_\nu^z - p_e^z\rho_\nu)}\prod_{i=1}^{4q}\left(\frac{\rho_i^y}{(\rho_i^x)^2}W_E^i(\rho_i^x,\rho_i^y)d\rho_i\right), \tag{5.3.4}$$

[9] Note that the leptonically decaying W boson is the only W boson in W+jets events.

[10] This is effectively imposing the narrow-width approximation on the W boson.

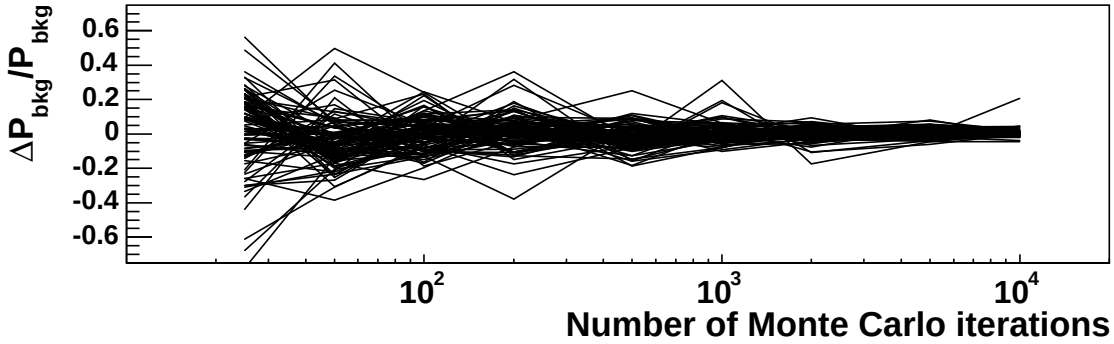

Figure 5.4: Fractional variation in calculated P_b as a function of number of Monte Carlo iterations.

where the superscripts x and y denote measured and parton level quantities respectively[11], and the form of the jet energy Transfer Functions is taken from Equation 6.0.2.

The Monte Carlo integration is then evaluated by using p.d.f.s for the four parton energies that are obtained from the observed jet energies and the jet energy Transfer Functions (see Section 6.1). For each Monte Carlo iteration those p.d.f.s are used to randomly generate the energies of the four partons, using which the P_b integrand of Equation 5.3.4 (excluding the Monte Carlo integration p.d.f.s W_E^i) is evaluated. The estimated P_b for an event is then just the average obtained from the Monte Carlo iterations:

$$P_b(\vec{x}) \approx \sum_{n_{\rm MC}} \left[\sum_{\rm perm}^{24} \sum_{p_\nu^z}^{2} |\mathcal{M}|^2 \frac{f(x^1_{\rm Bj})}{|\vec{q_1}|} \frac{f(x^2_{\rm Bj})}{|\vec{q_2}|} \frac{1}{\rho_e(\rho_e p_\nu^z - p_e^z \rho_\nu)} \prod_{i=1}^{4q} \left(\frac{\rho_i^y}{(\rho_i^x)^2} \right) \right] \frac{1}{n_{\rm MC}}. \qquad (5.3.5)$$

A convergence test was used to optimise the number of Monte Carlo iterations $n_{\rm MC}$ per event [1]. Figure 5.4 shows the fractional variation in P_b as a function of the number of Monte Carlo iterations using 100 simulated W+jets events. The choice of 400 iterations results in a maximum of 20% uncertainty on the value of P_b, requiring a reasonable ~ 13 minutes to process each event. This level of uncertainty would clearly not be sufficient for P_s, but since P_b does not contain any information about the top quark mass and acts essentially as an event-by-event discriminant, the approximate nature of P_b cannot severely affect the sensitivity of the method to m_t.

5.3.3 P_b normalisation

The W+jets matrix element has no m_t dependence, and to reduce calculation time the p.d.f. P_b is only evaluated at nominal $\Delta_{\rm JES}$ ($\Delta_{\rm JES} = 0$). As a result, the normalisation (including mean acceptance function) is independent of m_t and $\Delta_{\rm JES}$, and the normalisation of Equation 5.3.5 is written as the constant $\nu_{\rm bkg}$.

[11] The x and y superscripts are necessary to make the distinction between measured and parton level quantities only in the parts pertaining to the Transfer Function; all other quantities such as the matrix element, PDFs and Jacobian are parton-level.

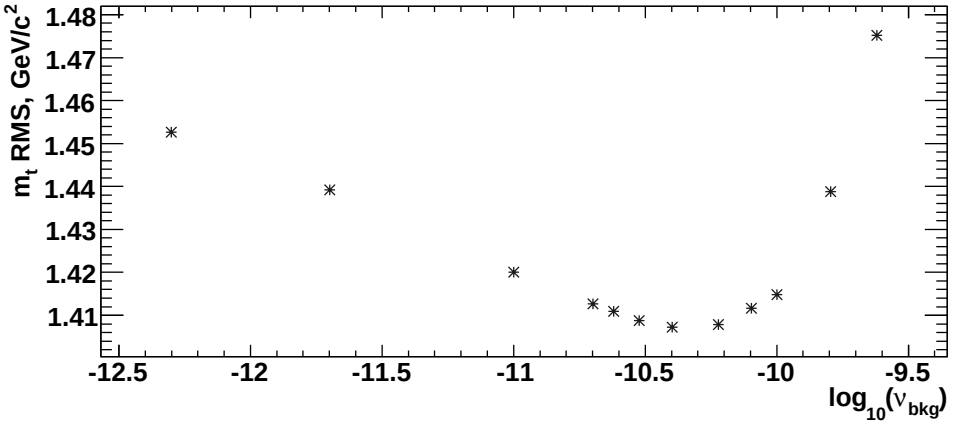

Figure 5.5: Expected statistical uncertainty on measured m_t versus $\log(\nu_{\text{bkg}})$.

Due to the nature of the chosen W+jets integration technique (Section 5.3.2), it is not possible to evaluate ν_{bkg} directly. The value of ν_{bkg} is thus somewhat arbitrary, and is a nuisance parameter of the measurement. It is chosen so as to optimise the performance of the analysis, based on studies of the expected statistical uncertainty of the measurement and of the sensitivity of the measurement to background events.

The first step towards setting ν_{bkg} is to look at how it affects the expected uncertainty on the top quark mass measurement, using pseudoexperiments with a full simulation of signal and background events as described in Section 7.1. The results are plotted in Figure 5.5, for pseudoexperiments simulated with a top quark mass of 175 GeV/c^2. The expected uncertainty is lowest within the range $10^{-11} < \nu_{\text{bkg}} < 10^{-10}$ [12], and the same behaviour is seen for other mass samples. However, it is also desirable to minimise the sensitivity of the measurement to background events. A higher ν_{bkg} provides a stronger discriminant against background events (see Section 5.6), and ν_{bkg} is therefore chosen at the high end of the range: $\nu_{\text{bkg}} = 10^{-10}$. The final normalised expression for P_b is therefore taken straight from Equation 5.3.5, but with $P_b \to \nu_{\text{bkg}} P_b$:

$$P_b(\vec{x}) = \nu_{\text{bkg}} \sum_{n_{\text{MC}}} \left[\sum_{\text{perm}}^{24} \sum_{p_\nu^z}^{2} |\mathcal{M}|^2 \frac{f(x_{\text{Bj}}^1)}{|\vec{q_1}|} \frac{f(x_{\text{Bj}}^2)}{|\vec{q_2}|} \frac{1}{\rho_e(\rho_e p_\nu^z - p_e^z \rho_\nu)} \prod_{i=1}^{4q} \left(\frac{\rho_i^y}{(\rho_i^x)^2} \right) \right] \frac{1}{n_{\text{MC}}}. \quad (5.3.6)$$

[12] Due to the neglect of constant factors in the background p.d.f. P_b the absolute value of ν_{bkg} has no physical meaning and can be seen as a relative normalisation between the signal and background p.d.f.s.

5.4 The Likelihood

The explicit expression for the logarithm of the likelihood function used in this analysis is given in Equation 5.4.1:

$$\log \mathcal{L}(\vec{\boldsymbol{x}}; m_t, \Delta_{\text{JES}}, \nu_{\text{sig}}) = \sum_{\text{events}} \log \left[\nu_{\text{sig}} P_s(x; m_t, \Delta_{\text{JES}}) + (1 - \nu_{\text{sig}}) P_b(x)\right], \tag{5.4.1}$$

where P_s and P_b are the normalised p.d.f.s for $t\bar{t}$ (Equation 5.2.30) and W+jets (Equation 5.3.6) events.

The log-likelihood function (Equation 5.4.1) is calculated on a two dimensional 31×17 grid in m_t and Δ_{JES}, spanning $145 \leq m_t \leq 205$ GeV/c^2 and $-4.8 \leq \Delta_{\text{JES}} \leq 4.8$, with a spacing between grid points of 2 GeV/c^2 in m_t and 0.6 in Δ_{JES}. The third likelihood parameter, the signal fraction parameter ν_{sig}, is allowed to vary continuously (within the constraint $0 \leq \nu_{\text{sig}} \leq 1$), and the likelihood function is maximised with respect to ν_{sig} at each point on the grid using the `MINUIT` numerical maximisation program [44]. The resulting surface described on the grid is the profile log-likelihood at maximum ν_{sig} (Figure 5.6).

The top quark mass, m_t, and the jet energy scale correction, Δ_{JES}, are then measured by making a two-dimensional parabolic fit to this surface[13], consistent with the expectation for the likelihood function to be Gaussian near its maximum. The maximum of the parabola gives the measured m_t and Δ_{JES}, while the measured ν_{sig} is taken from its value at the grid point of maximum likelihood.

To avoid any effects due to fit range, the fit is taken in a predefined "window" surrounding the grid point of maximum likelihood (Figure 5.6). The fit window is taken as a 9×7 grid-points rectangle centred on the grid point of maximum likelihood, corresponding to a range of ± 8 GeV/c^2 in m_t and ± 1.8 in Δ_{JES}. A total of 63 points are therefore used in the fit, and the absence of any fitting inaccuracies as a result of this choice was confirmed by increasing the number of points by a factor of 4 to 252 (i.e. halving the spacing between grid points to 1 GeV/c^2 in m_t and 0.3 in Δ_{JES}), which was seen to have negligible effect on the measurement (Figure 5.7).

The estimated 1σ statistical uncertainty of the measurement is represented by the ellipse corresponding to a change in log-likelihood $\Delta \log \mathcal{L} = 0.5$ from the maximum of the fitted parabola. Since m_t and Δ_{JES} are anti-correlated (a higher Δ_{JES} gives lower jet energies by Equation 4.3.1), the ellipse is inclined with respect to the m_t and Δ_{JES} axes (Figure 5.6). The measured m_t uncertainty, $\sigma_{m_t}^{\text{measured}}$, represents the overall statistical uncertainty on m_t, and therefore must include the additional uncertainties on m_t due to the uncertainties on the measured Δ_{JES}. Therefore, $\sigma_{m_t}^{\text{measured}}$ is taken from the δm_t along the extremum of the ellipse. Likewise, $\sigma_{\Delta_{\text{JES}}}^{\text{measured}}$ is taken from the $\delta(\Delta_{\text{JES}})$ along the extremum of the ellipse. The uncertainty on the measured ν_{sig} is estimated by `MINUIT`, but is not used in this analysis.

[13] The function used is $\log \mathcal{L} = a m_t^2 + b \Delta_{\text{JES}} m_t + c \Delta_{\text{JES}}^2 + d m_t + e \Delta_{\text{JES}} + f$.

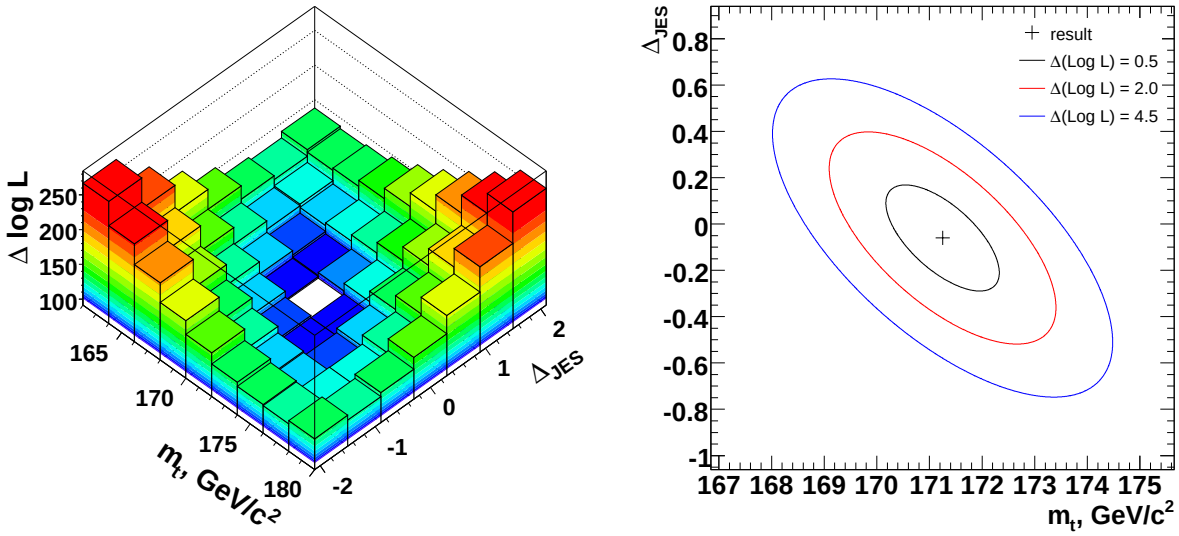

Figure 5.6: The 2D log-likelihood function is fit in a 9×7 grid-points rectangle centred on the grid point of maximum likelihood. The left plot shows the grid points used in the fit. Note that the plot shows $\Delta \log \mathcal{L}$, the decrease in $\log \mathcal{L}$ from its maximum, meaning the point of highest likelihood is at the minimum. The right plot shows the measurement result and the $\Delta \log \mathcal{L} = 0.5$, 2.0 and 4.5 contour ellipses of the parabolic fit, corresponding to the estimated 1, 2 and 3σ confidence intervals.

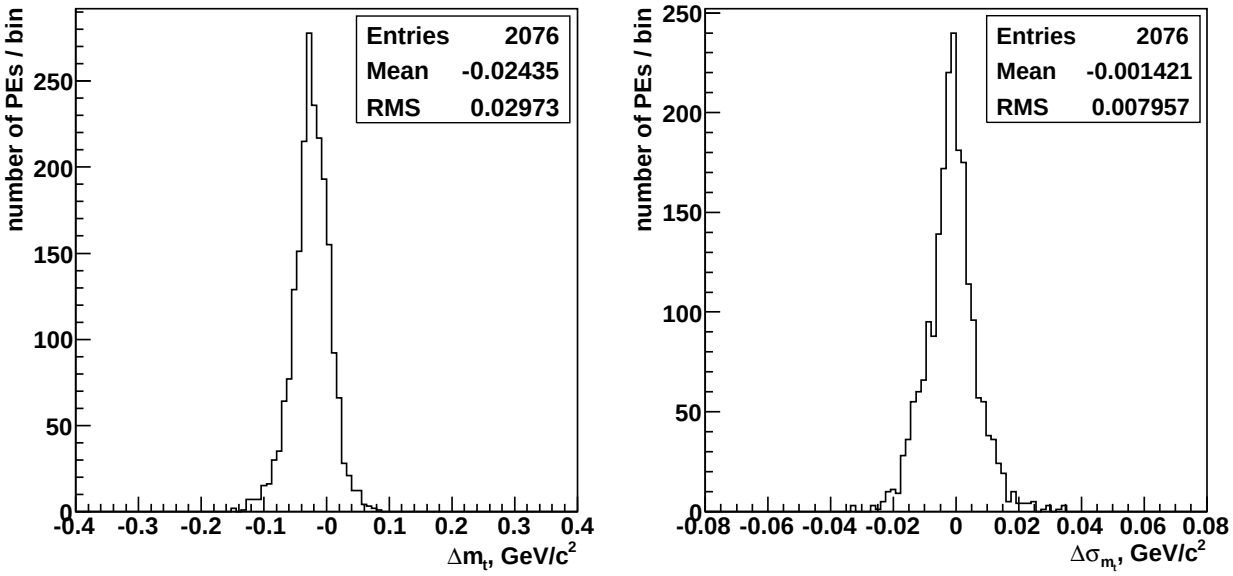

Figure 5.7: No significant difference is observed in the m_t measurement (Δm_t) or the estimated uncertainty ($\Delta \sigma_{m_t}$) when halving the spacing between the grid points used in the parabolic fit to the two-dimensional log-likelihood function.

The accuracy of the measured m_t, $\Delta_{\rm JES}$, $\sigma_{m_t}^{\rm measured}$ and $\sigma_{\Delta_{\rm JES}}^{\rm measured}$ are checked using simulated events and corrected where necessary in the measurement calibration (Section 7.3).

5.5 Good signal events

The PYTHIA $t\bar{t}$ events discussed in Section 4.2.1 accurately simulate the $t\bar{t}$ events that are observed in the CDF detector. After imposing the event selection requirements of Chapter 3, the $t\bar{t}$ simulated event sample represents the $t\bar{t}$ component of the data sample (expected to be 76%, see Table 4.2). However, the signal p.d.f. P_s does not accurately describe all of the selected $t\bar{t}$ events. It is therefore useful to separate the simulated events into two types: those that are well described by P_s are called "good" signal events, while those that are not are called "bad" signal events. Note that this distinction is only useful when referring to simulated events; it can never be known for certain which events in the experimental data are good or bad, or indeed which events are true $t\bar{t}$ and which are background.

Good signal events are defined as those for which the parton-level information confirms lepton+jets channel decays where the lepton is an electron or a muon, and the exactly-four final-state partons, associated with the two b-quarks and the two light quarks, have corresponding ("matched") measured jets. This eliminates the unwanted $t\bar{t}$ events (i.e. non lepton+jets channel events or events where the lepton is a tauon[14]) that sometimes pass the event selection. Note that this "good event" requirement is not identical to that imposed by the event selection as the requirements apply to the parton-level information of the simulated event. For example, a lepton+jets event with a final state tauon or an all-hadronic channel event may pass the event selection requirements due to the possibility of a jet faking an electron, but such events would not be classed as good based on the parton-level information.

There is also a complication in the process of matching jets with their corresponding partons, information that is not provided in the event simulation. The identification of a jet with a specific parton is not trivial due to the effects of hadronisation and radiation as well as detection and reconstruction. For example, initial or final-state radiation may be misinterpreted as a leading jet, or two partons close in (η, ϕ) space may deposit their energy in a single calorimeter cluster and be misinterpreted as a single jet. Matching therefore requires a close correspondence between the jet and parton directions in (η, ϕ) space: the jet centroid must be within a cone of $R = 0.4$ about the parton direction. This requirement must hold for all four final-state partons, and no overlap is allowed with any other pairs of jets and partons.

The samples of PYTHIA $t\bar{t}$ simulated events can thus be divided into good signal and bad signal events, where the bad signal events are those that do not conform to the good event criteria. About 58% of each PYTHIA $t\bar{t}$ sample is composed of good events. The bad signal events provide misinformation about m_t and $\Delta_{\rm JES}$, and can thus be considered as a sort of background in this analysis.

[14] Although the $t\bar{t}$ matrix element equally describes those lepton+jets events where the lepton is a tauon, those events are not well described by P_s due to the assumption of excellent identification and reconstruction of the charged lepton.

sample	$\overline{\ln P_s}$	$\overline{\ln P_b}$	% with $P_s > P_b$
W+light flavours	-84.66	-80.77	19.9%
$Wb\bar{b}$	-83.73	-80.01	21.2%
$Wc\bar{c}$	-83.56	-80.14	23.3%
Wc	-82.91	-79.89	23.6%
Z+light flavours	-83.58	-81.11	26.9%
WW	-82.54	-80.64	35.5%
WZ	-83.44	-80.40	24.2%
ZZ	-84.12	-81.05	32.4%
single top (t-channel)	-84.28	-81.19	26.8%
single top (s-channel)	-83.81	-81.26	34.0%
non-W	-85.55	-83.58	40.3%
$t\bar{t}$ signal	-82.13	-83.03	70.7%
$t\bar{t}$ signal (good subset)	-81.18	-83.48	85.4%
$t\bar{t}$ signal (bad subset)	-83.47	-82.40	50.1%
Observed (data)	-82.47	-82.51	59.5%

Table 5.1: Mean $\ln P_s$ and $\ln P_b$ for each different type of event, and the proportion of the events with $P_s > P_b$. Only events with $P_s \gtrsim P_b$ significantly affect the shape of the final two-dimensional likelihood function.

5.6 Test of signal and background p.d.f.s

P_b is calculated using only W+jets matrix elements (Section 5.3), but is used in this analysis to represent all events that are not $t\bar{t}$ signal. It is therefore important to test the response of the method to events from other background processes. Since P_b has no m_t or Δ_{JES} dependence, it is just a constant for each event and does not introduce any shape into the likelihood function. From Equation 5.4.1, it is clear that only events with $P_s \gtrsim P_b$ will significantly affect the shape of the final two-dimensional likelihood[15]. This behaviour is desirable so long as signal events generally have $P_s > P_b$ and background events have $P_s < P_b$.

Table 5.1 gives a summary of the mean $\ln P_s$ and $\ln P_b$ for each different type of event (where the mean is denoted by an overline, i.e. $\overline{\ln P_s}$ and $\overline{\ln P_b}$), and the proportion of the events with $P_s > P_b$. The distributions from which the numbers of Table 5.1 are derived are plotted in Figures 5.8 to 5.11. Note that P_s is calculated at $m_t = 175$ GeV/c^2 and $\Delta_{\text{JES}} = 0$ for the purpose of the comparison.

Figure 5.8 shows the relative response of P_s and P_b to W+jets background events of the four types. These are the background events theoretically best described by P_b, and have the highest $\ln P_b$ ($\overline{\ln P_b} \simeq -80$). They have $P_s > P_b$ only about 20% of the time, and are thus least likely to bias the likelihood function.

[15]Note that the presence of events with $P_s \ll P_b$ does have some effect on the two-dimensional likelihood function, since their presence will lower the maximised values of ν_{sig} at which the profile is taken.

Figures 5.9 and 5.10 show similar plots for the other types of background events expected to contribute to the final data sample. The results show that P_b performs almost as well as a representation of Z+light flavours, diboson, and single top backgrounds, events of which types have $\overline{\ln P_b} \simeq -81$. Events of these types typically have $P_s > P_b$ approximately 30% of the time but, as might be expected, WW background events appear most signal-like ($\overline{\ln P_s} = -82.54$) and events of that type have $P_s > P_b$ about 35% of the time. For non-W events, the behaviour is different, with significantly lower values of both $\overline{\ln P_s}$ and $\overline{\ln P_b}$. Non-W events do not satisfy either the signal or the background hypothesis, and 40% have $P_s > P_b$.

In Figure 5.11, similar results are shown for simulated $t\bar{t}$ events for $m_t = 175$ GeV/c^2 and $\Delta_{\mathrm{JES}} = 0$. Since bad signal events contribute misinformation about m_t and Δ_{JES}, it would also be useful if P_b was larger for those events. That turns out to be the case, with $\overline{\ln P_b} = -82.4$ for bad signal events and only $\overline{\ln P_b} = -83.5$ for good signal events. Good signal events also have significantly larger $\overline{\ln P_s}$, resulting in over 85% of good signal events with $P_s > P_b$ and only 50% of bad signal events. Finally, the results for the data sample of 578 events are plotted. 60% of events in data have $P_s > P_b$, and thus provide the primary contribution of information about m_t and Δ_{JES} in the measurement. Of these 344 events, assuming a 76% overall signal fraction and that 58% of all signal events are good signal events, 63% are good signal events, 27% are bad signal, and 10% are background. Since the bad signal events are not well described by the p.d.f. P_s, overall this analysis is able to extract information from about $58\% \times 85\% = 50\%$ of the selected true $t\bar{t}$ events. The P_s and P_b distributions seen in data are compared with the simulated distributions in Chapter 9 (Figures 9.4 and 9.5).

The fractions of events with $P_s > P_b$ are of course directly linked to the choice of the P_b normalisation parameter ν_{bkg}, and the results of this section thus serve as an indication of the correctness of the chosen value.

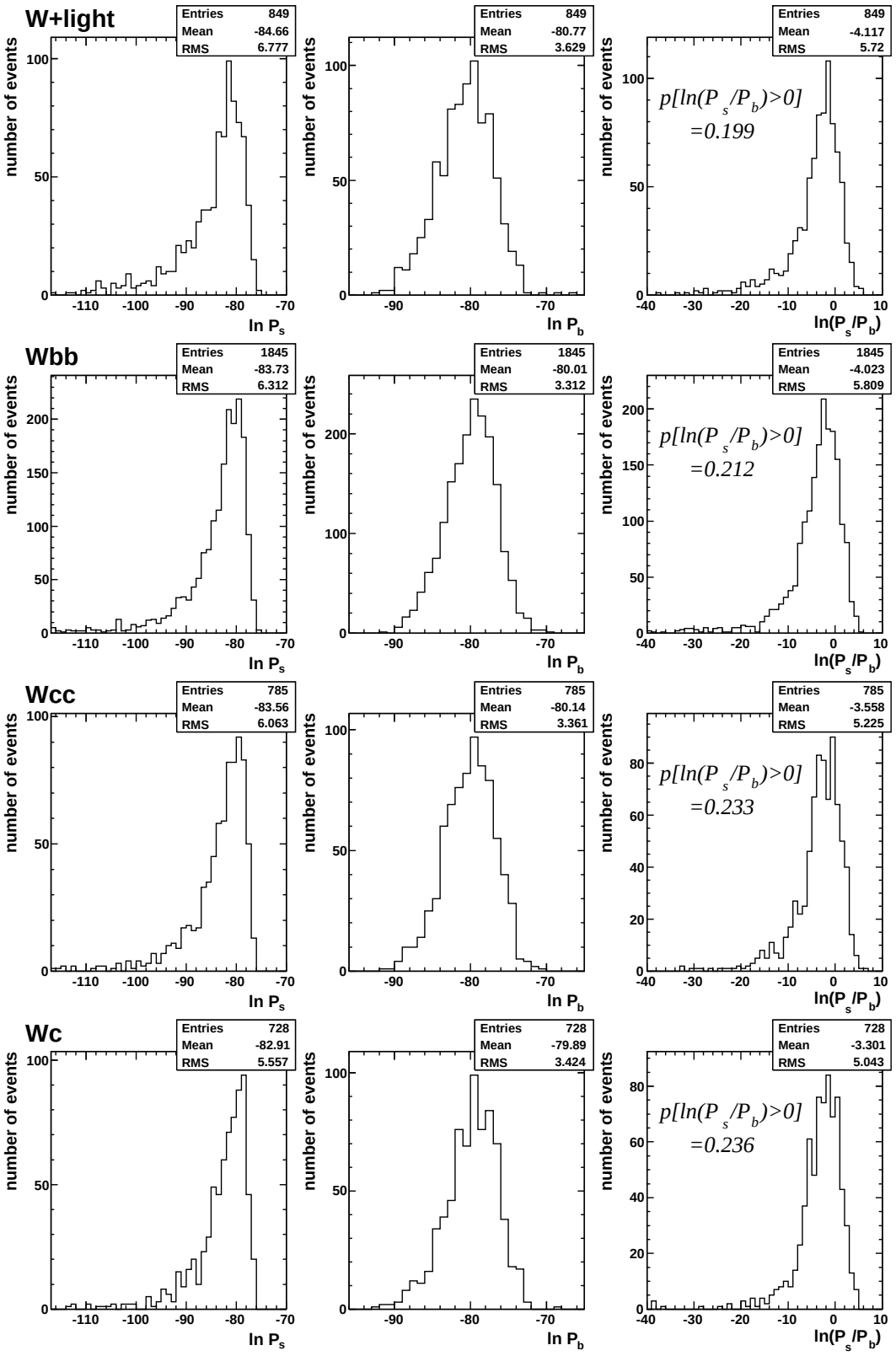

Figure 5.8: $\ln P_b$ and $\ln P_s(m_t = 175\ \mathrm{GeV/c^2}, \Delta_{\mathrm{JES}} = 0)$ distributions for W+jets events. These events typically have $\overline{\ln P_b} \simeq -80$, and have $P_s > P_b$ only about 20% of the time.

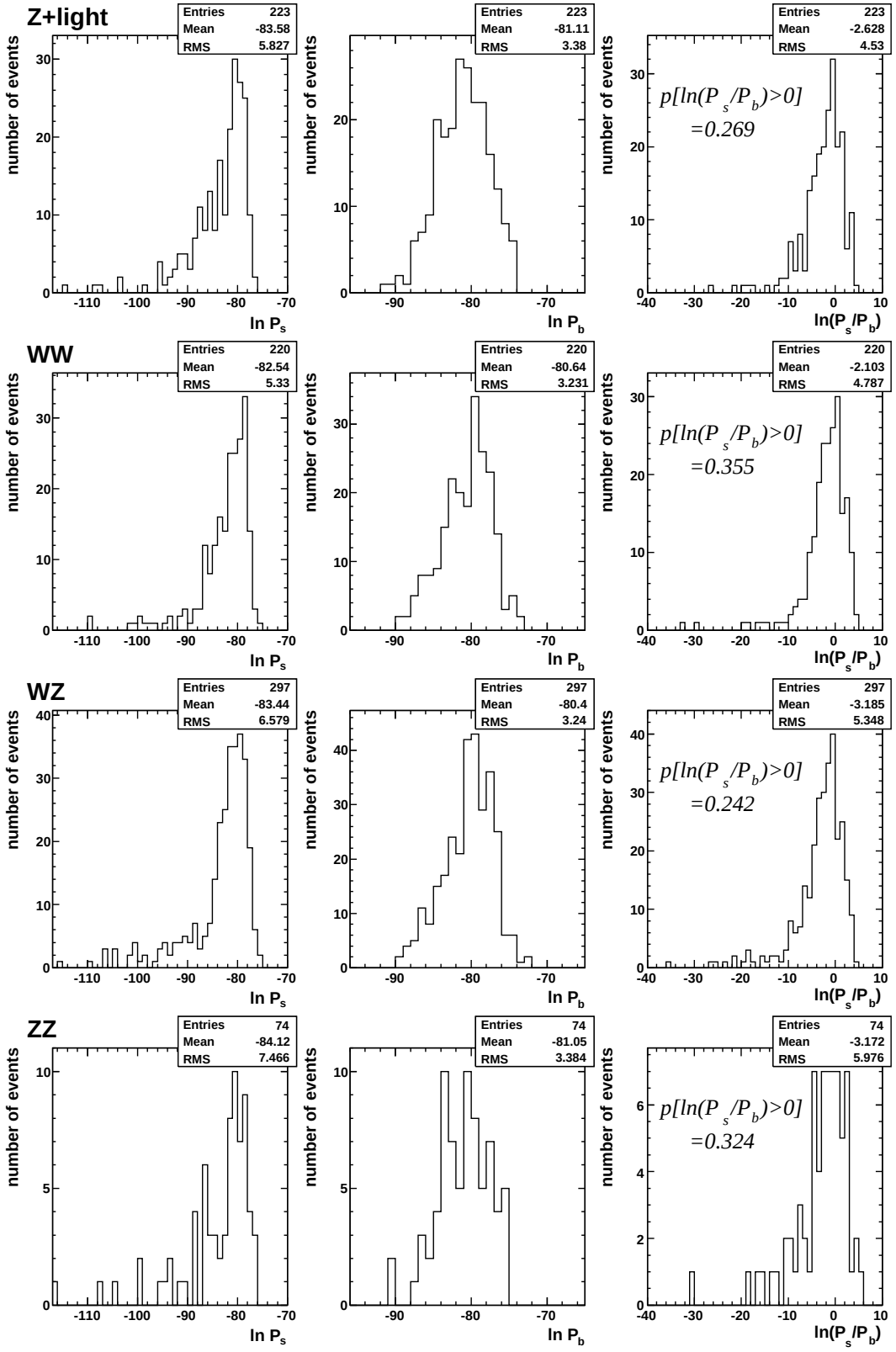

Figure 5.9: $\ln P_b$ and $\ln P_s(m_t = 175\ \mathrm{GeV/c^2}, \Delta_{\mathrm{JES}} = 0)$ distributions for Z+jets and Diboson events. These events typically have lower P_b than the W+jets events ($\overline{\ln P_b} \simeq -81$), but similar P_s, and thus have $P_s > P_b$ about 30% of the time.

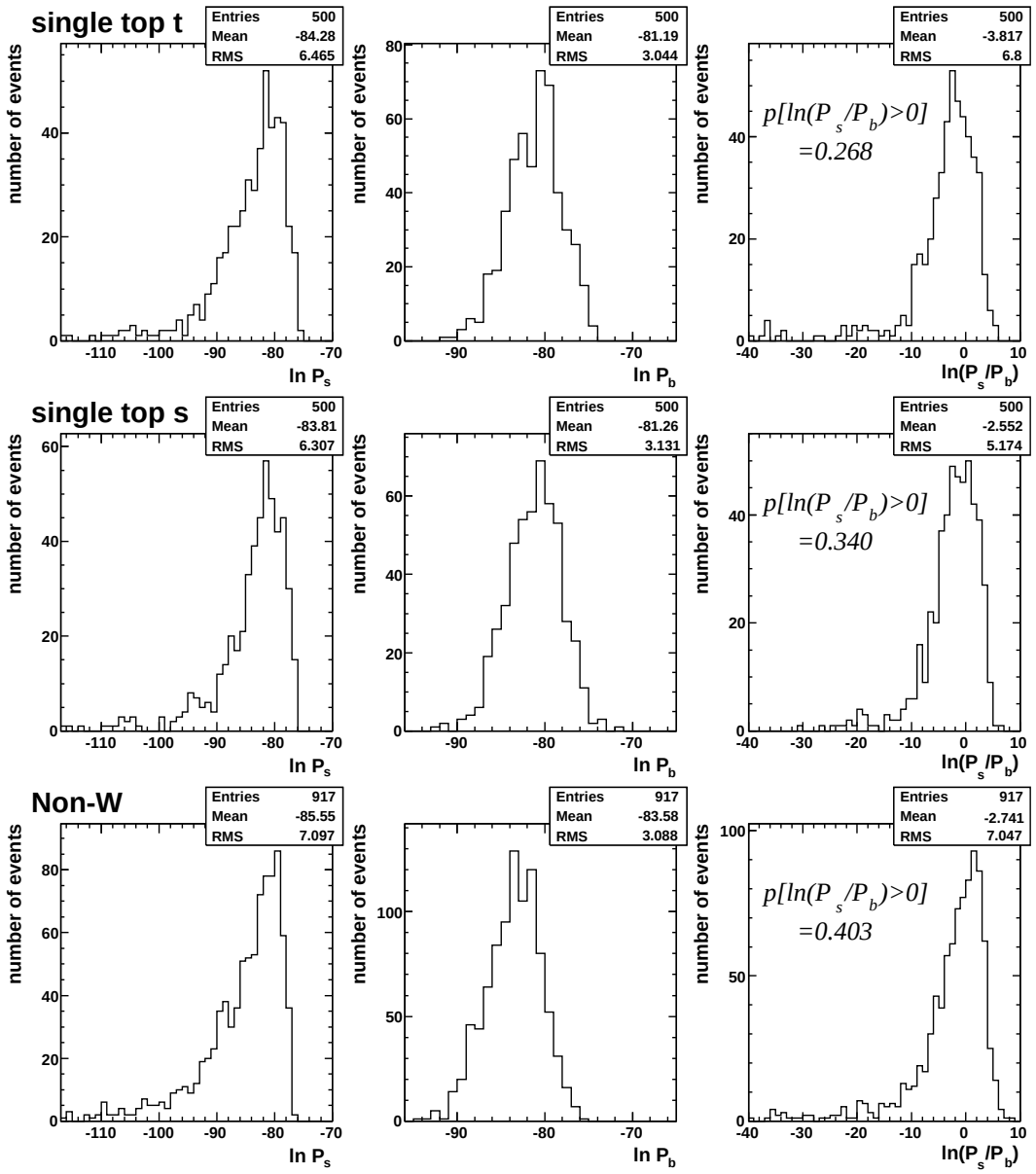

Figure 5.10: $\ln P_b$ and $\ln P_s(m_t = 175\ \mathrm{GeV/c^2}, \Delta_{\mathrm{JES}} = 0)$ distributions for single top and non-W events. The response of P_b and P_s to the single top events is similar to that to the Z+jets and Diboson events. For non-W events, the behaviour is different, with significantly lower values of both $\overline{\ln P_b}$ and $\overline{\ln P_s}$. Non-W events do not satisfy either the signal or background hypothesis, and 40% have $P_s > P_b$.

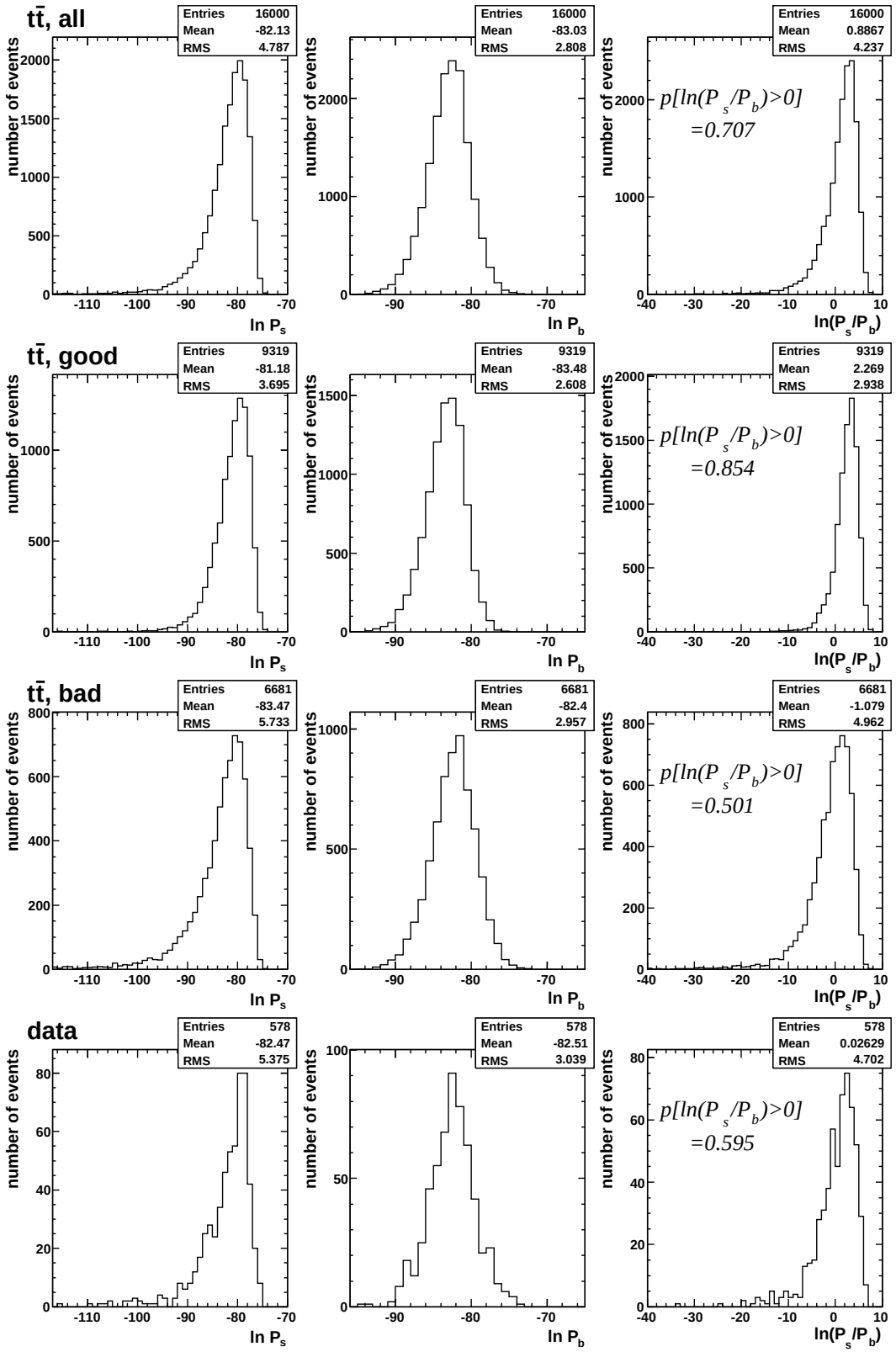

Figure 5.11: $\ln P_b$ and $\ln P_s(m_t = 175\ \mathrm{GeV/c^2}, \Delta_{\mathrm{JES}} = 0)$ distributions for $t\bar{t}$ and the real data events. P_b provides a discriminant against the bad signal events, with $\overline{\ln P_b} = -82.4$ for bad signal events and $\overline{\ln P_b} = -83.5$ for good signal events. Good signal events also have significantly larger $\overline{\ln P_s}$, resulting in over 85% of good signal events with $P_s > P_b$ and only 50% of bad signal events.

Chapter 6

The Transfer Function

The Transfer Function (TF) is a p.d.f. describing the probability density for an event with out-going partons (and charged lepton) with 3-momenta $\vec{y}$ to be measured as reconstructed 3-momenta[1] $\vec{x}$. The measured quantities $\vec{x}$ are taken after the corrections and cuts described in Chapter 3, and the TF therefore describes the mapping between the particle-level jets and the parton-level jets of Figure 3.3. The mapping between $\vec{y}$ and $\vec{x}$ is determined using PYTHIA simulated $t\bar{t}$ events, which contain all of the information about the original partons as well as the measured jets.

The TF describes detector resolution and reconstruction effects, including the deposition of energy from a parton outside the corresponding jet cone and the extra energy deposits from any spectator partons from the underlying event. It also describes physical effects in the hard-scattering and subsequent hadronisation process. All of these effects are simulated in the PYTHIA $t\bar{t}$ events.

The only constraint on the form of the TF is that it must be normalised such that each parton (or charged lepton) corresponds to one measured jet (or measured lepton), that is

$$\int W(\vec{x}, \vec{y}, \Delta_{\text{JES}}) \prod_{i}^{4q,\ell} d^3 p_i^x = 1. \tag{6.0.1}$$

Any choice of a specific form for the function $W(\vec{x}, \vec{y})$ requires assumptions about the nature of the p.d.f. In this analysis, the TF is initially expressed as

$$W(\vec{x}, \vec{y}, \Delta_{\text{JES}}) = \delta^3(\vec{p_l^y} - \vec{p_l^x}) \prod_{i=1}^{4} \frac{1}{(\rho_i^x)^2} \prod_{i=1}^{4} \left(\frac{\rho_i^x}{E_i^x} W_E^i(E_i^x, E_i^y, \Delta_{\text{JES}}) \right) W_A(\vec{\Omega}^x, \vec{\Omega}^y), \tag{6.0.2}$$

where x and y superscripts refer to reconstruction-level and parton-level quantities respectively, and the chosen forms of the various components are described and explained, along with any approximations involved, in the remainder of this section.

[1] Note that the Transfer Functions describe the mapping between the 3-momenta, and not the 4-momenta, because each parton is assumed to have a constant mass.

First, the lepton is assumed to be well measured, allowing the approximation of a delta function $\delta^3(\vec{p_l^y} - \vec{p_l^x})$ to represent the mapping to parton-level quantities.

The remainder of the TF is expressed in spherical coordinates, with the factors $(\rho_i^x)^{-2}$ in Equation 6.0.2 a natural consequence. The jet Energy TFs (ETFs), W_E^i, denote the parts of the TF describing the mapping between the parton-level energies E_i^y and the measured energies E_i^x of each jet i. The ETF response is assumed to be independent for each jet, allowing the description of the ETFs in the four separable components W_E^i. The factors ρ_i^x/E_i^x come from the additional changes of variables from jet momentum magnitudes ρ_i^x to energies E_i^x, chosen because it is the jet energies rather than their momenta that are measured in the calorimeters. Since the ETFs contain all of the information about the mapping between parton energies and jet energies, they must also describe any parameterised jet energy corrections. In this analysis, the jet energy scale correction Δ_{JES} (Section 4.3) is simultaneously measured along with m_t, and is a parameter of the ETFs.

The jet Angular TF (ATF), W_A, describes the mapping between the parton-level and measured jet angles. Unlike the ETF, the ATF is not assumed to be separable into parts for each jet (for reasons that will become apparent in Section 6.2), and thus simultaneously describes the angles of all four jets (as denoted by $\vec{\Omega}$).

The ETFs and the ATF are assumed to be independent, allowing their expression in the separated form of Equation 6.0.2. They can thus be parameterised independently, and are all separately normalised to 1.

Finally, the TF is assumed to be independent of the top quark mass. Note that there is not a part of the TF for the neutrino because it escapes through the detector unmeasured.

6.1 Energy Transfer Functions

Taking the form of the jet energy scale correction Δ_{JES} from Section 4.3, the ETFs of Equation 6.0.2 can be written

$$W_E^i(E_i^x, E_i^y, \Delta_{\text{JES}}) = W_E^i(E_j'(\Delta_{\text{JES}}), E_p), \tag{6.1.1}$$

where the labels x and y have been replaced with the subscripts j (jet) and p (parton) and $E_j' = E_j - \Delta_{\text{JES}} \cdot \sigma_j$ (see Equation 4.3.1). Recall that E_j is the Level-5-corrected measured jet energy, while E_j' also allows for a Δ_{JES} shift in calorimeter response.

Each W_E^i is parameterised by a double Gaussian distribution whose main variable is $\delta = E_j' - E_p$, that is, the difference between the Δ_{JES}-corrected jet energy and the parton energy:

$$W_E^i(E_j' - E_p) = W_E^i(\delta) = \frac{1}{N_{W_E}} \frac{1}{\sqrt{2\pi}(|p_2| + |p_3||p_5|)} \left[e^{\frac{-(\delta - p_1)^2}{2p_2^2}} + |p_3| \cdot e^{\frac{-(\delta - p_4)^2}{2p_5^2}} \right], \tag{6.1.2}$$

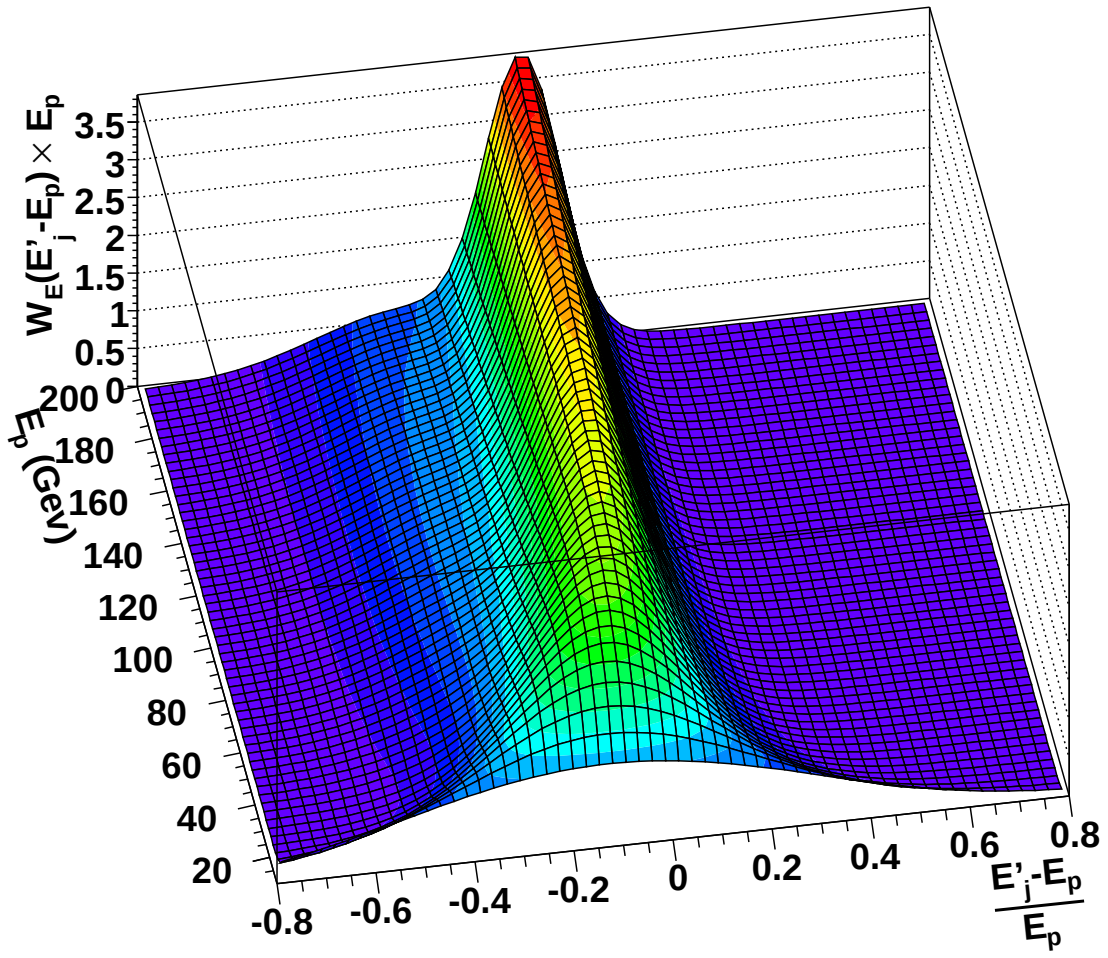

Figure 6.1: The b-jet ETF for $0.3 \leq |\eta| < 0.45$, plotted as a function of the parton energy E_p and the fractional difference in energy $\frac{E'_j - E_p}{E_p}$, so that the width of the plotted function illustrates the parameterised energy resolution at each E_p.

where N_{W_E} is the normalisation. The parameters p_n have a constant part and an E_p-dependent part: $p_n = a_n + b_n\, E_p$. Since the hadronisation process depends on quark flavour, there are a different set of parameters p_n for b-jets and "light" jets. Light jets here are defined as those produced from the decay of the hadronic-side W boson. In the signal p.d.f. P_s, for any given assignment of jet-parton identities, the two b-jet W_E^i take the b-jet parameters, while the two light jet W_E^i take the light jet parameters. In the background p.d.f. P_b, where no jet is explicitly identified as originating from a b-quark, all four jets take the light jet parameters.

The ETF parameters p_n for light and b-jets are determined by a `MINUIT` likelihood fit to `PYTHIA` simulated $t\bar{t}$ events. The largest sample of `PYTHIA` events is chosen to provide the most accurate fit: the $m_t = 175$ GeV/c^2 sample with 4.8 million events. These events contain all of the information about the original partons as well as the measured jets, allowing E_j and E_p to be determined for each jet and also the division of the jets into two samples containing only b-jets and only light jets.

To create realistic ETFs it is important to consider which of these simulated events to use in the fits. The first requirement is that the event passes the selection criteria of Section 3.3. This ensures a sample kinematically representative of that expected in data, although it also causes the shape of the ETF to have some dependence on the event selection criteria[2], effectively double-counting some of the effects described by the mean acceptance function[3]. Next, it is required that the event is good (see Section 4.2.1), that is, it is well described by the signal p.d.f. P_s. This is to prevent the ETF fit being biased by the bad signal events, and the requirement of good event jets to be well matched is also necessary because the ETF must provide a one-to-one mapping between partons and jets.

After event selection there are 61741 good events, each with four matched jets, providing 123482 b-quark and 123482 light quark jet-parton pairs to be used in the fits. Due to the $|\eta|$-dependence of calorimeter response, the ETFs are fit in 8 $|\eta|$ bins, each with roughly 15000 jet-parton pairs. In Figure 6.1, the b-jet ETF W_E^b for $0.3 \leq |\eta| < 0.45$ and $\Delta_{\text{JES}} = 0$ is plotted in 3D as a function of the parton energy E_p and the fractional difference in energy $\frac{E'_j - E_p}{E_p}$, so that the width of the plotted function illustrated the parameterised energy resolution at each E_p. All 8 $|\eta|$ bins of the ETFs for light- and b-jets are shown as projections in $\frac{E'_j - E_p}{E_p}$ in Figures 6.2 and 6.3.

6.1.1 Δ_{JES} dependence and normalisation

The dependence of the Δ_{JES}-corrected jet energies E'_j on the jet energy scale correction Δ_{JES} is given by Equation 4.3.1:

$$E'_j = E_j - \Delta_{\text{JES}} \cdot \sigma_j, \tag{6.1.3}$$

that is, Δ_{JES} denotes the number of σ_j (the one-sigma systematic uncertainty on the measured jet energies) by which the measured jet energies are shifted before being mapped to parton energies via the ETFs. The fractional uncertainty, σ_j/E_j, is plotted against jet transverse energy E_T in Figure 6.4 (note that this is the same distribution as plotted in Figure 4.1).

The fitted ETF parameters describe the jet-to-parton mapping in the nominal case of $\Delta_{\text{JES}} = 0$, as defined by the simulated events. However, the same parameters can be used to describe data with non-zero Δ_{JES} via the description of the JES correction provided by the use of E'_j rather than E_j in the ETFs (Equation 6.1.2). Any data with a non-zero Δ_{JES} (i.e. having jet energies E_j shifted up by $\Delta_{\text{JES}} \cdot \sigma_j$ relative to the simulation) will be described by the nominal distribution once the jet energies are corrected via Equation 6.1.3. The Δ_{JES} is constrained in the signal p.d.f. P_s of each event by the hadronic-side W boson Breit-Wigner distribution, which thus provides the measurement of Δ_{JES}.

[2]Most obviously, the jet energy cuts.

[3]The consequences of this problem are discussed in the Δ_{JES} part of the measurement calibration (Section 7.3).

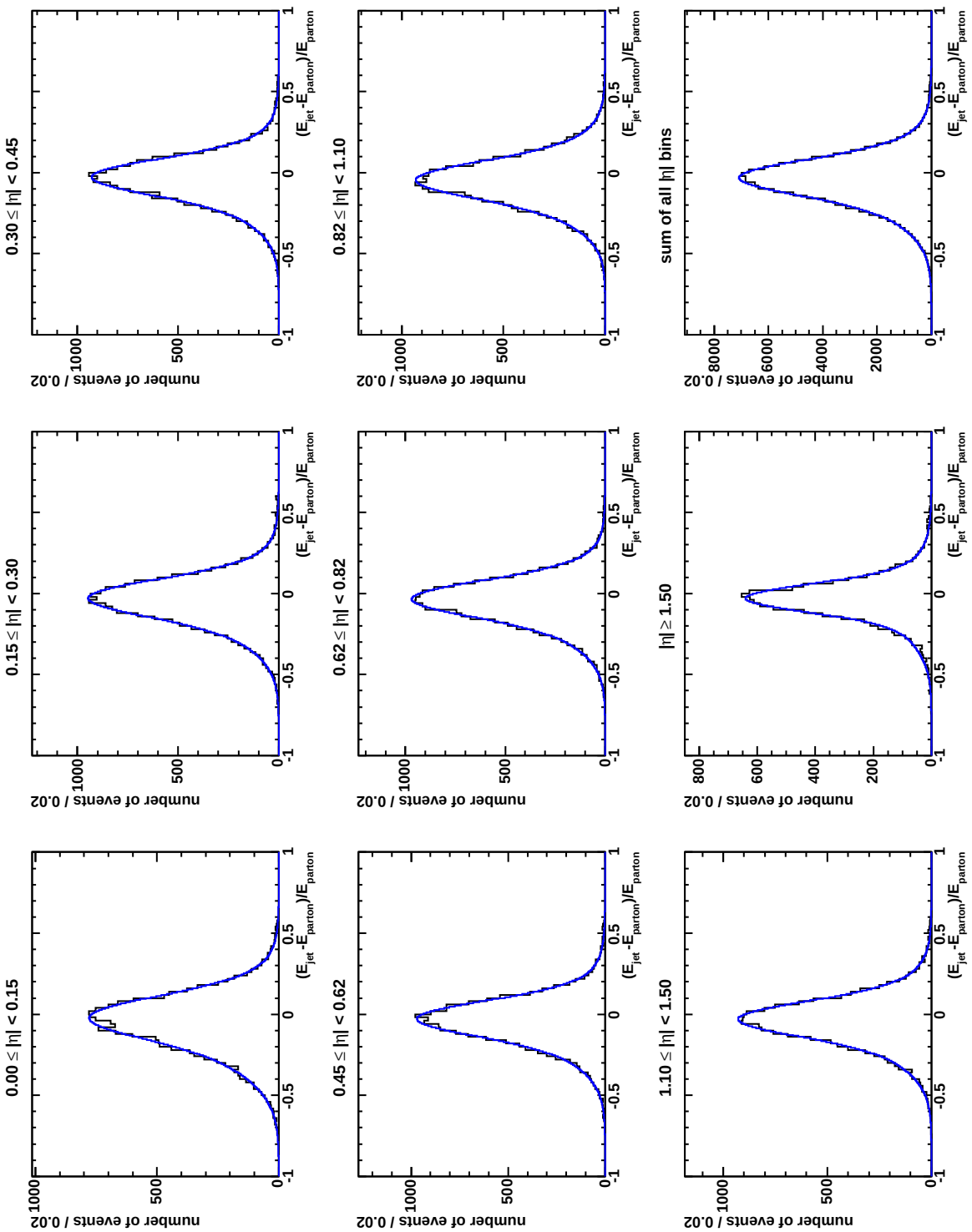

Figure 6.2: ETF for light jets (blue) compared with the fitted distributions (black), plotted as a projection in $\frac{E'_j - E_p}{E_p}$ in its 8 $|\eta|$ bins.

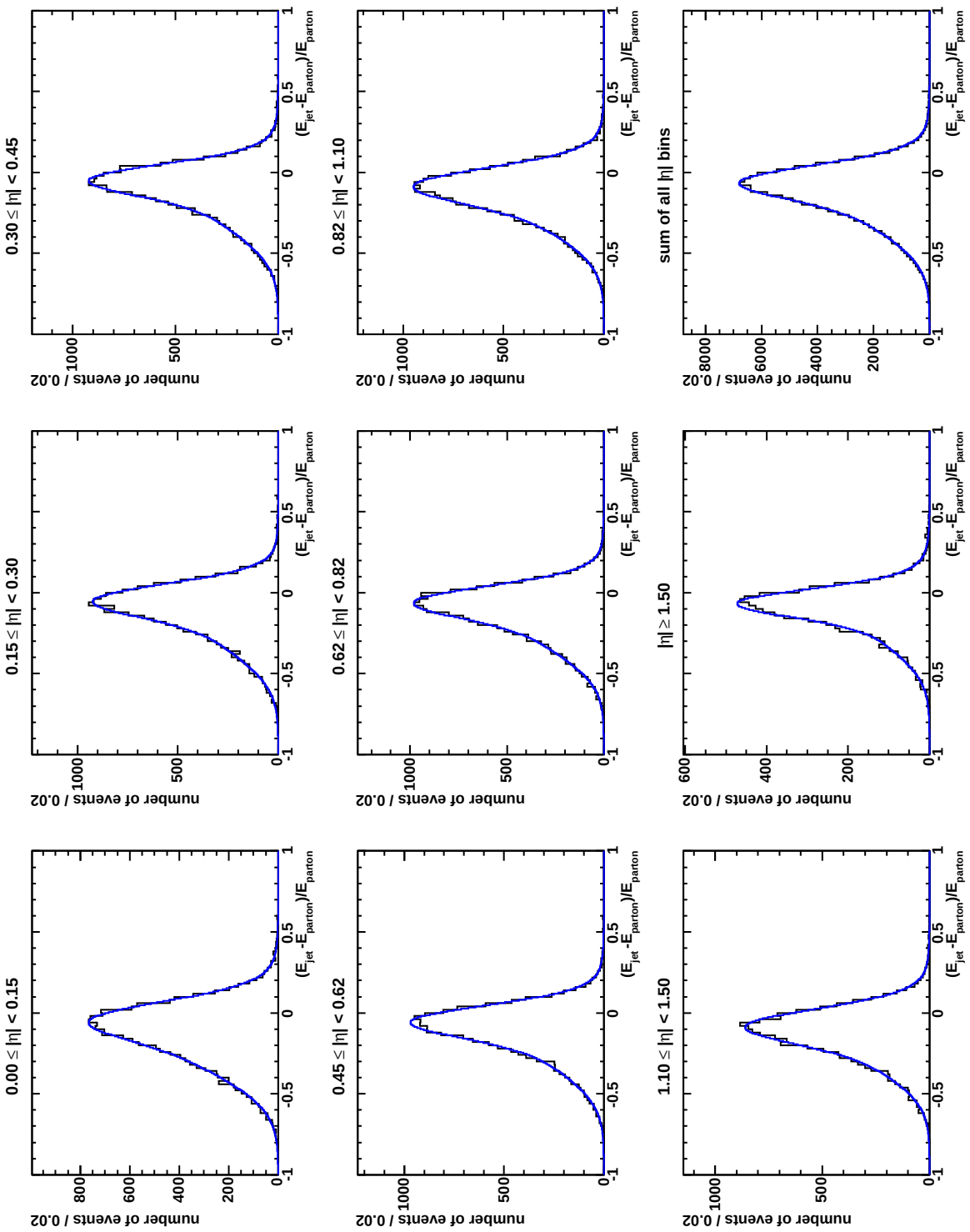

Figure 6.3: ETF for b-jets (blue) compared with the fitted distributions (black), plotted as a projection in $\frac{E'_j - E_p}{E_p}$ in its 8 $|\eta|$ bins.

In previous versions of this analysis [1] the normalisation factor N_{W_E} was omitted from the ETFs, with the result that they were not normalised with respect to Δ_{JES}. Since a scale-factor Δ_{JES} is simple and was used previously, it is instructive first to calculate the normalisation in that case, i.e. $E'_j = (1 + \Delta_{\text{JES}})\, E_j$.

Since Equation 6.1.2 is parameterised as a double Gaussian in E'_j it is also normalised in E'_j, and not in E_j. This can be seen by integrating Equation 6.1.2 over E_j:

$$\int W_E \left((1 + \Delta_{\text{JES}})\, E_j - E_p \right) dE_j = \frac{1}{N_{W_E}} \frac{1}{1 + \Delta_{\text{JES}}}. \tag{6.1.4}$$

In that case, the ETF for each jet therefore requires normalisation $N_{W_E} = 1/\left(1 + \Delta_{\text{JES}}\right)$, with the factor $(1 + \Delta_{\text{JES}})$ coming from the change of variables from E'_j to E_j.

With Δ_{JES} as defined in Equation 6.1.3, the integration becomes more complicated and the ETF normalisation N_{W_E} is given by

$$N_{W_E} = \int W_E(E'_j - E_p) dE_j = \int W_E(E'_j - E_p) \frac{dE_j}{dE'_j} dE'_j. \tag{6.1.5}$$

Equation 6.1.9 defines E'_j, so

$$N_{W_E} = \int W_E(E'_j - E_p) \frac{dE_j}{d(E_j - \Delta_{\text{JES}} \cdot \sigma_j)} dE'_j. \tag{6.1.6}$$

In order to be able to evaluate Equation 6.1.6 analytically, the function 6.1.3 is limited[4] to the form

$$E'_j = aE_j + b, \tag{6.1.7}$$

requiring that

$$\frac{\sigma_j}{E_j} = a' + \frac{b'}{E_j}, \tag{6.1.8}$$

where a' and b' are constants.

[4]The restriction is a result of the Gaussian parameterisation of W_E.

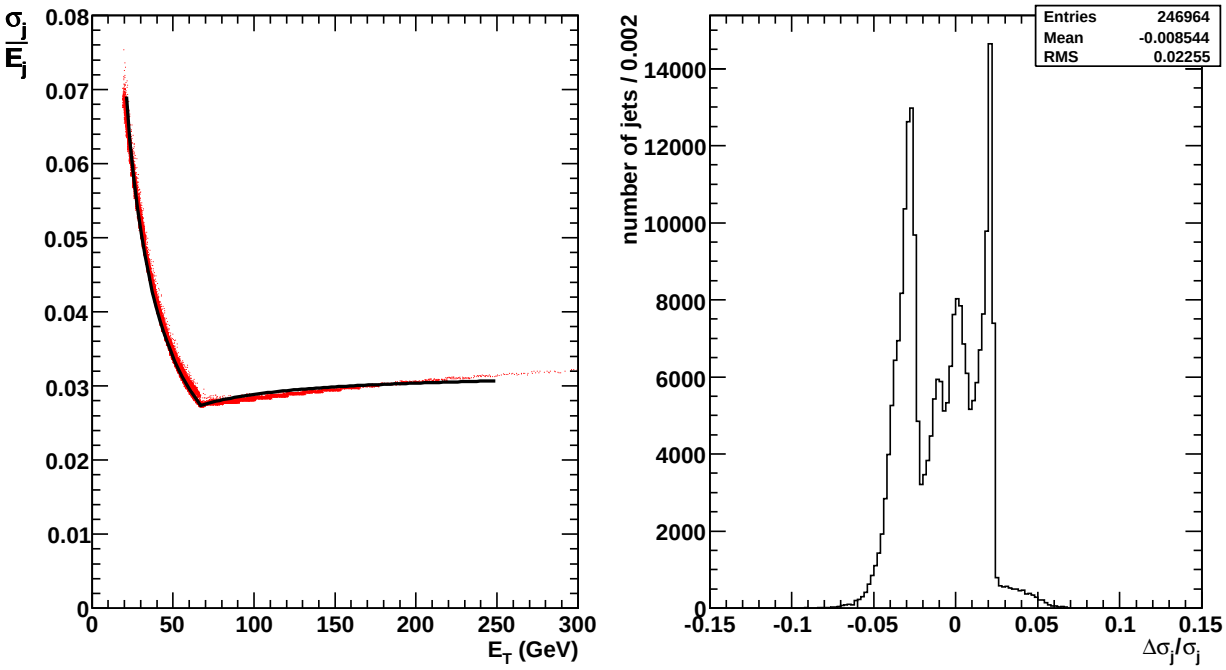

Figure 6.4: Left: the fractional jet energy uncertainty, σ_j/E_j, plotted against jet transverse energy E_T (red points), with fitted function in black. Right: the distribution of the fractional difference between the calculated and the fitted σ_j, $\Delta\sigma_j/\sigma_j$. The fitted function for σ_j agrees with the calculated value within 5%.

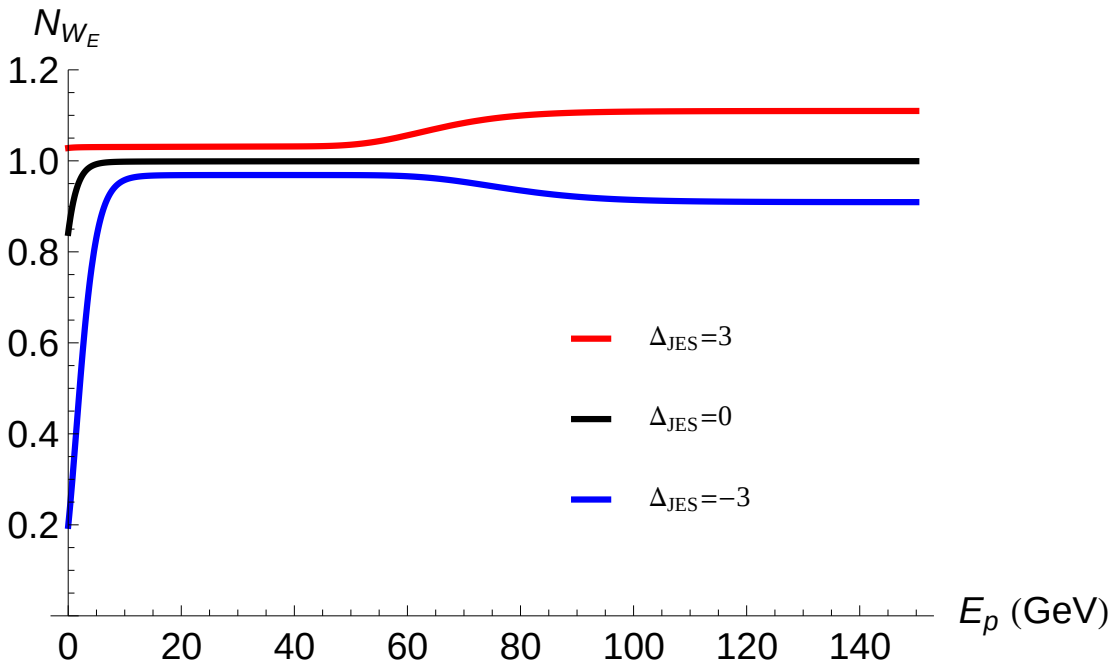

Figure 6.5: The ETF normalisation N_{W_E} for light jets, for $|\eta| = 0$ and $\Delta_{\text{JES}} = -3, 0, +3$. The two constant regions (visible for $\Delta_{\text{JES}} \neq 0$) correspond to the two parts of the σ_j function, and the transition between the two regions is "smeared" through the ETF. For $\Delta_{\text{JES}} = -3$, the normalisation is significantly less than 1 at low E_p because only a small part of the double-Gaussian E_j distribution has $E_j > 0$.

Fortunately, the distribution plotted in Figure 6.4 is narrow enough that it can be well approximated by a function, and a two-piece function in the required form 6.1.8 provides a good fit (Figure 6.4). The division between the two pieces of the function is chosen to be at $E_T = 67$ GeV, and the overall Δ_{JES} correction is thus defined by Equation (6.1.9):

$$\begin{aligned} E'_j &\equiv E_j - \Delta_{\text{JES}} \cdot \sigma_j \\ \sigma_j &\equiv H(67 - E_T)\,(k_1 E_j + l_1/s) + H(E_T - 67)\,(k_2 E_j + l_2/s) \\ s &\equiv \sin(\theta_j), \end{aligned} \tag{6.1.9}$$

where H is the Heaviside step function and θ_j is the polar angle of the jet. E_T is defined by $E_T \equiv E_j \sin(\theta_j)$, and the k_i and l_i parameters are taken from the fit in Figure 6.4: $k_1 = 0.00814$, $l_1 = 1.288$ GeV, $k_2 = 0.0319$, and $l_2 = -0.304$ GeV. Note that it is required that $(67\,k_1 + l_1) = (67\,k_2 + l_2)$ to ensure that σ_j is a continuous function.

With σ_j defined in two parts (Equation 6.1.9), the integral of Equation 6.1.6 for N_{W_E} is also split into two parts and is evaluated in Appendix B. This normalisation is E_p and $|\eta|$-dependent, and must be included inside the P_s integral of Equation 5.2.22.

The ETF normalisation N_{W_E} for light jets is plotted as a function of E_p for $|\eta| = 0$ and $\Delta_{\text{JES}} = -3, 0, +3$ in Figure 6.5. For low E_p and negative Δ_{JES} (i.e. jet energies shifted down relative to parton energies), the normalisation can be significantly less than 1 because only a small part of the double-Gaussian E_j distribution will have $E_j > 0$. However, due to the jet E_T cut ($E_T > 20$ GeV, see Section 3.3.4), such low parton energies are rarely encountered in the integration.

The definition of Δ_{JES} given by Equation 6.1.9 also introduces a complication in the generation of simulated events with shifted Δ_{JES}. The jet energy uncertainty σ_j is E_j-dependent, so once a jet has been shifted in energy its associated σ_j changes. Creating simulated event samples with non-zero Δ_{JES} thus requires special attention. The jet energies in the non-zero Δ_{JES} samples must be shifted such that the quantity $\Delta_{\text{JES}} \cdot \sigma_j$ at the new jet energies will restore the energies to their original $\Delta_{\text{JES}} = 0$ values. This is accomplished using Equation 6.1.10:

$$\begin{aligned} E_{\text{shift}} &= E_j^0 + \Delta_{\text{JES}} \cdot \sigma_{\text{shift}} \\ \sigma_{\text{shift}} &\equiv H(C - E_j^0)\,\frac{k_1 E_j^0 + l_1/s}{1 - k_1 \Delta_{\text{JES}}} + H(E_j^0 - C)\,\frac{k_2 E_j^0 + l_2/s}{1 - k_2 \Delta_{\text{JES}}} \\ C &\equiv \frac{67 - 67 k_1 \Delta_{\text{JES}} - l_1 \Delta_{\text{JES}}}{s}. \end{aligned} \tag{6.1.10}$$

Note that this is the same C as defined in Appendix B (Equation B.0.4).

6.2 Angular Transfer Functions

In previous versions of this analysis [1], the jet angles were assumed sufficiently well measured that the ATFs could be approximated by Dirac delta functions, that is

$$W_A(\vec{\Omega}^x, \vec{\Omega}^y) = \delta[\Omega^y_{j1} - \Omega^x_{j1}]\,\delta[\Omega^y_{j2} - \Omega^x_{j2}]\,\delta[\Omega^y_{bh} - \Omega^x_{bh}]\,\delta[\Omega^y_{bl} - \Omega^x_{bl}]. \tag{6.2.1}$$

This assumption is no longer made, and the ATFs discussed in this section are thus entirely new to the analysis.

6.2.1 Motivation

If the approximation of δ-function ATFs for the measured angles was valid, the measured angles would not look significantly different from the parton-level angles stored within the `PYTHIA` simulated events. This comparison can be made by looking at the angular resolution distributions, defined here as the difference between the parton angular quantity (y superscript) and the measured angular quantity (x superscript), that are obtained from `PYTHIA` $t\bar{t}$ events.

In Figure 6.6, the angular resolution distributions for the two light jets (from the hadronically decaying W boson) are plotted in $\Delta\cos(\theta) \equiv \cos(\theta^y) - \cos(\theta^x)$ and $\Delta\phi \equiv \phi^y - \phi^x$, where θ and ϕ are the polar and azimuthal jet angles constituting Ω. The $\Delta\cos(\theta)$ distribution is plotted instead of $\Delta\theta$ because $\Delta\cos(\theta)$ is the distribution for which the delta-function approximation was made in Equation 6.2.1 (i.e. $\delta[\Omega^y - \Omega^x] = \delta[\cos(\theta^y) - \cos(\theta^x)]\,\delta[\phi^y - \phi^x]$). Note that in this section, the quantity $\Delta\omega \equiv \omega^y - \omega^x$ for any measurable quantity ω.

At first look, Figure 6.6 seems to support the choice of delta function ATFs: the distributions are narrow and centered at zero. However, it is not sufficient to look at the angular resolutions in $\cos(\theta_i)$ and ϕ_i for the two jets individually, since any effect may not be visible in these variables. This can be seen by considering the 2D case of a pair of measured polar angles ϑ^x_1 and ϑ^x_2, each with an unbiased, symmetric distribution $\Delta\vartheta_i$ about its true ("parton") value. Now, imagine there is a correlation between ϑ^x_1 and ϑ^x_2. The distributions for $\Delta\vartheta_1$ and $\Delta\vartheta_2$ can still be the same unbiased, symmetric distributions as before. However, the distribution for $\Delta(\vartheta_2 - \vartheta_1)$ will now be biased (i.e. with non-zero mean) as a result of the correlation between the two angles.

This study was initially motivated by a discrepancy noticed in the 2-jet invariant mass of the hadronic-side W boson, m_W. Keeping parton-level jet energies, the use of the measured jet angles causes a large shift (~ 1 GeV/c^2) of m_W from its nominal value, whereas with parton-level jet angles the expected Breit-Wigner distribution is seen (Figure 6.7). This is clearly a major concern: the accuracy of the hadronic-side W boson mass reconstruction is very important to this analysis since it is used to measure the Δ_{JES}.

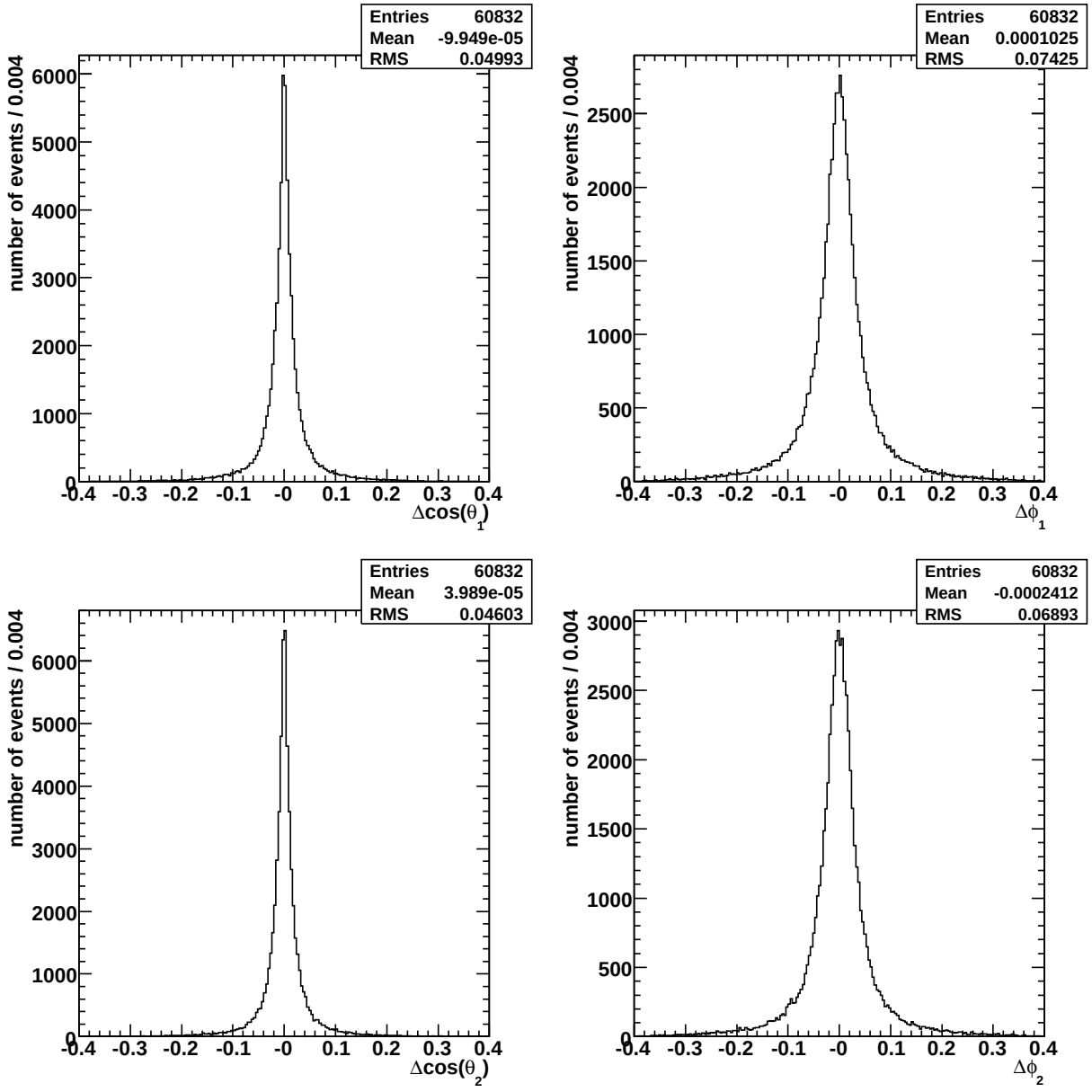

Figure 6.6: The angular resolution distributions for the measured angles $\cos(\theta_i)$ and ϕ_i of the two light jets from the hadronically decaying W boson. The distributions are narrow and centered at zero, ostensibly supporting the choice of δ-function ATFs.

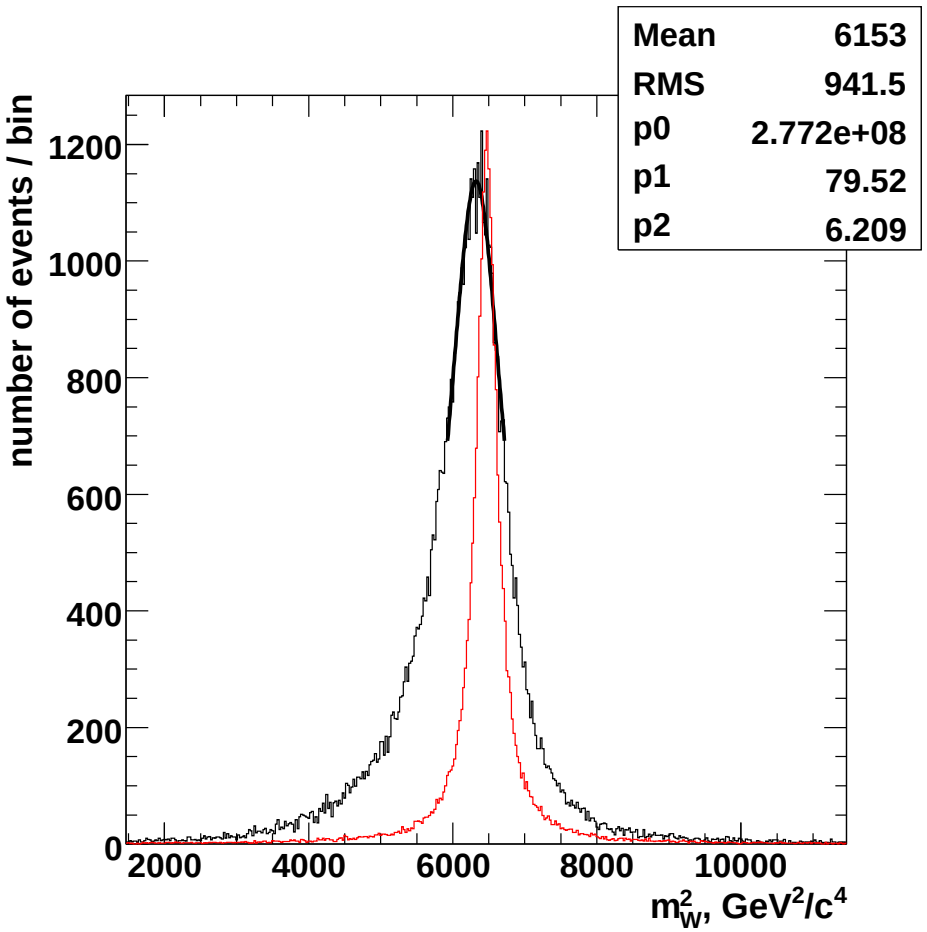

Figure 6.7: Reconstructed 2-jet invariant hadronic-side W boson mass squared m_W^2 for measured jet angles (black) and parton-level angles (red). The peak of the distribution for measured angles is fitted by a Breit-Wigner distribution, with the central mass reported as p1 = 79.52 GeV/c^2. The measured jet angles thus cause a -0.9 GeV/c^2 shift in the m_W peak from its parton-level value of 80.4 GeV/c^2. There is also significant skewness, causing the square-root of the mean m_W^2 to be even lower, $\sqrt{6153} = 78.4$ GeV/c^2. Note that parton-level energies are used in both distributions, so the observed effects are entirely due to the measured angles. Note also that for ease of comparison, the parton-level distribution is renormalised so that the height of its peak matches that of the distribution for measured angles.

The angular dependence of the reconstructed m_W can be clearly seen:

$$m_W \simeq 2E_1E_2(1-\cos(\alpha_{12})), \tag{6.2.2}$$

where α_{12} is the angle between the two jets. The angular component of the resolution of m_W (keeping parton-level energies so that $E_i = E_i^y$), is therefore given by

$$\frac{\Delta m_W}{m_W} = \frac{\cos(\alpha_{12}^x) - \cos(\alpha_{12}^y)}{1-\cos(\alpha_{12}^y)}, \tag{6.2.3}$$

dependent only on the resolution of $\cos(\alpha_{12})$.

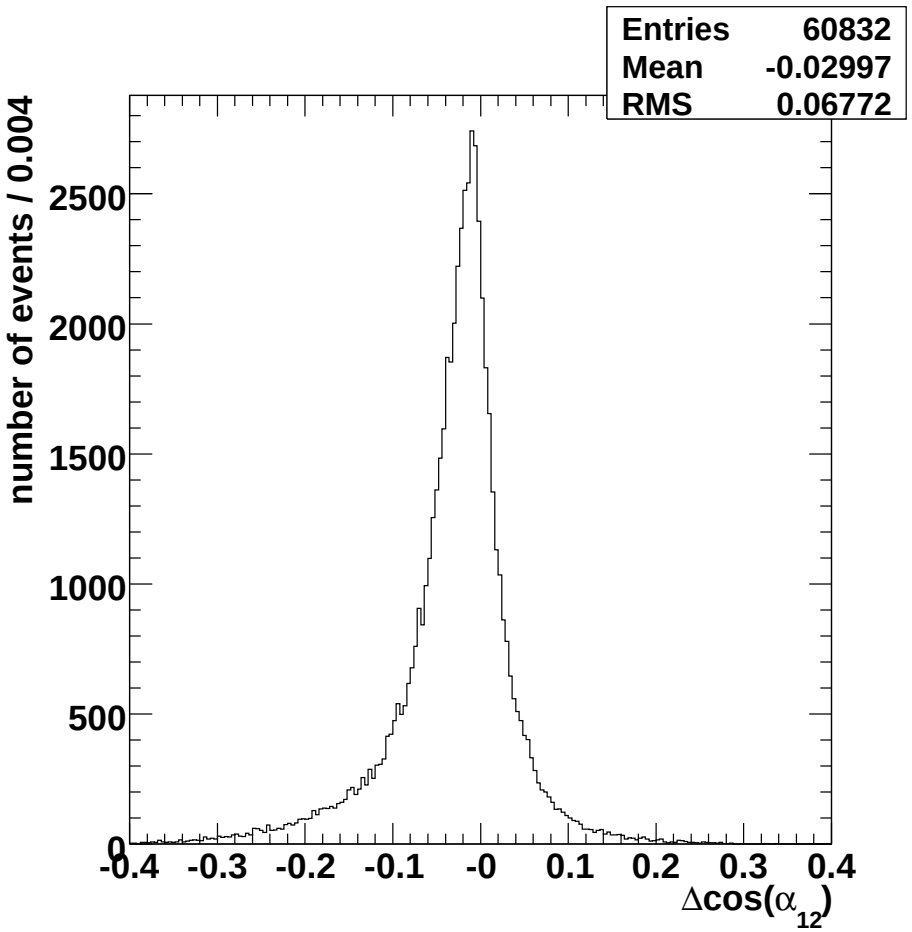

Figure 6.8: $\Delta\cos(\alpha_{12}) \equiv (\cos(\alpha_{12}^{y}) - \cos(\alpha_{12}^{x}))$ distribution. A bias and skewness similar to that seen in the m_W distribution of Figure 6.7 is seen.

It is therefore expected that the distribution of $\Delta\cos(\alpha_{12})$ will display a similar bias to that of the m_W distribution, and this is demonstrated in Figure 6.8. The angle α_{12} is, on average, shifted so that the two jets appear closer together than their parent partons, directly reducing the reconstructed m_W. An ATF for the light jets, in the variable $\Delta\cos(\alpha_{12})$, is introduced to describe this effect (Section 6.2.2). The ATFs for the b-jets will be discussed later (Section 6.2.4).

While it is apparent from Figures 6.6 and 6.8 that a bias can be present in $\cos(\alpha_{12})$ when no bias is seen in the individual jet angles, the plots do not determine whether the angular resolutions plotted in Figure 6.6 could themselves be the cause of the bias in $\cos(\alpha_{12})$. To test this, the parton-level angles were smeared using the distributions in Figure 6.6, and the results for α_{12} are plotted in Figure 6.9. No bias is seen, suggesting that the observed bias in $\cos(\alpha_{12})$ is not simply a resolution effect, and that there is some correlation between the measured angles of the two jets.

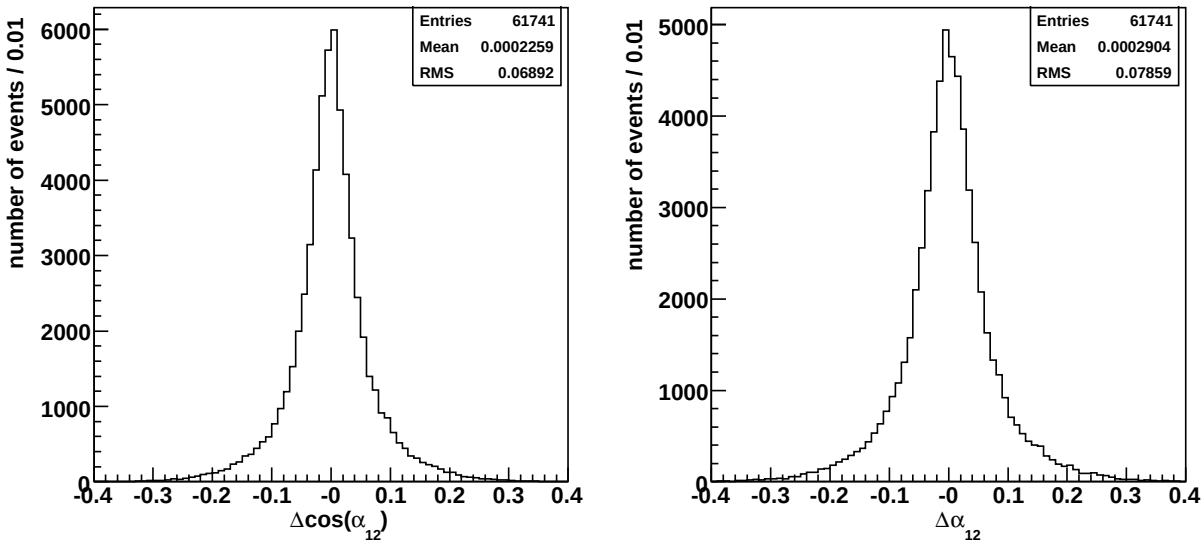

Figure 6.9: $\Delta\cos(\alpha_{12})$ and $\Delta\alpha_{12}$ distributions for smeared parton-level angles. The distributions used for the smearing of the parton angles were the angular resolution distributions for the original angles (Figure 6.6). No bias in $\Delta\cos(\alpha_{12})$ or $\Delta\alpha_{12}$ is observed.

6.2.2 Change of variables

The angles of the two light jets, jets 1 and 2, are initially described in terms of the angles θ_1, ϕ_1, θ_2 and ϕ_2. The ATF for the light jets must describe the resolution of $\cos(\alpha_{12})$ (Figure 6.8), and a change of variables to a coordinate system incorporating α_{12} is therefore necessary. This can be accomplished first by defining θ_{N12} and ϕ_{N12} as the angles of the vector normal to jets 1 and 2, in the original (x, y, z) coordinate system. After rotating the original coordinate axes by an angle θ_{N12} about the axis in the (x, y) plane defined by the unit vector $(-\sin(\phi_{N12}), \cos(\phi_{N12}))$, the normal to jets 1 and 2 points along the z' axis and the jets both lie in the (x', y') plane. The angles of jets 1 and 2 are then described by their angles in that plane, ϕ'_1 and ϕ'_2. α_{12} is just $\phi'_2 - \phi'_1$, and a further variable representing the angle of the line bisecting the two jets, c_{12}, is defined, where $c_{12} = \frac{\phi'_2+\phi'_1}{2}$.

The angle of the line bisecting the two jets, c_{12}, is chosen because it remains constant when α_{12} varies. This is also true of θ_{N12} and ϕ_{N12}, meaning that the angles of the two jets are described by α_{12} and three other variables that are independent of α_{12}; the light jet ATF can thus be parameterised using just the α_{12} variable. This description of α_{12} is also consistent with the required[5] symmetry between the two jets, with any change in α_{12} representing a rotation of the two jets either towards or away-from their centre c_{12}.

In the rotated (x', y', z') frame, the unit vectors denoting the directions of the jets are

$$\vec{j'_1} = \begin{pmatrix} \cos(\phi'_1) \\ \sin(\phi'_1) \\ 0 \end{pmatrix} = \begin{pmatrix} \cos(c_{12} - \frac{\alpha_{12}}{2}) \\ \sin(c_{12} - \frac{\alpha_{12}}{2}) \\ 0 \end{pmatrix}$$

[5]The two jets are treated as indistinguishable in P_s.

and

$$\vec{j_2'} = \begin{pmatrix} \cos(\phi_2') \\ \sin(\phi_2') \\ 0 \end{pmatrix} = \begin{pmatrix} \cos(c_{12} + \frac{\alpha_{12}}{2}) \\ \sin(c_{12} + \frac{\alpha_{12}}{2}) \\ 0 \end{pmatrix}.$$

These can be rotated to the lab (x, y, z) frame using a rotation matrix (for a rotation by an angle θ_{N12} about the $(-\sin(\phi_{N12}), \cos(\phi_{N12}))$ unit vector) calculated using Rodrigues' rotation formula:

$$\vec{j_1} = \begin{pmatrix} [c(\theta_{N12}) - 1]c(\phi_{N12})s(\phi_{N12})s(c_{12} - \frac{\alpha_{12}}{2}) + [c(\theta_{N12})c^2(\phi_{N12}) + s^2(\phi_{N12})]c(c_{12} - \frac{\alpha_{12}}{2}) \\ c(\phi_{N12})s(c_{12} - \frac{\alpha_{12}}{2} - \phi_{N12}) + c(\theta_{N12})s(\phi_{N12})c(c_{12} - \frac{\alpha_{12}}{2} - \phi_{N12}) \\ -s(\theta_{N12})c(c_{12} - \frac{\alpha_{12}}{2} - \phi_{N12}) \end{pmatrix},$$

using a shorthand notation $\cos(\varphi) = c(\varphi)$ and $\sin(\varphi) = s(\varphi)$, and

$$\vec{j_2} = \begin{pmatrix} [c(\theta_{N12}) - 1]c(\phi_{N12})s(\phi_{N12})s(c_{12} + \frac{\alpha_{12}}{2}) + [c(\theta_{N12})c^2(\phi_{N12}) + s^2(\phi_{N12})]c(c_{12} + \frac{\alpha_{12}}{2}) \\ c(\phi_{N12})s(c_{12} + \frac{\alpha_{12}}{2} - \phi_{N12}) + c(\theta_{N12})s(\phi_{N12})c(c_{12} + \frac{\alpha_{12}}{2} - \phi_{N12}) \\ -s(\theta_{N12})c(c_{12} + \frac{\alpha_{12}}{2} - \phi_{N12}) \end{pmatrix}.$$

The vectors $\vec{j_1}$ and $\vec{j_2}$ can also be written in terms of the original variables:

$$\vec{j_1} = \begin{pmatrix} \sin(\theta_1)\cos(\phi_1) \\ \sin(\theta_1)\sin(\phi_1) \\ \cos(\theta_1) \end{pmatrix}$$

$$\vec{j_2} = \begin{pmatrix} \sin(\theta_2)\cos(\phi_2) \\ \sin(\theta_2)\sin(\phi_2) \\ \cos(\theta_2) \end{pmatrix}.$$

Forming equations by setting the two expressions for both $\vec{j_1}$ and $\vec{j_2}$ equal, the original variables can be expressed in terms of the new variables.

The equations for $\cos(\theta_1)$ and $\cos(\theta_2)$ are simple:

$$\cos(\theta_1) = -\sin(\theta_{N12})\cos(c_{12} - \frac{\alpha_{12}}{2} - \phi_{N12}) \tag{6.2.4}$$

$$\cos(\theta_2) = -\sin(\theta_{N12})\cos(c_{12} + \frac{\alpha_{12}}{2} - \phi_{N12}), \tag{6.2.5}$$

but since inverse trigonometric functions are used care must be taken that ϕ_1 and ϕ_2 are defined in the correct range ($-\pi$ to $+\pi$). For this reason, ϕ_1 is calculated using

$$\phi_1 = 2\arctan(\tan(\frac{\phi_1}{2})), \tag{6.2.6}$$

where

$$\tan(\frac{\phi_1}{2}) = \frac{1-\cos(\phi_1)}{\sin(\phi_1)}, \tag{6.2.7}$$

and

$$\cos(\phi_1) = \frac{[c(\theta_{N12})-1]c(\phi_{N12})s(\phi_{N12})s(c_{12}-\frac{\alpha_{12}}{2}) + [c(\theta_{N12})c^2(\phi_{N12})+s^2(\phi_{N12})]c(c_{12}-\frac{\alpha_{12}}{2})}{\sin(\theta_1)} \tag{6.2.8}$$

$$\sin(\phi_1) = \frac{c(\phi_{N12})s(c_{12}-\frac{\alpha_{12}}{2}-\phi_{N12}) + c(\theta_{N12})s(\phi_{N12})c(c_{12}-\frac{\alpha_{12}}{2}-\phi_{N12})}{\sin(\theta_1)}, \tag{6.2.9}$$

and similarly for ϕ_2 (except with $-\frac{\alpha_{12}}{2} \rightarrow +\frac{\alpha_{12}}{2}$).

With the old variables defined in terms of the new variables, the Jacobian determinant may be calculated:

$$J = \left| \frac{\partial \cos(\theta_1)\partial\phi_1 \partial\cos(\theta_2)\partial\phi_2}{\partial\cos(\theta_{N12})\partial\phi_{N12}\partial\cos(\alpha_{12})\partial c_{12}} \right| = -1. \tag{6.2.10}$$

The light jet ATF may therefore be expressed in terms of $\cos(\alpha_{12})$ and the other new variables with no additional change-of-variables factors.

The change of variables provides 4 new variables that describe the 4 angles of the two light jets. The need for an ATF in $\cos(\alpha_{12})$ was immediately apparent from the discrepancy in the mass of the hadronic-side W boson (Figure 6.7), and a clear bias was seen in the $\cos(\alpha_{12})$ resolution (Figure 6.8). The need for ATFs in the other 3 variables may be assessed by looking at their resolutions (Figure 6.10). The distributions are narrow and centered at zero, and are therefore chosen to be represented by delta functions. This choice is primarily motivated by restrictions of CPU time.

6.2.3 Parameterisation

The ATF W_A is separated into the part describing $\cos(\alpha_{12})$, W_A^{12}, and the remaining angles:

$$W_A = W_A^{12}\left[\Delta\cos(\alpha_{12})\right]\delta\left[\cos(\theta^y_{N12})-\cos(\theta^x_{N12})\right]\delta\left[\phi^y_{N12}-\phi^x_{N12}\right]\delta\left[c^y_{12}-c^x_{12}\right]W_A^b[\vec{\Omega}^x_b,\vec{\Omega}^y_b], \tag{6.2.11}$$

where the transfer functions for the three remaining light jet angular variables ($\cos(\theta_{N12})$, ϕ_{N12}, and c_{12}) are approximated by Dirac delta functions, and the ATF W_A^b for the two b-jets will be discussed in Section 6.2.4.

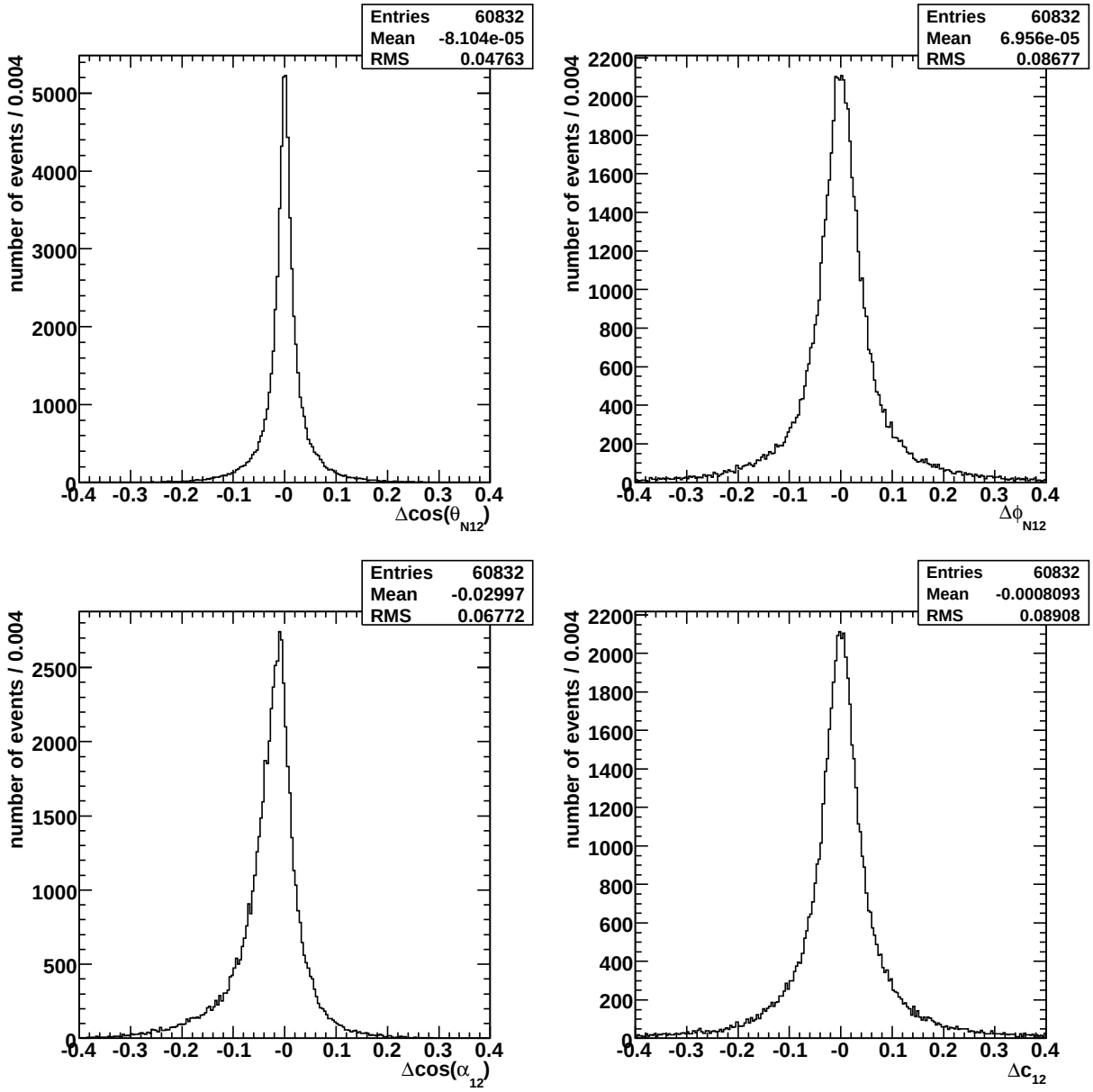

Figure 6.10: The angular resolution distributions for the transformed angular variables $\cos(\theta_{N12})$, ϕ_{N12}, $\cos(\alpha_{12})$ and c_{12} describing the two light jets from the hadronically decaying W boson.

W_A^{12} is written in terms of $\Delta\cos(\alpha_{12}) \equiv \cos(\alpha_{12}^y) - \cos(\alpha_{12}^x)$, and is parameterised by a skew-Cauchy distribution plus two Gaussian distributions:

$$\begin{aligned} W_A^{12}\left[\Delta\cos(\alpha_{12})\right] &= \frac{1}{p_0+p_4+p_7}\left(p_0\frac{1+\frac{2}{\pi}\arctan(p_3p_2X_1)}{\pi p_2(1+X_1^2)} + p_4\frac{e^{-\frac{1}{2}X_2^2}}{\sqrt{2\pi}p_6} + p_7\frac{e^{-\frac{1}{2}X_3^2}}{\sqrt{2\pi}p_9}\right) \\ X_1 &= \frac{\Delta\cos(\alpha_{12})-p_1}{p_2} \\ X_2 &= \frac{\Delta\cos(\alpha_{12})-p_5}{p_6} \\ X_3 &= \frac{\Delta\cos(\alpha_{12})-p_8}{p_9}, \end{aligned} \tag{6.2.12}$$

where the 9 parameters p_i are determined using the same sample of good `PYTHIA` events used in the ETFs (Section 6.1).

The parameters p_i are fit in 12 bins, and the resulting functions are illustrated in Figure 6.11. The first 10 bins are in $\cos(\alpha_{12}^x)$, and the need for the binning is evident from the changing shape of the function in the different bins. At low $\cos(\alpha_{12})$, the jets are roughly back-to-back and no significant skewness is seen, while as the jets get increasingly close together the bias and skewness both increase. The final two bins are for the jets produced roughly collinearly with the W boson, such that the cosine of the angle between the W direction and the jets in the W boson rest-frame $|\cos(\alpha_{\rm CM}))| > 0.8$. For such jets, little bias in $\cos(\alpha_{12})$ is observed. Note that the variation in the widths of the 12 functions is primarily an artifact of the gradient of the cosine function, with a small $\Delta\cos(\alpha_{12})$ representing a bigger change in angle at high $|\cos(\alpha_{12})|$.

Since the function W_A^{12} (Equation 6.2.12) is normalised from $-\infty$ to $+\infty$ in $\cos(\alpha_{12}^x)$, a correction is required due to the physical -1 to $+1$ range of $\cos(\alpha_{12}^x)$. This is evaluated numerically using *Mathematica* [45], and is a constant n_i (close to 1) for each fitted set of p_i. Unlike most constant normalisation factors, n_i cannot be neglected because it takes a different value for each of the 12 W_A^{12} bins; it therefore must be included to ensure the relative normalisation between bins, which is required because 2 different bins may be used in the sum over jet-parton assignments of Equation 5.2.30.

The light jet ATF W_A^{12} can be tested by plotting the $\Delta\cos(\alpha_{12})$ distribution before and after convolution with W_A^{12}. The results are shown in Figure 6.12, demonstrating that W_A^{12} removes the $\Delta\cos(\alpha_{12})$ bias.

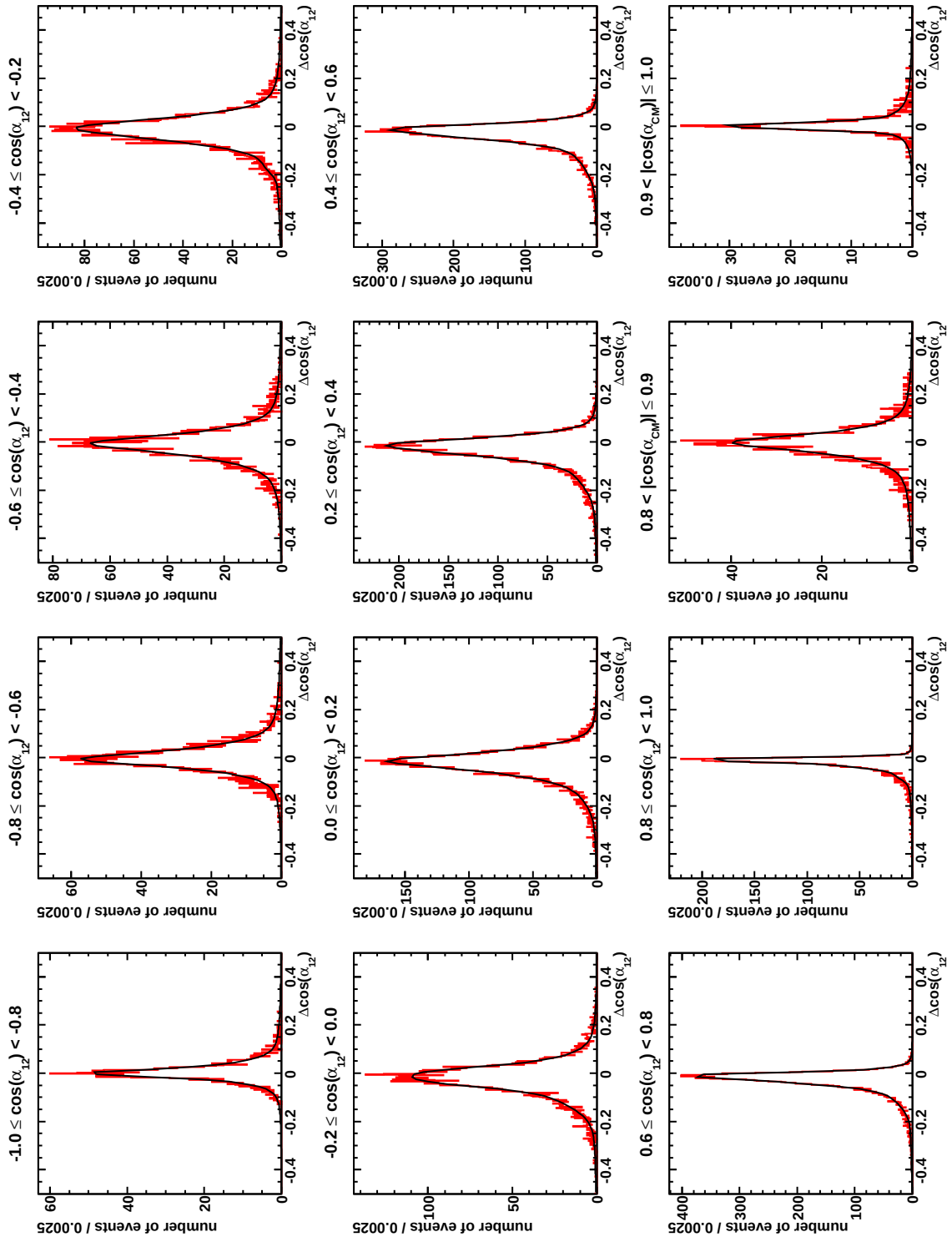

Figure 6.11: Angular Transfer Function W_A^{12} parameterisation in $\Delta\cos(\alpha_{12})$. The parameters are fit in the 12 labelled bins, with the red histograms showing the fitted distributions and the black lines showing the resulting functions.

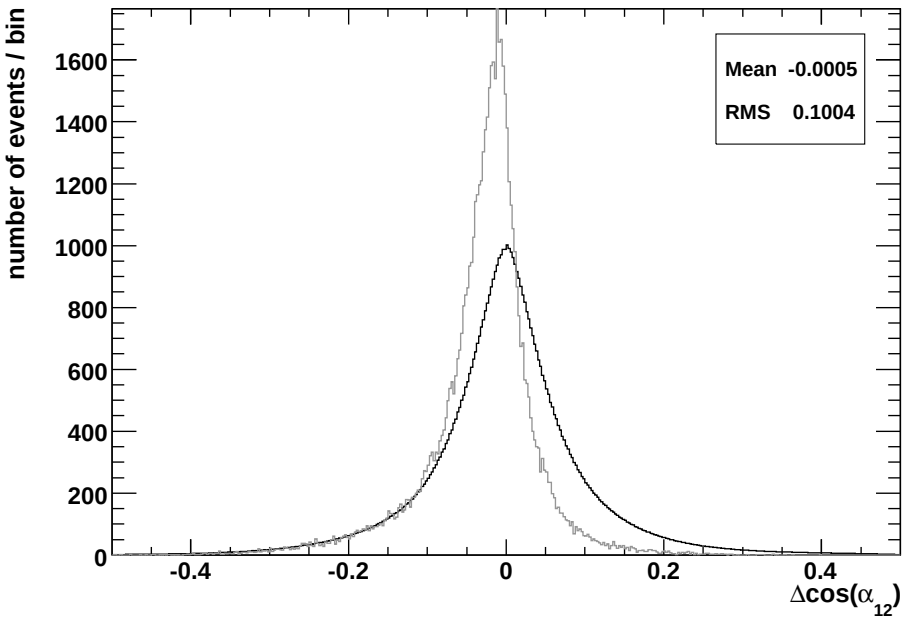

Figure 6.12: The $\Delta\cos(\alpha_{12})$ distribution before (grey) and after (black) convolution with the $\cos(\alpha_{12})$ ATF W_A^{12}. The bias is removed by the integration, with the corrected distribution having a mean of zero.

6.2.4 *b*-jet ATFs

The ATF W_A^{12} describes only the two hadronic-side W jets, and the ATF W_A^b for the two b-jets will be discussed in this section. It is separated into two components, W_A^{bh} for the hadronic-side b-jet and W_A^{bl} for the leptonic-side b-jet:

$$W_A^b[\vec{\Omega}_b^x, \vec{\Omega}_b^y] = W_A^{bh}[\Omega_{bh}^x, \Omega_{bh}^y]\, W_A^{bl}[\Omega_{bl}^x, \Omega_{bl}^y]. \tag{6.2.13}$$

Hadronic side *b*-jet ATF

The angular resolution distributions (Figure 6.13) in $\cos(\theta_{bh})$ and ϕ_{bh} for the hadronic-side b-jet again seem to support the choice of δ-function ATFs: the distributions are narrow and centred at zero.

By analogy to the effect seen in the angle α_{12} between the hadronic-side W-jets, where the jets appear closer together than their parent partons, a similar effect was postulated in the angle between the hadronic-side b-quark and W boson, α_{Wb}. The effect is indeed observed in the `PYTHIA` simulated events, with the hadronic-side b-quark on average shifted towards the W boson, reducing the measured top quark mass. However, it is only the angles of the b-jet that appear shifted, with the distribution for the angle of the reconstructed W boson in agreement with the parton-level information (Figure 6.14). Figure 6.15 shows the distribution of $\Delta\cos(\alpha_{Wb}) \equiv \cos(\alpha_{Wb}^y) - \cos(\alpha_{Wb}^x)$, and skewness is apparent along with a non-zero mean, although it should be noted that the effect is significantly smaller than that seen in $\Delta\cos(\alpha_{12})$.

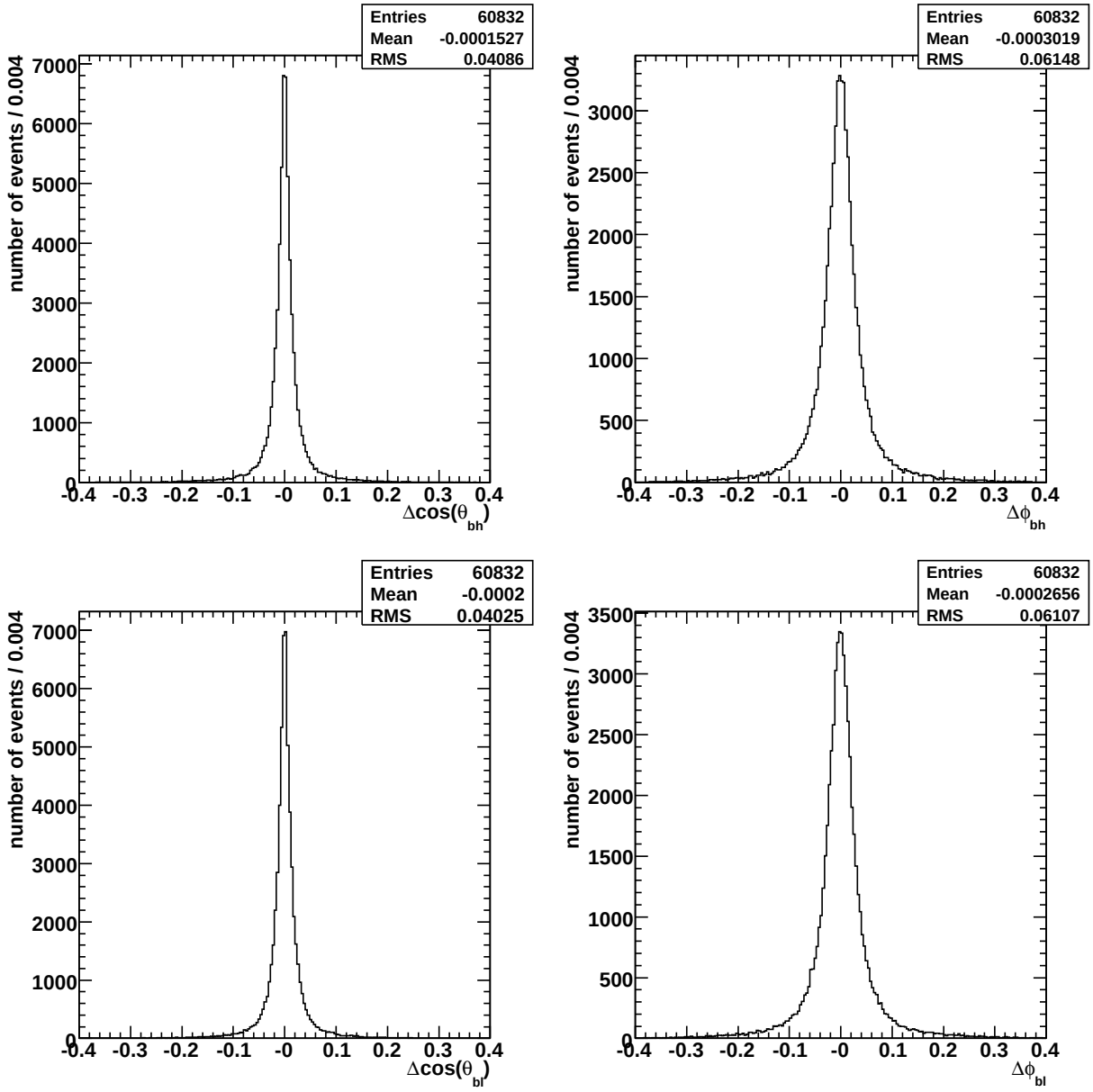

Figure 6.13: The angular resolution distributions for the measured angles $\cos(\theta_i)$ and ϕ_i of the two b-jets.

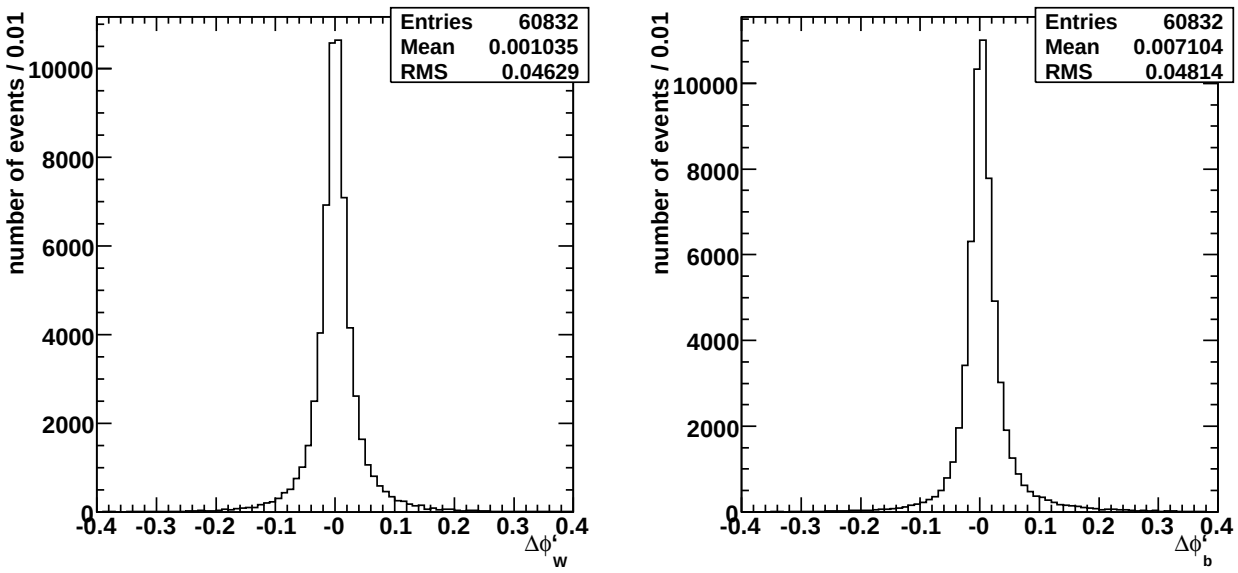

Figure 6.14: The angular resolution distributions $\Delta\phi'_W$ and $\Delta\phi'_b$, for the angles of the hadronic-side W boson and b-jet in their (x'', y'') plane. Only the $\Delta\phi'_b$ distribution is biased.

In much the same way as before, the change of variables to a coordinate system incorporating α_{Wb} is accomplished first by defining θ_{NWb} and ϕ_{NWb} as the angles of the normal to the hadronic-side b-jet and the reconstructed hadronic-side W boson (after any shift $\Delta\cos(\alpha_{12})$)[6] in the original (x, y, z) coordinate system. After rotating the original coordinate axes by an angle θ_{NWb} about the axis in the (x, y) plane defined by the unit vector $(-\sin(\phi_{NWb}), \cos(\phi_{NWb}))$, the vectors of the W boson and the b-jet lie in the (x'', y'') plane, with their normal pointing along the z'' axis, and their angles are described by ϕ'_W and ϕ'_b. α_{Wb} is just $\phi'_b - \phi'_W$, and this time the fourth variable c_{Wb} is chosen as $c_{Wb} = \phi'_W$. In this case, it is the angle $c_{Wb} = \phi'_W$ that remains constant when α_{Wb} varies (Figure 6.14).

The solution of the change of variables is very similar to that for α_{12}, and again it is found that the Jacobian determinant

$$J = \left| \frac{\partial\cos(\theta_W)\partial\phi_W\partial\cos(\theta_{bh})\partial\phi_{bh}}{\partial\cos(\theta_{NWb})\partial\phi_{NWb}\partial\cos(\alpha_{Wb})\partial c_{Wb}} \right| = -1. \tag{6.2.14}$$

Note that two additional integration variables ($d\cos(\theta_W)$ and $d\phi_W$, for the angles of the W boson) are introducted to allow for the change of variables. However, they are immediately subsumed by requiring the hadronic-side b-jet ATF W_A^{bh} to be a delta function in the quantities on which they depend (i.e. $\cos(\theta_{NWb})$, ϕ_{NWb} and c_{Wb}); only the angles of the b-jet (θ_{bh} and ϕ_{bh}) are affected by a change in $\cos(\alpha_{Wb})$, and the hadronic-side b-jet ATF describes the resolution in just the $\cos(\alpha_{Wb})$ variable:

$$W_A^{bh} = W_A^{Wb}\left[\Delta\cos(\alpha_{Wb})\right]\delta\left[\cos(\theta^y_{NWb}) - \cos(\theta^x_{NWb})\right]\delta\left[\phi^y_{NWb} - \phi^x_{NWb}\right]\delta\left[c^y_{Wb} - c^x_{Wb}\right]. \tag{6.2.15}$$

[6]The α_{Wb} ATF describes the movement of the hadronic-side b-jet towards the parton-level hadronic-side W boson, and must therefore be implemented after the α_{12} ATF.

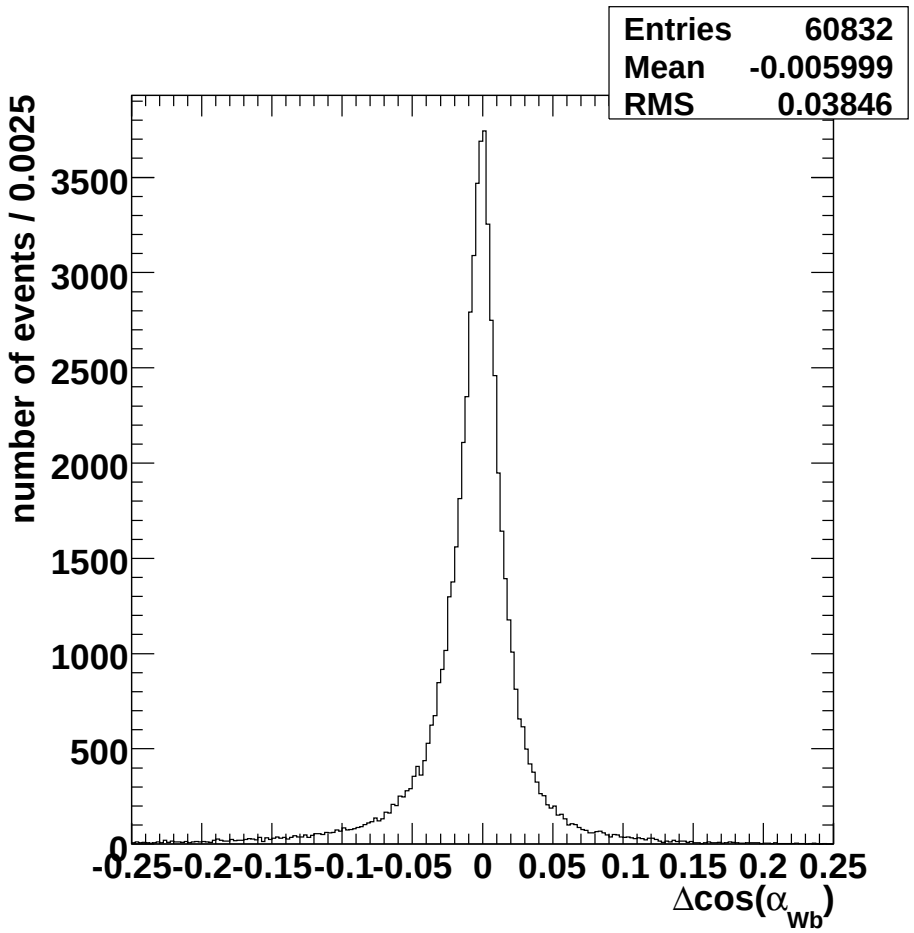

Figure 6.15: $\Delta\cos(\alpha_{Wb})$ distribution. Skewness is apparent along with a non-zero mean.

The $\cos(\alpha_{Wb})$ ATF W_A^{Wb} is parameterised by a skew-Cauchy distribution plus one Gaussian distribution, in the variable $\Delta\cos(\alpha_{Wb})$:

$$\begin{aligned} W_A^{Wb}\left[\Delta\cos(\alpha_{Wb})\right] &= \frac{1}{q_0+q_4}\left(q_0\frac{1+\frac{2}{\pi}\arctan(q_3q_2Y_1)}{\pi q_2(1+Y_1^2)}+q_4\frac{e^{-\frac{1}{2}Y_2^2}}{\sqrt{2\pi}q_6}\right) \\ Y_1 &= \frac{\Delta\cos(\alpha_{Wb})-q_1}{q_2} \\ Y_2 &= \frac{\Delta\cos(\alpha_{Wb})-q_5}{q_6}. \end{aligned} \tag{6.2.16}$$

The 6 parameters q_i are again determined using a fit to the same sample of good PYTHIA events, in 12 bins analogous to those for W_A^{12}, and the resulting 12 functions are illustrated in Figure 6.16.

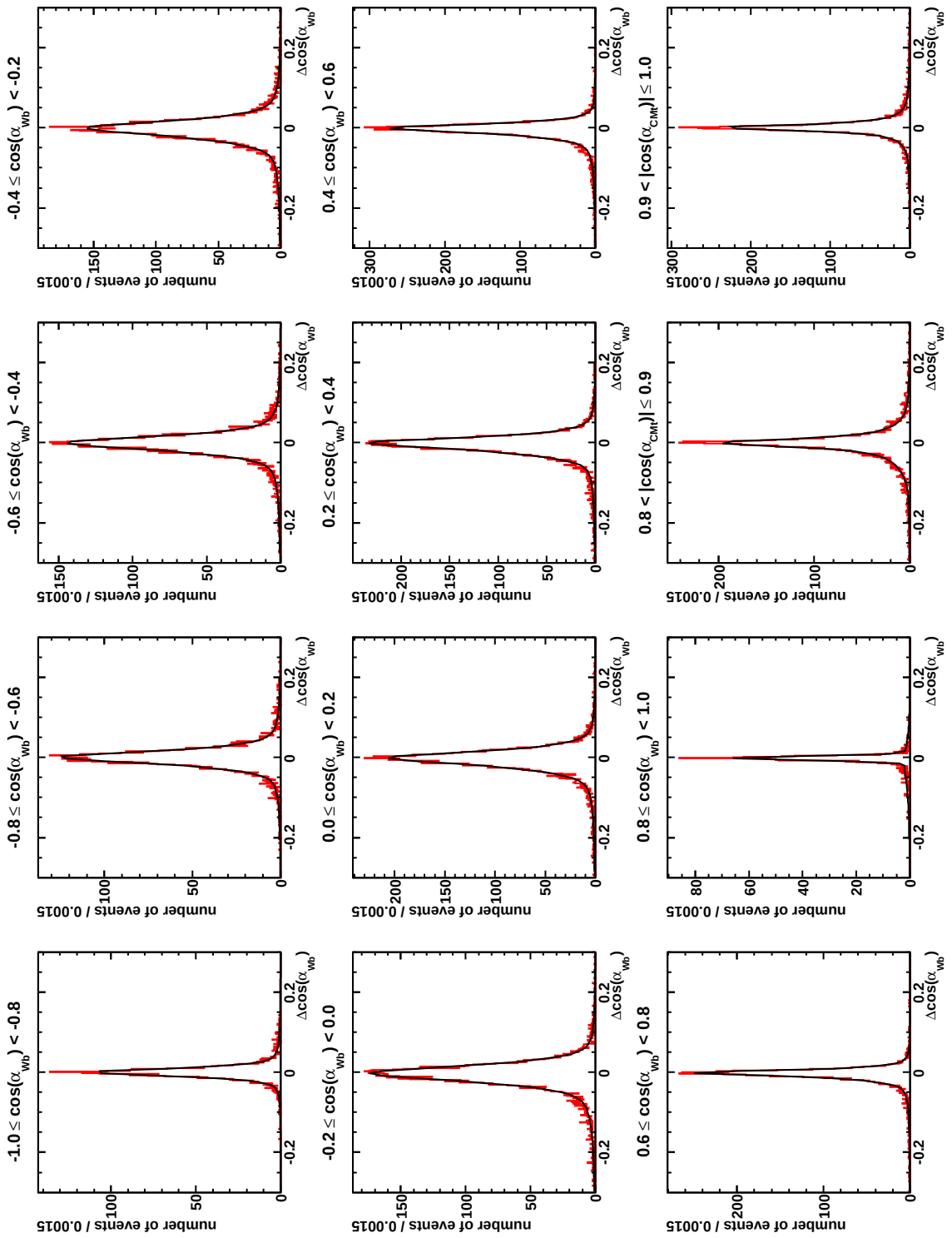

Figure 6.16: Angular Transfer Function W_A^{Wb} parameterisation in $\Delta\cos(\alpha_{Wb})$. The parameters are fit in the 12 labelled bins, with the red histograms showing the fitted distributions and the black lines showing the resulting functions.

Leptonic side b-jet ATF

The treatment of the leptonic-side b-jet remains the same as in previous versions of this analysis [1], and its ATF W_A^{bl} is approximated by a δ-function:

$$W_A^{bl} = \delta[\Omega_{bl}^x - \Omega_{bl}^y]. \tag{6.2.17}$$

This can be partly justified by the unbiased angular resolutions seen in Figure 6.13, and also by the fact that the overall resolution of the top quark mass measurement provided by the leptonic side is much lower than that of the hadronic side (largely due to the unknown p_z of the neutrino), and so the measurement is less sensitive to effects in the measured angles of the leptonic-side b-jet.

6.2.5 Test of ATFs

The angular transfer functions were introduced to correct the observed biases in $\cos(\alpha_{12})$ and $\cos(\alpha_{Wb})$, and thus in m_W and m_t. The performance of the ATFs can therefore be tested by plotting the reconstructed m_W and m_t distributions before and after convolution with the ATFs W_A^{12} and W_A^{Wb}. The results are shown in Figure 6.17, where the ATFs are seen to remove the bias and skewness in both m_W and m_t. Apart from correcting the bias, the introduction of the ATFs W_A^{12} and W_A^{Wb} also has the added benefit of describing the experimental resolution of the angles to which the measurement is most sensitive: those that most affect the reconstructed W boson and top quark masses.

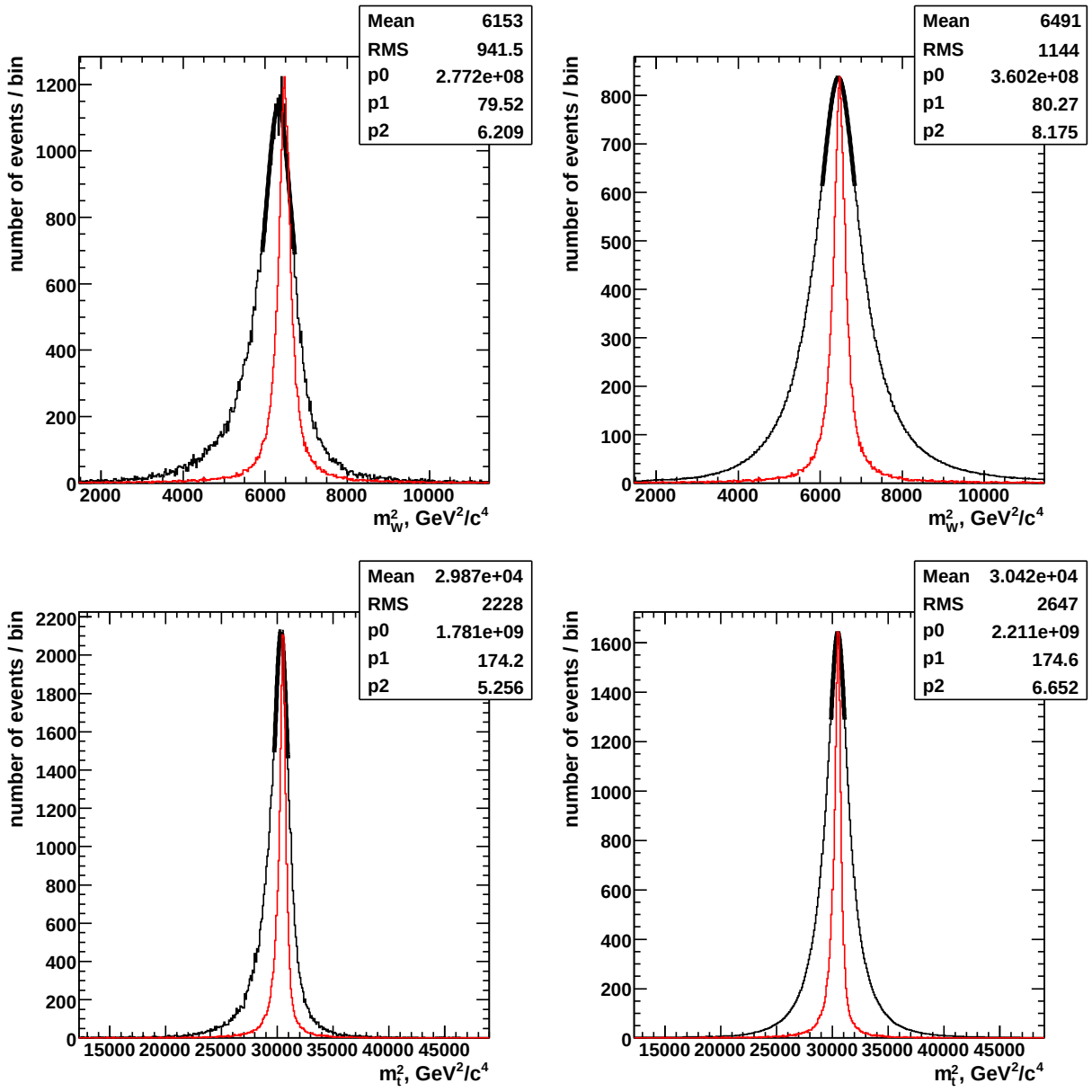

Figure 6.17: Reconstructed 2- and 3-jet invariant hadronic-side masses m_W^2 and m_t^2. On the left, the black histograms show the distributions using the original measured jet angles, while on the right they show the distributions after convolution with the ATFs. In all plots, the distributions seen with parton-level angles are overlaid in red for comparison, and the agreement is seen to be good after application of the ATFs, with the bias and skewness removed. As in Figure 6.7, the peaks of the black distributions are fitted by Breit-Wigners, with the central mass reported as the fitted "p1". Note that parton-level energies are used in all distributions. Note also that for ease of comparison, the parton-level distributions are renormalised so that the heights of their peaks match those of the distributions for measured angles.

6.3 Calculation of the integral in the signal p.d.f., P_s

As discussed in Section 5.2.4, the reduction of the number of dimensions in the integration for P_s is made possible by the approximations made in the construction of the Transfer Function. With the Transfer Function now fully parameterised, this can be demonstrated.

Starting from Equation 5.2.30, the fully normalised signal p.d.f. P_s is given by

$$P_s(\vec{x}) = \frac{1}{\overline{Acc}(m_t, \Delta_{\text{JES}})\,\sigma(m_t)} \frac{(2\pi)^4}{16\, n_{\text{assign}}} \sum_{\text{assign}}^{2,6,12} \int |\mathcal{M}(m_t)|^2 \frac{f(x^1_{\text{Bj}})}{|\vec{q_1}|} \frac{f(x^2_{\text{Bj}})}{|\vec{q_2}|} W(\vec{x}, \vec{y}, \Delta_{\text{JES}}) d\tilde{\Phi}$$

$$d\tilde{\Phi} = \frac{1}{(2\pi)^{18} 2^6} \frac{1}{2E_p E_{\bar{p}}} \frac{1}{J} \frac{\rho^2_{bh}\rho^2_{j1}\rho^2_{j2}\rho^2_{bl}}{E_{bh}E_{j1}E_{j2}E_{bl}E_l E_\nu} d^3p_l dm^2_{Wl} dm^2_{Wh} d\rho_{j1} d\Omega_{bh} d\Omega_{bl} d\Omega_{j1} d\Omega_{j2}.$$

The 14 dimensions of integration in the phase space $d\tilde{\Phi}$ are reduced to just 5 prior to the numerical evaluation of the integral, by integrating over the Dirac delta functions in the Transfer Function $W(\vec{x}, \vec{y}, \Delta_{\text{JES}})$.

Equation 6.0.2 gives $W(\vec{x}, \vec{y}, \Delta_{\text{JES}})$:

$$W(\vec{x}, \vec{y}, \Delta_{\text{JES}}) = \delta^3(\vec{p^y_l} - \vec{p^x_l}) \prod_{i=1}^{4} \frac{1}{(\rho^x_i)^2} \prod_{i=1}^{4} \left(\frac{\rho^x_i}{E^x_i} W^i_E(E^x_i, E^y_i, \Delta_{\text{JES}}) \right) W_A(\vec{\Omega}^x, \vec{\Omega}^y),$$

where, from Equation 6.2.11, the overall ATF W_A is expressed as

$$W_A = W^{12}_A \left[\Delta \cos(\alpha_{12})\right] \delta\left[\cos(\theta^x_{N12}) - \cos(\theta^y_{N12})\right] \delta\left[\phi^x_{N12} - \phi^y_{N12}\right] \delta\left[c^x_{12} - c^y_{12}\right] W^b_A[\vec{\Omega}^x_b, \vec{\Omega}^y_b],$$

with the b-jet ATF W^b_A defined as

$$\begin{aligned} W^b_A &= W^{bh}_A\, W^{bl}_A \\ W^{bh}_A &= W^{Wb}_A \left[\Delta \cos(\alpha_{Wb})\right] \delta\left[\cos(\theta^x_{NWb}) - \cos(\theta^y_{NWb})\right] \delta\left[\phi^x_{NWb} - \phi^y_{NWb}\right] \delta\left[c^x_{Wb} - c^y_{Wb}\right] \\ W^{bl}_A &= \delta[\Omega^x_{bl} - \Omega^y_{bl}]. \end{aligned}$$

After the changes of angular variables (Equations 6.2.10 and 6.2.14), the original $d\Omega^y_{j1}$, $d\Omega^y_{j2}$, and $d\Omega^y_{bh}$ angular integration variables in the phase space $d\tilde{\Phi}$ of the signal p.d.f. P_s have been converted to the new variables,

$$d\cos(\theta^y_{N12})\, d\phi^y_{N12}\, d\cos(\alpha^y_{12})\, dc^y_{12}\, d\cos(\theta^y_{NWb})\, d\phi^y_{NWb}\, d\cos(\alpha^y_{Wb})\, dc^y_{Wb}.$$

However, all angular integrations but for $d\cos(\alpha^y_{12})$ and $d\cos(\alpha^y_{Wb})$ are made trivial by the delta functions in W_A. Furthermore, the delta function for lepton 3-momentum in the TF eliminates the lepton momentum integration variables d^3p_l.

The expression for P_s thus becomes

$$P_s(\vec{x}; m_t, \Delta_{\mathrm{JES}}) = \mathcal{N} \sum_{\mathrm{assign}}^{2,6,12} \int |\mathcal{M}(m_t)|^2 \frac{f(x^1_{\mathrm{Bj}})}{|\vec{q_1}|} \frac{f(x^2_{\mathrm{Bj}})}{|\vec{q_2}|} \prod_{i=1}^{4} \left(\frac{1}{\rho^x_i E^x_i} W^i_E(\Delta_{\mathrm{JES}}) \right) W^{12}_A W^{Wb}_A d\tilde{\Phi}, \tag{6.3.1}$$

where

$$\mathcal{N} = \frac{1}{\overline{Acc}(m_t, \Delta_{\mathrm{JES}})\, \sigma(m_t)} \frac{(2\pi)^4}{16\, n_{\mathrm{assign}}}$$

$$d\tilde{\Phi} = \frac{1}{(2\pi)^{18} 2^6} \frac{1}{2E_p E_{\bar{p}}} \frac{1}{J} \frac{\rho^2_{bh} \rho^2_{j1} \rho^2_{j2} \rho^2_{bl}}{E_{bh} E_{j1} E_{j2} E_{bl} E_l E_\nu}\, dm^2_{Wl}\, dm^2_{Wh}\, d\rho_{j1}\, d\cos(\alpha_{12})\, d\cos(\alpha_{Wb}), \tag{6.3.2}$$

and where J is still defined by Equation 5.2.12. All quantities are parton-level ("y") except those explicitly given an x superscript. Thus, just five dimensions of integration remain in the expression for P_s, the evaluation of which was described in Section 5.2.4.

6.4 Summary

The Transfer Function, which describes the mapping between out-going partons and their resulting jets, is assumed to be separable into parts describing the jet energies and the jet angles: the ETFs and the ATFs. The ETFs, which take a similar form to that used in previous versions of this analysis [1], include an improved description of the jet energy scale correction (Δ_{JES}).

The ATFs are new feature in this analysis, and provide a description of the correlations observed between jet directions that significantly affect the observed hadronic-side W boson mass. Since the apparent W boson mass is utilised to measure Δ_{JES} and thus calibrate the measured jet energies, the ATFs are essential in providing an accurate measurement of Δ_{JES} and thus the top quark mass. The ATFs also describe the smaller correlation effect in the direction of the hadronic-side b-jet, which directly affects the reconstructed top quark mass.

Chapter 7

Measurement Calibration

The measurement method is tested using the simulated events described in Section 4.2. Many simulated datasets, or "pseudoexperiments", with known m_t, Δ_{JES}, and signal fraction, are created using these events, and the relationships between the known input variables and the corresponding measurements of the method are studied. Ideally, an exact correspondence would be seen. Any inconsistencies are seen in the tests of the linearity of the measurement response, and are corrected using parameterised calibration functions.

7.1 Pseudoexperiments

To match the dataset used by this analysis, the mean number of events in each pseudoexperiment must be 578, Poisson-fluctuated to reflect the expected variation in number of observed events were the experiment to be repeated. The total number of background events in each pseudoexperiment is also Poisson-fluctuated about its expected value of 24% of the total, although the proportions of the individual background types within total background sample are kept constant.

An "ensemble" of many hundreds of pseudoexperiments is required for any given set of input parameters (m_t, Δ_{JES}, and signal fraction) to accurately obtain both the mean measured values and the statistical uncertainty of the method for those parameters. For each input parameter α_{true}, the mean measured value α_{mean} is given by the mean of the distribution of the results $\alpha_{\mathrm{measured}}$ in the ensemble. The statistical uncertainty of the measurement is determined by the width of the distribution.

The "pull" associated with parameter α is defined as

$$\mathrm{pull}_{\alpha} \equiv \frac{\alpha_{\mathrm{measured}} - \alpha_{\mathrm{true}}}{\sigma_{\alpha}^{\mathrm{measured}}}, \tag{7.1.1}$$

where $\sigma_{\alpha}^{\mathrm{measured}}$ is the estimated uncertainty of the measurement (as determined by the fit to the log-likelihood function described in Section 5.4). The pull allows the comparison of the measured and true values of α, measuring the number of $\sigma_{\alpha}^{\mathrm{measured}}$ by which the measured

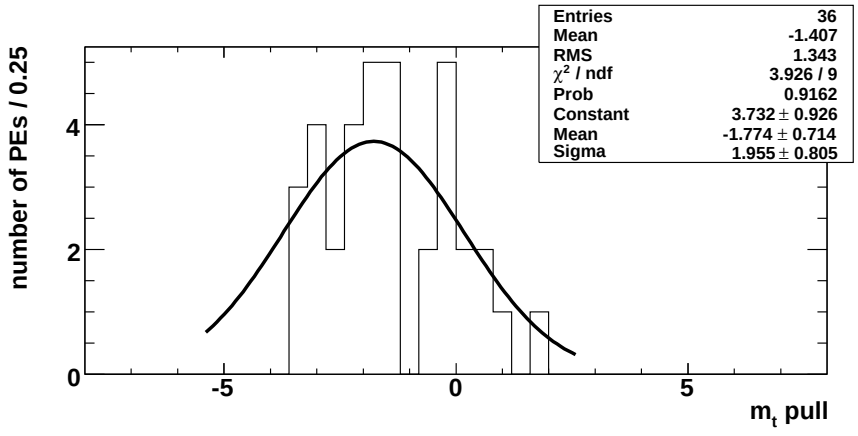

Figure 7.1: Pull distribution seen in pseudoexperiments (PEs) created using the 16000 PYTHIA $t\bar{t}$ events for $m_t = 175$ GeV/c^2, with full simulated background and no resampling. Without resampling, there are not enough pseudoexperiments to accurately measure the width of the distribution.

result is shifted from the true value. For an ideal measurement, the pull distribution is therefore expected to be a Gaussian distribution, centred at zero and with a width of one. The mean of the pull distribution, the "pull mean", measures the mean shift with respect to the true value. The width of the pull distribution, the "pull width", compares the true statistical uncertainty of the measurement with the estimated uncertainty $\sigma_\alpha^{\text{measured}}$. A pull width larger than one indicates an underestimation in $\sigma_\alpha^{\text{measured}}$, and $\sigma_\alpha^{\text{measured}}$ can thus be corrected by multiplication by the pull width.

A quantity known as the "residual" of α is also often used, and is defined as the shift in the mean measured α from its true value, i.e. $\bar{\alpha}_{\text{measured}} - \alpha_{\text{true}}$.

Ideally, each pseudoexperiment would be formed from a set of unique events, giving no statistical correlation between pseudoexperiment results. However, due to the large amount of CPU time needed to calculate the signal and background p.d.f.s P_s and P_b, the simulated events are resampled (with replacement) when creating an ensemble of pseudoexperiments. The resampling factor multiplies the number of pseudoexperiments in the ensemble. Resampling has no effect on the mean values measured in the ensemble, but does increase the knowledge of the widths of the pseudoexperiment result distributions, and thus knowledge of the statistical uncertainty of the measurement method.

The pull distribution seen without the use of resampling, in pseudoexperiments created using the 16000 PYTHIA $t\bar{t}$ events for $m_t = 175$ GeV/c^2 along with simulated background events, is shown in Figure 7.1. Even with 16000 $t\bar{t}$ events (the largest single sample used in this analysis), without resampling there are not enough pseudoexperiments to accurately measure the width of the distribution. The distribution seen with a resampling factor of 100 is shown in Figure 7.2, and allows for a reliable measurement of the pull width.

However, since resampling introduces correlations between pseudoexperiments, it is no longer trivial[1] to assign uncertainty estimates to the means or widths of the distributions seen

[1] Assuming Gaussian distributions, for example, the uncertainty on the mean is simply the RMS of the distribution of uncorrelated results.

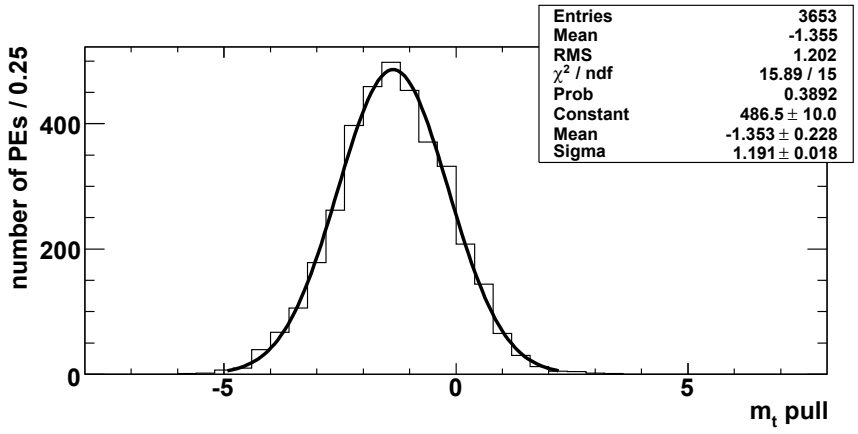

Figure 7.2: Pull distribution seen in pseudoexperiments (PEs) created using the 16000 PYTHIA $t\bar{t}$ events for $m_t = 175$ GeV/c^2, with full simulated background and resampling factor 100.

in an ensemble. These uncertainties can be estimated using the bootstrapping method [46]. Underpinning the bootstrapping method is the assumption that the set[2] of simulated events accurately represent their parent distribution. If this is valid, and for sufficiently large sets it will be, then the statistical uncertainty for any parameter of the set (for example, ensemble means or widths) can be estimated by the variation seen in the value of that parameter when using many sets of simulated events created by resampling-with-replacement, or "bootstrapping", the original set. The variation between the created sets is an estimate of the variation expected in true independent sets each selected from the parent distribution. Assuming Gaussian distributions, the estimated uncertainty for any given parameter is then given by the RMS of the distribution of the values of that parameter from the sets of bootstrapped simulated events.

7.2 Linearity of measurement response

Since the ultimate goal of the measurement is to extract the top quark mass from the events consistent with the $t\bar{t}$ lepton+jets hypothesis, it is sensible first to test its performance using simulated events only of this type (i.e. no simulated background events). Furthermore, since the P_s only accurately represents the "good" subset (Section 4.2.1) of those events (the matrix element describes good signal events, and the Transfer Functions are fit to good signal events), the use of only good simulated events represents an even more ideal scenario. Finally, the combinatorics background, always present in real data events, can also be removed in simulated events, replacing the average over jet-parton assignments in Equation 5.2.22 with just the single known correct identification. In this section, the linearity of the measurement response is tracked from this idealised case, through to the realistic case with full simulated background.

[2]Note that "set" refers to an entire sample of simulated events, e.g. 16000 events plus background for $m_t = 175$ GeV/c^2, and is distinct from the ensembles of pseudoexperiments that are created using events from the set.

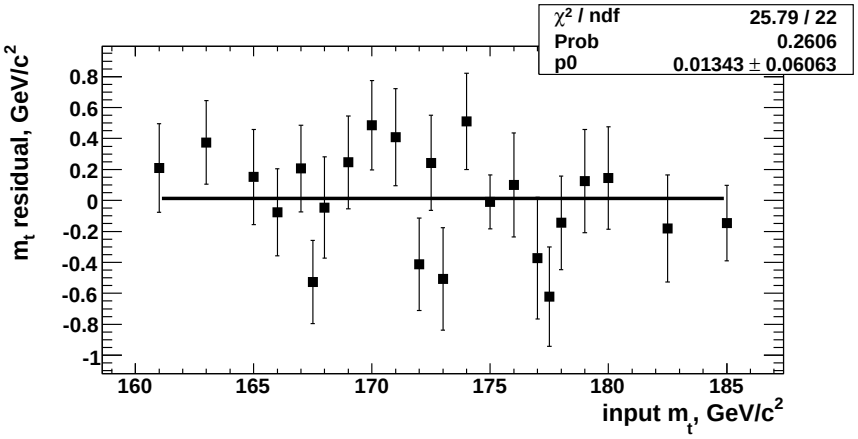

Figure 7.3: The m_t residual (mean measured m_t - input m_t) as a function of input m_t, using only good signal events and the correct jet-parton assignment. The residual is flat and consistent with zero.

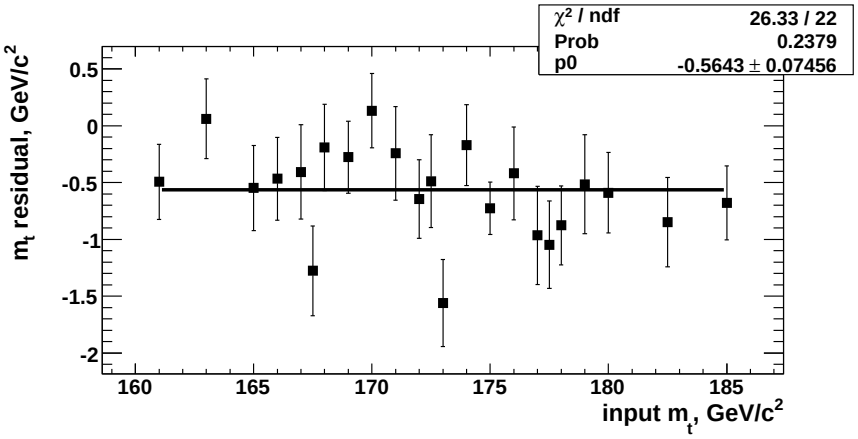

Figure 7.4: The m_t residual as a function of input m_t, using only good signal events but taking the average over the jet-parton assignments. The residual remains flat, but a significant bias is observed, shifting the mean residual to -0.6 GeV/c^2.

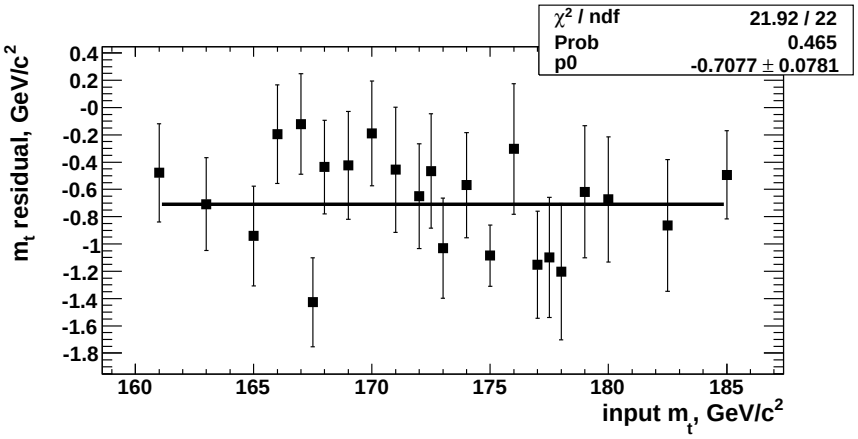

Figure 7.5: The m_t residual as a function of input m_t, now using all signal events and taking the average over the jet-parton assignments. The residual remains flat, but the bias is increased to -0.7 GeV/c^2.

Figure 7.3 shows the m_t residual (mean measured m_t - input m_t) as a function of input m_t, using only good signal events and the correct jet-parton assignment. As would be hoped, the residual is flat and consistent with zero, demonstrating that the method behaves as expected using only ideal events.

In Figure 7.4, the jet-parton assignment is reverted to the realistic case by taking the average of the remaining assignments after b-jet identification. The residual remains flat, but a significant bias is observed, shifting the mean residual to -0.6 GeV/c^2. This shift can be attributed to the misinformation from the incorrect jet-parton assignments.

In Figure 7.5, all $t\bar{t}$ events are used, including the "bad" signal events (events with jets not well matched to partons and those that did not match the decay hypothesis). This adds a further negative bias to the mean residual, shifting it to -0.7 GeV/c^2.

Finally, Figure 7.6 shows the m_t residual and pull width for the fully realistic simulation, with the addition of a 24% contribution of simulated background events to the pseudoexperiments. This again adds a negative bias to the residual, shifting it to -1.2 GeV/c^2; clearly the method is somewhat sensitive to the fraction of background events, and this is accounted for in the measurement calibration. However, the mean m_t pull width of 1.19 is significantly greater than one, indicating that the measured uncertainties $\sigma_{m_t}^{\text{measured}}$ are underestimated. Figure 7.7 shows the dependence of the Δ_{JES} residual and pull width on the input m_t, and again no slope is observed. However, the mean Δ_{JES} pull width of 1.16 indicates that an underestimation is also present in $\sigma_{\Delta_{\text{JES}}}^{\text{measured}}$. The underestimation of the measured uncertainties is corrected in the measurement calibration, and is understood to be a result of the misinformation provided by the incorrect jet-parton assignments, the bad signal events, and the background events.

7.3 Calibration Functions

The measurement calibration corrects for any shifts or non-linearities in the response of the measurement to the input parameters. The calibration functions were calculated using ensembles of pseudoexperiments (Section 7.1) using 17 simulated top quark mass samples in the range 165-185 GeV/c^2 (Section 4.2.1). The background events used in the pseudoexperiments were taken from the samples described in Section 4.4, with their relative fractions taken from Table 4.2. Samples with shifted Δ_{JES} between $+2$ and -2 were created for the $m_t = 165$, 175 and 185 GeV/c^2 samples, by shifting the jet energies of the samples using Equation 6.1.10. An additional 6 top quark mass points in the range 161-169 GeV/c^2 were added following the measurement of $m_t = 172.4$ GeV/c^2 (Chapter 9), to verify that the calibration was adequate at least ± 10 GeV/c^2 from this value. All ensembles of pseudoexperiments were created with resampling factor 100, and all errors were estimated using a bootstrap factor of 100.

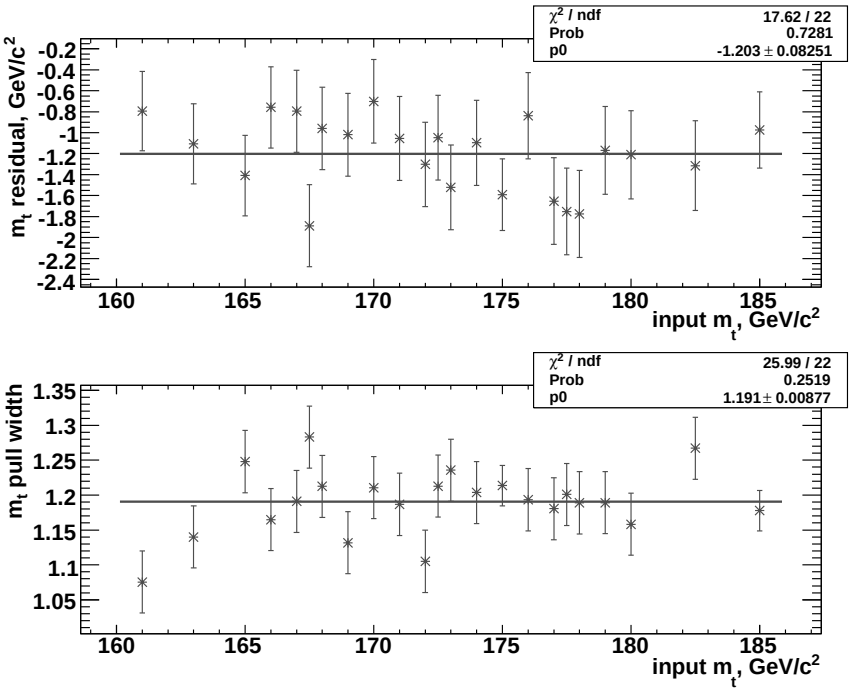

Figure 7.6: The m_t residual and pull width as a function of input m_t, using the fully realistic pseudoexperiment simulation including a 24% contribution of simulated background events. The residual remains flat, but the bias is increased to -1.2 GeV/c^2, while the pull width is flat but significantly greater than 1.

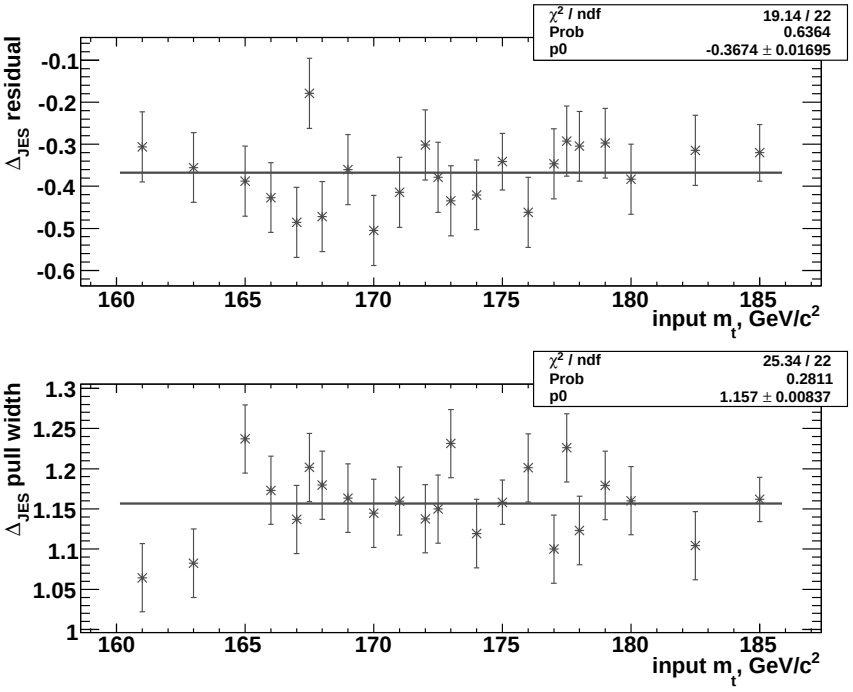

Figure 7.7: The Δ_{JES} residual and pull width as a function of input m_t, using the fully realistic pseudoexperiment simulation including a 24% contribution of simulated background events. The residual appears flat, but there is a bias of -0.4, while the pull width is flat but significantly greater than 1.

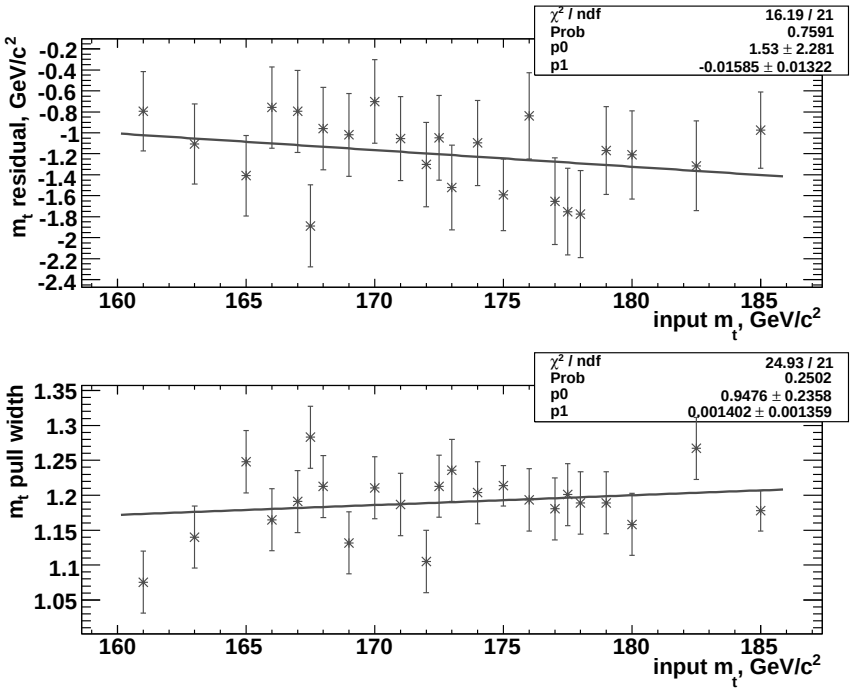

Figure 7.8: The m_t residual and pull width as a function of input m_t, using the fully realistic pseudoexperiment simulation including a 24% contribution of simulated background events. The fitted slopes ("p1") are consistent with zero.

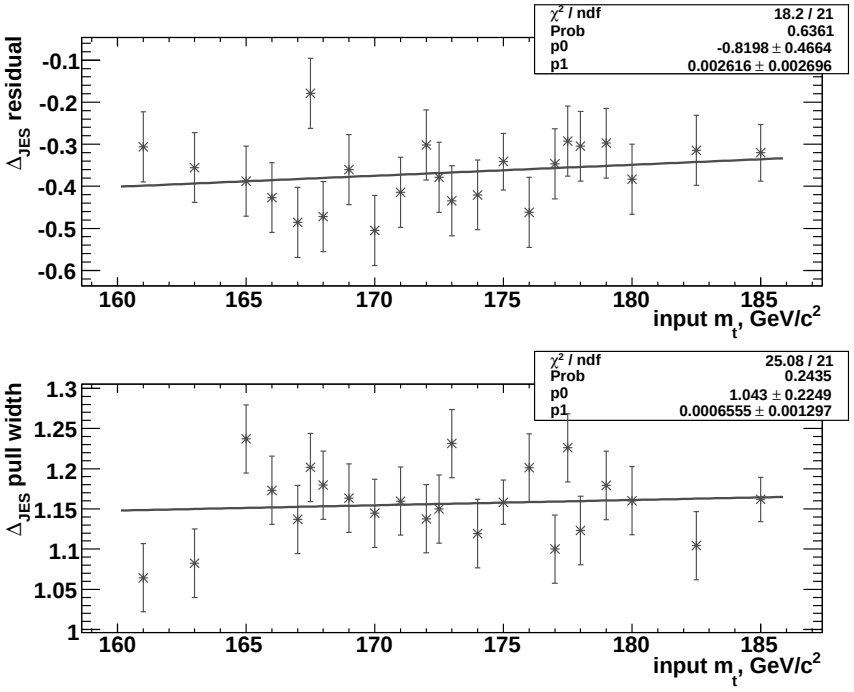

Figure 7.9: The Δ_{JES} residual and pull width as a function of input m_t, using the fully realistic pseudoexperiment simulation including a 24% contribution of simulated background events. The fitted slopes ("p1") are consistent with zero.

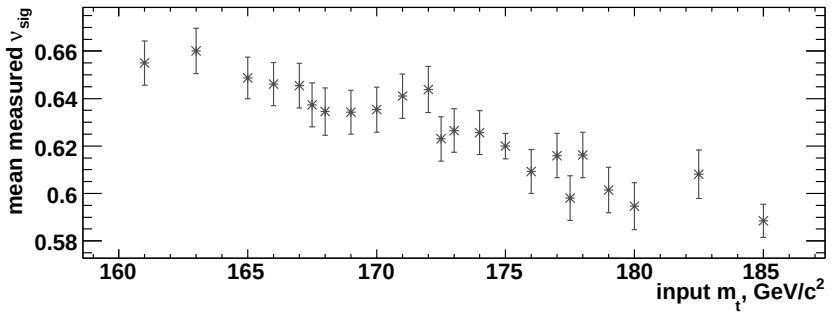

Figure 7.10: The measured ν_{sig} as a function of input m_t, using the fully realistic pseudoexperiment simulation including a 24% contribution of simulated background events.

The flatness of the residuals in Figures 7.6 and 7.7 suggests that no input-mass-dependent calibration of the measured mass and Δ_{JES}, or their pull widths, is required. This is confirmed by fitting slopes to the same points (Figures 7.8 and 7.9), where the fitted gradient is found to be consistent with zero in each case. Figure 7.10 shows a clear dependence of the measured signal fraction parameter ν_{sig} on the input mass. No calibration of ν_{sig} is attempted as it has little physical significance, and its value is not reported in the results of this analysis.

The next step is to look at the input-Δ_{JES} dependence of the measurement. Figure 7.11 shows the dependence of the Δ_{JES} and m_t residuals and pull-widths on the input Δ_{JES} of the simulated events. There is a definite slope in the residuals, which is at least partially explained by the double-counting of acceptance effects within the ETF parameterisation. In particular, the jet E_T cut directly affects the shape of the ETF for low-energy partons by underestimating the low-jet-energy probability density. The ETF therefore further underestimate the low-jet-energy probability density for positive Δ_{JES} (since in reality more low-energy jets will now pass the cut) and overestimates it for negative Δ_{JES} (since in reality fewer low-energy jets will now pass the cut), effectively scaling down the measured Δ_{JES} with respect to the input Δ_{JES} as observed in Equation 7.3.1. The dependence of the m_t residual on the input Δ_{JES} can be simply explained by the negative correlation between measured m_t and Δ_{JES}: if the measured Δ_{JES} is shifted down, the jet energies and thus the measured m_t are shifted up.

The input-Δ_{JES} dependence of the measurements are corrected using the Δ_{JES} calibration functions, taken directly[3] from the fits in Figure 7.11:

[3]In Figure 7.11, the Δ_{JES} residual $(\Delta_{\text{JES}}^{\text{measured}} - \Delta_{\text{JES}}^{\text{true}})$ is plotted as a function of $\Delta_{\text{JES}}^{\text{true}}$, i.e.

$$\Delta_{\text{JES}}^{\text{measured}} - \Delta_{\text{JES}}^{\text{true}} = \text{p0} + \text{p1}\,\Delta_{\text{JES}}^{\text{true}}.$$

Rearranging gives

$$\Delta_{\text{JES}}^{\Delta_{\text{JES}}-\text{corrected}} = \Delta_{\text{JES}}^{\text{true}} = \left(\Delta_{\text{JES}}^{\text{measured}} - \text{p0}\right) / \left(1 + \text{p1}\right).$$

The m_t residual is plotted as a function of $\Delta_{\text{JES}}^{\text{true}}$, and therefore must be corrected based on $\Delta_{\text{JES}}^{\Delta_{\text{JES}}-\text{corrected}}$.

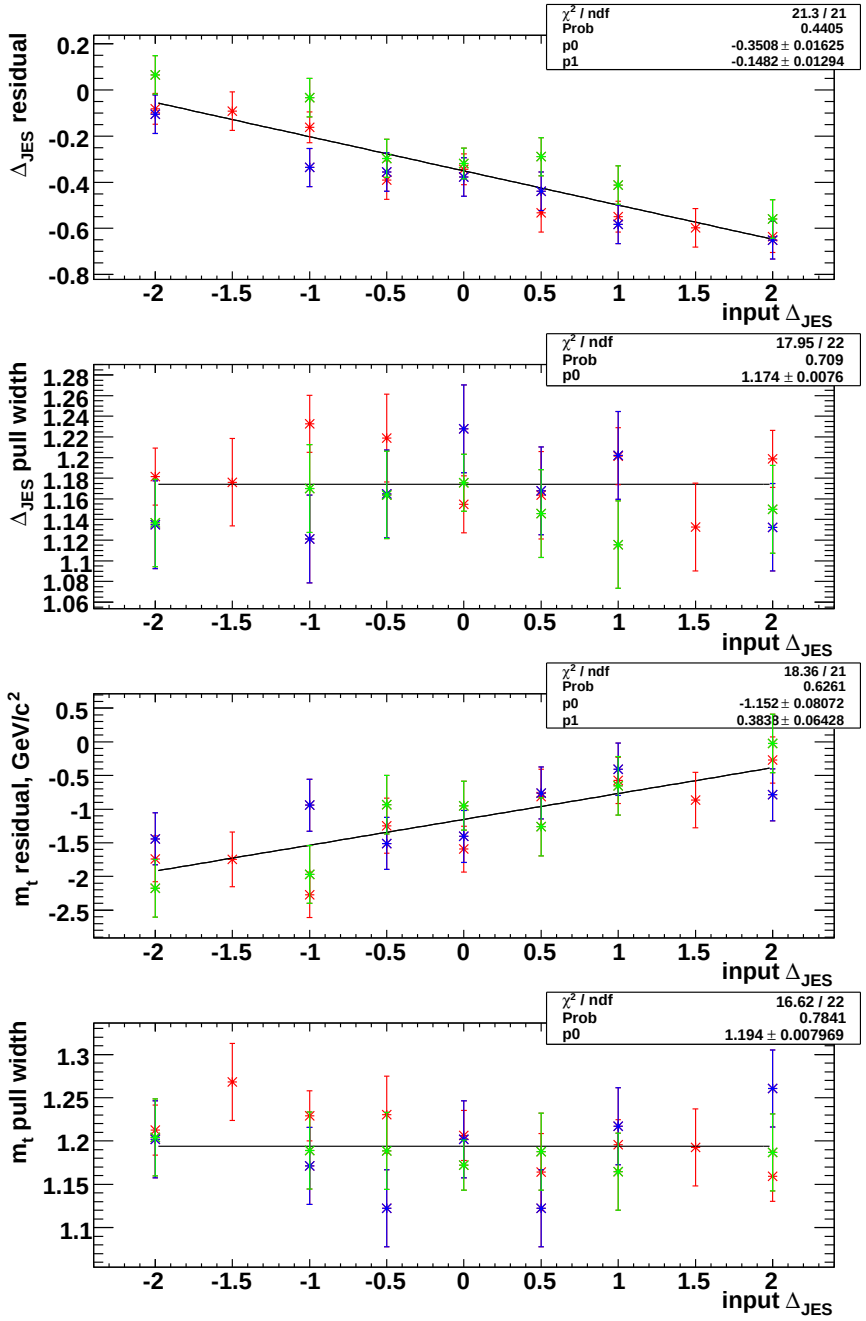

Figure 7.11: The dependence of the Δ_{JES} and m_t residuals and pull-widths on the input Δ_{JES}, and the fitted calibration functions for the residuals. The blue, red, and green points have input m_t of 165, 175 and 185 GeV/c^2 respectively, and are all used together in the fits. The χ^2 probabilities of the fits indicate that all of the points are consistent with the fitted functions.

$$\Delta_{\mathrm{JES}}^{\Delta_{\mathrm{JES}}-\mathrm{corrected}} = \frac{\Delta_{\mathrm{JES}}^{\mathrm{measured}} + 0.351}{1 - 0.148} \tag{7.3.1}$$

$$m_t^{\Delta_{\mathrm{JES}}-\mathrm{corrected}} = m_t^{\mathrm{measured}} + 1.152 - 0.384\,\Delta_{\mathrm{JES}}^{\Delta_{\mathrm{JES}}-\mathrm{corrected}}. \tag{7.3.2}$$

Note that since samples with three different simulated values of m_t are used in the fits (m_t = 165, 175 and 185 GeV/c^2), it is assumed that the Δ_{JES} calibration functions are independent of input m_t. This is a reasonable assumption given the χ^2 probabilities of the fits in Figure 7.11, and the systematic uncertainty related to this assumption is evaluated in Section 8.10. No dependence of the pull widths on the input Δ_{JES} is observed, and no Δ_{JES}-dependent calibration functions for the pull widths are introduced.

The performance of the Δ_{JES} calibration functions can be tested by recreating the ensembles of pseudoexperiments with the calibration functions in place. The results are shown in Figure 7.12, where it is seen that the Δ_{JES} calibration functions remove the dependence on input Δ_{JES}. Note that the calibration increases the Δ_{JES} pull width by a factor 1.378/1.174 = 1.174 (the mean Δ_{JES} pull width is fitted as "p0" in Figures 7.11 and 7.12). This is a direct consequence of the factor $1/(1 - 0.148) = 1.174$ in Equation 7.3.1, which scales up the Δ_{JES} while the measured Δ_{JES} uncertainty $\sigma_{\Delta_{\mathrm{JES}}}^{\mathrm{measured}}$, as yet uncorrected, remains constant. The Δ_{JES} pull width is thus multiplied by the same factor as the Δ_{JES} via Equation 7.1.1. The m_t pull width is also increased, by 6%, due to the negative Δ_{JES} dependence in Equation 7.3.2, meaning that the Δ_{JES} calibration increases the uncertainty of the final top quark mass measurement by about 6%[4].

The final test is the dependence of the measurement on the input signal fraction. Note that the signal fraction calibration is performed after the Δ_{JES} calibration, and so the pseudoexperiment results used in the following plots were all corrected using Equations 7.3.1 and 7.3.2. Ensembles of pseudoexperiments are created with signal fractions between 50% and 100%, with the proportions of the individual background types within total background samples kept constant, and the results are shown in Figure 7.13. Both the residuals and pull widths show a clear dependence on the input signal fraction. This is expected, as the bias caused by the background events naturally increases as the fraction of background events is increased. Since the variation of the signal fraction does not require the recalculation of the p.d.f.s P_s and P_b, the ensembles are created using all 17 simulated m_t samples. The m_t = 165 and 185 GeV/c^2 samples are highlighted in blue and green in the plots to demonstrate that the observed signal fraction dependence has no strong m_t-dependence.

[4]Note that the 6% increase in m_t uncertainty does not appear to be merely a calibration effect and thus avoidable, since preliminary tests with updated ETFs (and an updated mean acceptance function) requiring no Δ_{JES} calibration have shown a similar 6% increase in measured m_t uncertainty. The 6% increase due to Δ_{JES} calibration is therefore adding back the false decrease in measured uncertainty that is seen as a result of the method scaling down the measured Δ_{JES} by the factor $(1 - 0.148)$. That scaling down the measured Δ_{JES} does indeed cause an underestimate of the measurement uncertainty can be understood by considering the case when the jet energies are fixed (i.e. Δ_{JES} multiplied by 0): in that case the measured uncertainty on m_t no longer includes any contribution from the Δ_{JES} uncertainty.

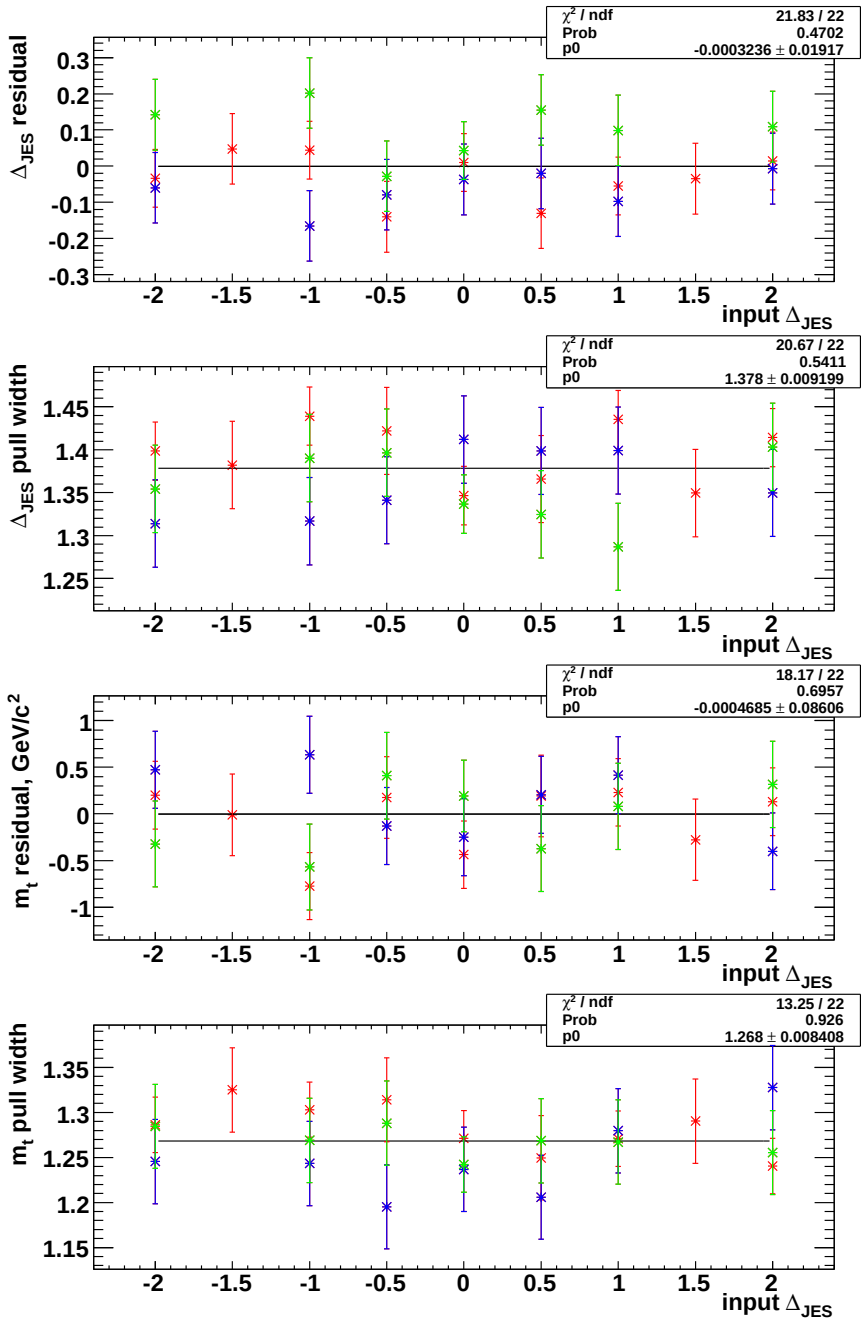

Figure 7.12: The dependence of the Δ_{JES} and m_t residuals and pull-widths on the input Δ_{JES}, after Δ_{JES} calibration. The blue, red, and green points have input m_t of 165, 175 and 185 GeV/c^2 respectively.

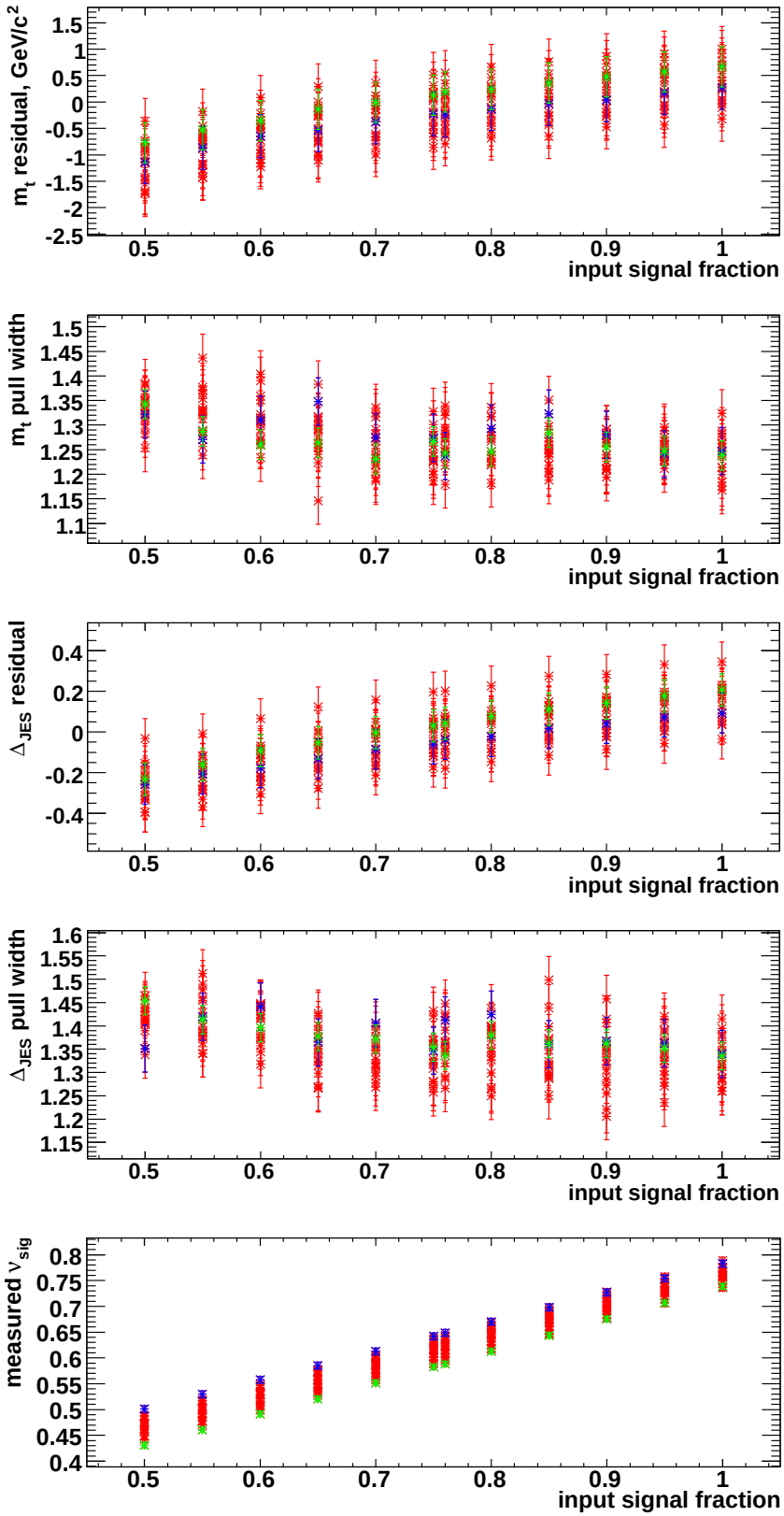

Figure 7.13: The dependence of the m_t and Δ_{JES} residuals and pull-widths, and the measured ν_{sig}, on the input signal fraction. The blue and green points have input m_t of 165 and 185 GeV/c^2 respectively, while red points represent the remaining 15 mass samples with $167.5 \leq m_t \leq 182.5$ GeV/c^2. All quantities have a clear dependence on the input signal fraction, but this is expected due to the bias caused by the background events.

However, the method does not directly measure the signal fraction, but it is strongly correlated with the measured signal fraction parameter ν_{sig} (bottom plot of Figure 7.13). It is therefore possible to parameterise the calibration with respect to the measured ν_{sig}, using the quadratic fits shown in Figure 7.14:

$$\begin{aligned} m_t^{\text{final}} &= m_t^{\Delta_{\text{JES}}-\text{corrected}} + 5.940 - 14.083\,\nu_{\text{sig}} + 7.662\,\nu_{\text{sig}}^2 \\ \sigma_{m_t}^{\text{final}} &= \left(1.829 - 1.575\,\nu_{\text{sig}} + 1.061\,\nu_{\text{sig}}^2\right)\sigma_{m_t}^{\text{measured}} \end{aligned} \tag{7.3.3}$$

$$\begin{aligned} \Delta_{\text{JES}}^{\text{final}} &= \Delta_{\text{JES}}^{\Delta_{\text{JES}}-\text{corrected}} + 1.426 - 3.337\,\nu_{\text{sig}} + 1.690\,\nu_{\text{sig}}^2 \\ \sigma_{\Delta_{\text{JES}}}^{\text{final}} &= \left(1.976 - 1.771\,\nu_{\text{sig}} + 1.222\,\nu_{\text{sig}}^2\right)\sigma_{\Delta_{\text{JES}}}^{\text{measured}}. \end{aligned} \tag{7.3.4}$$

Post-calibration, the dependencies on input signal fraction are removed (Figure 7.15).

The m_t and Δ_{JES} residuals, statistical uncertainties, pull means, and pull widths, after all calibrations, are shown in Figures 7.16 and 7.17. The residuals and pull widths are flat and unbiased, while the mean calibrated m_t uncertainty is in agreement with the RMS of the m_t distribution seen in pseudoexperiments.

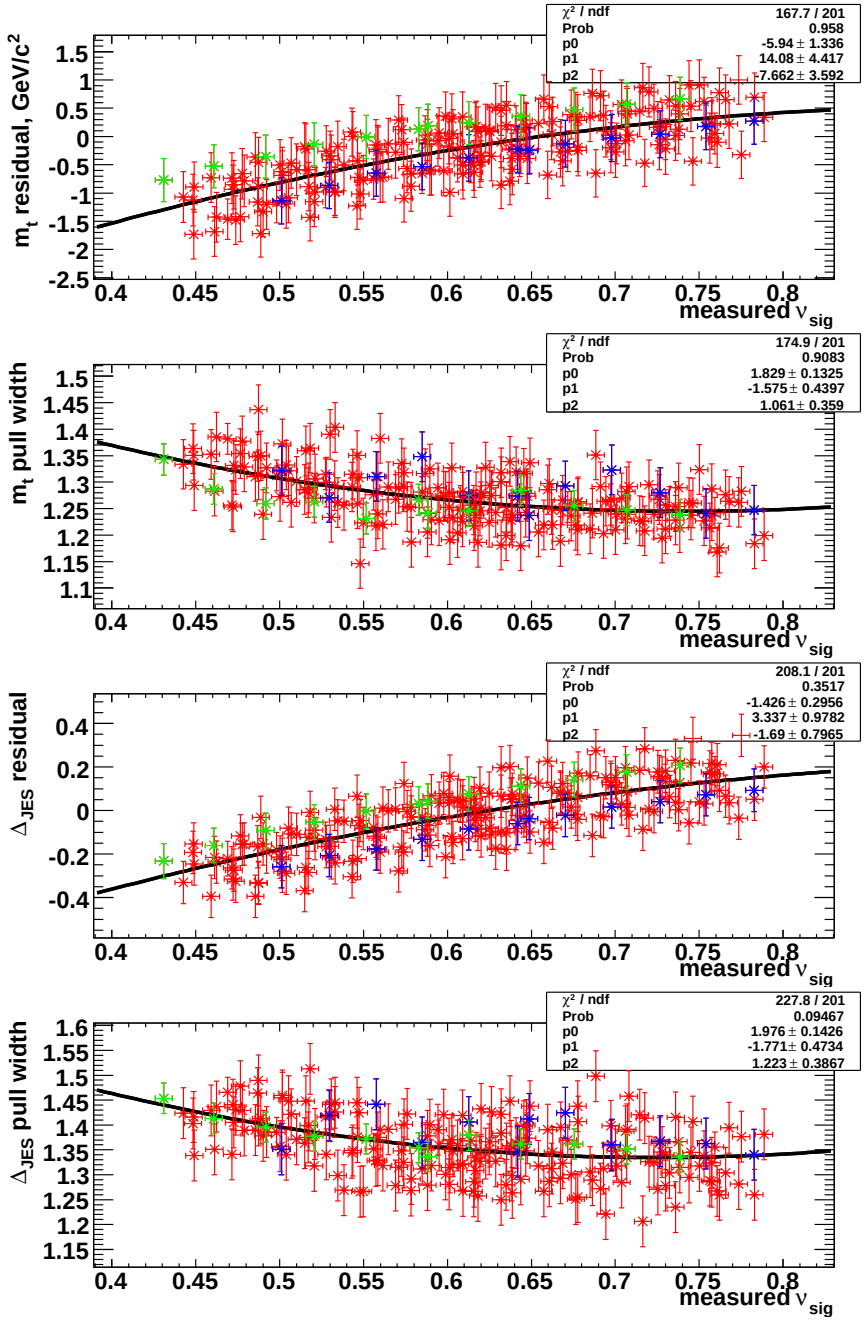

Figure 7.14: The dependence of the m_t and Δ_{JES} residuals and pull-widths on the measured ν_{sig}, and the fitted calibration functions. The blue and green points have input m_t of 165 and 185 GeV/c^2 respectively, while red points are used for the remaining 15 mass samples with $167.5 \leq m_t \leq 182.5$ GeV/c^2. All points are used together in the quadratic fits.

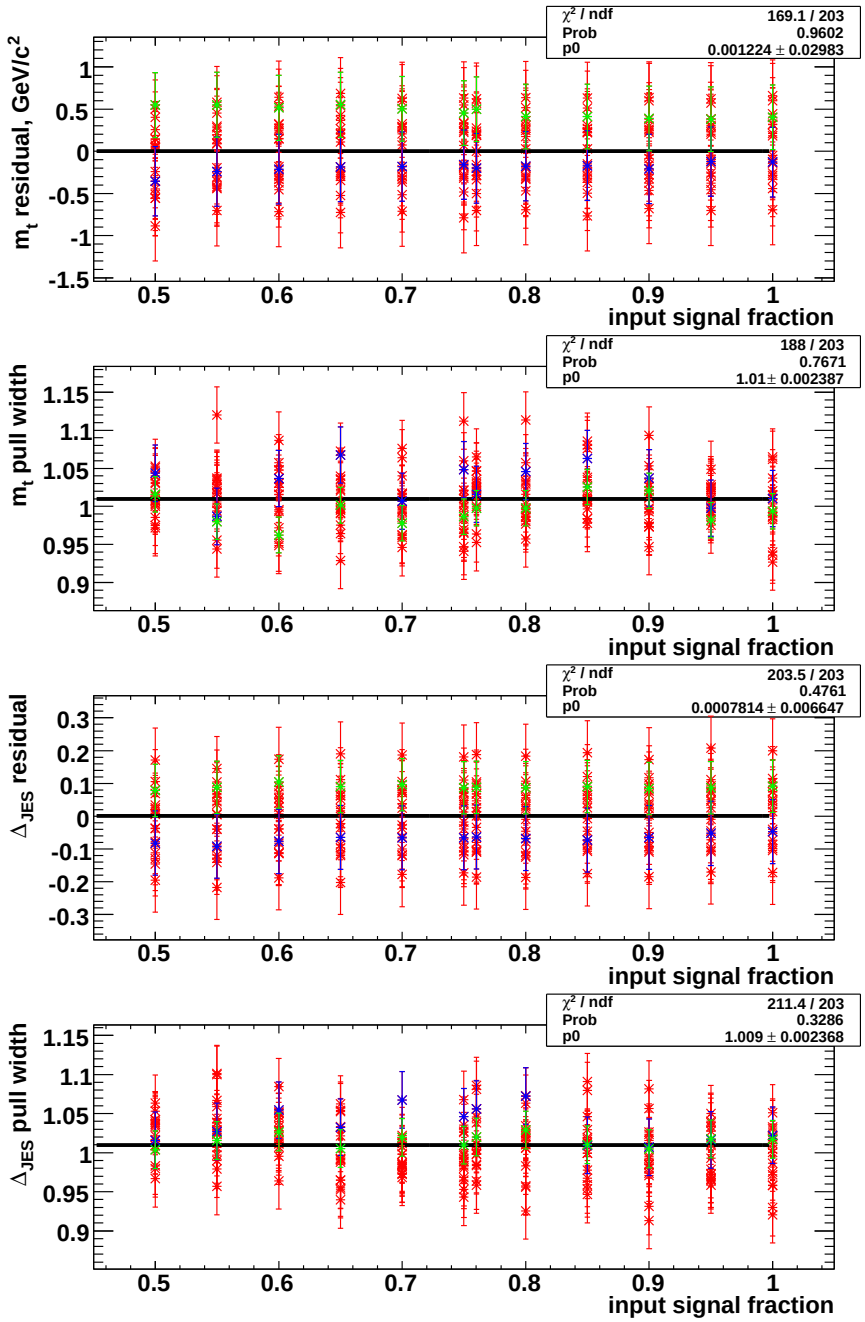

Figure 7.15: The dependence of the m_t and Δ_{JES} residuals and pull-widths on the input signal fraction, after ν_{sig} calibration. The blue and green points have input m_t of 165 and 185 GeV/c^2 respectively, while red points are used for the remaining 15 mass samples with $167.5 \leq m_t \leq 182.5$ GeV/c^2. The ν_{sig} calibration removes the dependence of the measurements on input signal fraction.

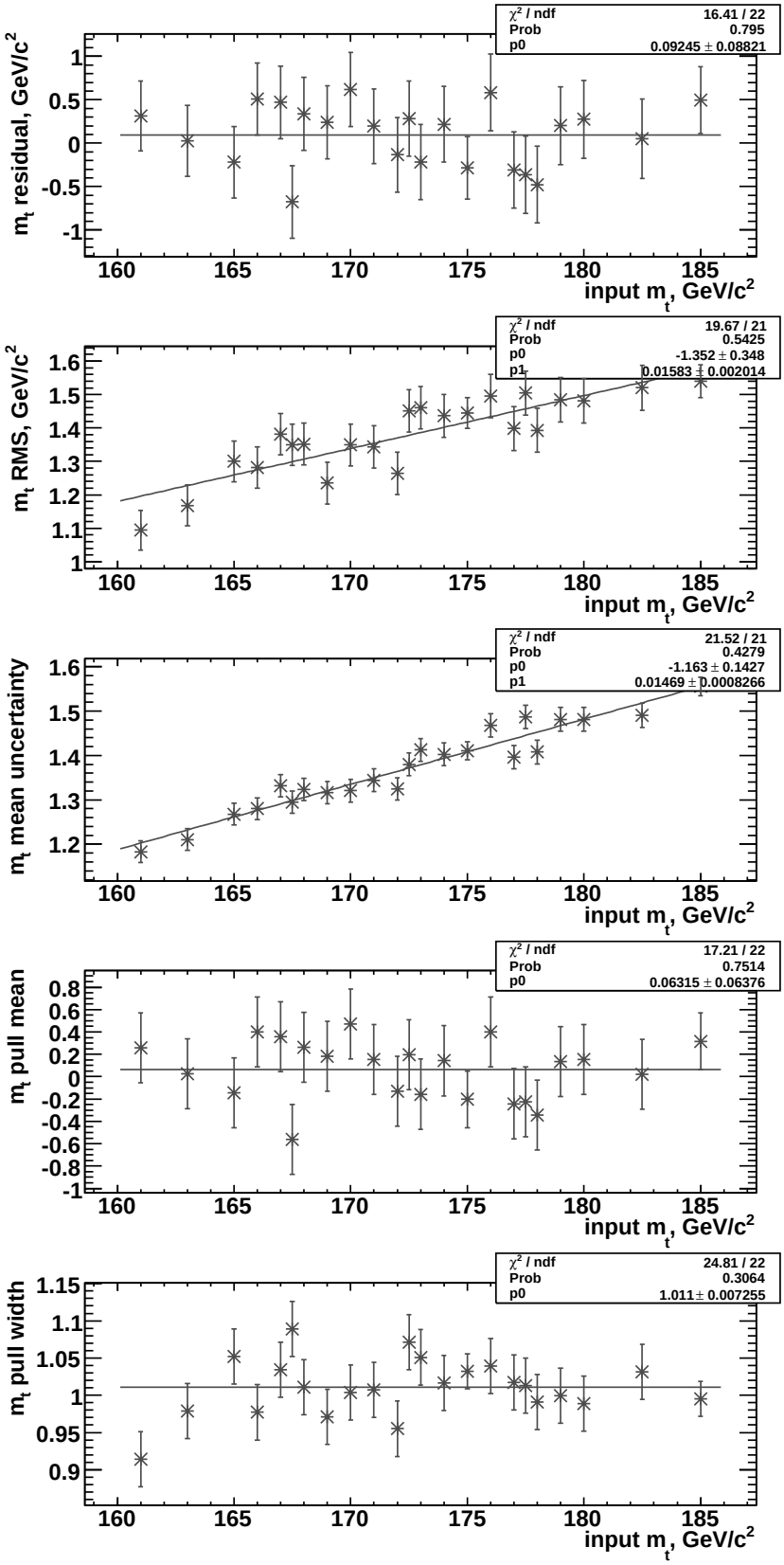

Figure 7.16: m_t and Δ_{JES} residuals, statistical uncertainties, pull means and pull widths, after measurement calibration. The residual is consistent with zero, the pull width is consistent with unity, and the calibrated uncertainty $\sigma_{m_t}^{\mathrm{final}}$ (third plot) is in agreement with the RMS of the ensemble m_t distribution (second plot).

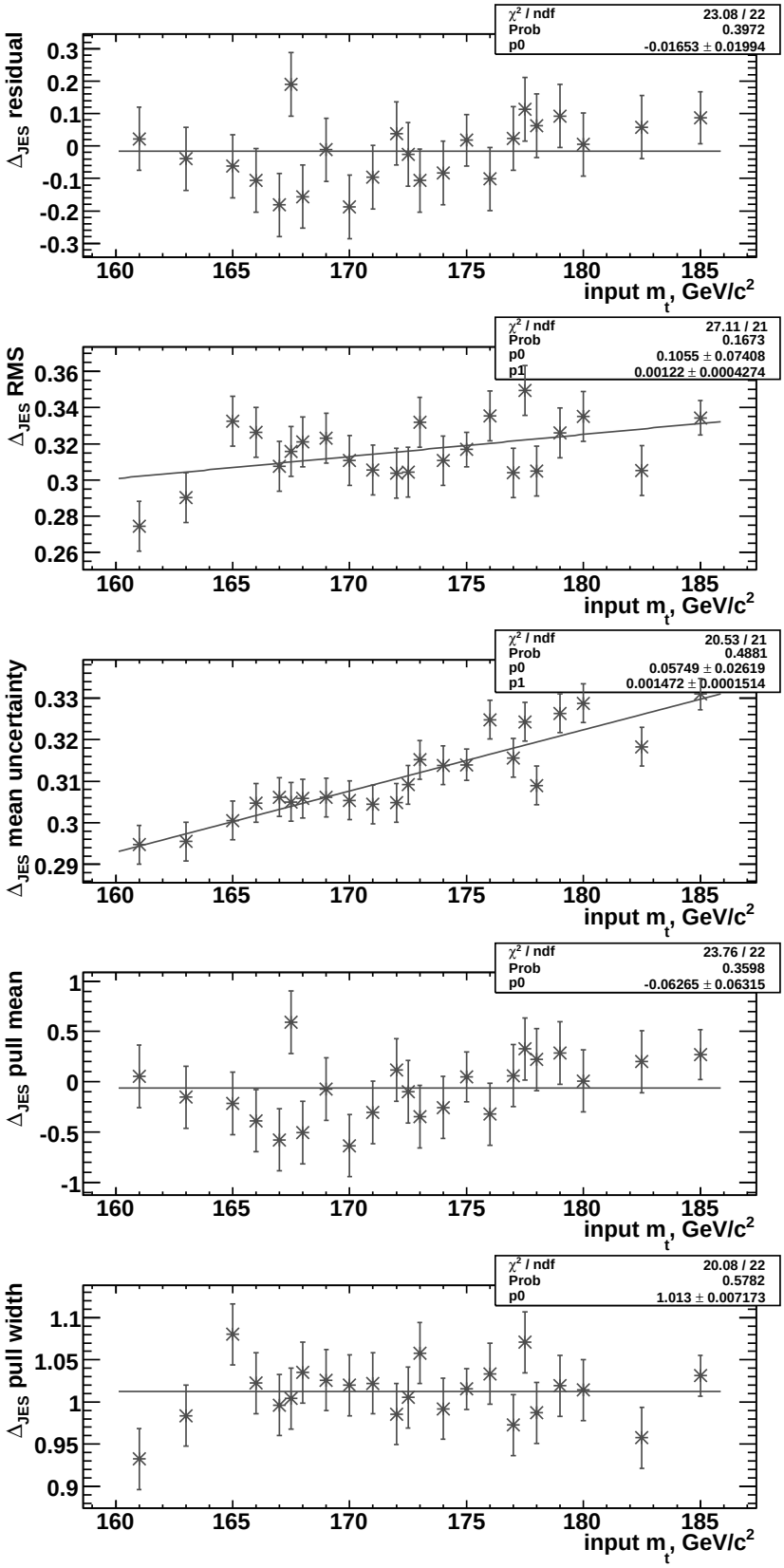

Figure 7.17: Δ_{JES} residuals, statistical uncertainties, pull means and pull widths, after measurement calibration. The residual is consistent with zero, the pull width is consistent with unity, and the calibrated uncertainty $\sigma^{\mathrm{final}}_{\Delta_{\mathrm{JES}}}$ (third plot) is in agreement with the RMS of the ensemble Δ_{JES} distribution (second plot).

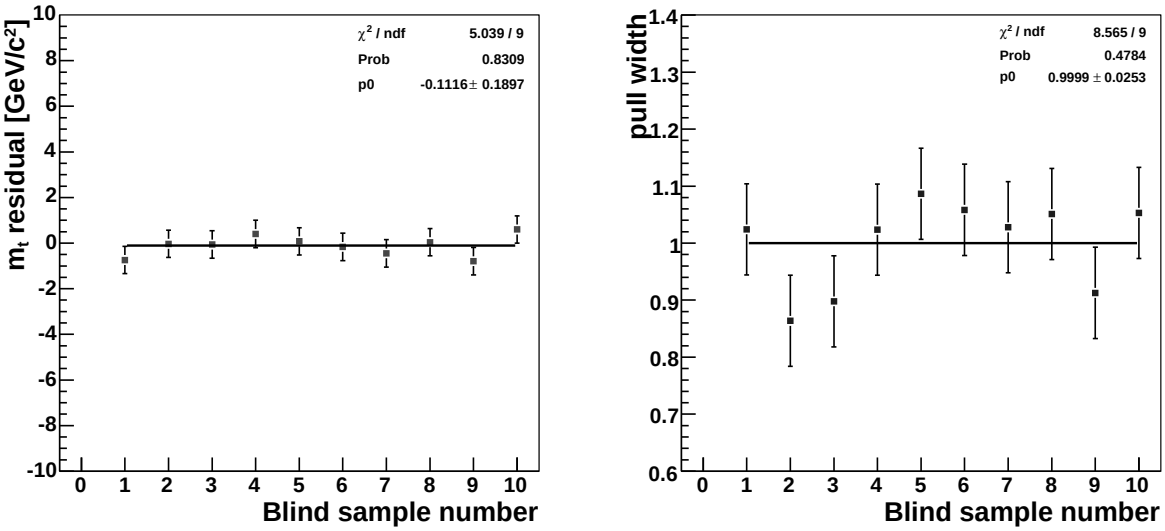

Figure 7.18: Results of the blind sample measurements. No bias is observed (the residual is consistent with zero), and the pull width is consistent with unity.

7.4 Summary

In an ideal measurement method, using perfectly representative p.d.f.s, calibration functions would be unnecessary. In this analysis, calibration functions are needed due to the approximations made in the construction of the event p.d.f.s. The choice of just two p.d.f.s (P_s and P_b) to represent all events is an inherent approximation, and approximations are also made in those two p.d.f.s (see Chapter 5).

When limiting events to those best described by the analysis p.d.f.s - the good signal events - the measurement response is observed to be unbiased with respect to m_t (Figure 7.3). If the experimental data could be restricted to events of this type, little calibration would be required. The unavoidable introduction into the sample of the bad signal events and the background events, which are not as well described by the analysis p.d.f.s, biases the measurement and necessitates the $\nu_{\rm sig}$-dependent calibration functions. Approximations in the Transfer Function (see Chapter 6) result in the $\Delta_{\rm JES}$-dependence of measurement response, which is corrected via the $\Delta_{\rm JES}$-dependent calibration functions.

Prior to looking at the experimental data, the dependability of the calibrated measurement method is verified by creating pseudoexperiments using ten samples of `PYTHIA` simulated $t\bar{t}$ events for which the true m_t is concealed, which are combined with the predicted 24% contribution of simulated background events. These "blind" pseudoexperiments thus exactly simulate the measurement procedure to be used for the experimental data. Once the results of the pseudoexperiments are obtained, they are compared with true values[5] of m_t, and the results are shown in Figure 7.18. The m_t residual is consistent with zero, and the pull width is consistent with unity.

[5]Known by the CDF top mass group convener.

Chapter 8

Systematic Uncertainties

There are a number of systematic uncertainties associated with this measurement, many as a result of assumptions made in event simulation, some related to detector effects, and others as a result of the implementation of the measurement. All of these uncertainties were estimated by following standard CDF top mass group prescriptions, and are assumed to be uncorrelated so they can be combined in quadrature to estimate the overall systematic uncertainty of the measurement.

The value of each "systematic" is typically estimated by comparing the measured m_t in two "shifted" pseudoexperiments in which the parameter of interest is shifted by $\pm 1\sigma$ about its assumed value. The systematic uncertainty Δm_t is then usually estimated as half the difference in measured m_t between the two samples. Since only the value of Δm_t is important, instead of the ensembles of pseudoexperiments described in Section 7.1, m_t is measured by combining all simulated events (in the correct proportions) into a single large pseudoexperiment. This does not affect the measured m_t, but significantly reduces computation time. All large pseudoexperiments are constructed using events generated with $m_t = 175$ GeV/c^2.

In some cases, the events in the shifted large pseudoexperiments are generated independently and the measured Δm_t can thus itself have a large statistical uncertainty. In such cases, the number of simulated events must be large enough that the statistical uncertainty on Δm_t is less than Δm_t itself. In other cases, where the same set of simulated events is used in the shifted samples but with different scale factors or weightings, the samples are strongly correlated and Δm_t can be accurately calculated using a sample of far fewer simulated events.

The calculation of each systematic is described in the following sections and the results are summarised in Table 8.1, where the overall systematic uncertainty is estimated to be 1.31 GeV/c^2. Note that systematic uncertainties are estimated only for the measured m_t, and not for the measured Δ_{JES}.

Systematics source	Expected contribution (GeV/c^2)
MC Generator	0.70
Residual JES	0.65
Colour Reconnection	0.56
b-jet energy	0.39
Background	0.45
ISR and FSR	0.23
Multiple Hadron Interactions	0.22
PDFs	0.13
Lepton Energy	0.12
Measurement Calibration	0.12
Total	1.31

Table 8.1: Contributions to the total expected systematic uncertainty.

8.1 Monte Carlo generator

The Monte Carlo (MC) generator systematic refers to the event generator used to create the simulated $t\bar{t}$ events. In this analysis, `PYTHIA 6.216` is used, and the simulated events are used to derive the Transfer Function and the mean acceptance function, and to calibrate the measurement method. It is hoped that `PYTHIA 6.216` provides an accurate simulation of the data events, but assumptions are made in the hadronisation models and the tuning of the underlying event.

`HERWIG 6.510` [47] is another $t\bar{t}$ leading-order event generator that is entirely independent of `PYTHIA`, using different matrix element calculation, radiation and hadronisation models, and event tuning. Unlike `PYTHIA 6.216`, it also simulates spin correlations.

It is not known whether the `PYTHIA` or `HERWIG` events more accurately simulate the $t\bar{t}$ events in data, and so the difference between the two can be taken as some measure of the general event simulation uncertainty. The systematic uncertainty Δm_t is therefore taken as the difference seen in measured mass when the simulated $t\bar{t}$ events are generated with `HERWIG 6.510` instead of `PYTHIA 6.216` (Table 8.2).

`PYTHIA` (GeV/c^2)	`HERWIG` (GeV/c^2)	Δm_t (GeV/c^2)
174.69 ± 0.23	173.98 ± 0.24	0.70 ± 0.33

Table 8.2: The MC generator systematic. The systematic uncertainty Δm_t is taken as the total difference between the mass measurements in the `PYTHIA` and `HERWIG` samples.

8.2 Residual Jet Energy Scale

Each Level i of the jet energy corrections of Section 3.2.4 has an associated systematic uncertainty, $\sigma^{\text{Level } i}$. The uncertainties for each Level are added in quadrature to calculate the combined jet energy scale uncertainty, σ_j (Section 4.3). In the parameterisation of the JES correction Δ_{JES} (Section 4.3), it is assumed that jet energies can be corrected by subtracting the quantity $\Delta_{\text{JES}} \cdot \sigma_j$. This is an approximation, since in reality each of the $\sigma^{\text{Level } i}$ might be independently shifted. The residual JES systematic can therefore be obtained by measuring the shift in measured m_t seen when shifting jet energies by $\pm\sigma^{\text{Level } i}$ for each of the six individual Levels (relative scale, multiple interactions, absolute scale, underlying event, out-of-cone, and splash-out).

To calculate the systematic uncertainty, thirteen samples (plus- and minus-shifted samples for each Level along with a nominal unshifted sample) of simulated events are therefore required. To minimise the statistical uncertainty of the final estimate, each sample is selected from the same set of 92264 `ttop75` events. The events are selected using the criteria of Section 3.3, resulting in approximately 2000 events in each sample. Each of the thirteen samples is then used to construct a single large pseudoexperiment. The background events in each large pseudoexperiment are taken from the largest single background source, $Wb\bar{b}$, with the jet energies altered in a similar manner. The systematic uncertainty $\delta_i m_t$ for each Level of jet energy corrections is then calculated by taking half the difference in measured m_t between the plus- and minus-shifted samples (Table 8.3). If half the difference between the nominal sample and either the plus- or the minus-shifted sample is larger, that is taken instead. The total systematic uncertainty Δm_t is calculated from the sum in quadrature of the six $\delta_i m_t$.

Level	$\delta_i m_t$ (GeV/c^2)
1 (Relative scale)	0.06
4 (Multiple interactions)	0.045
5 (Absolute scale)	0.51
6 (Underlying event)	0.03
7 (Out-of-cone)	0.40
8 (Splash-out)	0.07
Total Δm_t	0.65

Table 8.3: Components of the Residual JES systematic, which are summed in quadrature to calculate the total systematic Δm_t. The Level 4 component is given to an additional significant figure because it is used in the calculation of the Multiple Hadron Interactions systematic (Section 8.7).

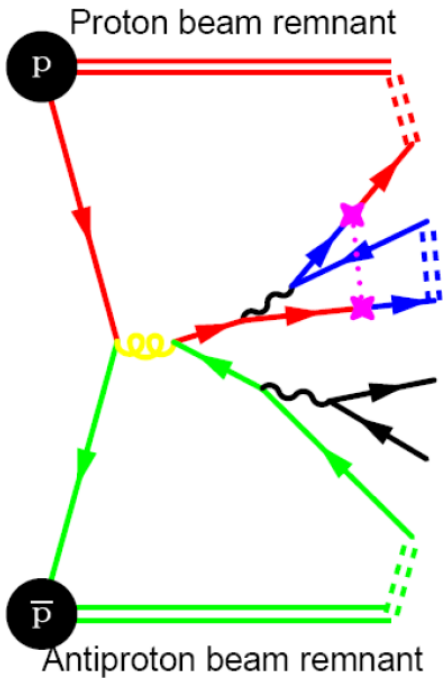

Figure 8.1: An example of colour reconnection. The colour flow of the hard interaction is not preserved. Note that this figure also shows the colour connections between the remnant proton and antiproton fragments and the top decay partons.

8.3 Colour Reconnection

In the early stages of top quark decay, the final-state quarks can be close enough (within the QCD distance of ~ 0.5 fm) that a QCD interaction can occur. Such an interaction is illustrated in Figure 8.1, where the b-quark from the initial top quark decay exchanges a gluon with one of the light quarks from the W boson decay. This cross-talk is called Colour Reconnection (CR), and distorts the event information. For example, the apparent W boson mass in events such as that illustrated in Figure 8.1 will not match the W boson pole mass.

Colour reconnection is thought to be strongly suppressed at the perturbative level [48], and mainly affects the quark fragmentation process. In `PYTHIA` events, it is therefore simulated phenomenologically as part of the fragmentation model, which is dependent on the tuning of the generator. To estimate the systematic uncertainty, two sets of `PYTHIA` $t\bar{t}$ events are used, one generated with "tune" `ACRpro` (with simulated CR) and the other with tune `Apro` (no simulated CR). The systematic uncertainty is taken as the total difference Δm_t between the mass measurements in the `ACRpro` and `Apro` event samples (Table 8.4).

`Apro` (GeV/c^2)	`ACRpro` (GeV/c^2)	Δm_t (GeV/c^2)
174.50 ± 0.23	175.05 ± 0.23	0.56 ± 0.33

Table 8.4: The colour reconnection systematic. The systematic uncertainty is taken as the total difference Δm_t between the mass measurements in the `ACRpro` and `Apro` event samples.

8.4 b-jet energy

Since the hadronisation process depends on quark flavour, and the jet energy corrections of Section 3.2.4 are primarily calculated for light jets, the Residual Jet Energy Scale systematic only accurately represents the uncertainty pertaining to the measurement of light jet energies. An additional b-jet energy systematic is therefore required, and is taken as the sum in quadrature of three components (Table 8.5).

First, the uncertainty of calorimeter response is different for b-jets and light jets. In simulated events, b-jets can be identified via matching to the known b-quark partons. To account for the systematic, two additional sets of simulated data are created by shifting the energies of such jets up and down by 1%. Since the variation in calorimeter response to b- and light-jets only corresponds to at most a 0.2% shift in b-jet energies [49], the uncertainty δm_t is taken as one tenth of the difference in measured mass between the two samples. The two samples of events are 100% correlated, so the statistical uncertainty on δm_t can be neglected. Note that this systematic also covers the assumption that the same Δ_{JES} applies to the two b-jets as to the two light-jets.

The second component of the b-jet systematic accounts for the uncertainty in the b- and c-quark semi-leptonic decay branching ratios (BRs), which are both varied by $\pm 1\sigma$. The change in branching ratios is simulated by reweighting[1] the contributions of events in the log-likelihood. The uncertainty δm_t is taken as half the difference between the two shifted m_t results.

Finally, the uncertainties in b fragmentation (the production of a B-hadron after a b-quark is produced) add an additional systematic uncertainty. Primarily, the uncertainty is in the fraction $\tilde{z}$ of the initial b-quark momentum that is carried by the B-hadron; this could affect m_t if it affected the measured b-jet energies. The fraction $\tilde{z}$ is described in `PYTHIA` by a distribution $f(\tilde{z})$ known as the Bowler parameterisation, with three free parameters. A change from the nominal `PYTHIA` Bowler parameters to those measured from fits to LEP and SLAC data [49] therefore provides a measure of systematic uncertainty. This is achieved by reweighting events based on the LEP and SLAC Bowler parameters, and the systematic uncertainty is taken as the largest change in m_t from nominal.

Systematic	δm_t (GeV/c^2)
Calorimeter response	0.13
Semi-leptonic BRs	0.14
Fragmentation	0.34
Total Δm_t	0.39

Table 8.5: Components of the b-jet energy systematic, which are summed in quadrature to calculate the total systematic Δm_t.

[1] The reweighting of events is achieved by multiplying the log of the event likelihood by the appropriate factor.

8.5 Background

The background systematic is taken as the sum in quadrature of three different systematic uncertainties (Table 8.6).

The first part reflects the uncertainty on the squared four-momentum transfer Q^2 (see Section 5.2.2) of the background events. Three large pseudoexperiments are created where the 24% background contribution is entirely composed of ALPGEN simulated $Wb\bar{b}$ events. One large pseudoexperiment has events generated with $Q^2 = m_W^2/4$, another has $Q^2 = 4m_W^2$, while the nominal sample has $Q^2 = m_W^2$. The systematic is taken as the largest shift in m_t from the nominal sample.

The next part accounts for the uncertainty in the overall signal fraction. Large pseudoexperiments are created where the input signal fraction is varied by $\pm 1\sigma$ from the "Method II For You" prediction of 76% (Table 4.2). Since the measurement is calibrated with respect to input signal fraction, this uncertainty is negligible. The systematic uncertainty associated with the calibration itself is considered as part of the Measurement Calibration Systematic (Section 8.10).

The final part accounts for uncertainties in background composition. Large pseudoexperiments are created where the 24% background contribution is taken entirely from each of the largest background sources: $Wb\bar{b}$, $Wc\bar{c}$, Wc, W+light flavours, and Non-W events. The systematic uncertainty is taken as the largest shift in m_t from the nominal result. The shifts seen for each background source are listed in Table 8.7, with the largest shift found in the $Wc\bar{c}$ sample. It is interesting to note that when the background sample is composed entirely of non-W events, the only large source of background events not well described by P_b (Section 5.3), a shift of just 0.02 GeV/c^2 is seen. The lack of a theoretical description of this type of event therefore does not seem to cause a bias in the measured m_t.

Systematic	δm_t (GeV/c^2)
Q^2	0.23
Signal fraction	0.03
Composition	0.39
Total Δm_t	0.45

Table 8.6: Components of the background systematic, which are summed in quadrature to calculate the total systematic Δm_t.

Background	Shift from nominal (GeV/c^2)
$Wb\bar{b}$	-0.30
$Wc\bar{c}$	-0.39
Wc	+0.27
W+light flavours	+0.04
Non-W	+0.02
Largest absolute shift	0.39

Table 8.7: The background composition systematic: the largest shift is seen when the background is composed entirely of $Wc\bar{c}$ events.

8.6 ISR and FSR

PYTHIA simulated $t\bar{t}$ samples can be generated with the amount of initial and final state radiation (ISR and FSR) increased and decreased by $\pm 1\sigma$ about its nominal value[2]. Since both the "more" and "less" samples give a larger measured m_t than the nominal sample, the systematic is taken as half the largest shift from nominal (Table 8.8).

More (GeV/c^2)	Less (GeV/c^2)	Nominal (GeV/c^2)	Δm_t (GeV/c^2)
175.15 ± 0.33	174.78 ± 0.32	174.69 ± 0.23	0.23 ± 0.20

Table 8.8: The ISR and FSR systematic. The systematic uncertainty Δm_t is taken as half of the largest difference among the mass measurements in the "More", "Less", and nominal samples.

8.7 Multiple Hadron Interactions

All of the PYTHIA $t\bar{t}$ simulated event samples have an average number of minimum bias interactions added on top of the hard scattering to account for the extra energy seen in the detector due to multiple $p\bar{p}$ interactions in a single bunch crossing (see the Level 4 "multiple interactions" jet energy correction, Section 3.2.4). However, since the MC samples were generated with a lower instantaneous luminosity than seen in recent data, the number of multiple interactions is underestimated, which could affect the measured m_t. The effect of multiple interactions can be related to the number of primary vertices N_p observed in the event (Figure 3.8); in the data sample, the mean N_p is $\bar{N}_p = 2.05$, compared with $\bar{N}_p = 1.50$ in the nominal PYTHIA sample. The systematic uncertainty is therefore estimated by re-weighting the PYTHIA events so that the proportion of events with each number of primary vertices matches that seen in data, and calculating the resulting difference in measured m_t. This effect is referred to as "known mismodelling".

[2]Since the effects are correlated, the amounts of ISR and FSR are simultaneously increased and decreased.

However, there is also the potential for "unknown mismodelling". Even with the correct number of primary vertices, the minimum bias events themselves could be mismodelled. In PYTHIA $t\bar{t}$ simulated events, the jet response does not have the expected dependence on number of primary vertices, and the remaining slope post-correction, ∼250 MeV/jet/vertex, is significantly larger than the typical Level 4 estimated JES uncertainty of ∼107 MeV/jet/vertex. This suggests that the Level 4 JES uncertainty, and thus the Level 4 component of the Residual JES uncertainty (Table 8.3), could be underestimated by a factor of the order 250/107 = 2.3. However, since the Level 4 component of the Residual JES uncertainty is evaluated using the nominal PYTHIA sample with $\bar{N}_p = 1.50$, and the Level 4 correction goes as roughly $(N_p - 1)$, the Level 4 component of the Residual JES uncertainty could be underestimated by a further factor of $(2.05-1)/(1.50-1) = 2.1$. Multiplying the Level 4 component of the Residual JES uncertainty (Table 8.3) by 2.3×2.1 therefore estimates the systematic uncertainty due to unknown mismodelling: $0.045\ \text{GeV/c}^2 \times 2.3 \times 2.1 = 0.22\ \text{GeV/c}^2$.

The overall systematic due to Multiple Hadron Interactions is taken as the largest of those due to known and unknown mismodelling (Table 8.9).

Systematic	δm_t (GeV/c^2)
Known mismodelling	0.21
Unknown mismodelling	0.22
Total Δm_t	0.22

Table 8.9: The Multiple Hadron Interactions systematic is taken as largest of the components due to known and unknown mismodelling.

8.8 PDF Uncertainties

The Parton Distribution Function (PDF) systematic uncertainty is taken as the sum in quadrature of three uncertainties (Table 8.10).

The first comes from the δm_t between two samples with different values for Λ_{QCD}, the energy scale for the running strong coupling constant: MRST72 (Λ_{QCD} = 228 MeV) and MRST75 (Λ_{QCD} = 300 MeV). The full difference is taken as the systematic uncertainty.

Next, events are reweighted to scale the percentage of gluon-gluon fusion events up from 5% (as seen in the LO PYTHIA samples) to 20% (conservatively taken 5% higher than the NLO gg fraction estimate of 15%). The full difference between these two results is taken as the systematic uncertainty.

Third, there are 20 free parameters used in the global fit that produces the CTEQ5L PDFs used in this analysis (Section 5.2.2). The 20×20 error matrix describing their uncertainties is diagonalised, determining 20 orthogonal eigenvector directions in the parameter space. Instead of generating a different set of simulated events for the $\pm 1\sigma$ shifts for each eigenvector, events in the nominal CTEQ5L sample are appropriately reweighted. The parton-level

information for each simulated event gives the partons i (e.g. u and $\bar{d}$) involved in the hard scattering, as well as their momentum fractions x^i_{Bj} and the Q^2 of the interaction. That information can be used to increase or decrease the weight of the event based on the ratio of the shifted and unshifted PDFs, $f_i^{\mathrm{shifted}}(x^i_{\mathrm{Bj}}, Q^2)/f_i(x^i_{\mathrm{Bj}}, Q^2)$. The sum in quadrature of all 20 $\pm 1\sigma$ half-differences in m_t is taken as the systematic.

Systematic	δm_t (GeV/c^2)
Λ_{QCD}	0.03
gg %	0.06
Eigenvectors	0.11
Total Δm_t	0.13

Table 8.10: Components of the PDFs systematic uncertainty, which are summed in quadrature to calculate the total systematic Δm_t.

8.9 Lepton Energy

Since electron and muon energies are measured by different detector components, the lepton energy systematic is taken as the sum in quadrature of the $\delta_i m_t$ from a $\pm 1\sigma$ shift in each of the lepton and muon energies.

To calculate the systematic uncertainty, five samples (plus- and minus-shifted samples for electrons and muons along with a nominal unshifted sample) of simulated events are therefore required. To minimise the statistical uncertainty of the final estimate, each sample is selected from the same set of 92264 `ttop75` events. The events are selected using the criteria of Section 3.3, resulting in approximately 2000 events in each sample. Each of the five samples is then used to construct a single large pseudoexperiment. The systematic uncertainties δm_t for electrons and muons are calculated by taking half the difference in measured m_t between the plus- and minus-shifted samples. If half the difference between the nominal sample and either the plus- or the minus-shifted sample is larger, that is taken instead. The total systematic uncertainty Δm_t is calculated from the sum in quadrature of the two δm_t (Table 8.11).

Lepton type	δm_t (GeV/c^2)
Electrons	0.10
Muons	0.07
Total Δm_t	0.12

Table 8.11: Components of the Lepton Energy systematic uncertainty, which are summed in quadrature to calculate the total systematic Δm_t.

8.10 Measurement Calibration Systematic

Two calibration functions are used in this analysis and each contributes an associated systematic uncertainty.

The Δ_{JES} calibration functions (Equations 7.3.1 and 7.3.2) are taken from linear fits to the mass and Δ_{JES} residuals as a function of input Δ_{JES}. The assumption is made that this Δ_{JES} dependence is independent of the top quark mass of the sample, and data from the 165, 175 and 185 GeV/c^2 m_t samples are combined to make the fit.

The Δ_{JES} calibration systematic is calculated by looking at how the measured m_t changes if only one of those three mass samples is used to calculate the calibration function. The results are shown in Table 8.12 and, conservatively, the largest difference is taken as the systematic. This accounts for two effects. First, it allows for the effect of any possible m_t-dependence of the calibration functions. Second, it accounts for the statistical uncertainty on the calibration functions as a result of the limited number of Monte Carlo events used in the fits. The uncertainty on the systematic is taken to be zero because the same events were used in the evaluation of each measured mass result (and so the uncertainties are 100% correlated). Note that the Δ_{JES} calibration systematic does not include the uncertainty on the constant term in the Δ_{JES} calibration of m_t (Equation 7.3.2) because that constant is re-calibrated in the subsequent ν_{sig} calibration, to which the systematic uncertainty is assigned.

Δ_{JES} calibration function fit sample m_t	Measured mass (GeV/c^2)
All m_t (nominal)	174.69
165 GeV/c^2	174.68
175 GeV/c^2	174.67
185 GeV/c^2	174.73
Biggest difference	0.06

Table 8.12: The Δ_{JES} calibration systematic is taken as largest difference in measured mass when using the four different calibration functions.

The ν_{sig} calibration of m_t (Equation 7.3.3) is taken from a quadratic fit to the mean m_t residual in pseudoexperiments created using different mean signal fractions. Since the samples at different mean signal fractions are 100% correlated (they all use the same MC events), the statistical uncertainty on the overall correction is the same as the statistical uncertainty on the mean residual at any given signal fraction. This is evaluated at the nominal signal fraction of 76%, and is found to be 0.10 GeV/c^2 (Figure 8.2).

There is also a possible systematic uncertainty related to the shape of function chosen for use in the ν_{sig} calibration. This effect is quantified from the change in measured m_t when the shape of the calibration function is varied, and is found to be negligible. The results of all calibration systematics are summarised in Table 8.13.

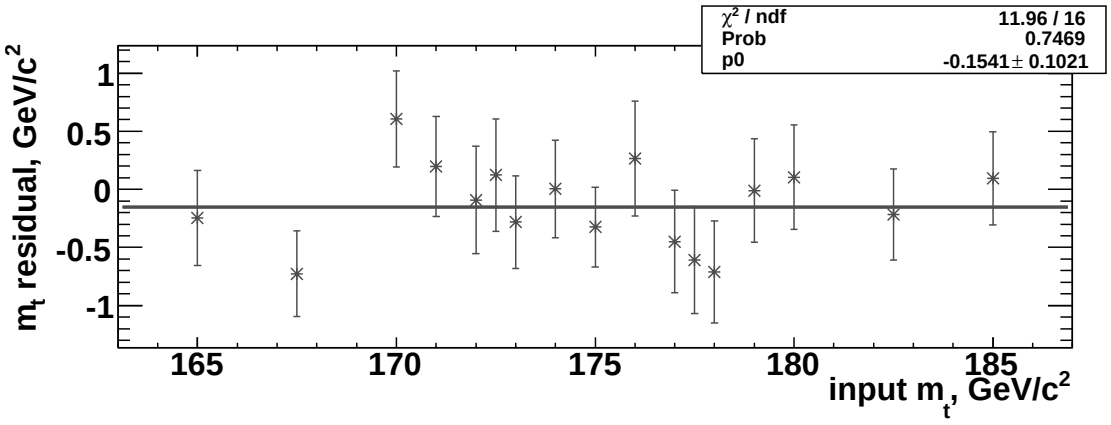

Figure 8.2: Measured m_t residual versus input m_t, after Δ_{JES} calibration. The uncertainty on the fitted mean m_t residual ("p0") is taken as the statistical uncertainty contribution to the ν_{sig} calibration systematic: 0.10 GeV/c^2.

Systematic source	Value (GeV/c^2)
ν_{sig} Fit function	0.02
ν_{sig} Statistical error	0.10
Δ_{JES} calibration	0.06
Overall Calibration Systematic	0.12

Table 8.13: The overall measurement calibration systematic is taken as the sum in quadrature of the Δ_{JES} and ν_{sig} calibration systematic uncertainties.

Chapter 9

Results

The measurement is made using the data sample of 578 events described in Section 4.1, representing approximately 3.2 fb^{-1} of integrated luminosity.

The profile log-likelihood in m_t and Δ_{JES}, after the maximisation with respect to ν_{sig} (Section 5.4), is shown in Figure 9.1. Note that the plot shows $\Delta \log \mathcal{L}$, the decrease in the profile log-likelihood from its maximum, meaning that the point of highest likelihood is at the minimum. Also shown are projections of the two-dimensional parabolic fit through the minimum grid point in m_t and Δ_{JES} (the blue lines), overlaying the projections of the $\Delta \log \mathcal{L}$ histogram. The resulting measurement, prior to application of the calibration functions, is $m_t^{\text{pre-cal}} = 171.25 \pm 1.07$ GeV/c^2, with $\Delta_{\text{JES}}^{\text{pre-cal}} = -0.06 \pm 0.23$ and $\nu_{\text{sig}} = 0.629 \pm 0.025$.

Applying the calibration functions 7.3.1, 7.3.2, 7.3.3 and 7.3.4, and including the overall systematic uncertainty of Chapter 8, the measurement becomes

$$\begin{aligned} m_t &= 172.38 \pm 1.36\,(\text{stat} + \Delta_{\text{JES}}) \pm 1.31\,(\text{syst})\ \text{GeV/c}^2 \\ m_t &= 172.38 \pm 1.88\,(\text{total})\ \text{GeV/c}^2, \end{aligned} \tag{9.0.1}$$

with $\Delta_{\text{JES}} = 0.34 \pm 0.31$. The central value and the contour ellipses corresponding to the 1, 2 and 3σ confidence intervals (68.3%, 95.4%, and 99.7% confidence levels) of the measurement are illustrated in Figure 9.2. The overall statistical uncertainty on the measured m_t, σ_{m_t}, is labelled "stat+Δ_{JES}" to reflect the fact it includes the uncertainty on m_t due to the statistical uncertainties on the measured Δ_{JES}, i.e. the uncertainty is given by entire width of the 1σ contour of Figure 9.2.

To check that the measurement of $\sigma_{m_t} = 1.36$ GeV/c^2 is reasonable, it is compared with the results seen in pseudoexperiments generated with $m_t = 172.5$ GeV/c^2 and $\Delta_{\text{JES}} = 0$ (Figure 9.3). The measured value is roughly in the middle of the distribution, with 40% of pseudoexperiments reporting a lower uncertainty.

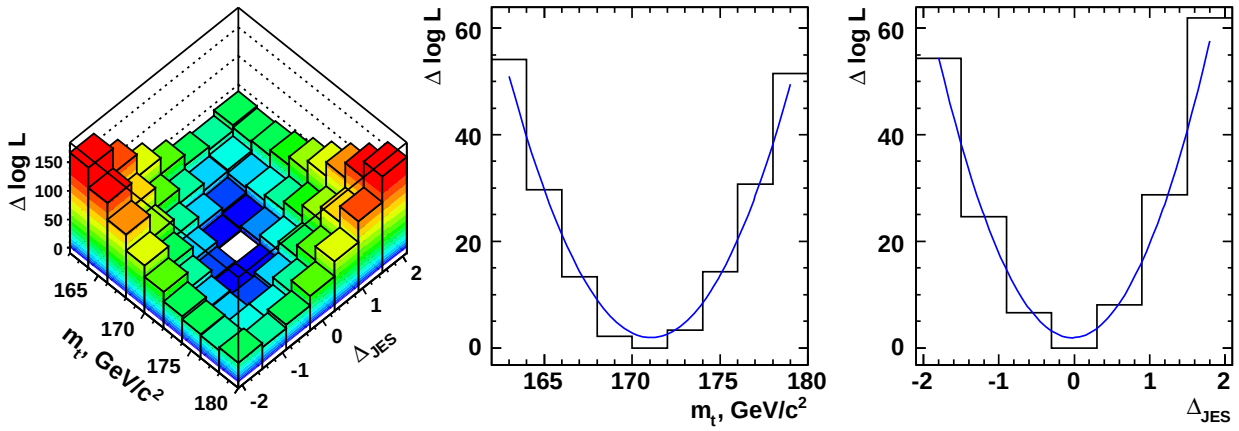

Figure 9.1: Left: The profile log-likelihood in m_t and Δ_{JES}, after the maximisation with respect to ν_{sig}. Right: the projections of the two-dimensional parabolic fit through the minimum grid point in m_t and Δ_{JES} (blue lines), overlaying the projections of the $\Delta \log \mathcal{L}$ histogram (in black).

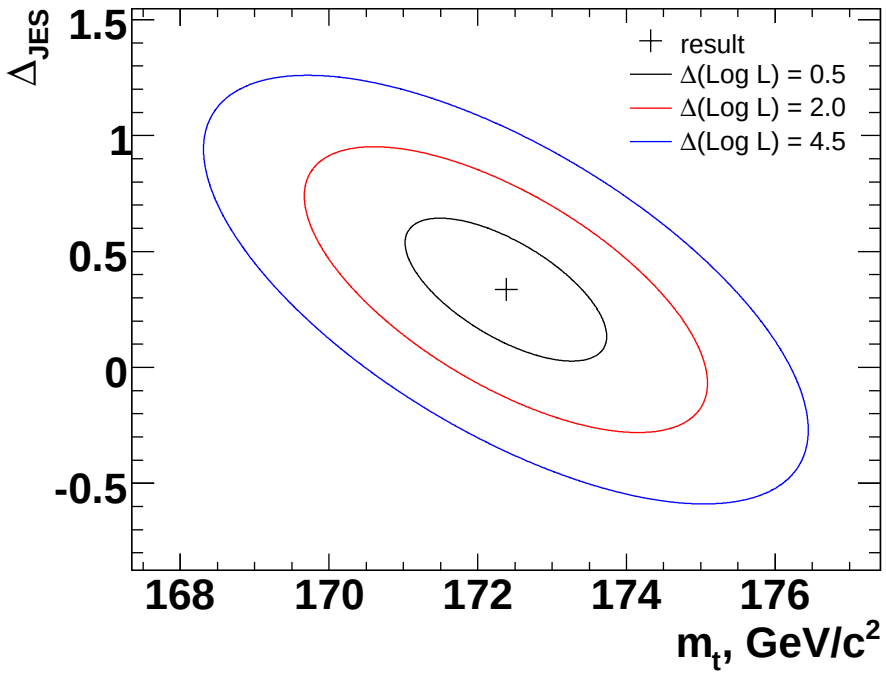

Figure 9.2: The measurement result and the contour ellipses of the parabolic fit corresponding to the 1, 2 and 3σ confidence intervals.

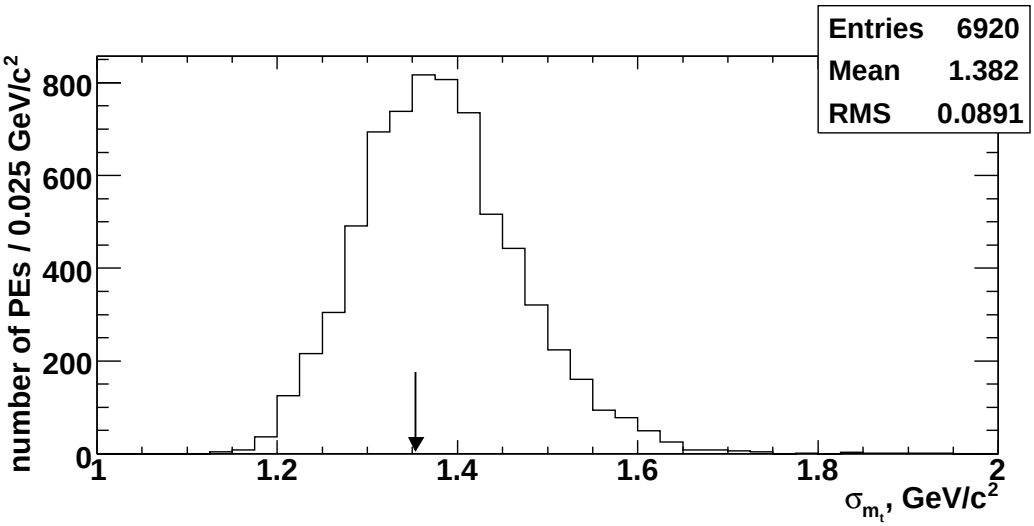

Figure 9.3: Distribution of σ_{m_t}, the expected statistical uncertainty on m_t, for pseudoexperiments generated with $m_t = 172.5$ GeV/c^2 and $\Delta_{\text{JES}} = 0$. The measured uncertainty of $\sigma_{m_t} = 1.36$ GeV/c^2 is indicated by an arrow; 40% of the pseudoexperiments have a lower uncertainty.

To check that the p.d.f.s P_s and P_b behaved as expected, their distributions in data are compared with those predicted from simulated events (Figures 9.4 and 9.5). No discrepancy is observed, confirming that the simulation of the $t\bar{t}$ and background processes is in good agreement with data, as was seen for the separate kinematic quantities in the validation plots of Section 4.5.

9.1 Subsamples

As a cross-check, it is interesting to check the consistency of the measurements made when using subsamples of events. Of the 578 total events, 250 had their primary lepton identified as a muon while the remaining 328 had an electron. The measurement results for these two subsamples are in good agreement, with $m_t^{\mu} = 172.7 \pm 2.3$ GeV/c^2 and $m_t^{e} = 172.2 \pm 1.7$ GeV/c^2, and are plotted in Figure 9.6. Note that the quoted errors are statistical only; the systematic uncertainties are not evaluated for subsamples.

Similarly, the measurement results for the 459 event subsample with 1 b-tag and the 117 event subsample with 2 b-tags are plotted in Figure 9.7. In this case, a discrepancy is observed, with the 2 b-tag sample giving a somewhat higher mass: $m_t^{2b} = 175.6 \pm 2.3$ GeV/c^2, compared with $m_t^{1b} = 171.1 \pm 1.7$ GeV/c^2. However, this is not a concern because separate calibration functions would be necessary to accurately make a measurement using subsamples divided by number of b-tags. Although the lower background fraction of the 2 b-tag sample should be partly compensated for by the ν_{sig}-dependence of the calibration functions, the different background composition in the 2-tag sample could alter the calibration functions. Furthermore, the calibration functions do not correct only for biases caused by background events, but also those caused by the bad signal events, and the combinatorics background from the incorrect jet-parton assignments in the average taken in the P_s for each event

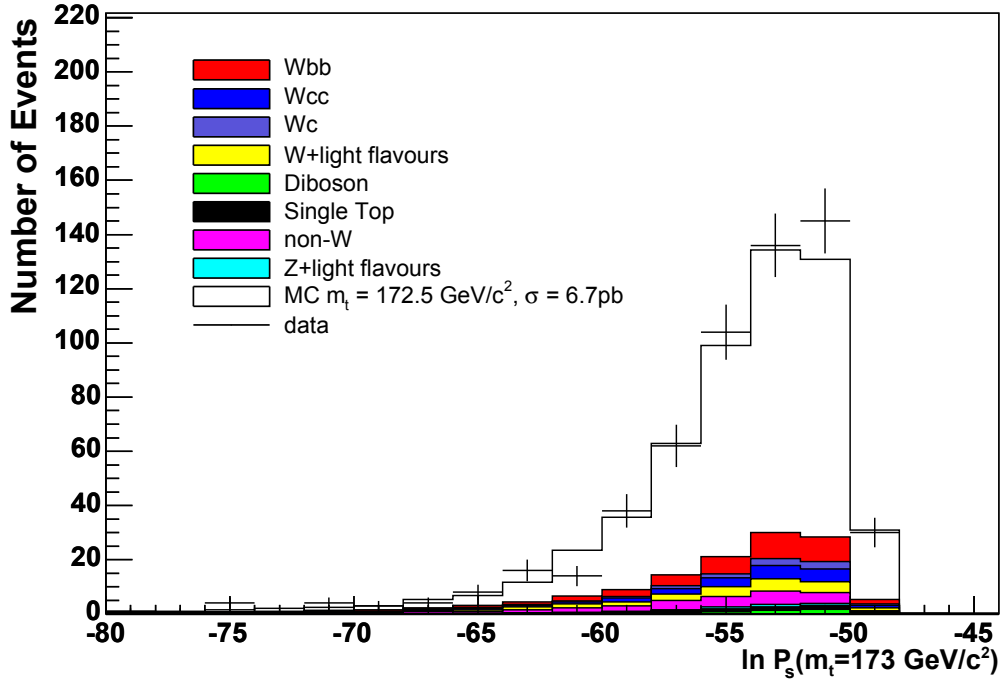

Figure 9.4: Comparison of the signal p.d.f. (P_s) distribution seen in data, with that expected from simulated events. P_s is taken at the grid point for $m_t = 173$ GeV/c^2 and $\Delta_{\mathrm{JES}} = 0$.

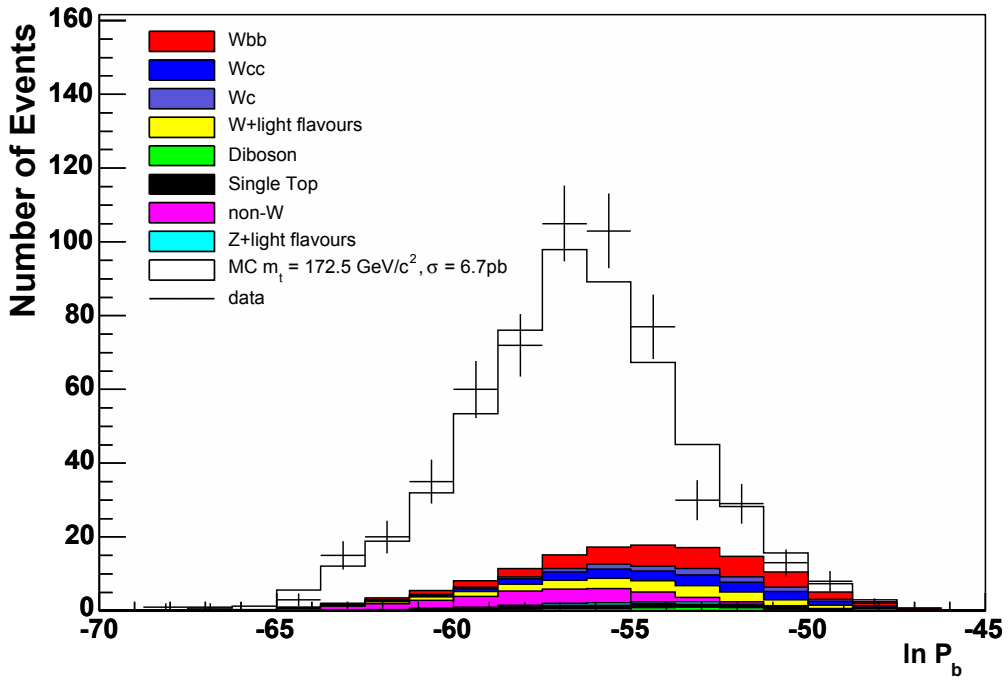

Figure 9.5: Comparison of the background p.d.f. (P_b) distribution seen in data, with that expected from simulated events.

(Section 7.2). Figures 7.3 and 7.4 demonstrate that the combinatorics background causes a reduction in the measured m_t, and Figure 7.5 suggests the same is true for the bad signal events. The 2 b-tag sample has less combinatorics background than the 1 b-tag sample (since there are only 2 possible jet-parton assignments in the average, instead of 6), and also fewer bad events (38%, compared with 43% in the 1-tag sample). The calibration functions therefore over-correct the measured m_t when used on a sample consisting only of 2-tag events, and also under-correct for a 1-tag sample. Separate calibration functions are therefore required for subsamples divided by the number of b-tags, and the calibration functions derived for this analysis are valid only for the combined sample.

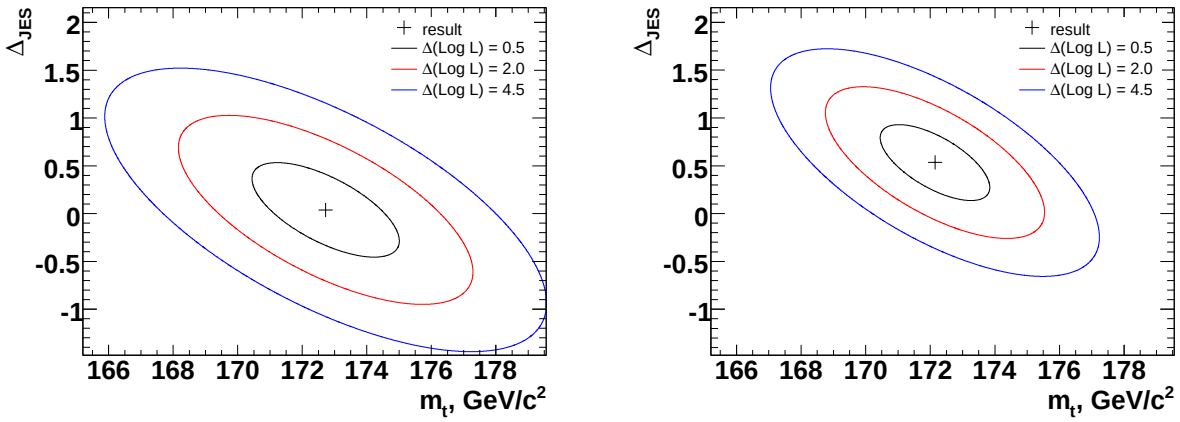

Figure 9.6: The measurement result using only electron events (left) and only muon events (right), and the contour ellipses of the parabolic fits corresponding to the 1, 2 and 3σ confidence intervals. The two results are consistent.

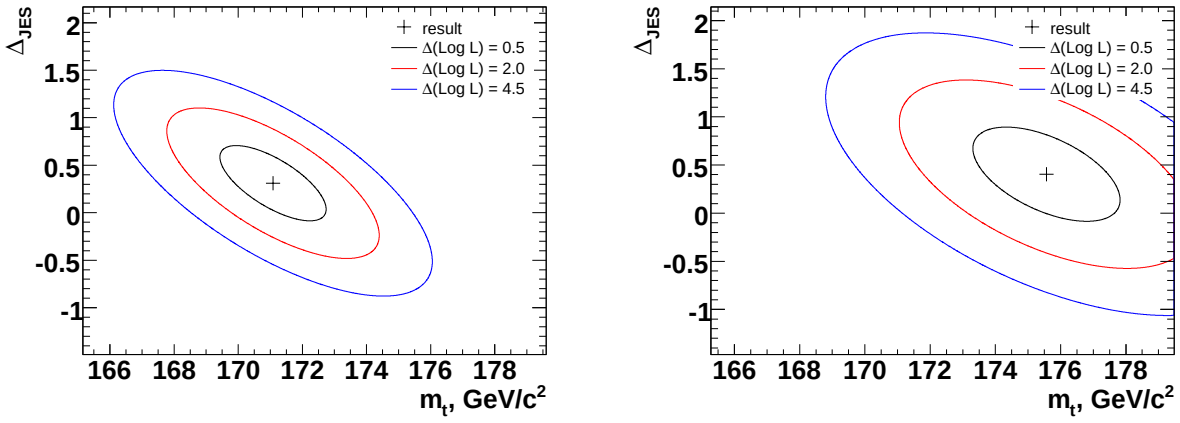

Figure 9.7: The measurement result using only 1 b-tag (left) and only 2 b-tag events (right), and the contour ellipses of the parabolic fits corresponding to the 1, 2 and 3σ confidence intervals. The results are not consistent because the measurement calibration is valid only for the combined sample.

Chapter 10

Conclusions

The top quark mass has been measured to a high precision, with the result (Equation 9.0.1)

$$m_t = 172.38 \pm 1.36\ (\text{stat} + \Delta_{\text{JES}}) \pm 1.31\ (\text{syst})\ \text{GeV/c}^2$$
$$m_t = 172.38 \pm 1.88\ (\text{total})\ \text{GeV/c}^2.$$

This result is in close agreement with the current (March 2009) world average m_t measurement of $m_t = 173.1 \pm 1.3$ GeV/c^2 [5] (Figure 10.1). Note that the world average does not incorporate the result of this measurement.

10.1 Higgs Boson Mass Constraints

As discussed in Section 1.2.3, constraints on the Standard Model Higgs boson mass, m_H, can be derived from m_t and other precision electroweak variables. The implications of the world average m_t on m_H have been derived, yielding $m_H = 87^{+35}_{-26}$ GeV/c^2, with 95% one-sided confidence level $m_H < 157$ GeV/c^2 (Figure 10.2).

The constraints imposed by using the top quark mass measured by this analysis, $m_t = 172.4 \pm 1.9$ GeV/c^2, instead of the world average, are found to be $m_H = 84^{+36}_{-26}$ GeV/c^2, with 95% one-sided confidence level $m_H < 156$ GeV/c^2 [50].

10.2 Improvements

The statistical and systematic contributions to the total top quark mass measurement uncertainty of this analysis are approximately equal. Since the statistical uncertainty decreases with the number of events in the data sample as $1/\sqrt{n}$, the systematic uncertainty can be expected to be the dominant uncertainty in future measurements.

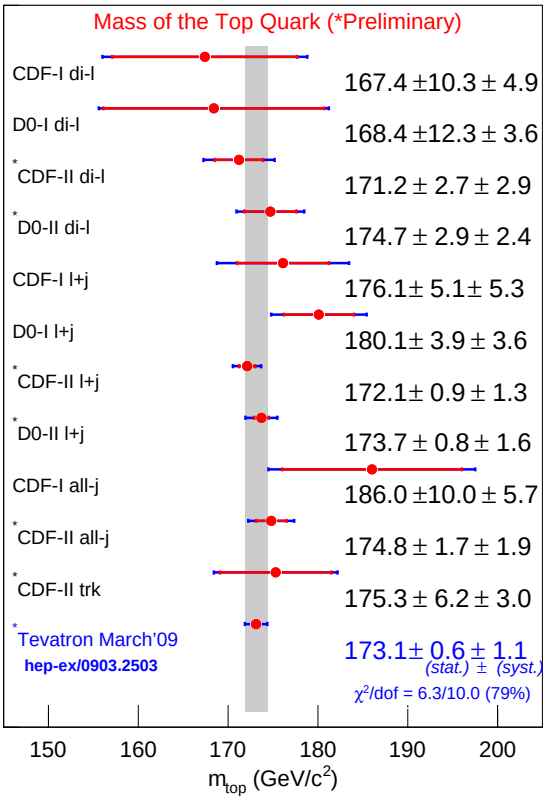

Figure 10.1: A summary of the most precise CDF and DØ m_t measurements in the various channels for Runs I and II, and the resulting world average m_t.

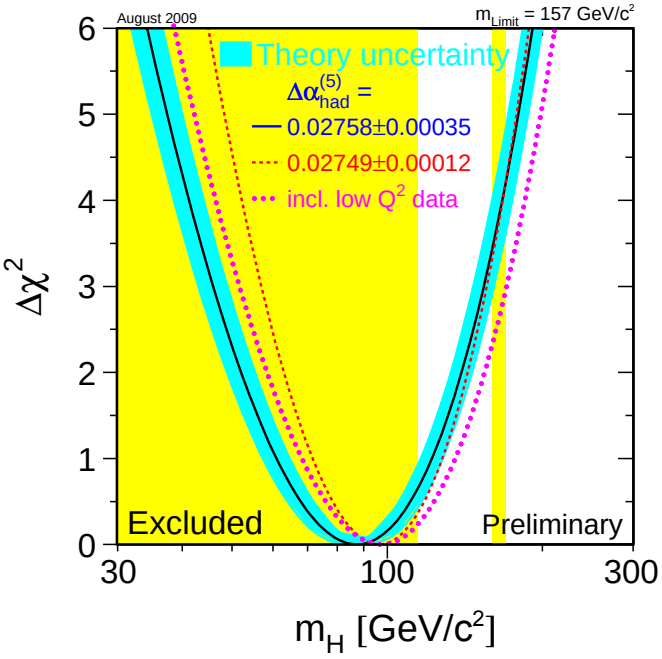

Figure 10.2: Constraints on the Standard Model Higgs boson mass, m_H, derived from the world average top quark mass, $m_t = 173.1 \pm 1.3$ GeV/c^2, and other precision electroweak variables.

While the systematic uncertainty estimates will not naturally decrease with n, the current estimates are in many cases conservative due to a lack of a full understanding or simulation of the effects. For example, the Monte Carlo generator systematic (Section 8.1), the largest single contribution to the systematic uncertainty, has no clearly defined $\pm 1\sigma$ shift, and partially incorporates some effects that are covered separately (for example, PDFs and ISR and FSR). The colour reconnection systematic, new to CDF analyses from Winter 2009 (Section 8.3), is almost certainly an overestimate, with the estimate coming from the difference between two extremes rather than the notional $\pm 1\sigma$.

The improvement of systematics is therefore a primary focus for future analyses. The CDF and DØ collaborations are making a joint effort to define a common way to evaluate their systematics, not only to avoid possible overlaps and double-counting but also to improve the knowledge of the effects, as well as studying possible sources thus far neglected.

There are also a number of avenues towards improving the physical description of the p.d.f.s used in this analysis, which could improve the statistical uncertainty of the measurement method as well as the accuracy of the systematic estimates. In the signal p.d.f. P_s, approximations such as the assumption of separable ATFs and ETFs (Chapter 6) might be revisited, and resolving the known issue with double-counting acceptance effects in the ETF could make the Δ_{JES} calibration unnecessary. Other effects, like possible transverse momentum of the $t\bar{t}$ system as a result of radiation or residual parton p_T, are not described at all and could be implemented.

In the background p.d.f. P_b, the integration procedure could be improved, allowing for a more precise evaluation of the p.d.f. as well as a calculation of the normalisation, eliminating the ν_{bkg} parameter. The assumption of no Δ_{JES}-dependence could also be revisited, possibly allowing for improved discrimination against background events. Furthermore, an additional p.d.f. describing non-W events might be considered, and perhaps also a p.d.f. to describe the "bad" signal events. The lack of a description of the bad signal events also causes a problem in the calculation of the $t\bar{t}$ mean acceptance function, which currently describes all generated $t\bar{t}$ events and not only the "good" subset, which are the only events truly described by P_s.

The statistical precision of the analysis might also be improved by tuning the event selection. Cuts dependent on P_s or P_b might be investigated. Furthermore, it is not necessarily ideal to analyse all of the data in a single large sample. The difference seen between the measurement results using the 1 and 2 b-tag samples (Figure 9.7) suggests that a separate calibration and measurement in those two cases might be an improvement. This makes sense given the significant differences in expected background composition, good event fraction, and combinatorics background in the two samples.

Appendix A

P_S: Solution of the change of variables

In Section 5.2.3, the integration variables $d\rho_{bh}$, $d\rho_{bl}$, $d\rho_{j2}$, and dp_ν^z are changed to m_{th}^2, m_{tl}^2, m_{Wh}^2, and m_{Wl}^2. The solution of this change of variables - that is, the solution for ρ_{bh}, ρ_{bl}, ρ_{j2}, and p_ν^z from known m_{Wh}^2, m_{Wl}^2, m_{th}^2, m_{tl}^2 - is described in this appendix. It is naturally decomposed into two parts: the hadronic side solution, and the leptonic side solution.

A.1 Hadronic Side

- New variables: m_{th}, m_{Wh}
- Original variables: ρ_{j_2}, ρ_{bh}
- Assumptions: $m_{j_1} = m_{j_2} = 0$, $m_{bh} = 4.8$ GeV/c^2

The momentum magnitude of the second light jet, ρ_{j_2}, can be easily calculated from the W boson mass-squared m_{Wh}^2 and the momentum magnitude of jet 1, ρ_{j_1}:

$$\begin{aligned} m_{W_h}^2 &= E_{W_h}^2 - \vec{p}_{W_h}^2 \\ m_{W_h}^2 &= (E_{j_1} + E_{j_2})^2 - (\vec{p}_{j_1} + \vec{p}_{j_2})^2 \\ m_{W_h}^2 &= m_{j_1}^2 + m_{j_2}^2 + 2\rho_{j_1}\rho_{j_2}(1 - \cos\theta_{12}) \\ \rho_{j_2} &\simeq \frac{m_{W_h}^2}{2\rho_{j_1}(1 - \cos\theta_{12})} \end{aligned} \tag{A.1.1}$$

The hadronic side top quark mass squared m_{th}^2 can be expressed in terms of the b-jet momentum magnitude ρ_{bh} as follows:

$$\begin{aligned} m_{th}^2 &= E_{th}^2 - \vec{p}_{th}^2 \\ m_{th}^2 &= m_{Wh}^2 + m_{bh}^2 + 2(E_{Wh}E_{bh} - \vec{p}_{Wh} \cdot \vec{p}_{bh}). \end{aligned}$$

Defining M as

$$M = \frac{(m_{th}^2 - m_{Wh}^2 - m_{bh}^2)}{2}, \tag{A.1.2}$$

this becomes

$$\begin{aligned} M &= E_{Wh}E_{bh} - \vec{p}_{Wh} \cdot \vec{p}_{bh} \\ M &= (\rho_{j_1} + \rho_{j_2})E_{bh} - (\rho_{j_1}\cos\theta_{b1} + \rho_{j_2}\cos\theta_{b2})\rho_{bh} \\ M &= PE_{bh} - D\rho_{bh}, \end{aligned}$$

where

$$P = \rho_{j_1} + \rho_{j_2} \tag{A.1.3}$$

$$D = (\rho_{j_1}\cos\theta_{b1} + \rho_{j_2}\cos\theta_{b2}). \tag{A.1.4}$$

Solving for ρ_{bh}:

$$\begin{aligned} M + D\rho_{bh} &= P\sqrt{(m_{bh}^2 + p_{bh}^2)} \\ M^2 + 2MD\rho_{bh} + D^2p_{bh}^2 &= P^2m_{bh}^2 + P^2p_{bh}^2 \\ 0 &= (D^2 - P^2)p_{bh}^2 + 2MD\rho_{bh} + M^2 - P^2m_{bh}^2 \\ \rho_{bh} &= \frac{-MD \pm P\sqrt{M^2 + m_{bh}^2(D^2 - P^2)}}{(D^2 - P^2)}, \end{aligned} \tag{A.1.5}$$

where only the negative square root corresponds to a physical solution since $P^2 > D^2$.

Finally, E_{bh} is defined as $E_{bh} = \sqrt{p_{bh}^2 + m_{bh}^2}$, where $m_{bh} = 4.8$ GeV/c^2, and the light jet energies are evaluated by assigning a light quark mass of 0.5 GeV/c^2:

$$E_{j_1} = \sqrt{\rho_{j_1} + 0.5^2} \tag{A.1.6}$$

$$E_{j_2} = \sqrt{\rho_{j_2} + 0.5^2}. \tag{A.1.7}$$

A.2 Leptonic Side

- New variables: m_{tl}, m_{Wl}
- Original variables: ρ_{bl}, p_ν^z
- Assumptions: $m_\ell = m_\nu = 0$, $m_{bh} = 4.8$ GeV/c^2

The solution to the leptonic side is more complicated because it also involves the calculation of the neutrino x and y momenta, which are constrained by setting the transverse momentum of the $t\bar{t}$ system equal to zero. A total of four variables must therefore be solved for, $\rho_{bl}, p_\nu^z, p_\nu^x$ and p_ν^y, requiring four independent equations in those variables.

Some short-hand symbols are defined to aid readability:

$$\hat{p_i} = \begin{pmatrix} \sin(\theta_i)\cos(\phi_i) \\ \sin(\theta_i)\sin(\phi_i) \\ \cos(\theta_i) \end{pmatrix} = \begin{pmatrix} sc_i \\ ss_i \\ c_i \end{pmatrix}.$$

Setting the overall transverse momentum equal to zero, the constants S_x and S_y are defined, relating known and unknown quantities:

$$\begin{aligned} 0 &= p^x_{j_1} + p^x_{j_2} + p^x_{bh} + p^x_{bl} + p^x_e + p^x_\nu \\ S_x &\equiv= p^x_{j_1} + p^x_{j_2} + p^x_{bh} + p^x_e \qquad \text{(A.2.1)} \\ S_x &= -p^x_{bl} - p^x_\nu \qquad \text{(A.2.2)} \end{aligned}$$

and similarly

$$S_y \equiv -p^y_{bl} - p^y_\nu. \qquad \text{(A.2.3)}$$

The first equation comes from combining Equations A.2.2 and A.2.3 and eliminating ρ_{bl}:

$$\rho_\nu((sc_\nu)(ss_{bl}) - (ss_\nu)(sc_{bl})) = S_y(sc_{bl}) - S_x(ss_{bl}) \equiv \alpha_0, \qquad \text{(A.2.4)}$$

where Equation A.2.4 defines α_0 and thus

$$\rho_\nu = \frac{\alpha_0}{(sc_\nu)(ss_{bl}) - (ss_\nu)(sc_{bl})}. \qquad \text{(A.2.5)}$$

The second equation comes from the similar solution for ρ_{bl}:

$$\rho_{bl} = \frac{S_y(sc_\nu) - S_x(ss_\nu)}{(sc_{bl})(ss_\nu) - (ss_{bl})(sc_\nu)}. \qquad \text{(A.2.6)}$$

The third equation comes from the leptonic side W boson mass:

$$\begin{aligned} m^2_{Wl} &= E^2_{Wl} - \vec{p}^{\,2}_{Wl} \\ m^2_{Wl} &= m^2_e + m^2_\nu + 2(E_eE_\nu - \vec{p_e}\cdot\vec{p}_\nu) \\ \frac{m^2_{Wl}}{2} &= E_eE_\nu - \vec{p_e}\cdot\vec{p}_\nu \\ \frac{m^2_{Wl}}{2} &= \rho_e\rho_\nu - \frac{p_{e_x}p_{\nu_x} + p_{e_y}p_{\nu_y} + p_{e_z}p_{\nu_z}}{\rho_e\rho_\nu}\rho_e\rho_\nu \\ \frac{m^2_{Wl}}{2\rho_e} &= \rho_\nu(1 - (sc_e)(sc_\nu) - (ss_e)(ss_\nu) - (c_e)(c_\nu)). \end{aligned}$$

Defining α_1 as:

$$\alpha_1 \equiv \frac{m^2_{Wl}}{2\alpha_0\rho_e}, \qquad \text{(A.2.7)}$$

the equation becomes

$$\frac{\alpha_1\alpha_0}{\rho_\nu} = (1 - (sc_e)(sc_\nu) - (ss_e)(ss_\nu) - (c_e)(c_\nu)), \tag{A.2.8}$$

where the variable c_ν is related to sc_ν and ss_ν by Equation A.2.9:

$$(sc_\nu)^2 + (ss_\nu)^2 + (c_\nu)^2 = 1. \tag{A.2.9}$$

The fourth equation comes from the leptonic side top quark mass, $m_{tl}^2 = E_{tl}^2 - \vec{p}_{tl}^2$, which will be returned to later.

The variable ρ_ν can now be eliminated by combining Equations A.2.5 and A.2.8:

$$\frac{\alpha_1\alpha_0}{\alpha_0}\left[(ss_{bl})(sc_\nu) - (sc_{bl})(ss_\nu)\right] = (1 - (sc_e)(sc_\nu) - (ss_e)(ss_\nu) - (c_e)(c_\nu))$$

$$\begin{aligned}
(c_e)(c_\nu) &= 1 - (sc_e)(sc_\nu) - \alpha_1(ss_{bl})(sc_\nu) - (ss_e)(ss_\nu) + \alpha_1(sc_{bl})(ss_\nu) \\
(c_e)(c_\nu) &= 1 - \left[(sc_e) + \alpha_1(ss_{bl})\right](sc_\nu) - \left[(ss_e) - \alpha_1(sc_{bl})\right](ss_\nu) \\
(c_\nu) &= \frac{1 - \beta_1(sc_\nu) - \beta_2(ss_\nu)}{(c_e)},
\end{aligned} \tag{A.2.10}$$

where β_1 and β_2 are defined as:

$$\beta_1 \equiv (sc_e) + \alpha_1(ss_{bl}) \tag{A.2.11}$$

$$\beta_2 \equiv (ss_e) - \alpha_1(sc_{bl}). \tag{A.2.12}$$

Substituting this expression into Equation A.2.9 gives an equation in just sc_ν and ss_ν:

$$(sc_\nu)^2 + (ss_\nu)^2 + \frac{1}{(c_e)^2}\left[1 - \beta_1(sc_\nu) - \beta_2(ss_\nu)\right]^2 = 1$$

$$\begin{aligned}
(c_e)^2(sc_\nu)^2 + (c_e)^2(ss_\nu)^2 + 1 - 2\beta_1(sc_\nu) - 2\beta_2(ss_\nu) + \\
2\beta_1\beta_2(sc_\nu)(ss_\nu) + \beta_1^2(sc_\nu)^2 + \beta_2^2(ss_\nu)^2 = (c_e)^2
\end{aligned}$$

$$\begin{aligned}
\left[(c_e)^2 + \beta_1^2\right](sc_\nu)^2 + 2\beta_1\beta_2(sc_\nu)(ss_\nu) + \left[(c_e)^2 + \beta_2^2\right](ss_\nu)^2 - \\
2\beta_1(sc_\nu) - 2\beta_2(ss_\nu) + \left[1 - (c_e)^2\right] = 0
\end{aligned}$$

$$a(sc_\nu)^2 + 2b(sc_\nu)(ss_\nu) + c(ss_\nu)^2 + 2d(sc_\nu) + 2e(ss_\nu) + f = 0, \tag{A.2.13}$$

where:

$$a = (c_e)^2 + \beta_1^2 \tag{A.2.14}$$

$$b = \beta_1\beta_2 \tag{A.2.15}$$

$$c = (c_e)^2 + \beta_2^2 \tag{A.2.16}$$

$$d = -\beta_1 \tag{A.2.17}$$

$$e = -\beta_2 \tag{A.2.18}$$

$$f = 1 - (c_e)^2. \tag{A.2.19}$$

Returning now to the equation for the top quark mass, with the intention of using it to eliminate ss_ν:

$$m_t^2 = E_t^2 - \vec{p}_t^2$$
$$m_t^2 = m_{Wl}^2 + m_{bl}^2 + 2(E_{Wl}E_{bl} - \vec{p}_{Wl} \cdot \vec{p}_{bl})$$

where the variable M_l is defined as in Equation A.1.2:

$$M_l = \frac{m_t^2 - m_{Wl}^2 - m_{bl}^2}{2}. \tag{A.2.20}$$

Now:

$$M_l = E_{Wl}E_{bl} - \vec{p}_{Wl} \cdot \vec{p}_{bl} \tag{A.2.21}$$
$$M_l = (E_e + E_\nu)E_{bl} - (\vec{p}_e + \vec{p}_\nu) \cdot \vec{p}_{bl} \tag{A.2.22}$$
$$M_l = \rho_e E_{bl} + \rho_\nu E_{bl} - \rho_e \rho_{bl} \cos\theta_{be} - \rho_{bl}\rho_\nu \left(\frac{\vec{p}_{bl} \cdot \vec{p}_\nu}{\rho_{bl}\rho_\nu} \right). \tag{A.2.23}$$

Now, making the assumption that $m_{bl} = 0$ so that $\rho_{bl} = E_{bl}$:

$$M_l = \rho_e \rho_{bl}(1 - \cos\theta_{be}) + \rho_{bl}\rho_\nu \left(1 - \frac{\vec{p}_{bl} \cdot \vec{p}_\nu}{\rho_{bl}\rho_\nu} \right) \tag{A.2.24}$$
$$\frac{M_l}{\rho_{bl}} = d_0 + \rho_\nu \left[1 - (sc_\nu)(sc_{bl}) - (ss_\nu)(ss_{bl}) - (c_\nu)(c_{bl}) \right], \tag{A.2.25}$$

where d_0 is defined as:

$$d_0 \equiv \rho_e(1 - \cos\theta_{be}). \tag{A.2.26}$$

Substituting Equation A.2.5 for ρ_ν and Equation A.2.10 for c_ν gives:

$$\frac{M_l}{\rho_{bl}} = d_0 + \frac{\alpha_0}{(sc_\nu)(ss_{bl}) - (ss_\nu)(sc_{bl})} \times$$

$$\left[1 - (sc_\nu)(sc_{bl}) - (ss_\nu)(ss_{bl}) - \frac{1 - \beta_1(sc_\nu) - \beta_2(ss_\nu)}{(c_e)}(c_{bl}) \right]$$

$$\left[(sc_\nu)(ss_{bl}) - (ss_\nu)(sc_{bl}) \right] \frac{M_l}{\rho_{bl}} =$$

$$(ss_{bl})(sc_\nu)d_0 - (sc_{bl})(ss_\nu)d_0 + \alpha_0 - \alpha_0(sc_{bl})(sc_\nu) - \alpha_0(ss_{bl})(ss_\nu) -$$
$$\frac{\alpha_0}{(c_e)}(c_{bl}) + \frac{\alpha_0\beta_1(c_{bl})}{(c_e)}(sc_\nu) + \frac{\alpha_0\beta_2(c_{bl})}{(c_e)}(ss_\nu)$$

$$\left[(sc_\nu)(ss_{bl}) - (ss_\nu)(sc_{bl}) \right] \frac{M_l}{\rho_{bl}} =$$

$$\alpha_0(1-\frac{(c_{bl})}{(c_e)})+\left[d_0(ss_{bl})-\alpha_0(sc_{bl})+\frac{\alpha_0\beta_1(c_{bl})}{(c_e)}\right](sc_\nu)+$$
$$\left[-d_0(sc_{bl})-\alpha_0(ss_{bl})+\frac{\alpha_0\beta_2(c_{bl})}{(c_e)}\right](ss_\nu)$$

$$\frac{M_l}{\rho_{bl}}=\frac{\gamma_0+\gamma_1(sc_\nu)+\gamma_2(ss_\nu)}{[(sc_\nu)(ss_{bl})-(ss_\nu)(sc_{bl})]}, \tag{A.2.27}$$

where:

$$\gamma_0=\alpha_0(1-\frac{(c_{bl})}{(c_e)}) \tag{A.2.28}$$
$$\gamma_1=\left[d_0(ss_{bl})-\alpha_0(sc_{bl})+\frac{\alpha_0\beta_1(c_{bl})}{(c_e)}\right] \tag{A.2.29}$$
$$\gamma_2=\left[-d_0(sc_{bl})-\alpha_0(ss_{bl})+\frac{\alpha_0\beta_2(c_{bl})}{(c_e)}\right]. \tag{A.2.30}$$

Substituting Equation A.2.6 into Equation A.2.27 to eliminate ρ_{bl} gives:

$$\frac{-M_l(sc_{bl})(ss_\nu)+M_l(ss_{bl})(sc_\nu)}{S_x(ss_\nu)-S_y(sc_\nu)}=\frac{\gamma_0+\gamma_1(sc_\nu)+\gamma_2(ss_\nu)}{(sc_\nu)(ss_{bl})-(ss_\nu)(sc_{bl})}, \tag{A.2.31}$$

which can be expressed as

$$A(sc_\nu)^2+2B(sc_\nu)(ss_\nu)+C(ss_\nu)^2+2D_2(sc_\nu)+2E(ss_\nu)=0, \tag{A.2.32}$$

where:

$$A=M_l(ss_{bl})^2+\gamma_1S_y \tag{A.2.33}$$
$$B=-M_l(ss_{bl})(sc_{bl})-\frac{1}{2}\gamma_1S_x+\frac{1}{2}\gamma_2S_y \tag{A.2.34}$$
$$C=M_l(sc_{bl})^2-\gamma_2S_x \tag{A.2.35}$$
$$D_2=\frac{1}{2}\gamma_0S_y \tag{A.2.36}$$
$$E=-\frac{1}{2}\gamma_0S_x. \tag{A.2.37}$$

Equations A.2.13 and A.2.32 can be solved for ss_ν. Multiplying Equation A.2.32 by the variable $cdiv \equiv c/C$ and subtracting the two equations gives:

$$a'(sc_\nu)^2+2b'(sc_\nu)(ss_\nu)+2d'(sc_\nu)+2e'(ss_\nu)+f=0,$$

where:

$$a'=a-(cdiv)A \tag{A.2.38}$$
$$b'=b-(cdiv)B \tag{A.2.39}$$
$$d'=d-(cdiv)D_2 \tag{A.2.40}$$
$$e'=e-(cdiv)E. \tag{A.2.41}$$

Solving for ss_ν gives:

$$ss_\nu = \frac{-f - a'(sc_\nu)^2 - 2d'(sc_\nu)}{2b'(sc_\nu) + 2e'}. \tag{A.2.42}$$

Thus can now be substituted back into Equation A.2.13 to solve for sc_ν. The square of ss_ν is written as

$$(ss_\nu)^2 = \frac{a'^2(sc_\nu)^4 + 4d'a'(sc_\nu)^3 + (2a'f + 4d'^2)(sc_\nu)^2 + 4d'f(sc_\nu) + f^2}{4\left[b'(sc_\nu) + e'\right]^2}$$
$$(ss_\nu)^2 = \frac{a'^2(sc_\nu)^4 + G_3(sc_\nu)^3 + G_2(sc_\nu)^2 + G_1(sc_\nu) + f^2}{4\left[b'(sc_\nu) + e'\right]^2}, \tag{A.2.43}$$

where:

$$G_3 = 4d'a' \tag{A.2.44}$$
$$G_2 = 2a'f + 4d'^2 \tag{A.2.45}$$
$$G_1 = 4d'f. \tag{A.2.46}$$

For convenience, ss_ν is rewritten with a similar denominator to $(ss_\nu)^2$:

$$ss_\nu = \frac{-a'(sc_\nu)^2 - 2d'(sc_\nu) - f}{2\left[b'(sc_\nu) + e'\right]} \times \frac{b'(sc_\nu) + e'}{b'(sc_\nu) + e'}$$
$$ss_\nu = \frac{-a'b'(sc_\nu)^3 - 2b'd'(sc_\nu)^2 - fb'(sc_\nu) - a'e'(sc_\nu)^2 - 2d'e'(sc_\nu) - fe'}{2\left[b'(sc_\nu) + e'\right]^2}$$
$$ss_\nu = \frac{\Lambda_3(sc_\nu)^3 + \Lambda_2(sc_\nu)^2 + \Lambda_1(sc_\nu) + \Lambda_0}{2\left[b'(sc_\nu) + e'\right]^2}, \tag{A.2.47}$$

where

$$\Lambda_3 = -a'b' \tag{A.2.48}$$
$$\Lambda_2 = -a'e' - 2b'd' \tag{A.2.49}$$
$$\Lambda_1 = -2d'e' - fb' \tag{A.2.50}$$
$$\Lambda_0 = -fe'. \tag{A.2.51}$$

With ss_ν and $(ss_\nu)^2$ defined in terms of sc_ν, they can be substituted into Equation A.2.13:

$$c(ss_\nu)^2 + 2b(sc_\nu)(ss_\nu) + 2e(ss_\nu) = -f - a(sc_\nu)^2 - 2d(sc_\nu).$$

Collecting like terms:

$$\beta_4(sc_\nu)^4 + \beta_3(sc_\nu)^3 + \beta_2(sc_\nu)^2 + \beta_1(sc_\nu) + \beta_0 = 0, \tag{A.2.52}$$

where:

$$\beta_4 = a'^2c + 4ab'^2 + 4b\Lambda_3 \tag{A.2.53}$$
$$\beta_3 = 8ab'e' + 8db'^2 + cG_3 + 4b\Lambda_2 + 4e\Lambda_3 \tag{A.2.54}$$
$$\beta_2 = 4ae'^2 + 16db'e' + 4b'^2f + cG_2 + 4b\Lambda_1 + 4e\Lambda_2 \tag{A.2.55}$$
$$\beta_1 = 8de'^2 + 8b'e'f + 4e\Lambda_1 + 4b\Lambda_0 + cG_1 \tag{A.2.56}$$
$$\beta_0 = cf^2 + 4e\Lambda_0 + 4fe'^2. \tag{A.2.57}$$

Solving for the four roots of Equation A.2.52 gives 4 possible solutions for sc_ν, of which up to 2 are real. These solutions can be substituted into Equations A.2.42 and A.2.10 to find ss_ν and then c_ν, which can then be used in Equations A.2.5 and A.2.6 to find ρ_ν and ρ_{bl}.

The values of the real solutions for ρ_{bl} give an idea of the validity of the $\rho_{bl} = E_{bl}$ approximation in Equation A.2.24. The approximation is worse for low ρ_{bl}, and always causes the solutions for ρ_{bl} to be too high (since $E_{bl} > \rho_{bl}$). The effect on the solutions can be seen by going back to the equation in which the approximation was first made (Equation A.2.23), and replacing E_{bl} not with ρ_{bl} but with $\rho_{bl}(1+\delta)$:

$$M_l = \rho_e E_{bl} + \rho_\nu E_{bl} - \rho_e \rho_{bl} \cos\theta_{be} - \rho_{bl}\rho_\nu \left(\frac{\vec{p}_{bl} \cdot \vec{p}_\nu}{\rho_{bl}\rho_\nu} \right) \tag{A.2.58}$$

$$M_l = \rho_e \rho_{bl}(1+\delta) + \rho_\nu \rho_{bl}(1+\delta) - \rho_e \rho_{bl} \cos\theta_{be} - \rho_{bl}\rho_\nu \left(\frac{\vec{p}_{bl} \cdot \vec{p}_\nu}{\rho_{bl}\rho_\nu} \right) \tag{A.2.59}$$

$$M_l = \rho_e \rho_{bl}(1+\delta-\cos\theta_{be}) + \rho_{bl}\rho_\nu \left(1 + \delta - \frac{\vec{p}_{bl} \cdot \vec{p}_\nu}{\rho_{bl}\rho_\nu} \right)$$

$$\frac{M_l}{\rho_{bl}} = \rho_e(1+\delta-\cos\theta_{be}) + \rho_\nu \left[1 + \delta - (sc_\nu)(sc_{bl}) - (ss_\nu)(ss_{bl}) - (c_\nu)(c_{bl}) \right]. \tag{A.2.60}$$

The remainder of the solution is then the same, with the exception of the redefinition of d_0 and γ_0 as follows:

$$d_0 \to \rho_e(1+\delta-\cos\theta_{be}) \tag{A.2.61}$$

$$\gamma_0 \to \alpha_0(1+\delta-\frac{(c_{bl})}{(c_e)}) \tag{A.2.62}$$

Setting $\delta = 0$ gives the original solutions. Since the overall approximation is small (i.e. δ is small), it is known that the true solutions are close to the approximate solutions. A lower limit on δ can therefore be set by taking the larger of the two real ρ_{bl} solutions:

$$\delta = \frac{\sqrt{\rho^2_{\text{larger}} - m^2_{bl}}}{\rho_{\text{larger}}} - 1 \tag{A.2.63}$$

Typically, $\delta \approx 0.01$. The resulting d_0 and γ_0 can be used to find the new solutions.

This iterative approach to the solution somewhat ameliorates the $\rho_{bl} = E_{bl}$ approximation in Equation A.2.24. The resulting larger ρ_{bl} solution is very close to satisfying the unapproximated equation (Equation A.2.23), and while the smaller ρ_{bl} solution is still too high (it really requires a slightly higher δ) it is also improved.

Finally, to ensure no solutions with large numerical error are retained, solutions with a negative b-quark or neutrino momentum magnitude are rejected and the sum of the squares

of sc_ν, ss_ν, and c_ν is required to be within the range $0.99 - 1.01$. To avoid double-counting, repeated solutions are also rejected.

A.3 Colliding parton z-momenta

The z-momenta $p^z_{q_i}$ of the incident partons are solved for using Equations 5.1.10, assuming massless colliding partons with no transverse momentum:

$$(|\vec{q_1}| + |\vec{q_2}|) \simeq E_{bh} + E_{bl} + E_{j_1} + E_{j_2} + \rho_e + \rho_\nu \tag{A.3.1}$$
$$(|\vec{q_1}| - |\vec{q_2}|) \simeq p^z_{j_1} + p^z_{j_2} + p^z_{bh} + p^z_{bl} + p^z_e + p^z_\nu, \tag{A.3.2}$$

where $p^z_{q_1}$ and $p^z_{q_2}$ are taken from half the sum and half the difference, i.e.

$$p^z_{q_1} = |\vec{q_1}| \tag{A.3.3}$$
$$p^z_{q_2} = -|\vec{q_2}|. \tag{A.3.4}$$

The momentum fractions x^i_{Bj} are obtained by dividing by the proton and antiproton momenta of 980 GeV/c:

$$x^1_{\mathrm{Bj}} = \frac{p^z_{q_1}}{980} \tag{A.3.5}$$
$$x^2_{\mathrm{Bj}} = \frac{p^z_{q_2}}{980}. \tag{A.3.6}$$

Appendix B

Jet Energy Transfer Function Normalisation

Each of the jet Energy Transfer Functions (ETFs) have the form (Equation 6.1.2)

$$W_E^i(E'_j - E_p) = W_E^i(\delta) = \frac{1}{\sqrt{2\pi}(p_2 + p_3 p_5)} \left[e^{\frac{-(\delta - p_1)^2}{2p_2^2}} + p_3 \cdot e^{\frac{-(\delta - p_4)^2}{2p_5^2}} \right], \tag{B.0.1}$$

where $E'_j = E_j - \Delta_{\text{JES}} \cdot \sigma_j$ (Equation 4.3.1) and the normalisation, from the requirement that

$$\frac{1}{N_{W_E}} \int_0^\infty W_E(E'_j - E_p) dE_j = 1, \tag{B.0.2}$$

is given by

$$N_{W_E} = \int_{C_0}^\infty W_E(E'_j - E_p) \frac{dE_j}{dE'_j} dE'_j, \tag{B.0.3}$$

where $C_0 = -\Delta_{\text{JES}} \cdot \sigma_j(0) = -\Delta_{\text{JES}} \cdot l_1/s$ from the change of variables.

Since σ_j is defined in two parts (Equation 6.1.9),

$$\begin{aligned} \sigma_j &\equiv H(67 - E_j s)\,(k_1 E_j + l_1/s) + H(E_j s - 67)\,(k_2 E_j + l_2/s) \\ s &\equiv \sin(\theta_j), \end{aligned}$$

the integral is also split into two parts: $C_0 \leq E'_j \leq C$ and $C \leq E'_j \leq \infty$, where C represents the cut-off point between the two functions at $E_T = 67$ GeV, expressed in terms of E'_j:

$$C = 67/s - \Delta_{\mathrm{JES}} \cdot \sigma_j(67/s) = \frac{67 - 67k_1\Delta_{\mathrm{JES}} - l_1\Delta_{\mathrm{JES}}}{s}. \tag{B.0.4}$$

That gives

$$N_{W_E} = \int_{C_0}^{C} W_E(E'_j - E_p)\frac{dE_j}{dE'_j}dE'_j + \int_{C}^{\infty} W_E(E'_j - E_p)\frac{dE_j}{dE'_j}dE'_j \tag{B.0.5}$$

$$N_{W_E} = \int_{C_0}^{C} W_E(E'_j - E_p)\frac{1}{1 - k_1\Delta_{\mathrm{JES}}}dE'_j + \int_{C}^{\infty} W_E(E'_j - E_p)\frac{1}{1 - k_2\Delta_{\mathrm{JES}}}dE'_j. \tag{B.0.6}$$

The result has several error functions (Erf):

$$\begin{aligned} N_{W_E} = {} & \frac{p_2\mathrm{Erf}\left(\frac{E_p - C_0 + p_1}{\sqrt{2}p_2}\right) - p_2\mathrm{Erf}\left(\frac{E_p - C + p_1}{\sqrt{2}p_2}\right) + p_3p_5\mathrm{Erf}\left(\frac{E_p - C_0 + p_4}{\sqrt{2}p_5}\right) - p_3p_5\mathrm{Erf}\left(\frac{E_p - C + p_4}{\sqrt{2}p_5}\right)}{2(1 - k_1\Delta_{\mathrm{JES}})(p_2 + p_3p_5)} \\ & + \frac{p_2 + p_3p_5 + p_2\mathrm{Erf}\left(\frac{E_p - C + p_1}{\sqrt{2}p_2}\right) + p_3p_5\mathrm{Erf}\left(\frac{E_p - C + p_4}{\sqrt{2}p_5}\right)}{2(1 - k_2\Delta_{\mathrm{JES}})(p_2 + p_3p_5)}. \end{aligned} \tag{B.0.7}$$

Bibliography

[1] B. N. Mohr. "A Precise Measurement of the Top Quark Mass". Ph.D. thesis, FERMILAB-THESIS-2007-05, CDF Internal Note 8793 (2007). 2, 46, 60, 68, 85, 88, 103, 106

[2] I. J. R. Aitchison, A. J. G. Hey & D. F. Brewer. "Gauge Theories in Particle Physics - a Practical Introduction. Volume 1: From Relativistic Quantum Mechanics to QED". Institute of Physics Publishing (2003). 3

[3] I. J. R. Aitchison, A. J. G. Hey & D. F. Brewer. "Gauge Theories in Particle Physics - a Practical Introduction. Volume 2: Non-Abelian Gauge Theories: QCD and the Electroweak Theory". Institute of Physics Publishing (2004). 3

[4] P. Renton. "Electroweak Interactions: An Introduction to the Physics of Quarks and Leptons". Cambridge, UK: Univ. Pr. (1990) 596 p. 3

[5] Tevatron Electroweak Working Group. "Combination of CDF and D0 Results on the Mass of the Top Quark". 3, 141

[6] David J. Gross & Frank Wilczek. "Asymptotically Free Gauge Theories. I". *Phys. Rev. D*, **8**, 10 (1973) 3633–3652. 3

[7] H. David Politzer. "Asymptotic Freedom: An Approach to Strong Interactions". *Phys. Rept.*, **14** (1974) 129–180. 3

[8] S. L. Glashow. "Partial Symmetries of Weak Interactions". *Nucl. Phys.*, **22** (1961) 579–588. 4

[9] A. Salam & J.C. Ward. "Electromagnetic and weak interactions". *Physics Letters*, **13**, 2 (1964) 168 – 171. ISSN 0031-9163. `http://www.sciencedirect.com/science/article/B6X44-46WWKCF-1H/2/136cded64929fb60240a06a75f99f18c` 4

[10] Steven Weinberg. "A Model of Leptons". *Phys. Rev. Lett.*, **19**, 21 (1967) 1264–1266. 4

[11] Peter W. Higgs. "Broken Symmetries and the Masses of Gauge Bosons". *Phys. Rev. Lett.*, **13**, 16 (1964) 508–509. 6

[12] C. Amsler et al. "Review of particle physics". *Phys. Lett.*, **B667** (2008) 1. 7, 55, 60

[13] L. Wolfenstein. "Violation of CP Invariance and the Possibility of Very Weak Interactions". *Phys. Rev. Lett.*, **13**, 18 (1964) 562–564. 7

[14] S. W. Herb, D. C. Hom, L. M. Lederman, J. C. Sens, H. D. Snyder, J. K. Yoh, J. A. Appel, B. C. Brown, C. N. Brown, W. R. Innes, K. Ueno, T. Yamanouchi, A. S. Ito, H. Jöstlein, D. M. Kaplan & R. D. Kephart. "Observation of a Dimuon Resonance at 9.5 GeV in 400-GeV Proton-Nucleus Collisions". *Phys. Rev. Lett.*, **39**, 5 (1977) 252–255. 7

[15] F. Abe et al. "Observation of top quark production in $\bar{p}p$ collisions". *Phys. Rev. Lett.*, **74** (1995) 2626–2631. 7, 53

[16] S. Abachi et al. "Observation of the top quark". *Phys. Rev. Lett.*, **74** (1995) 2632–2637. 7, 53

[17] Nikolaos Kidonakis & Ramona Vogt. "Theoretical top quark cross section at the Fermilab Tevatron and the CERN LHC". *Physical Review D (Particles and Fields)*, **78**, 7 (2008) 074005. `http://link.aps.org/abstract/PRD/v78/e074005` 8

[18] The CDF Collaboration: T. Aaltonen et al. "First Observation of Electroweak Single Top Quark Production". *submitted to Phys. Rev. Lett.*. `http://arxiv.org/abs/0903.0885v3` 8

[19] The DØ Collaboration: V.M. Abazov et al. "Observation of Single Top Quark Production". *submitted to Phys. Rev. Lett.*. `http://arxiv.org/abs/0903.0850v1` 8

[20] Nikolaos Kidonakis. "Single top quark production at the Fermilab Tevatron: Threshold resummation and finite-order soft gluon corrections". *Physical Review D (Particles and Fields)*, **74**, 11 (2006) 114012. `http://link.aps.org/abstract/PRD/v74/e114012` 9

[21] S. Heinemeyer, W. Hollik, D. Stöckinger, A. M. Weber & G. Weiglein. "Precise prediction for M_W in the MSSM". *Journal of High Energy Physics*, **8** (2006) 52–+. 12, 13

[22] FNAL Accelerator Division. "Operations Rookie Books". `http://www-bdnew.fnal.gov/operations/rookie_books/rbooks.html` 14

[23] R. Blair et al. "The CDF-II detector: Technical design report". FERMILAB-PUB-96-390-E. 14

[24] J. Marriner. "Stochastic cooling overview". *Nuclear Instruments and Methods in Physics Research A*, **532** (2004) 11–18. 15

[25] Anthony Allen Affolder et al. "CDF central outer tracker". *Nucl. Instrum. Meth.*, **A526** (2004) 249–299. 20

[26] D. Acosta, S. Klimenko, J. Konigsberg, A. Korytov, G. Mitselmakher, V. Necula, A. Nomerotsky, A. Pronko, A. Sukhanov, A. Safonov, D. Tsybychev, S. M. Wang & M. Wong. "The performance of the CDF luminosity monitor". *Nuclear Instruments and Methods in Physics Research Section A: Accelerators, Spectrometers, Detectors and Associated Equipment*, **494**, 1-3 (2002) 57 – 62. ISSN 0168-9002. `http://www.sciencedirect.com/science/article/B6TJM-46MC72K-7/2/ed5217079fb6c43833b35f53dc2c73de` 24

[27] Vaia Papadimitriou. "Luminosity measurements at hadron colliders". *Nuclear Instruments and Methods in Physics Research Section A: Accelerators, Spectrometers, Detectors and Associated Equipment*, **598**, 1 (2009) 14 – 18. ISSN 0168-9002. Instrumentation for Collding Beam Physics - Proceedings of the 10th International Conference on Instrumentation for Colliding Beam Physics. `http://www.sciencedirect.com/science/article/B6TJM-4T9M5YK-1/2/8426ffa4d6912c9ab9b85d339f3e6955` 24

[28] C Hays et al. "The COT Pattern Algorithm and Offline Code". CDF Note 6992 (2004). 28

[29] S. Lai et al. "An updated measurement of beam width at CDF". CDF Note 6492 (2003). 29

[30] F. Abe et al. "The Topology of three jet events in $\bar{p}p$ collisions at $\sqrt{s} = 1.8$ TeV". *Phys. Rev.*, **D45** (1992) 1448–1458. 29

[31] A. Bhatti et al. "Determination of the Jet Energy Scale at the Collider Detector at Fermilab". *Nucl. Instrum. Meth.*, **A566** (2006) 375–412. `http://arxiv.org/abs/hep-ex/0510047v1` 29, 32, 33

[32] T. Affolder et al. "Measurement of the top quark mass with the collider detector at Fermilab". *Physical Review D*, **63**, 3 (2001) 032003–+. 32

[33] A. Abulencia et al. "Measurement of the $t\bar{t}$ production cross section in $p\bar{p}$ collisions at $s = 1.96$ TeV using lepton+jets events with jet probability b-tagging". *Phys. Rev. D*, **74**, 7 (2006) 072006. 39, 40, 41

[34] T. Aaltonen et al. "Search for standard model Higgs boson production in association with a W boson at CDF". *Phys. Rev. D*, **78**, 3 (2008) 032008. 41

[35] T. Schwartz et al. "Method 2 Backgrounds for 1.12/fb Lepton+Jets Analyses". CDF Note 8766 (April 2007). 41, 49

[36] Torbjorn Sjostrand, Stephen Mrenna & Peter Skands. "PYTHIA 6.4 Physics and Manual". *JHEP*, **05** (2006) 026. 44, 60

[37] Michelangelo L. Mangano, Mauro Moretti, Fulvio Piccinini, Roberto Pittau & Antonio D. Polosa. "ALPGEN, a generator for hard multiparton processes in hadronic collisions". *JHEP*, **07** (2003) 001. 44

[38] Johan Alwall et al. "MadGraph/MadEvent v4: The New Web Generation". *JHEP*, **09** (2007) 028. 44

[39] H. L. Lai et al. "Global QCD analysis of parton structure of the nucleon: CTEQ5 parton distributions". *Eur. Phys. J.*, **C12** (2000) 375–392. 44, 60

[40] T. Schwartz et al. "Method II For You". CDF Note 9185 (February 2008). `http://www-cdf.fnal.gov/internal/physics/top/m2fu.shtml` 49

[41] Gregory Mahlon & Stephen J. Parke. "Angular correlations in top quark pair production and decay at hadron colliders". *Phys. Rev.*, **D53** (1996) 4886–4896. 58

[42] G. Peter Lepage. "A new algorithm for adaptive multidimensional integration". *Journal of Computational Physics*, **27**, 2 (1978) 192 – 203. ISSN 0021-9991. http://www.sciencedirect.com/science/article/B6WHY-4DD1X6M-1JP/2/eb68cbb6f3cbbf51002f1542f1716ddf 62

[43] F. A. Berends, H. Kuijf, B. Tausk & W. T. Giele. "On the production of a W and jets at hadron colliders". *Nuclear Physics B*, **357**, 1 (1991) 32 – 64. ISSN 0550-3213. http://www.sciencedirect.com/science/article/B6TVC-470F3NH-44/2/b7f8a26ceb2b0a83c16cbc979951c220 66

[44] F. James. "MINUIT - Function Minimization and Error Analysis - Reference Manual" (2000). http://wwwasdoc.web.cern.ch/wwwasdoc/minuit/minmain.html 70

[45] Wolfram Research Inc. "Mathematica Version 7.0". Champaign, IL (2008). 96

[46] J. Adelman & E. Brubaker. "The Bootstrap Technique and its Application to Analyses in the Top Mass Group". CDF Note 9081 (October 2007). 109

[47] G. Corcella et al. "HERWIG 6.5 release note". 126

[48] Victor S. Fadin, Valery A. Khoze & Alan D. Martin. "How suppressed are the radiative interference effects in heavy instable particle production?" *Phys. Lett.*, **B320** (1994) 141–144. 128

[49] J. Adelman & E. Brubaker. "b-JES systematic uncertainties for top quark mass measurements". CDF Note 9353 (June 2008). 129

[50] P. Renton. Private communication. 141